Lattice QCD Calculation of Beyond the Standard Model Kaon Mixing at the Physical Point

Julia Kettle

Doctor of Philosophy
The University of Edinburgh
December 2019

Abstract

This thesis presents beyond the standard (BSM) model kaon mixing results calculated on the lattice with simulations at the physical light quark mass. These results were calculated using RBC-UKQCD 2+1 flavour domain wall fermion simulations at the iso-spin symmetric limit, with pion masses ranging from the physical value up to 430 MeV. This thesis presents the bare results of BSM kaon mixing bag parameters and ratios, alongside strange and light meson masses and decay constants, it then details the renormalisation procedure and chiral continuum extrapolation. Finally the renormalised continuum physical point results of beyond the standard model bag parameters, ratio parameters and matrix elements and the standard model bag parameter are presented. The beyond the standard model kaon mixing matrix elements will improve upon previous calculations' precision, and these results will help address previous tensions seen in some of the BSM matrix elements. These quantities are important in the search for new physics.

Declaration

I declare that this thesis has been composed by myself and that the work has not been submitted for any other degree or professional qualification. I confirm that the work submitted is my own, except where work which has formed part of jointly-authored publications has been included. My contribution and those of the other authors to this work have been explicitly indicated below. I confirm that appropriate credit has been given within this thesis where reference has been made to the work of others. Some of the work presented in chapters 3, 4 and 5 is to be published (in preparation) [authors P.A. Boyle, N. Garron, R.J. Huspith, A. Juttner, **J. Kettle**, A. Khamseh, A. Soni, J.T. Tsang]. This study was conceived by all of the authors. All the data analysis presented in chapter 3 is my own work, using the UKQCD software UKhadron. An independent analysis was carried out by R.J Hudspith but did not enter the final results. The calculation of the propagators and vertex functions in chapter 4 was completely my work. This was done using RBC-UKQCDs Grid software, which I contributed to, writing the portion which performed the calculation of the landau-gauge fixed momentum source propagators, and bilinear and four-quark vertex functions as presented in chapter 4. All further stages of the calculation for the renormalisation were carried out by myself only, with C++ code written independently by myself. I carried out the continuum chiral extrapolation presented in chapter 5 using Python code I developed. This extrapolation was independently performed by N. Garron as a cross-check. The systematic error strategy was jointly decided by all authors. The gauge configurations were calculated by RBC-UKQCD as presented in papers [31][39]. The calculation of the propagators and correlations functions used in chapter 3 were calculated by RBC-UKQCD, with particular credit to Justus Tobias Tsang, as presented in [39].

Parts of this work have been published in [37] [36] .

(*Julia Kettle, December 2019*)

Acknowledgements

I want to thank my supervisor Peter Boyle, for all his work, and guidance throughout my PhD. I am grateful to all those who have given their time and insight freely, including everyone in RBC-UKQCD for their discussion and input, with special mention Justus Tobias Tsang, Ava Khamseh, Renwick, Jamie Hudspith, and Andreas Juettner, and especially Nicolas Garron for their invaluable contributions.

Thank you Anthony for being there throughout all the stresses and strains of the PhD, especially these past six months. And finally, thank you Mum for the lifetime of love and support, there's no way I would have been able to get here without it.

Lay Summary

The standard model of particle physics describes the fundamental particles and the three fundamental forces; the weak, strong and electromagnetic interactions. The standard model cannot describe some observed phenomenon such as gravity, and why there is more matter than antimatter. Therefore there is a search for new physics in order to extend the standard model.

One area of interest in this search is charge parity violation. If charge parity symmetry were conserved the laws of physics would look identical when a particle was swapped for its antiparticle and all space coordinates are simultaneously reversed. Charge parity (CP) is violated in the standard model by the weak force. However, the amount is too small to explain why a much larger amount of matter than anti-matter was created in the early universe. Therefore studying CP violation is considered fruitful in the search for new physics.

Kaon mixing is when a kaon, consisting of a strange quark and down quark, decays to its anti-particle and vice versa. It violates CP symmetry, and is responsible for the CP violation observed in many kaon decays. The amplitude of the kaon mixing operator in the standard model is connected to a measure of the degree of CP violation ϵ_K. It is possible to formulate four other operators that could be responsible for kaon mixing beyond the standard model, which can help in the search for new physics.

Lattice QCD is a method for calculating low energy interactions of hadrons, such as kaons, in which space-time is discretised into a 4D finite lattice to allow for a numerical calculation. In this thesis I perform a calculation of the BSM kaon mixing operators using lattice QCD. This calculation is the first to include lattices with quark masses equal to their true physical value, allowing for a better controlled extrapolation. The results here address, and help resolve, a tension that was seen between past calculations of these BSM kaon mixing operators.

Contents

List of Figures

List of Tables

Chapter 1

The Standard Model

The standard model (SM) of particle physics describes the behaviour of the fundamental particles under the strong, weak and electromagnetic forces. Whilst it is a very successful model, it does have shortcomings. For example: it is unable to account for (to the best of our knowledge) the degree of baryogenesis in the primordial universe; the fine-tuning problem; neutrino oscillations; the lack of unification; that it does not describe gravity. The shortcomings have led to a search for new physics beyond the standard model (BSM). The matter anti-matter asymmetry resulting from baryogenesis in particular points to charge-parity violation as an area in which to search for new physics. The primary motivation of this thesis is to explore BSM kaon-mixing interactions which violate charge-parity. In order to do this, we must first understand the background theory of the Electroweak sector, in which charge-parity is observed, and QCD which describes the interactions of strongly bounded hadrons, such as kaons. We will explore both of these topics and then go on to describe models of BSM kaon mixing in this chapter.

1.1 Quantum-Chromodynamics

The strong interaction is described by the non-abelian gauge theory Quantum-chromodynamics (QCD). It is based upon the gauge group $SU(3)_c$, acting upon

colour. Its Lagrangian is given by,

$$\mathcal{L}_{QCD} = \bar{\psi}_f(x)(i\not{D} - m_f)\psi_f(x) - \frac{1}{4}F^a_{\mu\nu}F^{a\mu\nu}, \tag{1.1}$$

where f indicates the quark flavours over which there is an implicit sum. The first term on the right contains the interaction between the quarks and the gluon gauge fields in the covariant derivative,

$$D_\mu\psi(x) = (\partial_\mu + igA^a_\mu t^a)\psi(x), \tag{1.2}$$

where t^a are the generators of the Lie algebra. The second term is the field strength tensor,

$$F^a_{\mu\nu} = \partial_\mu A^a_\nu + \partial_\nu A^a_\mu + gf^{abc}A^b_\mu A^c_\nu, \tag{1.3}$$

where g is the QCD coupling and f^{abc} are the structure constants of SU(3). There are 8 gluon gauge fields.

The QCD coupling is weak at high energies and strong at low energies. One consequence is colour confinement, in which colour singlets cannot exist, and instead quarks are bound within colour neutral hadrons. When considering the interaction of these hadrons, even if the interaction is an electromagnetic or weak interaction, QCD must be considered. On top of this, at the hadronic scale QCD cannot be studied with perturbation theory. This necessitates the use of the non-perturbative method of lattice QCD for the study of weak interactions of hadrons as will be discussed in chapter 2.

1.1.1 Chiral Symmetry

Consider the massless QCD Lagrangian,

$$\mathcal{L}_{QCD} = -\frac{1}{4}F^a_{\mu\nu}F^{\mu\nu}_a + i\bar{\psi}(x)\gamma^\mu D_\mu\psi, \tag{1.4}$$

where the quark fields ψ can be decomposed into their left and right handed components,

$$\begin{aligned} &\psi = \psi_L(x) + \psi_R(x) \ \ , \ \ \psi_{R/L}(x) = P_{R/L}\psi \\ &\bar{\psi}(x) = \bar{\psi}_L(x) + \bar{\psi}_R(x) \ \ , \ \ \bar{\psi}_{R/L}(x) = P_{L/R}\bar{\psi}(x). \end{aligned} \tag{1.5}$$

The chiral projectors are,

$$P_L = \frac{1-\gamma_5}{2} \quad , \quad P_R = \frac{1+\gamma_5}{2}. \tag{1.6}$$

This massless Lagrangian is invariant under the transformations,

$$\begin{aligned} \psi_L &\to U_L \psi_L, \\ \psi_R &\to U_R \psi_R, \end{aligned} \tag{1.7}$$

where $U_{L,R}$ are unitary matrices in the N_f dimension flavour space. The associated conserved currents are,

$$j^\mu_{L,R} = \bar{\psi}_{L,R} \frac{\sigma^a}{2} \gamma^\mu \psi_{L,R}, \tag{1.8}$$

where σ^a are the Pauli matrices if $N_f = 2$. The vector and axial currents come from,

$$\begin{aligned} j^{a\mu}_V &= j^\mu_R + j^\mu_L = \bar{\psi} \frac{\sigma^2}{2} \gamma^\mu \psi \\ j^{b\mu}_A &= j^\mu_R - j^\mu_L = \bar{\psi} \frac{\sigma^2}{2} \gamma^\mu \gamma_5 \psi. \end{aligned} \tag{1.9}$$

From these currents we can define the charges Q_a and Q_{5a} which have the algebra,

$$[Q_a, Q_b] = i\epsilon_{abc} Q_c \ \ ; \ \ [Q_{5a}, Q_b] = i\epsilon_{abc} Q_{5c} \ \ ; \ \ [Q_{5a}, Q_{5b}] = i\epsilon_{abc} Q_c. \tag{1.10}$$

Spontaneous Chiral Symmetry Breaking

The chiral group $SU_L(N_f) \times SU_R(N_f)$ breaks spontaneously to the subgroup $SU(N_f)$. Therefore the QCD vacuum satisfies,

$$Q_a \left|0\right\rangle = 0, \quad Q_{5a} \left|0\right\rangle \neq 0. \tag{1.11}$$

Considering $N_f = 2$ (which includes the up and down quarks which have masses well below the QCD scale) there are three massless spin-0 pseudoscalar bosons. In actuality, we don't have massless pseudoscalars, instead there are the three light psuedoscalar mesons, π^0, π^+, π^-. When considering the full $N_f = 3$ theory the pseudoscalar octet takes the place of the 8 spin-0 pseudoscalar bosons. The masses of these mesons are much lower than a typical hadronic mass. These mesons are

pseudo-Goldstone bosons as chiral symmetry is not exact. It is broken explicitly by the finite quark masses,

$$\mathcal{L}_{QCD,mass} = m_f \bar{\psi}_f \psi_f = m(\bar{\psi}_{f,L}\psi_{f,R} + \bar{\psi}_{f,R}\psi_{f,L}). \tag{1.12}$$

The quark condensate,

$$\langle 0|\bar{q}q|0\rangle \neq 0, \tag{1.13}$$

is the order parameter of this Spontaneous Chiral Symmetry Breaking (SCSB).

1.1.2 Chiral Perturbation Theory

Given the separation of scales of the pseudoscalar octet and the rest of the hadronic spectrum it is possible to build an effective theory with only the Goldstone pseudoscalars. In fact let us first consider an effective theory containing only the three pion pseudo-Goldstone bosons of $SU(2)_L \otimes SU(2)_R$ chiral symmetry. In this chiral effective theory the quark masses and momenta are used for power counting. The lowest order Lagrangian $\mathcal{L}_2$ can be written in terms of a variable,

$$U(\phi) = \exp(i\Theta(x)/f), \tag{1.14}$$

where f is a low energy constant (LEC) and σ_i are the Pauli matrices such that,

$$\Theta(x) \equiv \frac{\sigma_i}{\sqrt{2}}\phi_i = \begin{pmatrix} \pi^0/\sqrt{2} & \pi^+ \\ \pi^- & -\pi^0/\sqrt{2} \end{pmatrix}. \tag{1.15}$$

We then have an expression for the leading order chiral effective theory Lagrangian,

$$\mathcal{L}_2 = \frac{f^2}{8} tr(\partial_\mu U^\dagger \partial^\mu U) + \frac{f^2}{8} tr(U^\dagger \chi + \chi^\dagger U), \tag{1.16}$$

where $\chi = 2B\mathrm{diag}(m_l, m_l)$, and B is a low energy constant and m_l the mass of the light quarks. We follow the conventions of [2]. The LEC f is the pion decay constant at leading order, $f_\pi \approx 130\mathrm{MeV}$.

Since we are interested in the kaon sector we wish to reintroduce the kaon sector to $SU(2)$ chiral perturbation theory. The kaon fields are expressed as,

$$K = \begin{pmatrix} K^+ \\ K^0 \end{pmatrix} \qquad K^\dagger = \begin{pmatrix} \bar{K}^0 & K^- \end{pmatrix}. \tag{1.17}$$

The interaction of kaons with pions is given at leading order by the Lagrangian,

$$\mathcal{L}_K^{(1)} = D_\mu K^\dagger D^\mu K - M^2 K^\dagger K, \tag{1.18}$$

where the covariant derivative is constructed with the vector field V_μ,

$$D_\mu K = \partial_\mu K + V_\mu K, \tag{1.19}$$

which gives the interaction with the pion fields,

$$V_\mu = \frac{1}{2}(u\partial_\mu u^\dagger + u^\dagger \partial_\mu u), \tag{1.20}$$

where $u = \sqrt{(U)}$. The kaon masses are treated as order zero in the power counting scheme. The NLO Lagrangian is given in [2]. The expressions for the chiral expansions of the key quantities in this thesis can be found in [40].

1.2 The Electroweak sector

At high energy scales the interactions in the electroweak (EW) sector are described by the symmetry group $SU(2)_L \otimes U(1)_Y$. The Lagrangian for the electroweak sector at this scale (before spontaneous symmetry breaking (SSB)) is given by four parts:

$$\mathcal{L}_{EW} = \mathcal{L}_{Yukawa} + \mathcal{L}_{gauge} + \mathcal{L}_{Higgs} + \mathcal{L}_{fermion}. \tag{1.21}$$

The Yukawa term describes the interactions between the fermions and the higgs field,

$$\mathcal{L}_{Yukawa} = -Y^u_{ij} h^\dagger \overline{Q}_i u_j - Y^d_{ij} h \overline{Q}_i d_j - Y^e_{ij} h \overline{L}_i e_j - Y^\nu_{ij} h^\dagger \overline{L}_i \nu_j + h.c.\,, \tag{1.22}$$

where h is the higgs particle, Y_{ij} is the Yukawa coupling and where Q is the left-handed quark doublet, u and d are the right handed up and down quark singlets respectively, L is the left handed lepton doublet, and e and ν are the right handed lepton singlet and right handed neutrino. The fermion term is,

$$\mathcal{L}_{fermion} = \overline{Q_i} i \not{D} Q_i + \overline{u_i} i \not{D} u_i + \overline{d_i} i \not{D} d_i + \overline{L_i} i \not{D} L_i, + \overline{e_i} i \not{D} e_i \tag{1.23}$$

where L and i are the left-handed doublet and right-handed singlet leptons. The Higgs term is,

$$\mathcal{L}_{Higgs} = |D_\mu h|^2 - \lambda(|h|^2 - \frac{v^2}{2})^2, \tag{1.24}$$

and the term describing the Gauge bosons is,

$$\mathcal{L}_{gauge} = -\frac{1}{4} W_a^{\mu\nu} W^a_{\mu\nu} - \frac{1}{4} B^{\mu\nu} B_{\mu\nu} \tag{1.25}$$

The gauge bosons of the EW sector are the three isospin gauge bosons, W^a and the hypercharge gauge boson B. Spontaneous symmetry breaking to $U(1)_{em}$ gives rise to the two massive weak bosons, $W^\pm$ and Z^0, and the massless electromagnetic vector boson, the photon (γ).

For our purposes we are concerned mainly with the parts of the Lagrangian describing the weak interactions; the neutral and charged currents. The neutral current Lagrangian can be written as,

$$\mathcal{L}_{NC} = e J^{em}_\mu A^\mu + \frac{g}{cos\theta_W} (J^3_\mu - sin^2\theta_W J^{em}_\mu) Z^\mu \tag{1.26}$$

where,
$$J^{em}_\mu = \sum_f Q_f \overline{f} \gamma_\mu f \tag{1.27}$$
$$J^3_\mu = \sum_f I^3_f \overline{f} \gamma_\mu \frac{1-\gamma^5}{2} f, \tag{1.28}$$

are the electromagnetic and neutral weak current respectively. I^3_f and Q_f are the third component of the isospin and the charge of the left handed fermion f_L. g is the $SU(2)_L$ coupling constant. The charged current Lagrangian is,

$$\mathcal{L}_{CC} = \frac{-g}{2\sqrt{2}} (J^+_\mu W^{+\mu} + J^-_\mu W^{-\mu}), \tag{1.29}$$

where,

$$J^+_\mu = \bar{u}_f \gamma_\mu (1-\gamma_5) d'_f + \bar{\nu}_l \gamma_\mu (1-\gamma_5) l. \tag{1.30}$$

$\bar{u}_f = \{\bar{u}, \bar{c}, \bar{t}\}$ and $d'_f = \{d', s', b'\}$ are weak eigenstates. l indicate the leptons $\{e, \mu, \sigma\}$ while $\bar{\nu}_l$ are the corresponding anti-neutrinos. This charged

current interaction is flavour changing, whereby fermions interact as their weak eigenstates, allowing for flavour mixing.

1.2.1 CKM Matrix

The Cabibbo Kobayashi Maskawa (CKM) matrix [85] describes the mixing between the weak and mass eigenstates of the left-handed fermions; d, s and b,

$$\begin{pmatrix} d' \\ s' \\ b' \end{pmatrix} = \begin{pmatrix} V_{ud} & V_{us} & V_{ub} \\ V_{cd} & V_{cs} & V_{cb} \\ V_{td} & V_{ts} & V_{tb} \end{pmatrix} \begin{pmatrix} d \\ s \\ b \end{pmatrix} = \hat{V}_{CKM} \begin{pmatrix} d \\ s \\ b \end{pmatrix} \tag{1.31}$$

It is the extension of the four quark mixing matrix, described by a single Cabibbo angle [53]. The CKM matrix determines the amount of flavour changing observed in the charged weak interactions. It is a unitary matrix $\hat{V}_{CKM}\hat{V}^{\dagger}_{CKM} = 1$. The elements of the CKM matrix can have an imaginary component with the consequence of charge parity violation $V_{ij} \neq V^{*}_{ji}$.

The CKM matrix can be parametrised by three mixing angles θ_{ij} and a phase δ,

$$\hat{V}_{CKM} = \begin{pmatrix} c_{12}c_{13} & s_{12}c_{13} & s_{13}e^{-i\delta} \\ -s_{12}c_{23} - c_{12}s_{23}s_{13}e^{i\delta} & c_{12}c_{23} - s_{12}s_{23}s_{13}e^{i\delta} & s_{23}c_{13} \\ s_{12}s_{23} - c_{12}c_{23}s_{13}e^{i\delta} & -c_{12}s_{23} - s_{12}c_{23}s_{13}e^{i\delta} & c_{23}c_{13} \end{pmatrix}. \tag{1.32}$$

$s_{ij} = \sin(\theta_{ij})$ and $c_{ij} = \cos(\theta_{ij})$.

From experiment it is known that $s_{13} \ll s_{23} \ll s_{12} \ll 1$ [95]. This hierarchy can be made clear by using the Wolfenstein parametrisation [101]. This parametrisation is defined by,

$$\begin{aligned} s_{12} = \lambda \quad , \quad s_{23} = A\lambda^2 \\ s_{13}e^{i\delta} = A\lambda^3(\rho + i\eta), \end{aligned} \tag{1.33}$$

and the CKM matrix can then be written as,

$$\hat{V}_{CKM} = \begin{pmatrix} 1 - \lambda^2/2 & \lambda & A\lambda^3(\rho - i\eta) \\ -\lambda & 1 - \lambda^2/2 & A\lambda^3 \\ A\lambda^3(1 - \rho - i\eta) & -A\lambda^2 & 1 \end{pmatrix}, \tag{1.34}$$

where the size of η dictates the degree of CP violation.

1.2.2 Charge Parity Symmetry

The parity operator, $\hat{P}$ inverts all space coordinates such that $\hat{P}\psi(t,\vec{x}) = \psi(t,-\vec{x})$. Parity is conserved when a physical process is invariant under this transformation. Parity is conserved in the strong and electromagnetic interactions but parity conservation was proven to be violated in the weak sector in 1956 by Wu [102].

The charge conjugation operator, $\hat{C}$ reverses the sign of all electric charges. For Dirac fields, this corresponds to a transformation of particles into their anti-particles,

$$\hat{C}\psi = \bar{\psi}. \tag{1.35}$$

Charge Parity (CP) is conserved when a physical process is invariant under the charge conjugation and parity transformation. It is conserved in the strong and electromagnetic interaction. Evidence for charge-parity violation in the weak sector was first found in the Cronin and Fitch kaon regeneration experiment [60].

Let us consider again the charged currents of quark interactions in the weak sector, recalling that the weak eigenstates are related to the mass eigenstates via the CKM matrix, $d'_f = \hat{V}_{CKM} d_f$, where $d_f = \{d, s, b\}$. The Lagrangian can be written,

$$\mathcal{L}_{CC,q_L} = \frac{-g}{2\sqrt{2}}\left(\bar{u}_i\gamma_\mu(1-\gamma_5)W^{+\mu}V_{ij}d_j + \bar{d}_j\gamma_\mu(1-\gamma_5)W^{-\mu}V^*_{ij}u_i\right). \tag{1.36}$$

Its charge-parity conjugation is,

$$\mathcal{L}_{CC,q_L} = \frac{-g}{2\sqrt{2}}\left(\bar{u}_i\gamma_\mu(1-\gamma_5)W^{+\mu}V^*_{ij}d_j + \bar{d}_j\gamma_\mu(1-\gamma_5)W^{-\mu}V_{ij}u_i.\right) \tag{1.37}$$

It is clear to see that Charge-Parity is conserved if $V_{ij} = V^*_{ij}$. Charge-parity is violated in the weak sector because the CMK matrix is complex, and so the size of the phase δ corresponds to the degree of CP violation in the standard model.

Charge Parity violation, and the degree of it is considered a very important topic. Charge-parity violation is required to explain the imbalance of matter and antimatter observed in the universe, but the degree of violation observed in the standard-model is not great enough to explain the degree of this imbalance.

For this reason, CP violation is considered an important area in search for new physics. Given it is so small in the standard model, the background against which (potentially small) new physics contributions are seen is small, allowing for potential new physics effects to be more easily seen.

1.2.3 Charge-Parity Violation in the Kaon Sector

The Kaon sector is very important in the study of charge parity violation, as mentioned previously the first discovery of charge-parity violation was in kaon decays observed in the Cronin and Fitch experiment [60]. We observe two neutral kaon mesons, K_L and K_S, with very similar mass, but very different lifetimes. L and S refer to the long and short lifetimes. These particles were considered to be the CP eigenstates,

$$|K_+\rangle = \frac{1}{\sqrt{2}}(|K^0\rangle + |\bar{K}^0\rangle) \quad , \quad |K_-\rangle = \frac{1}{\sqrt{2}}(|K^0\rangle - |\bar{K}^0\rangle), \tag{1.38}$$

where $|K^0\rangle$ and $|\bar{K}^0\rangle$ are the strong and EM eigenstates. Consider that the primary decay modes of kaons are to pions. Pions have CP conjugation of -1. If CP were conserved then we would observe the decay of positive CP kaons to two pions, and of negative CP kaons to three pions. Given the increased mass of the three pion decay mode reduces the phase space available, this would explain the vastly different lifetimes of the two neutral kaons.

Cronin and Fitch [60] measured the decay of $|K_L\rangle$, controlling for the regeneration of $|K_S\rangle$. Even after subtracting for the regeneration of $|K_S\rangle$, they still found a statistically significant number of events in the energy region of two pions. This could only be explained by the decay of $|K_L\rangle$ into two pions, thus breaking CP conservation.

In fact the long and short lifetime eigenstates are not exact CP eigenstates but are actually admixtures,

$$\begin{aligned} |K_L\rangle &= \frac{1}{\sqrt{1+\tilde{\epsilon}}}(|K_+\rangle + \tilde{\epsilon}\,|K_-\rangle) \\ &= \frac{1}{\sqrt{2(1+\tilde{\epsilon})}}\Big((1+\tilde{\epsilon})\,|K^0\rangle + (1-\tilde{\epsilon})\,|\bar{K}^0\rangle\Big), \end{aligned} \tag{1.39}$$

and,

$$\begin{aligned} |K_S\rangle &= \frac{1}{\sqrt{1+\tilde{\epsilon}}}(|K_-\rangle + \tilde{\epsilon}\,|K_+\rangle) \\ &= \frac{1}{\sqrt{2(1+\tilde{\epsilon})}}\Big((1+\tilde{\epsilon})\,|K^0\rangle - (1-\tilde{\epsilon})\,|\bar{K}^0\rangle\Big), \end{aligned} \tag{1.40}$$

where $\tilde{\epsilon}$ is a small complex parameter.

Let us consider a more general superposition of the strong eigenstates,

$$\psi(t) = a(t)\,|K^0\rangle + b(t)\,|\bar{K}^0\rangle\,, \tag{1.41}$$

where $a(t)$ and $b(t)$ are time dependent arbitrary coefficients. $\psi(x)$ can be written as,

$$\psi(t) = \begin{pmatrix} a(t) \\ b(t) \end{pmatrix}, \tag{1.42}$$

in the subspace of $|K^0\rangle$ and $|\bar{K}^0\rangle$.

The wavefunction $\psi(x)$ must satisfy,

$$i\frac{\partial\psi}{\partial t} = H\psi, \tag{1.43}$$

where H is the Hamiltonian,

$$H = M - \frac{i}{2}\Gamma, \tag{1.44}$$

where M and Γ are Hermitian matrices, that correspond to the mass term and exponential decay respectively. If transitions between $|K^0\rangle$ and $|\bar{K}^0\rangle$ are allowed then the non-diagonal terms are non-zero. Charge-Parity-Time symmetry implies that $M/\Gamma_{11} = M/\Gamma_{22}$ and $M/\Gamma_{21} = M/\Gamma^*_{12}$, so H can be expressed,

$$H = \begin{pmatrix} M - i\Gamma & M_{12} - i\Gamma_{12} \\ M^*_{12} - i\Gamma^*_{12} & M - i\Gamma \end{pmatrix} \tag{1.45}$$

The states $|K_L\rangle$ and $|K_S\rangle$ are the eigenstates of H with eigenvalues $M_L - \frac{i}{2}\Gamma_L$ and $M_S - \frac{i}{2}\Gamma_S$ respectively. It is straightforward to show that the eigenvalues of H are,

$$\lambda_\pm = M - \frac{i}{2}\Gamma \pm \sqrt{(M_{12} - \frac{i}{2}\Gamma_{12})(M^*_{12} - \frac{i}{2}\Gamma^*_{12})}, \tag{1.46}$$

which can be written as,

$$\lambda_{\pm} = M_{\pm} + \frac{i}{2}\Gamma_{\pm} = M \mp Re(F) - \frac{i}{2}(\Gamma \pm 2Im(F)), \tag{1.47}$$

where $F = \sqrt{(M_{12} - \frac{i}{2}\Gamma_{12})(M_{12}^* - \frac{i}{2}\Gamma_{12}^*)}$, and $\lambda_S = \lambda_+$ and $\lambda_L = \lambda_-$. We then define,

$$\Delta M \equiv M_+ - M- = 2 * Re(F) \ \ , \ \ \Delta\Gamma \equiv \Gamma_+ - \Gamma_- = 4 * Im(F). \tag{1.48}$$

Recalling from equations 1.39 and 1.40 that the eigenstates have values $\begin{pmatrix} 1+\tilde{\epsilon} \\ \pm(1-\tilde{\epsilon}) \end{pmatrix}$ and using the eigenvalues to solve for these eigenstates it is straightforward to arrive at,

$$\begin{aligned} \frac{1+\tilde{\epsilon}}{1-\tilde{\epsilon}} &= \pm 2\frac{M_{12} - i\Gamma_{12}}{\Delta M + \frac{i}{2}\Delta\Gamma} \\ &= \pm\sqrt{\frac{M_{12} - \frac{i}{2}\Gamma_{12}}{M_{12}^* - \frac{i}{2}\Gamma_{12}^*}}. \end{aligned} \tag{1.49}$$

Note that the sign is determined by whether we choose $\Delta M \equiv M_{K_S} - M_{K_L}$ or $\Delta M \equiv M_{K_L} - M_{K_S}$. By choosing the former, the sign becomes positive.

Let us return to $K \to \pi\pi$ decays. Recall that the decays $K \to \pi^0\pi^0$ $K \to \pi^+\pi^-$ are both possible. We define,

$$\eta_{00} = \frac{A[K_L \to \pi^0\pi^0]}{A[K_S \to \pi^0\pi^0]}, \tag{1.50}$$

and,

$$\eta_{+-} = \frac{A[K_L \to \pi^+\pi^-]}{A[K_S \to \pi^+\pi^-]}. \tag{1.51}$$

There are two mechanisms by which the K_L can decay to $\pi\pi$: direct and indirect CP violation. Direct CP violation occurs when the dominant odd CP eigenstate in the admixture decays to $\pi\pi$, directly violating CP. Indirect CP violation occurs when the decay happens due to the small even CP portion of the admixture decaying the even CP $\pi\pi$. This indirect CP violation is a result of the mixing between K^0 and $\bar{K}^0$ responsible for admixture of the CP eigenstates in K_S and K_L.

The direct and indirect modes are parametrised through ϵ' and ϵ respectively.

They are defined by ,

$$\epsilon = \frac{A[K_L \to (\pi\pi)_0]}{A[K_S \to (\pi\pi)_0]}, \tag{1.52}$$

and,

$$\epsilon' = \frac{1}{\sqrt{2}}\left(\frac{A[K_L \to (\pi\pi)_2]}{A[K_S \to (\pi\pi)_2]} - \epsilon\frac{A[K_S \to (\pi\pi)_2]}{T[K_S \to (\pi\pi)_0]}\right), \tag{1.53}$$

where I indicates the isospin.

We can relate ϵ to $\tilde{\epsilon}$. Let us express the decay amplitudes given in equations 1.52 and 1.53 in terms of the decay amplitudes of the strong eigenstates. Let us write,

$$A[K^0 \to (\pi\pi)_{I=0}] = A_0 e^{i\delta_0}, \quad A[\bar{K}^0 \to (\pi\pi)_{I=0}] = A_0^* e^{i\delta_0}, \tag{1.54}$$

and,

$$A[K^0 \to (\pi\pi)_{I=2}] = A_2 e^{i\delta_2}, \quad A[\bar{K}^0 \to (\pi\pi)_{I=2}] = A_2^* e^{i\delta_2}, \tag{1.55}$$

where A_I includes only the weak interaction phases. The phases from the strong interaction are separated out completely in in e^{δ^I} where δ^I are the pion-pion scattering phase shifts for $\pi\pi$ scattering in the I = 0 and 2 states, and so they are the same for both the kaon and anti-kaon's decays. It is clear then, that,

$$A[K_{S/L} \to (\pi\pi)_0] = N((1+\tilde{\epsilon})A_0 \pm (1-\tilde{\epsilon})A_0^*)e^{i\delta_0}, \tag{1.56}$$

and,

$$A[K_{S/L} \to (\pi\pi)_2] = N((1+\tilde{\epsilon})A_2 \pm (1-\tilde{\epsilon})A_2^*)e^{i\delta_2}, \tag{1.57}$$

such that,

$$\begin{aligned}\epsilon &= \frac{(1+\tilde{\epsilon})A_0 + (1-\tilde{\epsilon})A_0^*}{(1+\tilde{\epsilon})A_0 - (1-\tilde{\epsilon})A_0^*} \\ &= \frac{\tilde{\epsilon} + i\frac{Im(A_0)}{Re(A_0)}}{1 + i\tilde{\epsilon}\frac{Im(A_0)}{Re(A_0)}} \\ &\approx \tilde{\epsilon} + i\frac{Im(A_0)}{Re(A_0)}.\end{aligned} \tag{1.58}$$

With some further algebra and recalling 1.49 [47],

$$\epsilon = \frac{e^{i\pi/4}}{\sqrt{2}\Delta M_K}(Im(M_{12}) + 2\frac{Im(A_0)}{Re(A_0)}Re(M_{12})). \tag{1.59}$$

Thus the degree of indirect CP violation can be related to kaon mixing, which is

responsible for M_{12} and ΔM_K. A good review of CP violation in the kaon sector is presented in [88].

1.3 Kaon Mixing

1.3.1 Kaon Mixing in the Standard Model

Kaon mixing in the standard model is a $\Delta S = 2$ flavour changing neutral current (FCNC) responsible for the off-diagonal element M_{12} in the Hamiltonian above.

$$M_{12} = \frac{\langle K^0 | H^{\Delta S=2} | \bar{K}^0 \rangle}{2M_K}. \tag{1.60}$$

This has to be a one-loop weak process, and is dominated by the box diagrams, an example of which is shown in figure 1.1. We should note that, we are neglecting

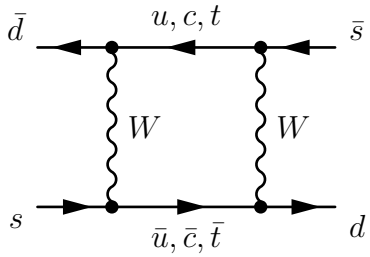

Figure 1.1 *W exchange box diagram*

long-distance contributions here. The amplitude for this diagram is,

$$\begin{aligned} -i\mathcal{M} = \left(\frac{-ig_2}{\sqrt{2}}\right)^4 \int \frac{d^4k}{(2\pi)^2} iD^W_{\mu\nu}(k) iD^W_{\rho\sigma}(k) \\ \times (\bar{v}_d \gamma_\mu (1-\gamma_5) iS(k) \gamma_\rho (1-\gamma_5) v_s) \\ \times (\bar{u}_d \gamma_\sigma (1-\gamma_5) iS(k) \gamma_\nu (1-\gamma_5) u_s) \end{aligned} \tag{1.61}$$

where u and v are the spinor wavefunctions, $D^W_{\mu\nu}(k)$ is the W boson propagator, which is,

$$D^W_{\mu\nu}(k) = \frac{-g^{\mu\nu}}{k^2 - M_W^2 + i\varepsilon}. \tag{1.62}$$

$S(k)$ is the sum of the up quark propagators,

$$S(k) = \sum_{U=u,c,t} \frac{\lambda_U}{\not{k} - m_U + i\varepsilon}, \tag{1.63}$$

where $\lambda_U = V_{Us}V_{Ud}^*$. With the help of $\sum_{U=u,c,t} V_{Us}V_{Ud}^* = 0$ $S(k)$ can be written as,

$$S(k) = \sum_{U=c,t} \frac{\lambda_U}{\not{k} - m_U + i\varepsilon} - \frac{\lambda_u}{\not{k} - m_u + i\varepsilon}. \tag{1.64}$$

From this we can see that if the up, charm and top quark had the same mass, that there would be no mixing, demonstrating the GIM mechanism [74]. With some algebra, the amplitude can be expressed as,

$$\mathcal{M} = \frac{G_F^2}{M_W^2}(\lambda_t^2 T_{tt} + \lambda_c^2 T_{cc} + 2\lambda_c\lambda_t T_{ct})(\bar{v}_d\gamma_\mu(1-\gamma_5)v_s)(\bar{u}_d\gamma^\mu(1-\gamma^5)u_s), \tag{1.65}$$

where $G_F = g_2^2/(4\sqrt{2}M_W^2)$ is the Fermi constant, and by taking $m_u = 0$,

$$T_{U_1U_2} = \frac{4i}{\pi^2 M_W^2}\int d^4k \frac{1}{k^2(1-k^2/M_W^2)}\frac{m_{U_1}^2}{k^2 - m_{U_1}^2}\frac{m_{U_2}^2}{k^2 - m_{U_2}^2}. \tag{1.66}$$

By looking at the scales of the ratios quark masses to W boson mass, alongside the CKM matrix, we can see that diagram with charm quarks dominates. Of course, here we have not included all contributing diagrams, neglecting gluonic contributions.

Operator Product Expansion and Effective Weak Hamiltonian

We instead rely on the operator product expansion. This allows us to separate out the scales of the weak Hamiltonian such that we have a short-distance portion, which can be calculated perturbatively and a long-distance part which typically is calculated non-perturbatively.

$$\mathcal{H}_{eff} = \frac{G_F}{2}\sum_i V_{CKM}^i C_i(\mu) Q(\mu)_i. \tag{1.67}$$

Q_i are the long-distance local operators which dictate the decays. $C(\mu)$ are the short-distance Wilson coefficents which, alongside the CKM factors, describe how strongly the operators enter the Hamiltonian. The scale μ is in principle arbitrary, but it is typical to choose $O(1-2GeV)$ for kaon decays, as $O(m_K)$ is too low to allow for the perturbative calculation of the Wilson coefficients. The scale of the local operators and the Wilson coefficients must be the same, as must the renormalisation scheme, so that the final amplitudes are scale and scheme independent.

For standard model kaon mixing, the $\Delta S = 2$ weak Hamiltonian including leading and next to leading QCD corrections, takes the form [47],

$$\mathcal{H}_{eff}^{\Delta S=2} = \frac{G_F^2}{16\pi^2} M_W^2 [\lambda_c^2 \eta_1 S_0(x_c) + \lambda_t^2 \eta_2 S_0(x_t) + 2\lambda_c \lambda_t \eta_3 S_0(x_c, x_t)] C'(\mu) O^{\Delta S=2}, \tag{1.68}$$

where $O_K^{\Delta S=2} = (\bar{s}\gamma_\mu(1-\gamma_5)d)(\bar{s}\gamma_\mu(1-\gamma_5)d)$ is called the four-quark operator, S_0 are the electro-weak box contributions, called the Inami Lim functions [80], η_{qq} are short-distance QCD corrections and $C'(\mu)$ is a scale dependent coefficient which cancels the running of the operator. The forms of the Inami Lim functions and short-distance QCD corrections go beyond the scope of this thesis but can further details can found in [80] and in [78][50] respectively. A thorough review can be found in [47].

Bag Parameter

At this point we introduce the standard model bag parameter, defined by,

$$\langle \bar{K}^0 | O_K^{\Delta S=2} | K^0 \rangle \equiv \frac{8}{3} B_K(\mu) f_K^2 m_K^2, \tag{1.69}$$

where f_K and m_K are the kaon decay constant and mass respectively. Using the two above equations we can directly relate the standard model bag parameter to the indirect CP violation parameter ϵ,

$$M_{12} = \frac{G_R^2}{12\pi} M_W^2 [\lambda_c^2 \eta_1 S_0(x_c) + \lambda_t^2 \eta_2 S_0(x_t) + 2\lambda_c \lambda_t \eta_3 S_0(x_c, x_t)] C'(\mu) m_K f_K^2 B_K(\mu). \tag{1.70}$$

Here we are considering only the short distance contributions. There are also long distance contributions to ϵ_K both through the dispersive M_{12} and via absorptive Γ_{12}, which arise through the insertion of two $\Delta S = 2$ operators such as shown in the Feynman diagram in figure 1.3. These long distance contributions are estimated to be of order 5% [49][58]. For a discussion and analysis of these contributions see [49] [48]. There have also been lattice calculations of long distance effects [58][17][30].

It is worth commenting on the normalisation of the bag parameter. $B_K(\mu)$ is actually defined as,

$$B_K(\mu) = \frac{\langle \bar{K}^0 | O_K^{\Delta S=2} | K^0 \rangle}{\langle \bar{K}^0 | O_K^{\Delta S=2} | K^0 \rangle_{VSA}}. \tag{1.71}$$

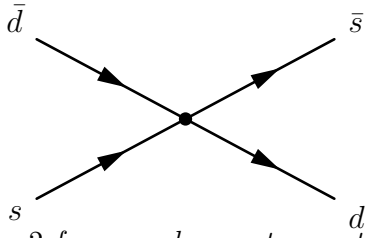

Figure 1.2 *The $\Delta S = 2$ four quark operator contribution to kaon mixing.*

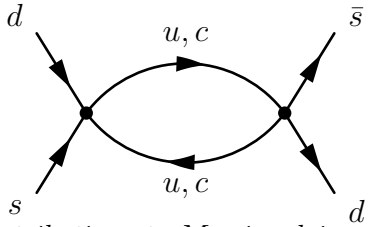

Figure 1.3 *The contributions to M_{12} involving two $\Delta S = 1$ operators.*

VSA is the vacuum saturation approximation, whereby the vacuum is inserted in all possible ways between all possible quark-antiquark pairs in the fields of the four-quark operator,

$$\begin{aligned}\langle \bar{K}^0|O_K^{\Delta S=2}|K^0\rangle_{VSA} =& 2\Big(\langle \bar{K}^0|\bar{s}_a\gamma^\mu(1-\gamma_5)d^a|0\rangle \langle 0|\bar{s}_b\gamma^\mu(1-\gamma_5)d^b|K^0\rangle \\ &+ \langle \bar{K}^0|\bar{s}_a\gamma^\mu(1-\gamma_5)d^b|0\rangle \langle 0|\bar{s}_b\gamma^\mu(1-\gamma_5)d^a|K^0\rangle \Big),\end{aligned} \tag{1.72}$$

where a, b are colour indices which are summed over. Using [88],

$$\langle 0|\bar{s}_b\gamma^\mu(1-\gamma_5)d^a|K^0(p)\rangle = -i\frac{\delta_b^a}{N_c}f_K p_\mu e^{-ip.x}, \tag{1.73}$$

where we normalise by N_c,the number of colours, we find,

$$\begin{aligned}\langle \bar{K}^0|O_K^{\Delta S=2}|K^0\rangle_{VSA} &= \frac{2}{N_c^2}f_K^2p^2[\delta_a^a\delta_b^b + \delta_a^b\delta_b^a] \\ &= 2\frac{N_c+1}{N_c}f_K^2M_K^2.\end{aligned} \tag{1.74}$$

We can see immediately how this relates to the initial expression in equation 1.69. In practice, in lattice calculations the approximation used is,

$$B_K(\mu) = \frac{\langle \bar{K}^0|O_K^{\Delta S=2}|K^0\rangle}{\frac{8}{3}\langle \bar{K}^0|\bar{s}\gamma^\mu\gamma_5 d|0\rangle \langle 0|\bar{s}\gamma^\mu\gamma_5 d|K^0\rangle}. \tag{1.75}$$

Table 1.1 *Values of $|\epsilon|$ derived from theory and from experiment in units of 10^{-3}. The theoretical values derived from the standard model differ, largely depending on the value of V_{cb} used. [42] uses $|V_{cb}| = 4.06 \times 10^{-3}$ given in [24] taken from an average of the inclusive and exclusive values. Whereas [20] presents values for both the inclusive and exclusive value of $|V_{cb}|$.*

method	ϵ_K	
experiment	2.228 ± 0.001	[95]
lattice inputs (inclusive $\|V_{cb}\|$)	2.035 ± 0.178	[20]
lattice inputs (exclusive $\|V_{cb}\|$)	1.570 ± 0.156	[20]
theory (averaged $\|V_{cb}\|$)	1.81 ± 28	[42]

1.3.2 Status of the Standard Model and Experiment

The value of ϵ as measured experimentally is very well known. The most recent value published by PDG [95] is given in table 1.1. There have been several calculations of ϵ_K in the standard model [41][42][20][19]. All calculations have taken as inputs, a mix of lattice QCD results, experimental values, and some theoretical calculations such as QCD corrections.

There does appear to be some room for new physics, but this is heavily correlated with the tension in the determination of $|V_{cb}|$. The inclusive determination is based on calculations of the semi-leptonic decay rates of B hadrons using OPE and heavy quark effective theory (HQET) frameworks. These decay rates are calculated in terms of $|V_{cb}|$, m_b and non-perturbative matrix elements [21]. The exclusive determination is done by studying the decay rate for $\bar{B}_0 \to D^{*+} l^- \bar{\nu}_l$ as a function of the recoil kinematics of the D^{*+} meson [21]. Recent studies [76][27] have suggested this tension may be resolved, with the exclusive value shifted towards the inclusive value, albeit with increased errors. A parameterisation developed by Caprini, Lellouch, and Neubert (CLN), which uses dispersion relations to bound hadronic form factors and relations at $1/m_Q$ in the heavy quark expansion, is used in the exclusive determination. [76] and [27] argue that this parameterisation does not well describe experimental data and suggest a new parameterisation, which results in this shift towards the inclusive value. However these results are in tension with Lattice QCD and heavy quark effective theory (HQET) [25]. As such more investigation would be required before any conclusive statements about the room for new physics in ϵ can be made.

The degree of direct CP violation, measured by the ratio with indirect CP violation, ϵ'/ϵ is less well known. The first observations of direct CP violation in

the kaon sector came from the NA31[52], NA48[65] and KTeV[1] collaborations. The current value [95] is given as $\mathrm{Re}(\epsilon'/\epsilon)1.65 \pm 0.26 \times 103$, showing that while direct CP violation exists it is far smaller than indirect CP. There have now been some calculations of direct CP violation in kaon decays in lattice QCD [17].

1.4 Beyond the Standard Model Kaon Mixing

Beyond the standard model a generic effective weak ($\Delta S = 2$) Hamiltonian can be constructed, in which the standard model and seven additional four-quark operators appear,

$$\mathcal{H}^{\Delta S=2} = \sum_{i=1}^{5} C_i(\mu) O_i(\mu) + \sum_{i=1}^{3} \tilde{C}_i(\mu) \tilde{O}_i(\mu), \tag{1.76}$$

where, in the so-called SUSY basis introduced in [69], the even parity operators are,

$$\begin{aligned}
O_1 &= (\bar{s}_a \gamma_\mu (1-\gamma_5) d_a)(\bar{s}_b \gamma_\mu (1-\gamma_5) d_b) \\
O_2 &= (\bar{s}_a (1-\gamma_5) d_a)(\bar{s}_b (1-\gamma_5) d_b) \\
O_3 &= (\bar{s}_a (1-\gamma_5) d_b)(\bar{s}_b (1-\gamma_5) d_a) \\
O_4 &= (\bar{s}_a (1-\gamma_5) d_a)(\bar{s}_b (1+\gamma_5) d_b) \\
O_5 &= (\bar{s}_a (1-\gamma_5) d_b)(\bar{s}_b (1+\gamma_5) d_a).
\end{aligned} \tag{1.77}$$

As parity is conserved in our framework, the domain wall fermion (DWF) discretisation of QCD, the parity transformed $\tilde{O}_i$ operators (obtained from $O_{i=1,2,3}$ by swapping the chirality [69]) can be neglected. The operators above have an odd parity contributions coming from the cross current terms, but only the parity even portion contributes in our framework and so these are neglected. The parity transformed operators, $\tilde{O}_{1,2,3}$, differ from $O_{1,2,3}$ only in the parity odd cross terms which are neglected, hence they are not considered. The operator O_1 belongs to the $(27,1)$ representation of the chiral group $(SU(3)_L \times SU(3)_R)$, while operators $O_{2,3}$ belong to the $(6,6)$ representation and $O_{4,5}$ to the $(8,8)$ group [14]. It is important to note that this basis of operators contain all linearly independent dimension 6, $\Delta S = 2$, four-quark operators with the right colour and Lorentz structure. There are other bases that it's possible to work in, such as the Buras

basis [51] but all bases are just linear transformations of each other. The operators $O_{i=1\to5}$ are model independent although the Wilson coefficents are dependent upon the model of new physics considered.

1.4.1 Bag Parameters

As for the SM, we define the BSM bag parameters as the ratios over their vacuum saturation approximations, however the VSAs take a different form,

$$\langle \bar{K}^0|O_i|K^0\rangle_{VSA} = N_i\left(\frac{M_K}{m_s(\mu)+m_d(\mu)}\right)^2 M_K^2 f_K^2 B_i(\mu), \tag{1.78}$$

where the normalisation constants are $N_i = (-5/3, 1/3, 2, 2/3)$. This definition matches the convention in [71] [14] [22] but there is some disagreement as to the best parametrisation [63].

I will comment in more detail on the lattice measurements of these parameters in chapter 2, as well as provide a brief summary of previous lattice results.

1.4.2 Ratio Parameters

An alternative parametrisation is to instead work with the ratios of the BSM matrix element to SM matrix element such that,

$$R_i(\mu) = \frac{\langle \bar{K}^0|O_i|K^0\rangle}{\langle \bar{K}^0|O_1|K^0\rangle}. \tag{1.79}$$

The use of ratios to parameterise BSM kaon mixing elements was first proposed in [63]. We follow [14] in defining the ratio parameter on the lattice as,

$$R_i\left(\frac{m_P^2}{f_P^2}, a^2, \mu\right) = \left[\frac{f_K^2}{m_K^2}\right]_{Exp.}\left[\frac{m_P^2}{f_P^2}\frac{\langle \bar{P}|O_i(\mu)|P\rangle}{\langle \bar{P}|O_1(\mu)|P\rangle}\right]_{Lat.}, \tag{1.80}$$

where m_P and f_P are the strange-light pseudo-scalar mass and decay constant, respectively, measured on the lattice. At the physical point, this form reduces to

a pure ratio of the BSM to SM matrix element:

$$R_i(\mu) = R_i\left(\frac{m_K^2}{f_K^2}, a = 0, \mu\right) = \frac{\langle \bar{K}^0 | O_i(\mu) | K^0 \rangle}{\langle \bar{K}^0 | O_1(\mu) | K^0 \rangle}. \tag{1.81}$$

By including the ratio of the mass and decay constant in the expression, the leading $1/m_P^2$ in the chiral expansion is cancelled thus the mass extrapolation is better controlled near the chiral limit. The ratio parameters have some advantages over the bag parameters. There is no explicit quark mass dependence in the expression for the ratio parameters so that the BSM matrix elements can be recovered from the ratio parameters R_i, the SM bag parameter B_1 and the experimentally measured kaon mass and decay constant only. Whereas to recover them from the BSM bag parameters requires inputting the down and strange quark mass. Additionally, the similarity of the numerator and denominator means we might expect some cancellation of errors.

1.4.3 Alternative Basis

In practice we find it convenient to work in a different basis, which we refer to as the lattice basis, and we consider only the colour-unmixed operators,

$$\begin{aligned}
Q_1 &= (\bar{s}_a \gamma_\mu (1-\gamma_5) d_a)(\bar{s}_b \gamma_\mu (1-\gamma_5) d_b) \\
Q_2 &= (\bar{s}_a \gamma_\mu (1-\gamma_5) d_a)(\bar{s}_b \gamma_\mu (1+\gamma_5) d_b) \\
Q_3 &= (\bar{s}_a (1-\gamma_5) d_a)(\bar{s}_b (1+\gamma_5) d_b) \\
Q_4 &= (\bar{s}_a (1-\gamma_5) d_a)(\bar{s}_b (1-\gamma_5) d_b) \\
Q_5 &= \frac{1}{4}(\bar{s}_a \sigma_{\mu\nu} (1-\gamma_5) d_a)(\bar{s}_b \sigma_{\mu\nu} (1-\gamma_5) d_b),
\end{aligned} \tag{1.82}$$

which are obtained by Fierz transforming the equivalent colour mixed operators, as detailed in section D of the appendix. Taking only the colour unmixed simplifies the contraction over the colour indices.

The parity even parts are,

$$
\begin{aligned}
Q_1^+ &= (\bar{s}_a\gamma_\mu d_a)(\bar{s}_b\gamma_\mu d_b) + (\bar{s}_a\gamma_\mu\gamma_5 d_a)(\bar{s}_b\gamma_\mu\gamma_5 d_b) \\
Q_2^+ &= (\bar{s}_a\gamma_\mu d_a)(\bar{s}_b\gamma_\mu d_b) - (\bar{s}_a\gamma_\mu\gamma_5 d_a)(\bar{s}_b\gamma_\mu\gamma_5 d_b) \\
Q_3^+ &= (\bar{s}_a d_a)(\bar{s}_b d_b) - (\bar{s}_a\gamma_5 d_a)(\bar{s}_b\gamma_5 d_b) \\
Q_4^+ &= (\bar{s}_a d_a)(\bar{s}_b d_b) + (\bar{s}_a\gamma_5 d_a)(\bar{s}_b\gamma_5 d_b) \\
Q_5^+ &= \sum_{\nu>\mu} (\bar{s}_a\gamma_\mu\gamma_\nu d_a)(\bar{s}_b\gamma_\mu\gamma_\nu d_b).
\end{aligned}
\tag{1.83}
$$

We refer to these operators as $VV+AA$, $VV-AA$, $SS-PP$, $SS+PP$ and TT. The lattice calculation and renormalisation, as will be detailed in the next chapters, are performed in this basis.

Chapter 2

Lattice QCD

2.1 Introduction

Lattice QCD is a non-perturbative formulation of QCD which allows for the calculation of low energy phenomena, introduced in 1974 by Kenneth Wilson in his paper "Confinement of Quarks" [100]. It involves discretising Euclidean space-time into a 4 dimensional hyper-cubic lattice, which acts as an ultra-violet regulator. This regularisation is non-perturbative allowing us to access low energy hadronic physics.

2.2 Path Integral

Lattice QCD relies upon the path integral formulation of QCD. The generating functional for a single flavour is,

$$W[\eta, \bar{\eta}, J] = \int \mathcal{D}A_\mu \mathcal{D}\psi \mathcal{D}\bar{\psi} \exp(\int d^4x \mathcal{L} + JA_\mu + \bar{\eta}\psi + \eta\bar{\psi}), \tag{2.1}$$

where J, η and $\bar{\eta}$ are the source terms and the integral is over all possible paths of the fields. A time-ordered operator O can then be found from the functional

derivative of the generating functional,

$$\begin{aligned}\langle 0|O|0\rangle &= \frac{1}{Z}\frac{\delta^j}{\delta J^j}\frac{\delta^k}{\delta \eta^k}\frac{\delta^l}{\delta \bar{\eta}^l}W[\eta,\bar{\eta},J]|_{J=\eta=\bar{\eta}=0} \\ &= \frac{1}{Z}\int \mathcal{D}A_\mu \prod_i^{n_f} \mathcal{D}\bar{\psi}^i \mathcal{D}\psi^i O e^{iS[A_\mu,\bar{\psi}^2,\psi^2]},\end{aligned} \tag{2.2}$$

where $S[A_\mu,\bar{\psi}^2,\psi^2] = \int d^4x\mathcal{L}$ is the action, i indicates the fermion flavour, j,k and l depend on the operator O and Z is the partition function, defined as,

$$Z = \int \mathcal{D}A_\mu \prod_i^{n_f} \mathcal{D}\bar{\psi}^i \mathcal{D}\psi^i e^{iS[A_\mu,\bar{\psi}^2,\psi^2]}. \tag{2.3}$$

Recall the QCD Lagrangian is,

$$\mathcal{L}(x) = \sum_i^{n_f} \bar{\psi}^i(x)(i\gamma_\mu D_\mu + m^i)\psi^i(x) - \frac{1}{2}tr(F_{\mu\nu}(x)F^{\mu\nu}(x)), \tag{2.4}$$

where we have made the x dependence and the sum over flavours explicit, and the field strength tensor is given by,

$$F_{\mu\nu}(x) = \partial_\mu A_\nu(x) - \partial_\nu A_\mu(x) + ig[A_\mu(x), A_\nu(x)], \tag{2.5}$$

where g is the QCD coupling constant. The action can be split into the fermionic and gauge parts, and as the fermionic fields are Grassman variables, they can be integrated out. We also apply a Wick rotation, $t \to it$, into Euclidean space,

$$\langle 0|O|0\rangle = \frac{1}{Z}\int \mathcal{D}A_\mu O \prod_i^{n_f} \det(i\gamma_\mu D_\mu + m^i) e^{-S_G[A_\mu]}. \tag{2.6}$$

While we have greatly simplified this expression, and the Wick rotation has allowed the paths with small action to dominate, we still have infinite possible paths and thus degrees of freedom. Thus we discretise space-time into a finite-volume hypercubic lattice, with spacing a between the lattice sites, such that the number of paths is now finite.

2.3 Discretised Action

Of course we now require a discretised version of the lattice. This discretised action must still return the continuum action as we take the lattice spacing to zero. The lattice consists of a set of fields which are either defined on the lattice sites, or on the links between the sites.

The fermion fields, $\psi(x)$, $\bar{\psi}(x)$, are placed on the lattice sites while the gauge fields exist on the lattice links. They are included via the gauge links, or parallel transport matrices, $U_\mu(x)$,

$$U_\mu(x) = e^{igA_\mu(x)}. \tag{2.7}$$

The notation here indicates a field along the path from x to $x + \hat{\mu}$.

2.3.1 Gauge Invariance

The QCD action must maintain the invariance under the local SU(3) transformations. The fermion fields transform as,

$$\begin{aligned} \psi_a(x) &\to \Omega_{ab}(x)\psi_b(x) \\ \bar{\psi}_a(x) &\to \bar{\psi}_b(x)\Omega^\dagger_{ba}(x), \end{aligned} \tag{2.8}$$

where the colour transformation has been made explicit. The colour indices will typically be dropped in the rest of this work.

Let us recall that the gauge field $A_\mu(x)$ transform as,

$$A^a_\mu \to A^a_\mu - \frac{1}{g}\partial_\mu \alpha^a - f^{abc}\alpha^b A^c_\mu. \tag{2.9}$$

The gauge links transform as,

$$U_\mu(x) \to \Omega(x)U_\mu(x)\Omega^\dagger(x+\hat{\mu}), \tag{2.10}$$

since $\Omega(x) = e^{i\alpha(x)} = e^{i\alpha^a(x)t^a}$.

2.3.2 Gauge Action

Any string of k gauge link variables connecting two points x_0 and x_1,

$$P[U] = U_{\mu_0}(x)U_{\mu_1}(x+\hat{\mu}_0)\cdots U_{\mu_k-1}(x_1-\hat{\mu}_{k-1}), \tag{2.11}$$

transforms as,

$$P[U] \to \Omega(x_0)P[U]\Omega^{\dagger}(x_1), \tag{2.12}$$

given the cancellation of the inner gauge rotations. Thus a gauge invariant object can be constructed by either including fermion fields at the start and end,

$$\bar{\psi}(x_0)P[U]\psi(x_1), \tag{2.13}$$

or by taking the trace of a closed loop, $\mathcal{L}$, of link variables,

$$L[U] = \mathrm{tr}\Big[\prod_{(x,\mu)\in\mathcal{L}} U_{\mu}(x)\Big]. \tag{2.14}$$

The plaquette $U_{\mu\nu}$ is the shortest closed loop we can construct, consisting of four link variables,

$$U_{\mu\nu} = U_{\mu}(x)U_{\nu}(x+\hat{\mu})U_{-\mu}(x+\hat{\mu}+\hat{\nu})U_{-\nu}(x+\hat{\nu}). \tag{2.15}$$

The Wilson gauge action is a sum over all plaquettes in the lattice,

$$S_G^{\mathrm{W}}[U] = \frac{\beta}{N}\sum_x\sum_{\mu<\nu}\mathrm{Re}(\mathrm{tr}[1-U_{\mu\nu}(x)]), \tag{2.16}$$

where the factor $\beta = 2N/g^2$ is so that the continuum action is recovered.

Recalling the relation between the link variables, $U_{\mu}(x)$ and the gauge field $A_{\mu}(x)$, and the Baker-Campbell-Hausdorf formula for the product of exponentials of

matrices we can write the gauge action as,

$$\begin{aligned} U_{\mu\nu} =& \exp\Big(iaA_\mu(x) + iaA_\nu(x+\hat{\mu}) - iaA_\mu(x+\hat{\nu}) - iaA_\nu(x) \\ & - a^2[A_\mu(x), A_\nu(x+\hat{\mu})] - a^2[A_\mu(x+\hat{\nu}), A_\nu(x)] \\ & + a^2[A_\mu(x), A_\mu(x+\hat{\nu})] + a^2[A_\mu(x), A_\nu(x)] \\ & + a^2[A_\nu(x+\hat{\mu}), A_\mu(x+\hat{\nu})] + a^2[A_\nu(x+\hat{\mu}), A_\nu(x)] + \mathcal{O}(a^3) \Big). \end{aligned} \tag{2.17}$$

By Taylor expanding the fields and including terms up to $\mathcal{O}(a^2)$, the plaquette reduces to,

$$\begin{aligned} U_{\mu\nu} &= e^{ia^2(\partial_\mu A_\nu(x) - \partial_\nu A_\mu(x) + i[A_\mu(x), A_\nu(x)]) + \mathcal{O}(a^3)} \\ &= e^{ia^2 F_{\mu\nu}(x) + \mathcal{O}(a^3)} \end{aligned} \tag{2.18}$$

By substituting this expression into the Wilson Gauge action we see it becomes,

$$S_G^{\mathrm{W}}[U] = \frac{a^4}{g^2} \sum_x \sum_{\mu<\nu} tr[F_{\mu\nu}(x) F^{\mu\nu}(x)]. \tag{2.19}$$

Thus the recovery of the correct continuum action becomes clear. This is not the only possible lattice gauge action, merely the simplest. Including Wilson loops of other shapes can lead to more gauge invariant quantities. The next simplest Wilson loop to the plaquette is the 1×2 rectangle, $R_{\mu\nu}(x)$. This is allows for gauge actions of the form,

$$S_G^{\mathrm{Improved}} = \beta \sum_x tr\left[(1 - 8c_1) \sum_{\mu<\nu} U_{\mu\nu} + c_1 \sum_{\mu\neq\nu} R_{\mu\nu} \right]. \tag{2.20}$$

c_1 is a free coefficient. The Iwasaki gauge action, which is the action used in all simulations included in this thesis, takes $c_1 = 0.331$ [82][81]. This value is chosen from renormalisation group improvement (RGI), but the details are beyond the scope of this thesis.

2.3.3 Fermion Action

Naive Discretisation of the fermion action

The fermion action in continuum QCD is given by,

$$S_F[\psi, \bar{\psi}, A_\mu] = \sum_f^{N_f} \int d^4x \bar{\psi}^{(f)} \Big(\gamma_\mu(\partial_\mu + iA_\mu) + m \Big) \psi^{(f)}, \tag{2.21}$$

where f indicates the fermion flavour. We must discretise the QCD action so that it is defined on the finite lattice, but that it returns the correct continuum action as we take the lattice spacing to zero, and maintains the same gauge invariance as the continuum action. The discretised covariant derivative is,

$$D_\mu \to \frac{1}{2a}(U_\mu(x)\delta(x+\hat{\mu}, y) - U_{-\mu}(x)\delta(x-\hat{\mu}, y)). \tag{2.22}$$

We can now give the gauge invariant naive discretised fermion action for fermions in an external gauge field U [72],

$$\begin{aligned} S_F[\psi, \bar{\psi}, U] &= a^4 \sum_x \bar{\psi}(x) \Big(\sum_{\mu=1}^{4} \gamma_\mu \frac{U_\mu(x)\psi(\vec{x}+\hat{\mu}) - U_{-\mu}(x)\psi(\vec{x}-\hat{\mu})}{2a} + m\psi(x) \Big) \\ &= \sum_{x,y} \bar{\psi}(x) D(x,y) \psi(y) \end{aligned} \tag{2.23}$$

where D is the naive Dirac operator defined as,

$$D(x,y) = m\delta(x,y) + \frac{1}{2a} \sum_{\mu=1}^{4} \gamma_\mu (U_\mu(x)\delta(x+\hat{\mu}, y) - U_{-\mu}(x)\delta(x-\hat{\mu}, y)). \tag{2.24}$$

The Fourier transform of the naive Dirac operator is [72],

$$\begin{aligned}\tilde{D}(p,q) &= \frac{1}{V}\sum_{x,y} e^{-iapx} D(x,y) e^{iaqy} \\ &= \frac{1}{V}\sum_{x,y} e^{-ia(p-q)x} \sum_{\mu} \gamma_\mu \frac{e^{iaq_\mu} - e^{-iaq_\mu}}{2a} + m \\ &= \delta(p,q)\left(m + \frac{i}{a}\sum_{\mu}\gamma_\mu \sin(p_\mu a)\right),\end{aligned} \tag{2.25}$$

with inverse,

$$\tilde{D}^{-1}(p) = \frac{m - ia^{-1}\sum_\mu \gamma_\mu \sin(ap_\mu)}{m^2 + a^{-2}\sum_\mu \sin^2(ap_\mu)}. \tag{2.26}$$

As we take the mass to zero, it is clear to see that as well as the pole at $p = (0,0,0,0)$ there are also poles at the other corners of the Brioullin zone, $p_\mu = 0, \pi/a$. This is referred to as the doubling problem.

To solve this Wilson proposed [100] modifying the Dirac operator,

$$D_W(x,y) = (\frac{4}{a} + m\delta(x,y)) + \frac{1}{2a}\sum_{\mu=1}^{4}(1-\gamma_\mu)(U_\mu(x)\delta(x+\hat{\mu},y) - U_{-\mu}(x)\delta(x-\hat{\mu},y)). \tag{2.27}$$

such that the momentum space operator is,

$$\tilde{D}_W(p) = m + \frac{i}{a}\sum_\mu \gamma_\mu \sin(p_\mu a) + \frac{1}{a}\sum_\mu (1 - \cos(p_\mu a)). \tag{2.28}$$

The pole at $p = (0,0,0,0)$ has the correct mass, while the doublers get an additional factor of 2/a for every $p_\mu = \pi/a$. In the continuum limit the doubler's masses become infinitely large and decouple from the theory.

2.3.4 Chiral Symmetry on the Lattice and Domain Wall Fermions

Chiral symmetry is conserved by the continuum QCD Lagrangian in the massless limit. It is helpful to express this by the condition,

$$\{D, \gamma_5\} = 0. \tag{2.29}$$

The Wilson fermion action explicitly breaks chiral symmetry, even in the massless limit. This is particularly problematic when studying weak matrix elements, and can often lead to operator mixing which does not occur in the continuum. This is not an easily overcome problem, according to the Nielsen Ninomiya theorem [93], a free fermion lattice action which is chirally invariant, translationally invariant and local must have doublers.

Ginsparg and Wilson [73] suggest a new condition for chiral symmetry on the lattice,

$$\{D, \gamma_5\} = aD\gamma_5 D. \tag{2.30}$$

It is argued in [89] that the lattice fermion action has chiral symmetry if this relation holds.

Domain Wall Fermions in Euclidean Space

The domain wall fermion (DWF) action was proposed by Callan and Harvey [54] and a discretised version by Kaplan [84]. Consider a 5 dimensional euclidean space-time, where we denote the 5th dimension as s. In this space-time there is a fermion with a mass dependent on s,

$$m(s) = m\theta(s) = \begin{cases} +m & s > 0 \\ -m & s < 0 \end{cases}. \tag{2.31}$$

The Dirac equation can be written,

$$\not{D} + \gamma_5 \partial_s + m(s)\Psi(x, s) = 0, \tag{2.32}$$

The 4 dimensional fields are the eigenvectors of the covariant 4D Dirac operator,

$$\gamma_\mu D_\mu \psi_n(x) = -\lambda_n \psi_n(x). \tag{2.33}$$

Let us consider this in the chiral basis, where,

$$\gamma_\mu = \begin{pmatrix} 0 & \sigma_\mu \\ \bar{\sigma}_\mu & 0 \end{pmatrix}, \tag{2.34}$$

and,

$$\gamma_5 = \begin{pmatrix} -1 & 0 \\ 0 & 1 \end{pmatrix}, \tag{2.35}$$

and $\sigma_\mu \equiv (1, \sigma^i)$, where σ^i are the Pauli matrices. We separate the fermion fields into their left-handed and right handed components. The 5D fields can be factorised into a function of s and the 4D fields [83],

$$\begin{aligned} \Psi_L(x,s) &= \textstyle\sum_n b_n(s)\psi_{L,n}(x) \\ \Psi_R(x,s) &= \textstyle\sum_n f_n(s)\psi_{R,n}(x). \end{aligned} \tag{2.36}$$

Equation 2.32 can be written in matrix form as,

$$\left[\begin{pmatrix} 0 & \sigma_\mu D_\mu \\ \bar{\sigma}_\mu D_\mu & 0 \end{pmatrix} + \begin{pmatrix} \partial_s & 0 \\ 0 & \partial_s \end{pmatrix} + \begin{pmatrix} m(s) & 0 \\ 0 & m(s) \end{pmatrix} \right] \begin{pmatrix} \sum_n b_n(s)\psi_{L,n}(x) \\ \sum_n f_n(s)\psi_{R,n}(x) \end{pmatrix} = 0. \tag{2.37}$$

It is straightforward to show,

$$\begin{aligned} (\partial_s + m(s))b_n(s) &= \lambda_n f_n(s) \\ (-\partial_s + m(s))f_n(s) &= \lambda_n b_n(s). \end{aligned} \tag{2.38}$$

While at first look it appears the eigenvalues to be of order $m(s)$, when $\lambda_n = 0$ [83],

$$\begin{aligned} f_0(s) &= Ne^{-\int_0^s m(s')ds'} = Ne^{-m|s|} \\ b_0(s) &= Ne^{\int_0^s m(s')ds'} = Ne^{m|s|}. \end{aligned} \tag{2.39}$$

The solution for $f_0(s)$ is localised near the mass defect, falling exponentially with distance in s, so there is a single massless right-handed fermion near the domain wall. The solution for $b_0(s)$ is discarded as it grows exponentially in $|s|$ and so is not normalisable. Of course this, only applies for infinite s, and when there is a finite 5th dimension and periodic boundary conditions both modes are included. Because of the gap between this eigenvalue and the rest of the spectrum, at low energies only the massless chiral fermion is encountered.

Domain Wall Fermions on the Lattice

When discretising the action, naively one replaces the derivatives with the standard lattice derivatives. However this leads to the doubling problem as before. However by adding a 5D Wilson term, as proposed by Kaplan [84], we remove these. With finite fifth dimension and periodic boundary conditions, both solutions in equation 2.39 are normalisable. The end result is a theory where opposite chirality 4d fermions exist on a two domain walls, but which exponentially decay in the 5th dimension so that the overlap between the two fermions is small provided the size of the fifth dimension is sufficiently large. The expression for the discretised DWF action is then [72],

$$\begin{aligned} D_{DWF}(s,s') =& (D_W+1)\delta(s,s') - (1-\delta(s,L_S-1))D_- P_L \delta(s+1,s') \\ & - (1-\delta(s,0))D_- P_R \delta(s-1,s') \\ & + m\Big(P_L \delta(s,L_S-1)\delta(s',0) + P_R \delta(s,0)\delta(s',L_S-1) \Big) \end{aligned} \tag{2.40}$$

where L_s is the number of sites in the 5th dimensions, $D_W = D_W(M_5)$ where M_5 is the height of the domain wall, and is chosen to minimise chiral symmetry breaking.

The four dimensional fermion fields $\psi(x)$ are,

$$\begin{aligned} \psi(x) &= P_L \Psi(x,0) + P_R \Psi(x, L_s - 1) \\ \bar{\psi}(x) &= \bar{\Psi}(x, L_s - 1) P_L + \bar{\Psi}(x,0) P_R. \end{aligned} \tag{2.41}$$

It has been shown [32] that domain wall fermion formalism, in the limit of infinite L_S, is equivalent to Neuberger's overlap operator [92],

$$D_{ov} = \frac{1+m}{2} + \frac{1-m}{2}\gamma_5 \epsilon(H), \tag{2.42}$$

where ϵ is the sign function of some suitable $H = \gamma_5 D^{kernel}$ where $D^{kernel} = D_W$ is the simplest choice.

The Shamir [98] and the Moebius [46][43][45] formulations of domain wall fermions are defined by the kernels,

$$D^{Shamir} = \frac{a_5 D^W(M_5)}{2 + a_5 D^W(M_5)} \tag{2.43}$$

and,

$$D^{Moebius} = \frac{(b_5 + c_5)D^W(M_5)}{2 + (b_5 - c_5)D^W(M_5)}, \tag{2.44}$$

respectively. The Moebius kernel is a rescaling of the Shamir kernel,

$$D^{Moebius} = \alpha \frac{a_5 D^W(M_5)}{2 + a_5 D^W(M_5)} \equiv \alpha D^{Shamir}, \tag{2.45}$$

where $a_5 = b_5 - c_5$ and $\alpha a_5 = b_5 + c_5$. As the sign function is scale invariant, it is clear that the two actions are identical in the infinite L_S limit.

We can write a generalised DWF action [44] which can describe both the Moebius and Shamir formulations,

$$\begin{aligned} D^{DWF}(s,s') =& (D_+)\delta(s,s') - (1 - \delta(s, L_S - 1))D_- P_L \delta(s+1, s') \\ & - (1 - \delta(s,0))D_- P_R \delta(s-1, s') \\ & + m\Big(D_- P_L \delta(s, L_S - 1)\delta(s', 0) + D_- P_R \delta(s,0)\delta(s', L_S - 1) \Big), \end{aligned} \tag{2.46}$$

where $D_+ = b_5 D^W(M_5) + 1$ and $D_- = c_5 D^W(M_5) - 1$.

Residual Mass

The domain wall action has a symmetry $\psi \rightarrow e^{i\alpha^a \frac{t^a}{2}}\psi$, with associated five dimensional conserved currents,

$$\begin{aligned} j_u(x,s) &= \frac{1}{2}(\bar{\psi}(x + \hat{\mu}, s)(1 + \gamma_\mu)U_\mu^\dagger(x)t^a\psi(x,s) - \bar{\psi}(x,s)(1 - \gamma_\mu)U_\mu(x)t^a\psi(x + \hat{\mu}, s)) \\ j_5(x,s) &= \frac{1}{2}(\bar{\psi}(x, s+1)(1 + \gamma_5)U_5^\dagger(x)t^a\psi(x,s) - \bar{\psi}(x,s)(1 - \gamma_5)U_5(x)t^a\psi(x, s+1)). \end{aligned} \tag{2.47}$$

The associated conserved 4D vector current is,

$$\mathcal{V}_\mu^a(x) = \sum_{s=0}^{L_s - 1} j_\mu^a(x,s). \tag{2.48}$$

Following, [68],the axial current transformation is defined to be $\psi \to e^{i\alpha^a \frac{t^a}{2} q(s)\psi}$, where $q(s) = \text{sgn}(\frac{L_s-1}{2} - s)$. The corresponding conserved axial current is,

$$\mathcal{A}^a_\mu(x) = \sum_{s=0}^{L_s-1} q(s) j^a_\mu(x,s). \tag{2.49}$$

We can also construct a vector and axial current from the four dimensional quark fields,

$$V^a_\mu(x) = \bar{\psi}(x) t^a \gamma_\mu \psi(x), \quad A^a_\mu(x) = \bar{\psi}(x) t^a \gamma_\mu \gamma_5 \psi(x), \tag{2.50}$$

which are related to the conserved currents by,

$$\mathcal{V}^a_\mu(x) = Z_V V^a_\mu, \quad \mathcal{A}^a_\mu(x) = Z_A A^a_\mu \tag{2.51}$$

With a finite L_s and non-zero quark masses, chiral symmetry is broken and the axial current has $\mathcal{A}^a_\mu(x)$ divergence,

$$a\Delta\mu \mathcal{A}^a_\mu(x) = 2am_f J^a_5(x) + 2J^a_{5q}, \tag{2.52}$$

where $J^a_5(x) = j^a_5(x, L_s)$ and $J^a_{5q}(x) = j^a_5(x, L_s/2 - 1)$. The first term is due to non-zero quark masses, while the second, called the *midpoint term*, results from the finite L_s. The axial Ward identity is therefore altered,

$$a\Delta\mu \langle \mathcal{A}^a_\mu(x) O(y) \rangle = 2 \langle am_f J^a_5(x) O(y) \rangle + 2 \langle J^a_{5q} O(y) \rangle + i \langle \delta^a O(y) \rangle \tag{2.53}$$

The Ward identities must be recovered in the continuum limit, and so the two J_5 terms must be combined, giving an effective quark mass,

$$m_{eff} = m + m_{res}, \tag{2.54}$$

and,

$$J_{5q} = am_{res} J_5(x) - \frac{Z_{\mathcal{A}} - 1}{2} \partial_\mu \mathcal{A}^a_\mu(x) O(y). \tag{2.55}$$

For the domain wall fermion formulation, $Z_{\mathcal{A}}$, the renormalisation of the 5D conserved vector current is typically 1 and so the last term can often be neglected. We, therefore, measure m_{res} using,

$$am_{res} = \frac{\langle 0 | J_{5q} | \pi \rangle}{\langle 0 | J_5 | \pi \rangle}, \tag{2.56}$$

This term vanishes as the pion mass goes to zero, and so we define the chiral limit as $m \to -m_{res}$.

No novel measurements of m_{res} were made during this work, as they had already been made on the same ensembles in previous work. They are given in [31].

2.4 Simulation and Measurements

When treating the discretised path integral, the fermion path integrals are typically formally integrated out, as Grassman variables are difficult to treat computationally. This leaves an integration over the gauge fields,

$$Z = \prod_{x,\mu} \int dU_\mu \det(D(U)) \exp(-S_G[U]) \tag{2.57}$$

This can be viewed as a sum over all possible gauge field configurations, U_i, whose probability is weighted according to,

$$P(U_i) = \det(D(U_i)) \exp(-S_G[U_i]). \tag{2.58}$$

Therefore the Green's function of an operator can be evaluated as,

$$\begin{aligned} \langle O(U, S(U)) \rangle &= \frac{1}{Z} \prod_{x,\mu} \int dU_\mu O(U, S(U)) \det(D(U)) \exp(-S_G[U]) \\ &\approx \sum \frac{1}{N} \sum_i^N O(U, S(U)) \end{aligned} \tag{2.59}$$

where $S(U) = D^{-1}(U)$ is the fermion propagator.

The generation of these ensembles of gauge configurations requires a Monte-Carlo algorithm for generation. An exact hybrid MonteCarlo algorithm was used for the generation of all ensembles used in this work. This is beyond the scope of this thesis but details can be found in [31].

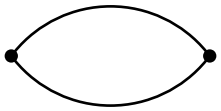

Figure 2.1 *The connected contribution to the two-point correlator.*

Figure 2.2 *The disconnected contribution to the two-point correlator.*

2.4.1 Correlation Functions

The operator expectation value of $\bar{\psi}(y)\psi(x)$ is given by,

$$\langle\bar{\psi}(y)\psi(x)\rangle = \int \mathcal{D}A_\mu \det(D) D^{-1}(y,x) e^{S[A_\mu]}. \tag{2.60}$$

The fermion propagator $S(y,x)$ is defined by,

$$D(z,y)S(y,x) = \delta_{zx}. \tag{2.61}$$

The local correlator $C_{\Gamma_1\Gamma_2}(t_f,t_i)$ is,

$$\begin{aligned} C_{\Gamma_1\Gamma_2}(t_f,t_i) &= \langle O_{\Gamma_1}(t_f) O_{\Gamma_2}(t_i)\rangle \\ &= \sum_{x,y} tr(\bar{\psi}(y,t_f)\Gamma_1\psi(y,t_f)\bar{\psi}(x,t_i)\Gamma_2\psi(x,t_i)) \\ &= \sum_{x,y} tr\Big(S(y,t_f;x,t_i)\Gamma_1 S(x,t_i;y,t_f)\Gamma_2\Big) \\ &\quad - tr\Big(S(y,t_f;y,t_f)\Gamma_1\Big) tr\Big(S(x,t_i;x,t_i)\Gamma_2\Big) \end{aligned} \tag{2.62}$$

The summation is over the spatial dimensions only, and indicates the sum over the sources and sinks. The second term on the last line is the disconnected diagram. The connected and disconnected diagrams are shown in figures 2.1 and 2.2 respectively. Both terms are calculated in the lattice calculation and combined so that the bare results presented in chapter 3 include both terms.

In Euclidean space-time, it is easy to show with insertion of the complete set of

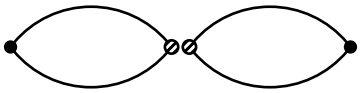

Figure 2.3 *The disconnected contribution to the three-point correlator.*

states, that the ground-state dominates at large time,

$$\begin{aligned}\langle O_{\Gamma_1}(t_f)O_{\Gamma_2}(t_i)\rangle &= \sum_n \langle 0|O_{\Gamma_1}|n\rangle \langle n|O_{\Gamma_2}|0\rangle e^{-E_n(t_f-t_i)} \\ &\to \langle 0|O_{\Gamma_1}|n\rangle \langle n|O_{\Gamma_2}|0\rangle e^{-m(t_f-t_i)},\end{aligned} \tag{2.63}$$

allowing for easy measurement of the mass. In practice, due to the finite volume of our lattice simulation, there is also a propagator propagating backwards from the other end of the finite time-extent.

$$C_{\Gamma_1\Gamma_2}(t_f,t_i) = \langle 0|O_{\Gamma_1}|n\rangle \langle n|O_{\Gamma_2}|0\rangle \left(e^{-m(t_f-t_i)} \pm e^{-m(L_t-1-(t_f-t_i))}\right). \tag{2.64}$$

Similarly, the matrix elements for the fourquark operators are,

$$\begin{aligned}\langle \bar{K}^0(t_f)|O_{\Gamma\Gamma}(t)|K^0(t_i)\rangle &= \sum_{z_1,z_2}\sum_y\sum_{x_1,x_2} \langle 0|\, s(z_1,t_f)\bar{d}(z_2,t_f)(\bar{s}\Gamma d\bar{s}\Gamma d)(y,t)s(x_1,t_i)\bar{d}(x_2,t_i)\,|0\rangle \\ &= 2\Bigg(tr\left[(\gamma^5 S_s^\dagger(z_1,t_f;y,t)\gamma^5)\Gamma S_d(y,t;z_2,t_f)\right] \\ &\quad \times tr\left[(\gamma^5 S_s^\dagger(x_1,t_i;y,t)\gamma^5)\Gamma S_d(y,t;x_2,t_i)\right] - \\ &\quad tr\Bigg[(\gamma^5 S_s^\dagger(z_1,t_f;y,t)\gamma^5)\Gamma S_d(y,t;z_2,t_f) \\ &\quad \times (\gamma^5 S_s^\dagger(x_1,t_i;y,t)\gamma^5)\Gamma S_d(y,t;x_2,t_i)\Bigg]\Bigg),\end{aligned} \tag{2.65}$$

where the connected and disconnected diagrams are shown in figures 2.4 and 2.3 respectively. As with the two-point correlation functions both parts are calculated and the bare lattice results include both terms.

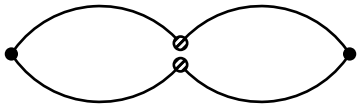

Figure 2.4 *The connected contribution to the three-point correlator*

2.4.2 Lattice Sources

We obtain the propagators by inverting the Dirac matrix D, which is of size $(N_L^3 \times N_T \times N_c \times N_s)^2$. Even an $N_L = 24$, $N_T = 64$ lattice in QCD, where $N_c = 3$, $N_s = 4$, this has over 10^{14} entries. To circumvent this, the inversion is done with only the elements orginating from some lattice source $\eta(\vec{x}, \tau)$.

$$\psi(\vec{y}, t) = \sum D^{-1}(\vec{y}, t; \vec{x}, \tau)\eta(\vec{x}, \tau) \tag{2.66}$$

The point source is typically defined as $\eta(\vec{x}, \tau) = \delta_{x_0 x}\delta_{\tau_0,\tau}\mathbb{1}_{N_s\times N_s}\mathbb{1}_{N_c\times N_c}$, where the unit spin and colour matrices denote the 12 possible spin and colour sources. A wall source is defined by $\eta(\vec{x}, \tau) = \delta_{\tau_0\tau}\mathbb{1}_{N_s\times N_S}\mathbb{1}_{N_c\times N_c}$ such that all sites within the spatial volume are included for one specific time-slice.

$\mathbb{Z}_2$ Sources

While volume averaged sources are more expensive they decrease the vulnerability to local fluctations in the gauge fields. It is possible to use stochastic sources [34], where the elements are randomly drawn from some a distribution $\mathcal{D}$ that is symmetric about zero,

$$\eta_{a\alpha}^{(n)}(x) \in \mathcal{D} | n = 1 \cdots N. \tag{2.67}$$

Here a and α are the colour and spin indices respectively. In the limit of large statistics,

$$\langle \eta_{a\alpha}^{(n)}(x)\eta_{b\beta}^{\dagger(n)}(y)\rangle \equiv \frac{1}{N}\eta_{a\alpha(x)}^{(n)}\eta_{b\beta}^{\dagger(n)}(y) \to \delta_{xy}\delta_{ab}\delta_{\alpha\beta}. \tag{2.68}$$

It was demonstrated in [62] that $\mathbb{Z}_2$ noise followed the orthonormality condition in 2.68 better than Gaussian noise.

We can define now a $\mathbb{Z}_2$ wall source,

$$\eta^{(n)}(\vec{x}, \tau|t) = \delta_{\tau,t} \otimes \Xi^{(n)}(\vec{x}), \tag{2.69}$$

where $\Xi^{(n)}(\vec{x})$ is a 12 component column vector representing the spin and colour. Its elements are chosen stochastically,

$$\Xi^{(n)}(\vec{x}) \in \mathcal{D}|n = 1 \cdots 12. \tag{2.70}$$

In [34] it was demonstrated that the use of stochastic sources can give an improvement in statistics for equivalent computational cost for two-point meson correlators.

Gaussian Smeared Sources

A Wuppertal (Gaussian) scalar-propagator smeared source [77], $S(\mathbf{x}', \mathbf{0})$ is defined by the 3D Gordon Klein equation,

$$K(\mathbf{x}, \mathbf{x}')\eta(\mathbf{x}', \mathbf{0}) = \delta_{\mathbf{x},\mathbf{0}} \tag{2.71}$$

where,

$$K(\mathbf{x}, \mathbf{x}') = \delta_{\mathbf{x},\mathbf{x}'} - \kappa_s \sum_{\mu} \{\delta_{\mathbf{x}',\mathbf{x}-\hat{\mu}} U_{\mu}^{\dagger}(\mathbf{x} - \hat{\mu}) + \delta_{\mathbf{x}',\mathbf{x}+\hat{\mu}} U_{\mu}(\mathbf{x})\}. \tag{2.72}$$

The result is a "shell-model" wave function, where each quark is localised around the origin within a radius r which is determined by κ_s, the scalar hopping parameter. For sink smearing, where this needs to be solved for every time slice for every spin component, this becomes significantly expensive. In this case we turn to Jacobi smearing [4]. We instead solve equation 2.71 as a power series in κ_s for some finite power N.

2.5 Statistical Techniques

The raw correlation functions are obtained on a number of different configurations, n_c, forming a distribution,

$$Y = \{y_i\} \; ; \; 1 \leq i \leq n_c \tag{2.73}$$

When fitting, we take the mean of these configurations,

$$\bar{Y} = \frac{1}{n_c} \sum_{i=1}^{n_c} y_i \tag{2.74}$$

to obtain the results, but we wish to know the uncertainty on this mean. This can be done using either jackknife or bootstrap resampling.

2.5.1 Jackknifing

In jackknife resampling [96][97] we can form a new distribution Y_j by omitting element y_j,

$$Y_j = \{y_i\} \; ; \; 1 \leq i \leq n_c \; ; \; i \neq j, \tag{2.75}$$

which has a mean,

$$\bar{Y_j} = \frac{1}{n_c} \sum_{i=1, i \neq j}^{n_c} y_i. \tag{2.76}$$

A jackknife distribution can be formed,

$$Y_{JK} = \{\bar{Y_j}\} \; ; \; 1 \leq j \leq n_c. \tag{2.77}$$

The standard deviation of the this jackknife distribution is,

$$\hat{\sigma}_{JK} = \frac{n_c - 1}{n_c} \sum (\bar{Y_j} - \bar{Y}_{JK})^2, \tag{2.78}$$

and the mean is the same as the original distributions mean.

2.5.2 Bootstrapping

Bootstrap resampling [64] is random resampling with replacement. For distribution Y with n_c elements, a new distribution Y_b is formed.

$$Y_j^b = \{y_i\} \; ; \; 1 \leq i \leq N_b \; ; \; y_i = \text{rand}(y_k). \tag{2.79}$$

This process is repeated some number N_b times to form a distribution of the means of these bootstrap resamples,

$$Y_B = \{\bar{Y}_j^b\} \; ; \; 1 \leq j \leq N_b. \tag{2.80}$$

This is expected to follow a gaussian distribution, and so we can find the standard deviation either directly,

$$\sigma_B = \frac{1}{N_b} \sum (\bar{Y}_B - \bar{Y}_j^b)^2, \tag{2.81}$$

or by finding the values of $\bar{Y}_j^b$ at the 16th and 84th percentile which bound the 68% confidence interval.

Chapter 3

Lattice Measurement Results

In this chapter the analysis of eight different 2+1 flavour domain wall fermion ensembles is detailed. These ensembles consist of three coarse, four medium and one fine ensemble (spanning from approximately 1.7GeV to 2.8GeV) labelled as C, M and F.

Ensembles C1 and C2 are both of lattice dimension $24^3 \times 64$, with an inverse lattice spacing of 1.7848(50)GeV, while M1 and M2 have dimensions $32^3 \times 64$ fermion action and an inverse spacing of 2.3833(86)GeV. Both these sets of ensembles have a Shamir domain wall fermion action. C1/2 were first analysed in [2], but the number of configurations was doubled for [9] where M1/2/3 were first analysed.

Ensembles C0 and M0, of lattice dimensions $48^3 \times 96$ and $64^2 \times 128$ respectively, are both simulated with unitary physical light quark masses using a Moebius domain wall fermion action. These are detailed in [31] where they were included in a global fit with other ensembles, including C1/2 and M1/2/3 to recalculate the lattice spacings and quark masses of all included ensembles. These values are used in this manuscript.

In [39], calculations were rerun on all ensembles with the strange quark masses partially quenched so that the valence strange quark masses could take their physical values, while the sea strange mass was slightly mistuned. Reweighting in the sea-strange was performed in [31] and the effect was found to be small. The new runs were also performed with Gaussian smearing on the sources and sinks. Finally, ensemble F1 is of dimension $48^3 \times 96$ with an inverse spacing of 2.774(10)GeV and a domain wall fermion action. It was first analysed in [39] but

has since been updated to include Gaussian source smearing and physical valence strange quark mass. It has however been discovered that gauge configurations of this ensemble were mistakenly generated with a Shamir action, but with the propagators calculated with a Moebius action. This leads to a partial quenching. The Moebius and Shamir action are identical in the limit of infinite L_S, while with finite L_S where there is some residual chiral symmetry breaking, with the Moebius action represents a scaling in the Shamir action. A Moebius action with the same L_S as a Shamir action would have a smaller chiral symmetry breaking effect and residual mass. It is argued in [31] that the differences in the 4D approximation to QCD of each action are equal in magnitude to the level of residual chiral symmetry breaking. While the difference in action for the sea and valence quarks is expected to have a small impact, the effects have not been fully studied and understood. Therefore this ensemble is excluded from any calculation of central values of physical quantities in this thesis, for the sake of prudence. We do however present fit results from this ensemble, as some error analysis relies upon it. It should be noted that at the time of submission 350 trajectories of F1 with the partial quenching removed have been produced by RBC-UKQCD. Therefore future analyses by RBC-UKQCD will include F1 in the central value, but unfortunately timing did not allow for inclusion in this thesis.

Simulation parameters of all the ensembles listed above are given in table 3.1.

In the rest of this chapter we will describe the quantities measured and provide plots and tables of the fits and results.

Table 3.1 *Summary of the ensembles used in this work. C, M and F stand for coarse, medium and fine, respectively. M and S stand for Möbius and Shamir kernels, respectively.*

name	L/a	T/a	kernel	source	a^{-1}[GeV]	m_π[MeV]	$n_{configs}$	am_l^{uni}	am_s^{sea}	am_s^{val}	am_s^{phys}
C0	48	96	M	Z2GW	1.7295(38)	139	90	0.00078	0.0362	0.0358	0.03580(16)
C1	24	64	S	Z2W	1.7848(50)	340	100	0.005	0.04	0.03224	0.03224(18)
C2	24	64	S	Z2W	1.7848(50)	430	101	0.01	0.04	0.03224	0.03224(18)
M0	64	128	M	Z2GW	2.3586(70)	139	82	0.000678	0.02661	0.0254	0.02539(17)
M1	32	64	S	Z2GW	2.3833(86)	303	83	0.004	0.03	0.02477	0.02477(18)
M2	32	64	S	Z2GW	2.3833(86)	360	76	0.006	0.03	0.02477	0.02477(18)
M3	32	64	S	Z2GW	2.3833(86)	410	81	0.008	0.03	0.02477	0.02477(18)
F1	48	96	S/M	Z2GW	2.774(10)	234	98	0.002144	0.02144	0.02132	0.02132(17)

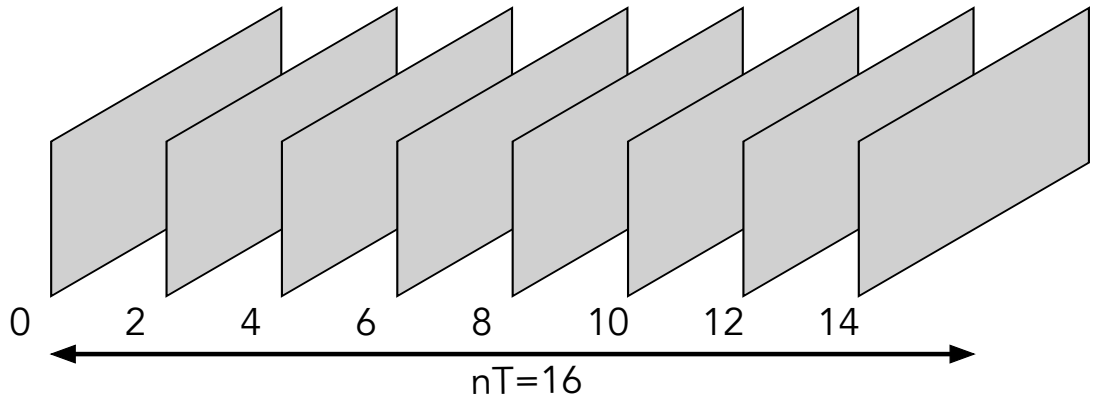

Figure 3.1 *An illustration of the multi-hit strategy, for an example ensemble with $n_T = 16$ whereby the Z2 Gaussian Wall sources are inserted onto every other time-slice.*

3.1 Measurement Strategy

Rather than performing the calculation for only $t_i = 0$, where t_i is the time-slice at which the source is inserted, we instead perform the calculation for a number of different values of t_i. We refer to each one of these as a hit, with N_{hit} indicating the number of times this is done. For all our ensembles we choose $N_{hit} = n_T/2$ and perform the calculation with the source on alternate time-slices. We then average over all the hits to obtain one value of the correlation function for each value of t (the sink time) and each configuration. An illustration of this principle is given in figure 3.1.

A similar strategy is employed for the three-point correlation functions, however we need to consider not only the source and the sink, but also the four-quark operator. The four-quark operator is fixed at the origin ($t = 0$), while t_i and t_f, the source and sink time, are varied, as illustrated in figure 3.2.

As before $N_{hit} = nT/2$ with the calculation performed with a source on every other time-slice. For each value of t_i we do not perform the calculation for every value of t_f but instead choose a subset. The values of $\Delta t = t_f - t_i$ are the same for each value of t_i. Before fitting the correlation functions, we perform a shift on the data of size $-t_i$ such that $t_i = 0$ and $t_f = \Delta t$ for all hits. All correlation functions for a constant value of Δt are averaged. This is illustrated in figure 3.3. This reduces variance but the only assumption of statistical independence made is about the different configurations and not different sources on same configuration.

Finally we can choose between the various values of Δt based on the length of plateau and amount of noise exhibited by the correlation functions.

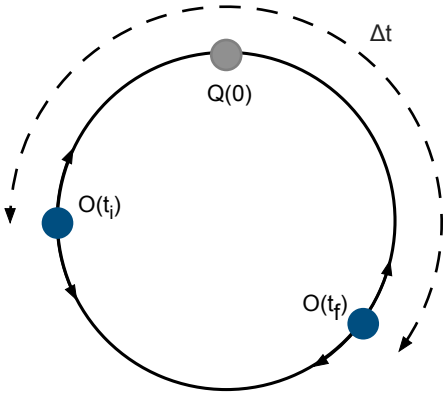

Figure 3.2 *When calculating the three-point correlators, the four-quark function is fixed at the time origin, while the source and sink times, t_i and t_f respectively, are varied. We choose every other time-slice for t_i, then we choose some range of values for the time separation, $\Delta t = t_f - t_i$, which determines the values of t_f. When t_i and t_f are far from the time origin, the ground states dominate.*

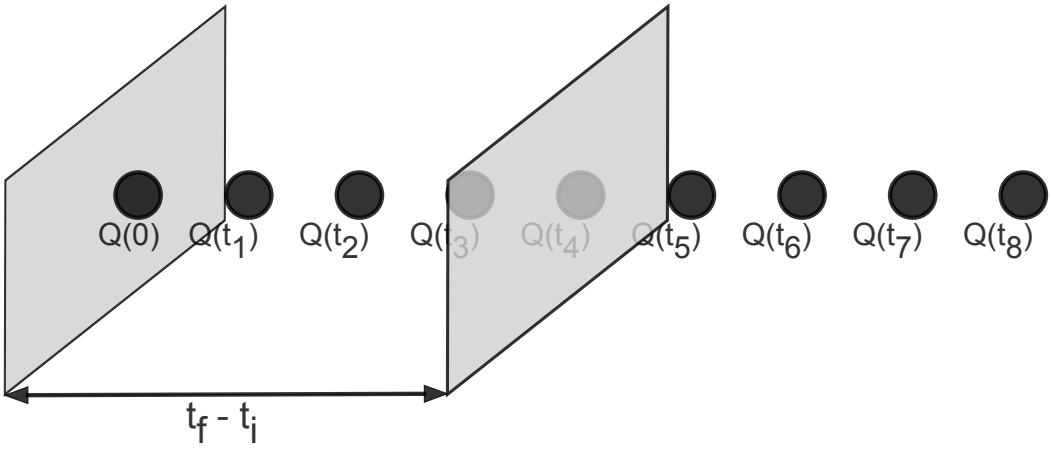

Figure 3.3 *An illustration of the multi-hit strategy for the three-point correlation functions. After performing a shift, the Z2 Gaussian Wall Source and Sink exist at times $t_i = 0$ and $t_f = \Delta t$ respectively for every hit, while t, the time-slice of the four-quark operator varies for each hit. Before fitting, all the correlation functions are averaged, essentially averaging over the four-quark operator time. This set-up is repeated for several values of Δt.*

3.2 Axial Current Renormalisation

The local axial current, A_μ, and the conserved axial current $\mathcal{A}_\mu$, are related by the renormalisation coefficient Z_A as detailed in section 2.3.4.

We can express the local axial current renormalisation as:

$$Z_A = \frac{\langle \mathcal{A}(x)\pi(0)\rangle}{\langle A_\mu(x)\pi(0)\rangle} \tag{3.1}$$

We define the correlators for the conserved and local axial current as,

$$C(t+1/2) = \sum_{\vec{x}} \langle \mathcal{A}_0(\vec{x},t)\pi(\vec{0},0)\rangle \,, \tag{3.2}$$

and,

$$L(t) = \sum_{\vec{x}} \langle A_0(\vec{x},t)\pi(\vec{0},0)\rangle \,. \tag{3.3}$$

The 1/2 in the argument of C is there since the conserved axial current is not defined on the lattice sites, but on the links between sites.

We can then find the local axial current renormalisation from an appropriate average of ratios of the correlators at t and at $t+1/2$ in equations 3.2 and 3.3:

$$Z_A(t) = \frac{1}{2}\left(\frac{C(t+1/2)+C(t-1/2)}{2L(t)} + \frac{2C(t+1/2)}{L(t)+L(t+1/2)}\right). \tag{3.4}$$

We fit this ratio of correlators to a constant to obtain Z_A. We have not explicitly labelled the source and sink smearing of the correlators here. Since this is a ratio of correlators, provided each as the same source and sink smearing there is cancellation of any scaling introduced by the smearing amplitude. Strictly speaking Z_A should be obtained at the chiral limit, by extrapolating in light quark mass to the chiral limit. However given that for C0, M0 and F1, we have only one value of the light quark mass, we just take the value at the simulated light quark mass. For C1/2 and M1/2/3 we are able to extrapolate the chiral limit, as shown in figure 3.4 and find that the value of Z_A is adjusted by an order of 0.05% even for the heaviest pions. Given that the masses of the pions are significantly less for C0, M0 and F1, the chiral extrapolation should have an even smaller effect on these ensembles, and hence taking Z_A at the simulated light

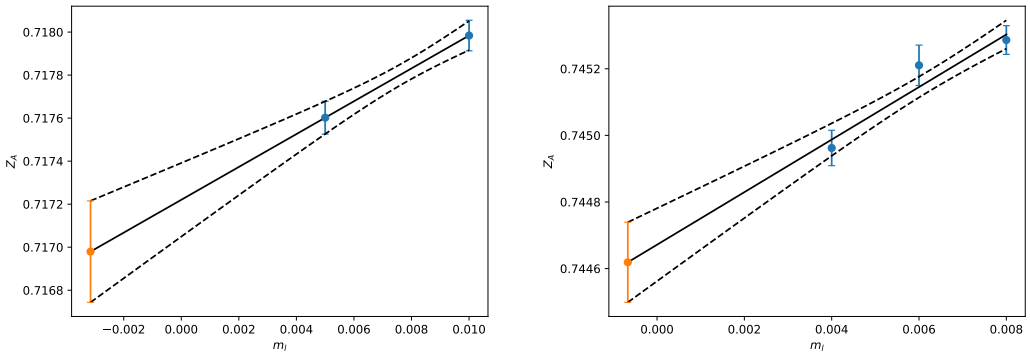

(a) *Coarse Ensembles C1 & C2.* $m_{res} = 0.003154(15)$

(b) *Medium Ensembles M1, M2 & M3.* $m_{res} = 0.0006697(34)$

Figure 3.4 *Chiral extrapolation of the axial current renormalisation Z_A. The extrapolation is performed to $-m_{res}$.*

Table 3.2 *Results for Z_A.*

	Z_A
C0	0.711964(43)
C1	0.71698(24)
M0	0.743462(47)
M1	0.74462(12)
F1	0.761137(37)

quark mass is justified. The results for Z_A are given in table 3.2.

3.3 Pseudoscalar Effective Mass

The two point correlation function $C_{\Gamma_1\Gamma_2}(t)$, with currents Γ_i can be expressed as,

$$C^{s_1 s_2}_{\Gamma_1\Gamma_2}(t, t_i) \equiv \sum_{\mathbf{x},\mathbf{y}} \langle O^{s_1}_{\Gamma_1}(t, \mathbf{x}) O^{s_2}_{\Gamma_2}(t_i, \mathbf{y}) \rangle = \sum_k N^{s_1 s_2(k)}_{\Gamma_1\Gamma_2} \left(e^{-E^{(k)}(t-t_i)} \pm e^{-E^{(k)}(T-(t-t_i))} \right). \tag{3.5}$$

The interpolating operators O_Γ have the quantum numbers of the desired meson, either π or K in this work. Γ_j indicates the current of the operator, where we consider the axial (A) and pseudoscalar current (P). s_j indicates the type of source and sink. T is the time extent of the lattice. The correlator amplitudes,

$N^{s_1 s_2 (k)}_{\Gamma_1 \Gamma_2}$, are defined by,

$$N^{s_1 s_2 (k)}_{\Gamma_1 \Gamma_2} = \frac{M^{s_1 (k)}_{\Gamma_1} (M^{s_2 (k)}_{\Gamma_2})^*}{2E^{(k)}}, \tag{3.6}$$

with a standard relativistic normalisation over the energy states $E^{(k)}$, where $M^{s_j (k)}_{i,\Gamma_j}$ are the matrix elements,

$$M^{s_j (k)}_{\Gamma_j} = \langle \pi^{(k)}, K^{(k)} | O^{s_j \dagger}_{\Gamma_j} | 0 \rangle \, . \tag{3.7}$$

Notice that the expression on the right is a sum over the energy states, k, including the excited state. However at large times ($0 \ll t \ll T$) the ground state dominates and we can neglect the excited states:

$$C^{s_1 s_2}_{\Gamma_1 \Gamma_2}(t, t_i) \xrightarrow{t_i \ll t \ll T} \frac{M^{s_1}_{\Gamma_1} (M^{s_2}_{\Gamma_2})^*}{2am} \left(e^{-am(t-t_i)} \pm e^{-am(T-(t-t_i))} \right). \tag{3.8}$$

We can obtain values of the effective mass directly from the data, by taking ratios of the correlators,

$$am_{eff}(t) = \cosh^{-1} \left(\frac{C(t-1) + C(t+1)}{2C(t)} \right). \tag{3.9}$$

The pseudoscalar masses am and amplitudes M_Γ are found by simultaneously fitting to several correlation functions. The different channels, AA, PA, PP, where P represents the pseudoscalar current and A the axial current, share the same effective pseudoscalar mass m and so by simultaneously fitting them, we can increase the degrees of freedom in the fit.

For C1 and C2 where there is no source or sink smearing, we can drop the source index, s_j. We simultaneously fit C_{AA}, C_{PP} and C_{PA} to obtain the effective mass, m, and the products of amplitudes N_{AA}, N_{PP} and N_{PA}.

For the other ensembles we also need to consider the source and sink smearing. Here we consider $s_j = \{SS, SL\}$, where the S indicates smeared and L local, and the first letter indicates the source smearing and the latter sink smearing. It should be noted that in practice $s_1 = s_2$ in all cases and so we drop s_2 so that for example C^{SSSS}_{AA} becomes C^{SS}_{AA}. Here we simultaneously fit C^{SS}_{AA}, C^{SL}_{AA}, C^{SS}_{PP} and C^{SL}_{PA} to obtain m and the products of amplitudes N^{SS}_{AA}, N^{SL}_{AA}, N^{SS}_{PP} and N^{SL}_{PA}.

In the case of sink smearing, the smearing factors are the same for a source at time t and a sink at time t. As a result of averaging over all correlators which share the same time separation in the multihit strategy, a temporal correlation is introduced. See subsection 3.3.1 for a more detailed explanation and discussion of this effect.

We should note that the fits are uncorrelated, as is the case for all quantities listed here, but they were consistently cross-checked with independent correlated fits and the differences were found to be sub-statistical. The time range of the fits were chosen by fitting for a variety of ranges and choosing a range which both had a reasonable value of χ^2 and was a reasonably large time range. We folded the data before performing the fits here. This allowed us to avoid the noisy data points near $T/2$ without needlessly discarding data.

Example plots of the effective mass values and fit results for the physical point ensembles are shown in figures 3.5 to 3.8 with the remaining plots shown in appendix A. We also show for illustrative purposes plots of the correlation function and fit in figure 3.9.

Note that when fitting to different channels simultaneously, the channels with the least noise tend to dominate the fit and constrain the size of the errors. This means that when viewing the plots of the fits for the noisy channels, AA in particular, at first glance the errors on the fit appear very small.

Also note that for the channel AA with smeared sources and sinks, the data points for some time slices are missing and there superficially appears to be a bias above the fit line. This is an artefact of the high level of noise. The effective mass is gained by taking the inverse cosh on a ratio of correlators shown in equation 3.9, and this is only defined in the region $\frac{C(t-1)+C(t+1)}{2C(t)} \geq 1$. Due to the very high levels of noise, for some time-slices this restriction was not met, and so these were omitted from the plotting, leading to the appearance of bias. However they were present in the fit, which was performed according to equation 3.8.

The results of the fits are given in table 3.4.

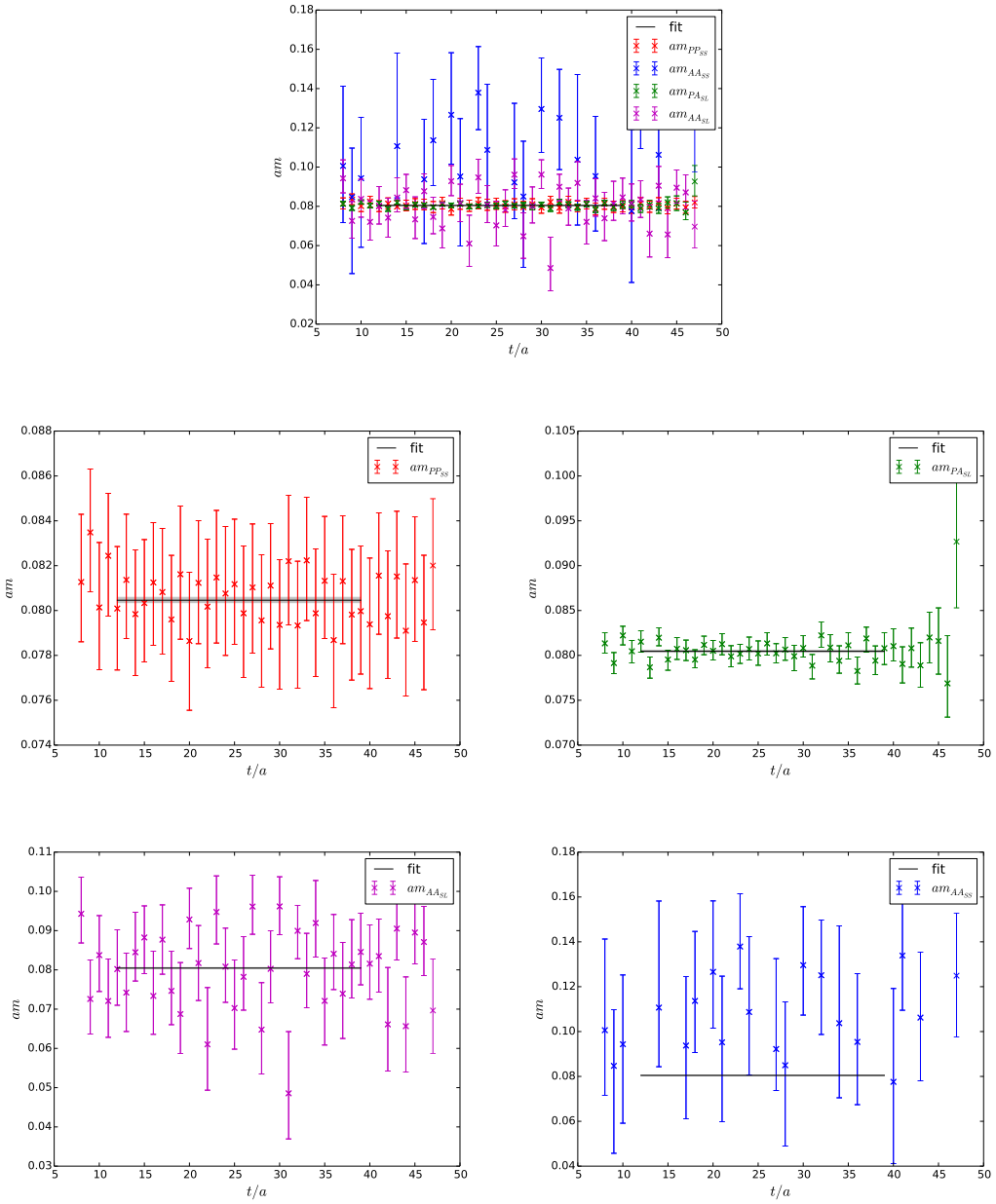

Figure 3.5 *Effective mass for the pion on ensemble C0.*

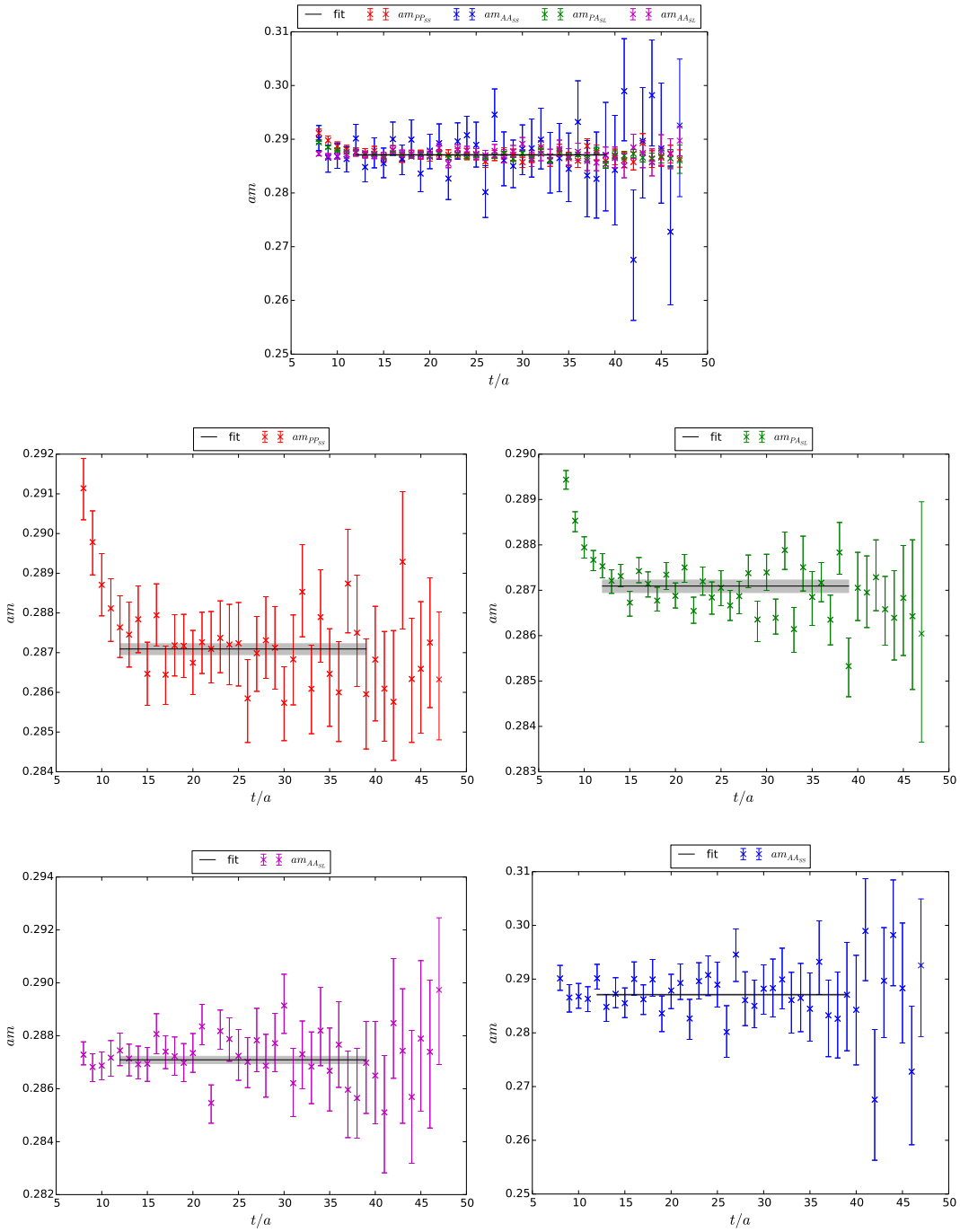

Figure 3.6 *Effective mass for the kaon on ensemble C0.*

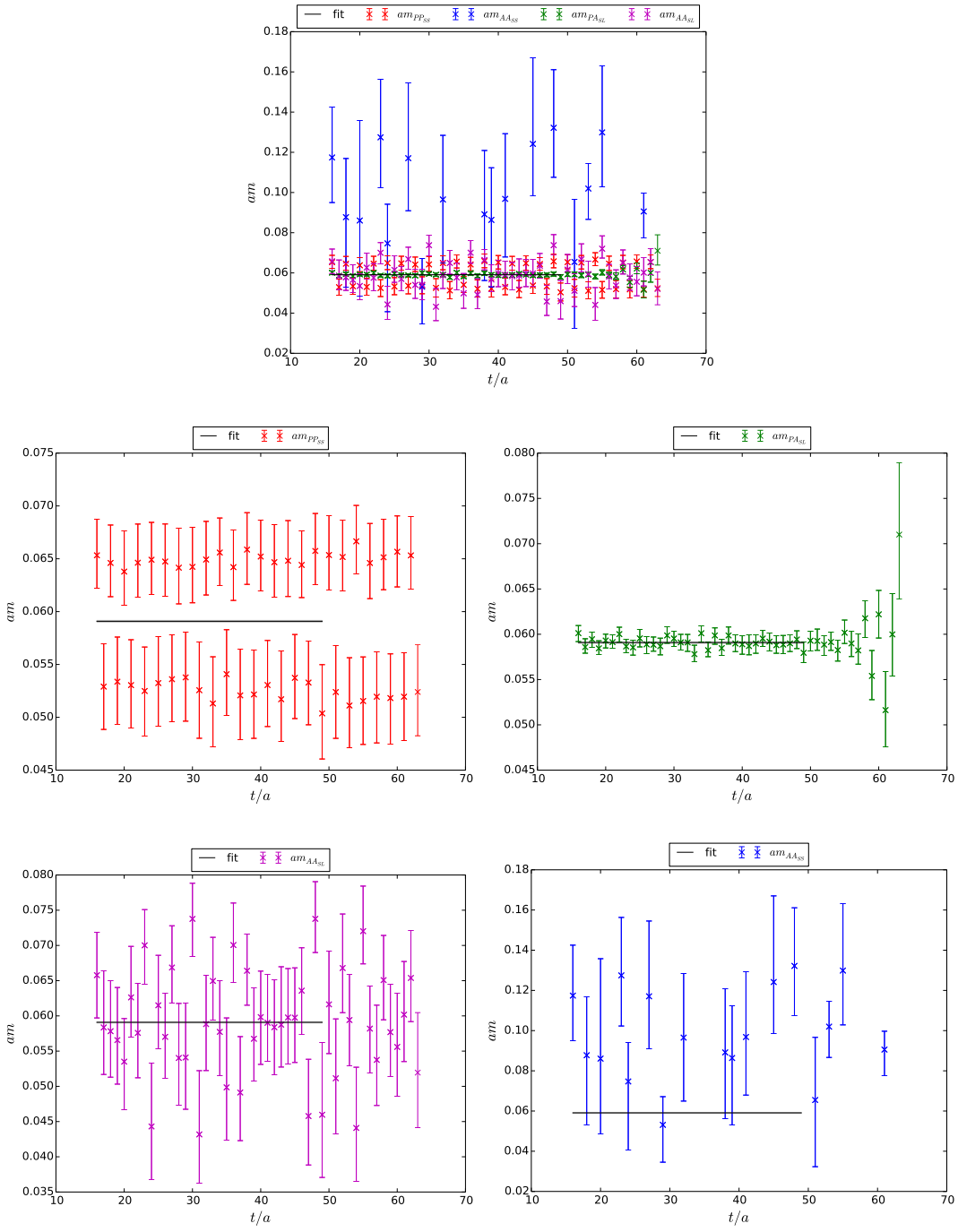

Figure 3.7 *Effective mass for the pion on ensemble M0.*

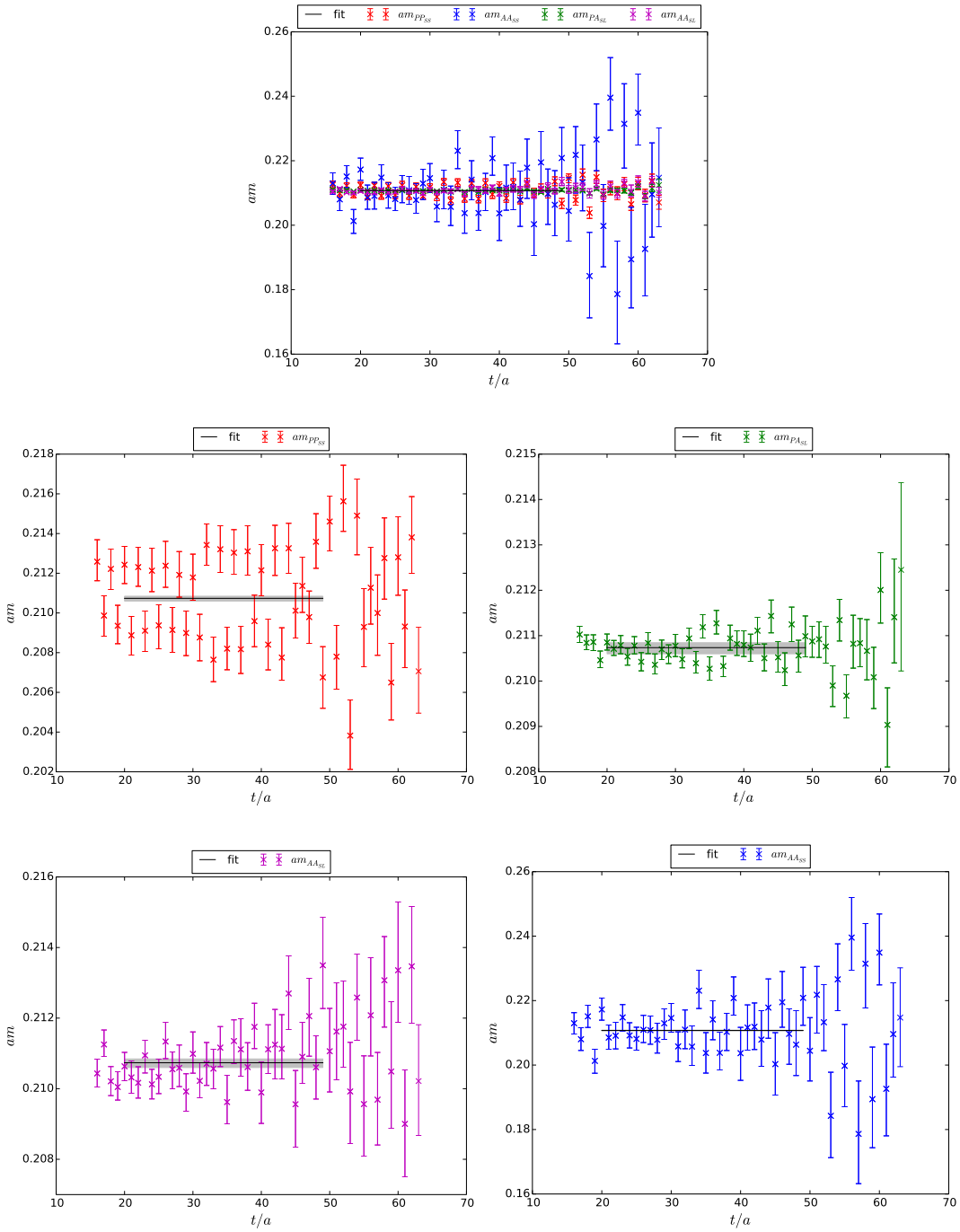

Figure 3.8 *Effective mass for the kaon on ensemble M0.*

Table 3.3 *The fit ranges for each fit type for each ensemble are presented here in lattice units.*

	$(t_{min} - t_{max})/a$							
	C0	C1	C2	M0	M1	M2	M3	F1
m_{sl}	12-40	12-31	12-24	20-50	11-24	11-24	11-24	16-40
m_{ll}	12-40	12-24	12-24	16-50	10-24	9-24	11-24	12-40
B_1	12-28	12-20	10-16	8-34	10-22	10-22	9-19	12-28
B_2	9-31	7-25	10-16	14-38	11-21	11-21	8-20	7-33
B_3	7-33	7-25	10-16	9-43	11-21	11-21	10-18	7-33
B_4	10-28	7-25	10-16	12-38	10-22	10-22	10-18	12-28
B_5	10-28	8-25	10-16	13-39	10-22	10-22	10-18	12-28
R_2	11-29	12-20	10-16	14-36	12-20	13-19	13-19	12-28
R_3	11-29	12-20	10-16	13-37	12-20	12-20	13-19	12-28
R_4	13-27	11-21	10-16	16-38	12-20	12-20	12-20	12-28
R_5	12-28	11-21	10-16	17-37	12-20	12-20	12-20	12-28

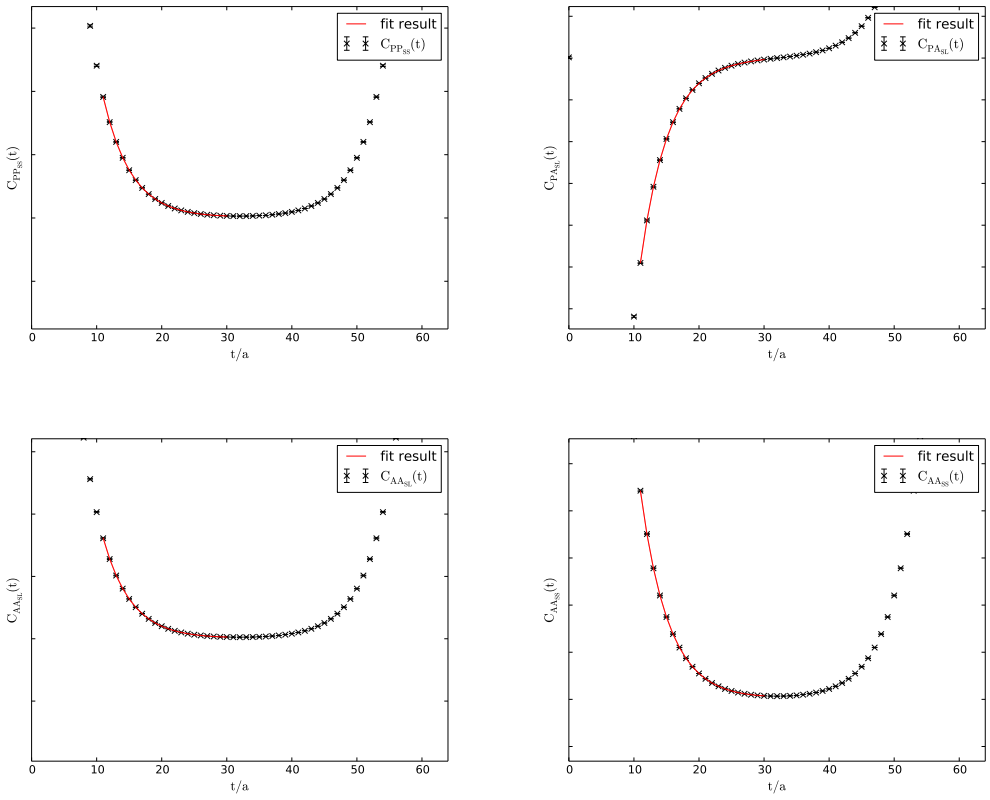

Figure 3.9 *Correlator fits for the kaon on ensemble M2. The scale of the exponential is such that the errors on the fit and the data-points are too small to discern by eye, but one can get an impression of the scale of the errors when looking at the effective mass plots.*

3.3.1 Temporal Correlations in Correlation Functions with Smeared Sources and Sinks

An oscillatory behaviour in some of the fits can be seen. This is a consequence of the temporal correlation introduced by source and sink smearing combined with the multi-hit strategy. The smearing function is a function of gauge fields on each time-plane then the sink time-plane is included in the set of sources. Let us consider this by considering the source-averaged correlators,

$$\begin{aligned} C^{s_1 s_2}_{\Gamma_1\Gamma_2}(\tau) &= \frac{1}{N_{hit}} \sum_{t_i} C^{s_1 s_2}_{\Gamma_1\Gamma_2}(t_i+\tau, t_i) \\ &= \frac{1}{N_{hit}} \sum_{t_i} \sum_{\mathbf{x},\mathbf{y}} \langle O^{s_1}_{\Gamma_1}(t_i+\tau, \mathbf{x}) O^{s_2}_{\Gamma_2}(t_i, \mathbf{y}) \rangle \\ &= \frac{1}{N_{hit}} \sum_{t_i} \sum_{\mathbf{x},\mathbf{y}} S(t_i+\tau, \mathbf{x}) S(t_i, \mathbf{y}). \end{aligned} \tag{3.10}$$

We use S to indicate all $O^{s_i}_{\Gamma_i}$ where s_i is smeared and we have dropped Γ_i from the notation for simplicity. Let us consider an example case on a lattice with $n_T = 8$, with sources on every other time-slice. When $\tau = 1$,

$$C^{SS}(\tau=1) = \frac{1}{N_{hit}} \sum_{\mathbf{x},\mathbf{y}} \Big(S(1)S(0) + S(3)S(2) + S(5)S(4) + S(7)S(6) \Big) \tag{3.11}$$

the smearing calculated on each time-slice appears only once, however when we consider $\tau = 2$,

$$C^{SS}(\tau=2) = \frac{1}{N_{hit}} \sum_{\mathbf{x},\mathbf{y}} \Big(S(2)S(0) + S(4)S(2) + S(6)S(4) + S(0)S(6) \Big) \tag{3.12}$$

we can see that there is repetition of smearing functions which will lead to a correlation which is not present when $\tau \notin \{t_i\}$. Therefore there will exist a correlation between all correlation functions with values of $\tau \in \{t_i\}$ as all will have the above effect. When the frequency of the sources changes, so does the pattern observed in the effective mass, as we can see in figure 3.10, which gives further evidence that the oscillations is due to correlations arising from the multi-hit strategy.

Figure 3.11 shows the correlation matrices for channel PP_{SS} pion correlators on M0, where this effect was most pronounced. Figure 3.12 shows the correlation

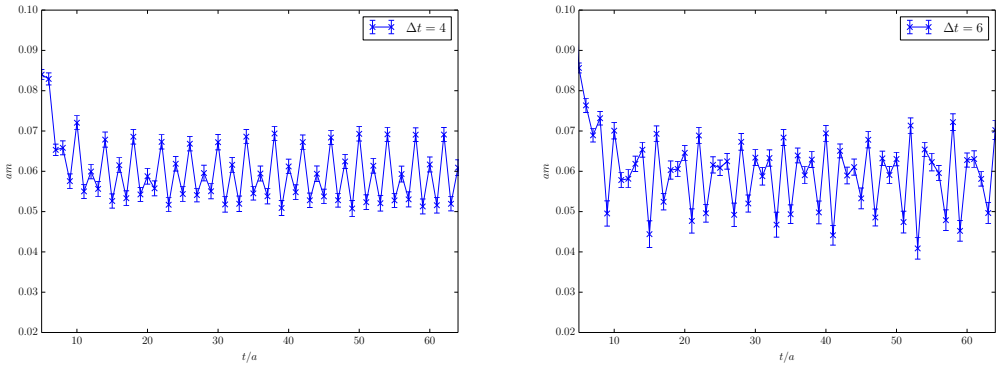

(a) *Sources on every fourth time-slice.* **(b)** *Sources on every sixth time-slice.*

Figure 3.10 *Effective mass plots for the pion for channel PP_{SS} on ensemble M0.*

matrices for the PP_{SS} pion effective mass on M0. The division of adjacent correlators performed to calculate the effective mass, amplifies the effect and introduces anti-correlations between adjacent time-slices. The effective mass calculated directly from the correlation functions (using equation 3.9) is used only for plotting, we take the result for m_{eff} from fitting the correlation functions, which do not show the same degree of temporal correlations. There are no signs of overall bias, and so we are confident that the correlation functions are still unbiased estimators. The multi-hit strategy is still favoured, given the significant reduction in variance it gives, and we conclude that if every time-slice had been used there would have been no such visible effect.

As an extra check, I present here both an uncorrelated and correlated fit of the channel PP_{SS} pion correlators on M0, where this effect was greatest. The χ^2/d.o.f were acceptable for both. For the uncorrelated fit it was less than 1 and was of order 2 for the correlated fit. Both fits were single channel fits, and had the same time range of $t_{fit} = [16, 50]$ with results,

$$m_{eff}^{\text{correlated}} = 0.059127(60) \qquad m_{eff}^{\text{uncorrelated}} = 0.059097(60). \tag{3.13}$$

Given that both methods present consistent and acceptable fits, even for the ensemble and quantity displaying the highest temporal correlation, the fit strategy employed is justified.

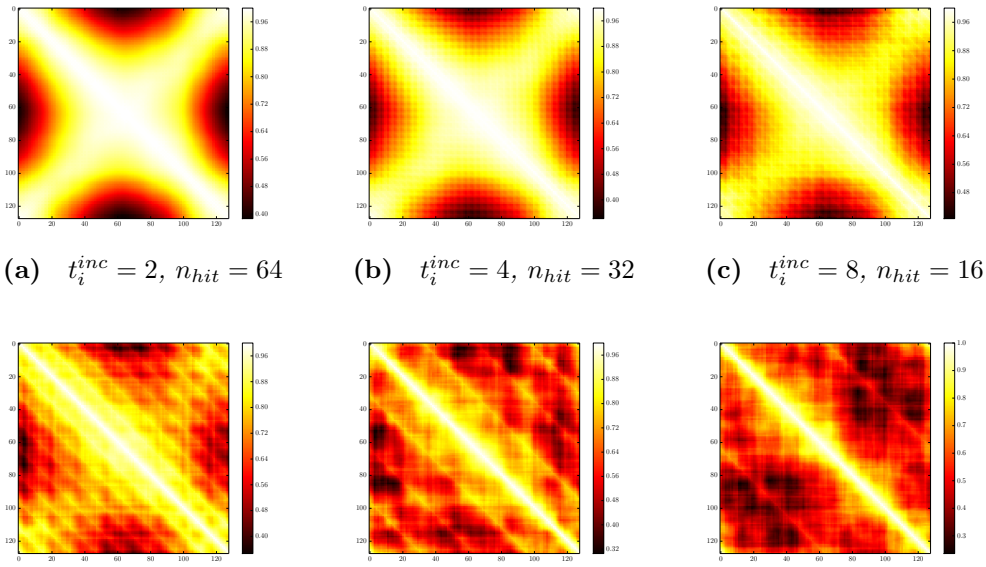

(a) $t_i^{inc} = 2$, $n_{hit} = 64$ **(b)** $t_i^{inc} = 4$, $n_{hit} = 32$ **(c)** $t_i^{inc} = 8$, $n_{hit} = 16$

(d) $t_i^{inc} = 16$, $n_{hit} = 8$ **(e)** $t_i^{inc} = 32$, $n_{hit} = 4$ **(f)** $t_i^{inc} = 64$, $n_{hit} = 2$

Figure 3.11 *The correlation matrices for the correlators $C_{PP}^{SS}(t)$ for different values of t_i^{inc}, the source time increment in the multi-hit strategy. Increased correlations between correlators separated by t_i^{inc} can be seen, with the pattern become especially clear as t_i^{inc} increases.*

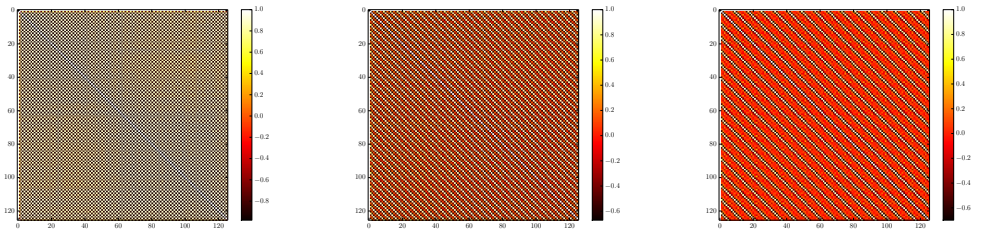

(a) $t_i^{inc} = 2$, $n_{hit} = 64$ **(b)** $t_i^{inc} = 4$, $n_{hit} = 32$ **(c)** $t_i^{inc} = 8$, $n_{hit} = 16$

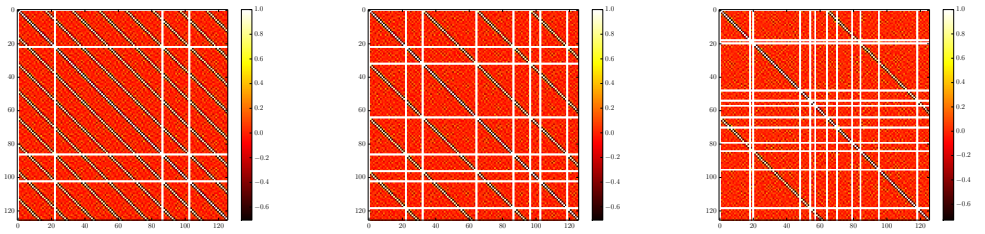

(d) $t_i^{inc} = 16$, $n_{hit} = 8$ **(e)** $t_i^{inc} = 32$, $n_{hit} = 4$ **(f)** $t_i^{inc} = 64$, $n_{hit} = 2$

Figure 3.12 *The correlation matrices for the effective masses* $m_{eff,PP}^{SS}(t)$ *for different values of* t_i^{inc}*, the source time increment in the multi-hit strategy. It can be seen that the correlations between values separated by* t_i^{inc} *have become far more pronounced. There is also anti-correlation between values separated by* $t_i^{inc} \pm 1$*. The horizontal and vertical white lines indicate values of* m_{eff} *which could not be calculated when* $(C(t+1) + C(t-1))/(2C(t)) > 1$*. It should be noted that the frequency of these increase as* n_{hit} *and therefore the statistics decrease, causing an increase in the noise.*

3.4 Decay Constant

The pseudoscalar decay constant is defined by the time-component of the conserved axial current at zero momentum,

$$\langle 0|A_4^C(\vec{p}=0)|\pi/K\rangle = Z_A \langle 0|A_4^L(\vec{p}=0)|\pi/K\rangle = mf. \tag{3.14}$$

This can be rewritten in terms of the amplitudes, as defined in equation 3.7,

$$f = Z_A \frac{M_A}{m}, \tag{3.15}$$

but it is more useful to write this in terms of the correlator amplitudes, $N_{\Gamma_1\Gamma_2}$, which we obtain directly,

$$f = Z_A \sqrt{\frac{2}{am}\frac{N_{PA}^2}{N_{PP}}} = Z_A \sqrt{\frac{2}{am} N_{AA}^2}. \tag{3.16}$$

When we consider smeared ensembles this expression becomes,

$$f = Z_A \sqrt{\frac{2}{am}\frac{(N_{PA}^{SLSL})^2}{(N_{PP}^{SSSS})}} = Z_A \sqrt{\frac{2}{am}\frac{(N_{AA}^{SLSL})^2}{(N_{AA}^{SSSS})}}, \tag{3.17}$$

where the correlator amplitudes are selected so that the smearing factors cancel. In practice we use the form of the decay constant on the left as the AA channel is noisier and we wish to avoid it.

Table 3.4 *Values of masses and decay constants for the light-light and strange-light pseudoscalar meson for each ensemble. Here the subscripts ll and sl represent the mesons with 2 light quarks and a light and strange quark respectively. The values were obtained from a simultaneous fit of multiple channels. For C1/2, with no smearing, we simultaneously fit the AA, AP and PP channels, while for all others, which have smeared sources and sinks,* $\mathrm{AA_{SL}}$, $\mathrm{AA_{SS}}$, $\mathrm{PA_{SL}}$, $\mathrm{PP_{SS}}$ *were included in the fit. The decay constants were calculated from the AP and PP channel amplitudes as described in equations 3.16 and 3.17*

	m_{ll}	m_{sl}	f_{ll}	f_{sl}
C0	0.08046(13)	0.28709(15)	0.07596(09)	0.090496(83)
C1	0.19041(45)	0.30613(42)	0.08511(18)	0.09446(17)
C2	0.24124(40)	0.32497(40)	0.09098(15)	0.09824(50)
M0	0.059087(85)	0.21074(12)	0.05551(17)	0.06630(18)
M1	0.12731(37)	0.22479(38)	0.06190(26)	0.06988(23)
M2	0.15128(40)	0.23210(40)	0.06455(23)	0.07125(22)
M3	0.17271(40)	0.24033(44)	0.06711(25)	0.07280(23)
F1	0.08410(17)	0.18519(21)	0.050812(89)	0.058320(58)

3.5 Four-Quark Operators

The three point correlation functions $C_{Q_j}(t_f, t, 0)$ of the four-quark operators can be expressed as,

$$C_{Q_j}(t_f,t,0) = \sum_k \Bigg[\frac{1}{(2E^{(k)})^2} \langle 0|P^{SS}|\bar{K}^{(k)}\rangle \langle \bar{K}^{(k)}|Q_j(t)|K^{(k)}\rangle \langle K^{(k)}|P^{SS}|0\rangle \times (e^{-E^{(k)}(t_f-t)} \pm e^{-E^{(k)}(T-(t_f-t))}) \times (e^{-E^{(k)}t} \pm e^{-E^{(k)}(T-t)}) \Bigg], \tag{3.18}$$

where the pseudoscalar meson, P_i, is annihilated at time t_f and and always created at time 0, hence why 0 is used directly in place of t_i. k labels the energy states including the excited states. The operator $Q_j^{4Q}(t)$ is one of the five four-quark operators given in 1.83, which describe SM and BSM meson mixing. The operators P are the pseudoscalar current operators. Notice that there is a summation over the energy states (k), but at large times, $0 \ll t \ll t_f$, the ground state dominates and assuming negligible "around the world" contributions, we can write,

$$C_{O_j}(t_f,t,0) \xrightarrow{t_i \ll t \ll t_f} \frac{1}{(2am)^2} \langle 0|P^{SS}|\bar{K}\rangle \langle \bar{K}|Q_j(t)|K\rangle \langle K|P^{SS}|0\rangle \, (e^{-amt_f} \pm e^{-am(T-t_f)}). \tag{3.19}$$

3.5.1 Ratios

We can directly obtain the ratios of BSM to SM matrix elements by taking the ratios of the BSM to SM three-point correlation functions,

$$\begin{aligned} R_j(a) &= \frac{\langle \bar{K}|Q_j(t)|K\rangle}{\langle \bar{K}|Q_1(t)|K\rangle} \\ &= \lim_{0\ll t\ll t_f} \frac{C_{Q_j}(t_f,t,0)}{C_{Q_1}(t_f,t,0)}, \end{aligned} \tag{3.20}$$

where $j = \{2...5\}$, as all other terms in the correlation functions cancel. This is explicitly written as function of the lattice spacing a, to indicate that this is a lattice measurement with dependence on the spacing. This must be renormalised in order to be considered in the continuum. We should also note that this is not the full definition of the ratio parameter we use when extrapolating to the physical point, which is given in equation 1.80. This is an intermediate step which must be combined with the lattice results for the pseudoscalar meson mass and decay constant.

Several values of Δt, the separation between t_i and t_f, had been run for each ensemble. The final value presented was chosen to ensure the plateau was sufficiently large to fit to the ground state. The time ranges of the fits were chosen to balance the need for a sufficiently large fit range to increase the degrees of freedom in the fit, while ensuring the χ^2 of the fit was reasonable. It should be noted that for M_0 there was some ambiguity and thus choice over the optimal time separation to choose. A systematic was applied in which, the standard deviation of the fit results for different (sensible) choices of time separation was included as an error before renormalisation or inclusion in the global fit. This was applied to C0, M0 and F1 only. The effect was at the sub-percentage level for all ensembles and typically far smaller than the statistical error. Only for M0 was the systematic similar in size to the statistical error, but was still less than 1%. We present plots of the fits for the physical point ensembles in figures 3.13 and A.15. The results are in in table 3.5. The remaining plots for the other ensembles are given in the appendix.

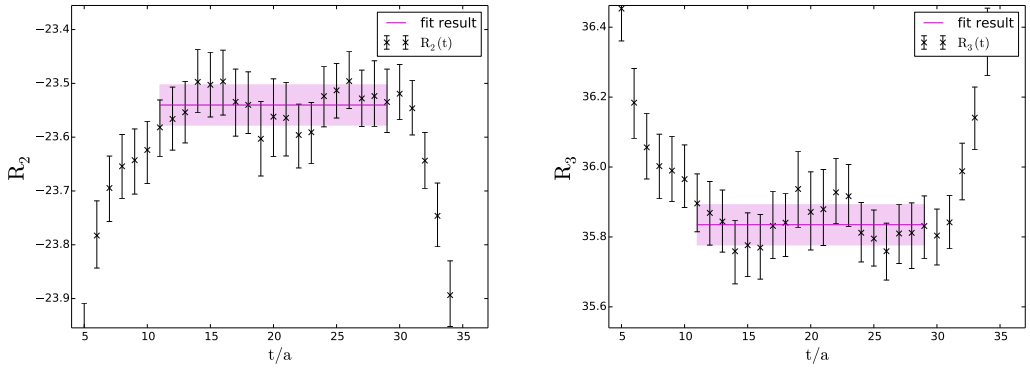

(a) *VV-AA* **(b)** *SS-PP*

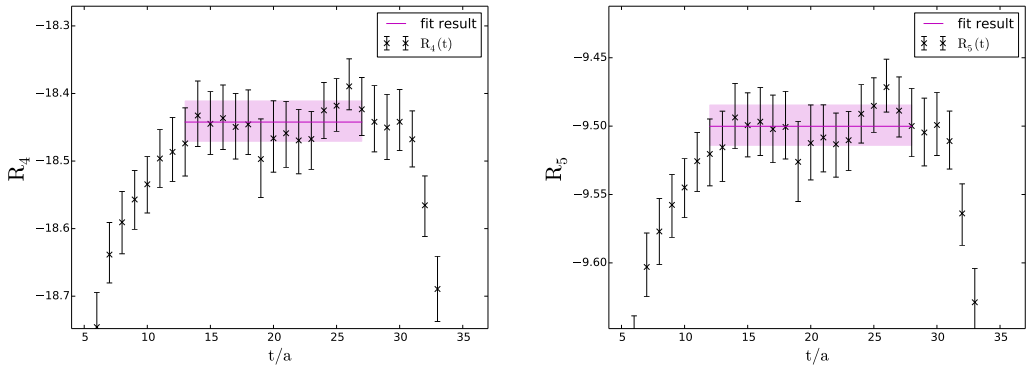

(c) *SS+PP* **(d)** *TT*

Figure 3.13 *Ratio parameter fits for ensemble C0.*

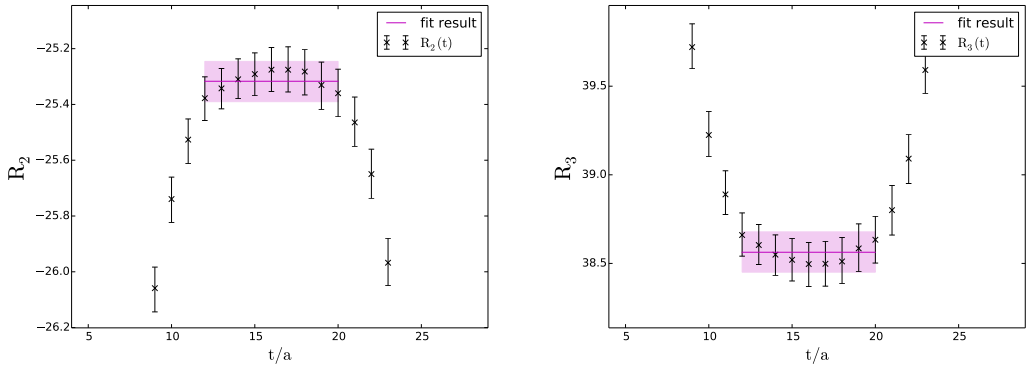

(a) *VV-AA* **(b)** *SS-PP*

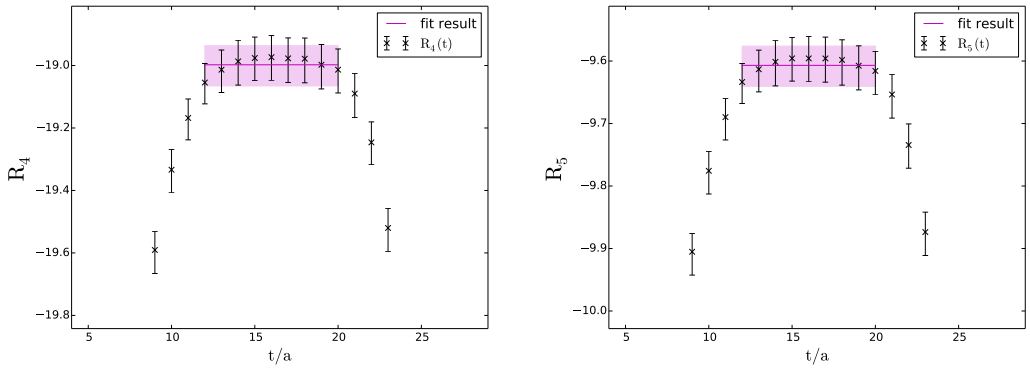

(c) *SS+PP* **(d)** *TT*

Figure 3.14 *Ratio parameter fits for ensemble M1.*

Table 3.5 *Values of the direct ratios of the BSM matrix elements to the SM matrix element, $\frac{\langle \bar{P}|Q_i|P\rangle}{\langle \bar{P}|Q_1|P\rangle}$. These were found by fitting the ratio of correlators to a constant at large times.*

	R_2	R_3	R_4	R_5
C0	-23.540(37)	35.835(59)	-18.442(30)	-9.500(16)
C1	-20.517(44)	31.006(70)	-16.585(51)	-8.547(28)
C2	-18.382(36)	27.621(54)	-15.035(39)	-7.765(20)
M0	-28.179(45)	43.165(70)	-20.574(30)	-10.392(17)
M1	-25.317(72)	38.56(11)	-18.998(66)	-9.607(32)
M2	-23.670(52)	35.980(76)	-17.855(65)	-9.037(35)
M3	-22.263(54)	33.727(82)	-16.994(64)	-8.606(31)
F1	-28.565(53)	43.705(84)	-20.661(54)	-10.364(29)

3.5.2 Bag Parameters

To obtain the standard model bag parameter from the four-quark operator three point correlation function we must recall the form of two-point correlation functions at large times,

$$\begin{aligned} C_{PA}^{SLSL}(t_f,t) &= \frac{\langle 0|P^{SL}|\bar{K}\rangle\langle\bar{K}|A_0^{SL}|0\rangle}{2am_K}\left(e^{-am_K(t_f-t)}-e^{-am_K(T-(t_f-t))}\right) \\ C_{AP}^{SLSL}(t,t_i) &= \frac{\langle 0|A_0^{SL}|K\rangle\langle K|P^{SL}|0\rangle}{2am_K}\left(e^{-am_K(t-t_i)}-e^{-am_K(T-(t-t_i))}\right). \end{aligned} \tag{3.21}$$

Thus we can extract the bag parameter, at large correlation times, as,

$$\begin{aligned} B_K(a) &= \frac{C_{Q_1^{4Q}}(t_f,t,0)}{\frac{8}{3}C_{i,PA}^{SLSL}(t_f,t)C_{i,AP}^{SLSL}(t,0)} \\ &= \frac{\langle 0|P^{SS}|\bar{K}\rangle\langle\bar{K}|Q_j(t)|K\rangle\langle K|P^{SS}|0\rangle}{\frac{8}{3}\langle 0|P^{SL}|\bar{K}\rangle\langle\bar{K}|A_0^{SL}|0\rangle\langle 0|A_0^{SL}|K\rangle\langle K|P^{SL}|0\rangle} \\ &\times \frac{\left(e^{-am_K(t_f-t)}-e^{-am_K(T-(t_f-t))}\right)\left(e^{-am_Kt}-e^{-am_K(T-t)}\right)}{\left(e^{-am_K(t_f-t)}-e^{-am_K(T-(t_f-t))}\right)\left(e^{-am_Kt}-e^{-am_K(T-t)}\right)} \\ &= \frac{\langle\bar{K}|Q_1^{4Q}(t)|K\rangle}{\frac{8}{3}\langle\bar{K}|A_0|0\rangle\langle 0|A_0|K\rangle}. \end{aligned} \tag{3.22}$$

The form of the three point correlator inserted in the above expression does not neglect the "around the world" contributions and so does not exactly match the form given in 3.19 but is closer to that in 3.18. Alternatively one can neglect the "around the world" contributions in both the two-point and three-point

correlators to arrive at the same expression. The cancellation of the matrix elements relies upon the smearing factors cancelling between matrix elements of different elements. The cancellation of the masses in the normalisation of the correlators is implicit.

Similarly the BSM bag parameter is,

$$\begin{aligned} B_j(a) &= \frac{\langle \bar{K}|Q_j^{4Q}(t)|K\rangle}{N_j \langle \bar{K}|P|0\rangle \langle 0|P|K\rangle} \\ &= \frac{C_{Q_j^{4Q}}(t_f,t,0)}{\frac{8}{3}C_{PP}^{SLSL}(t_f,t)C_{PP}^{SLSL}(t,0)}. \end{aligned} \tag{3.23}$$

where N_j are the normalisation factors given in section 1.4.1.

We choose Δt and the fit range in the same way as the ratio parameters, and again fit to a constant. Plots of the fits for C0 and M0 are shown in figure 3.15 with the remaining ensembles fits given in appendix A. Results are presented in table 3.6.

Table 3.6 *Values of the bag parameters for each ensemble. These were found by fitting the ratio of the three-point correlators normalised by the values N_i and the appropriate two-point correlators to a constant at large times.*

	B_1	B_2	B_3	B_4	B_5
C0	0.58332(82)	0.91842(59)	0.93209(60)	0.57577(45)	0.49430(38)
C1	0.5887(12)	0.9205(15)	0.9275(14)	0.59517(91)	0.51128(78)
C2	0.59749(78)	0.9268(11)	0.9285(12)	0.60645(76)	0.52209(65)
M0	0.55936(59)	0.90549(65)	0.92451(66)	0.52767(44)	0.44429(34)
M1	0.5630(11)	0.9038(17)	0.9179(18)	0.5425(10)	0.45724(83)
M2	0.56676(94)	0.9090(17)	0.9206(16)	0.54815(90)	0.46239(74)
M3	0.5720(12)	0.9120(17)	0.9208(16)	0.55692(90)	0.47013(77)
F1	0.54925(83)	0.8958(13)	0.9135(12)	0.51815(89)	0.43317(72)

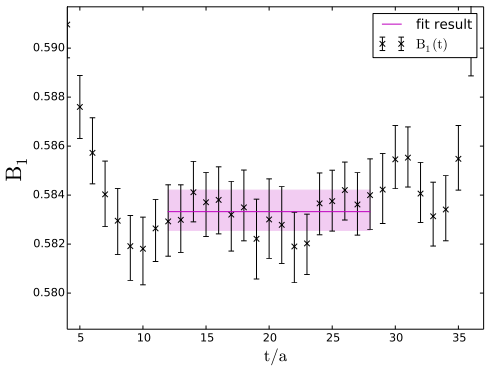

(a) *VV+AA*

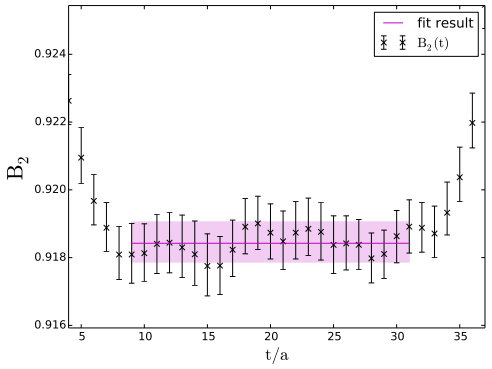

(b) *VV-AA*

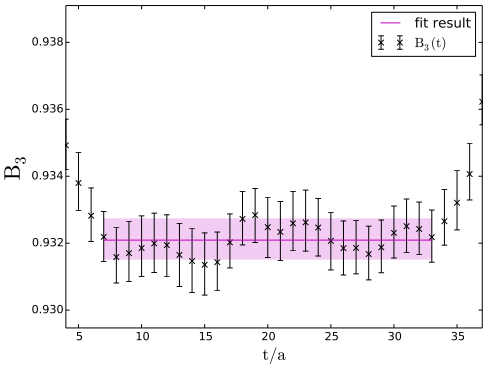

(c) *SS-PP*

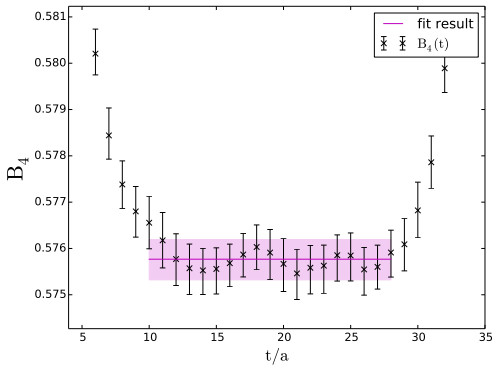

(d) *SS+PP*

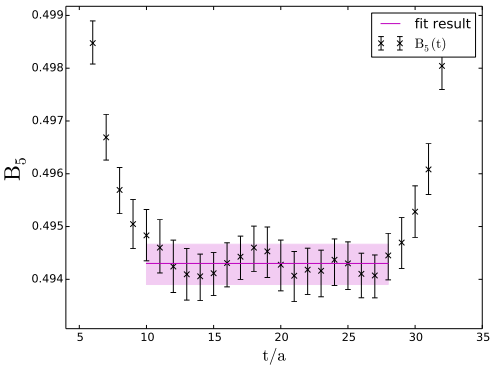

(e) *TT*

Figure 3.15 *Bag parameter fits for ensemble C0.*

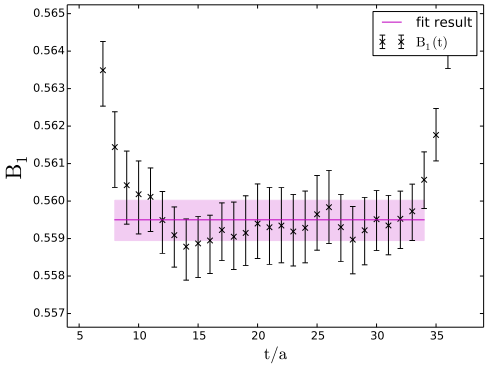

(a) *VV+AA*

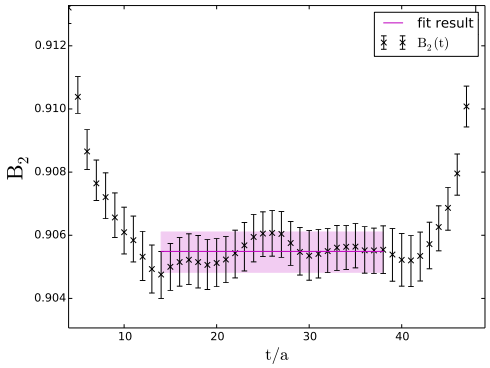

(b) *VV-AA*

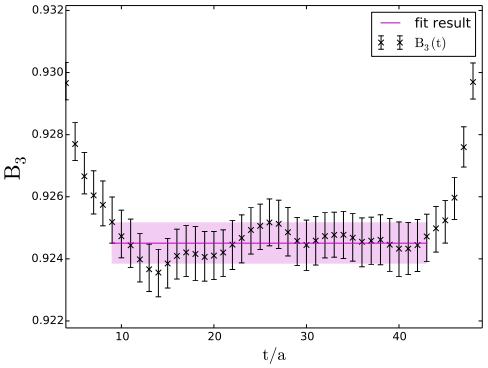

(c) *SS-PP*

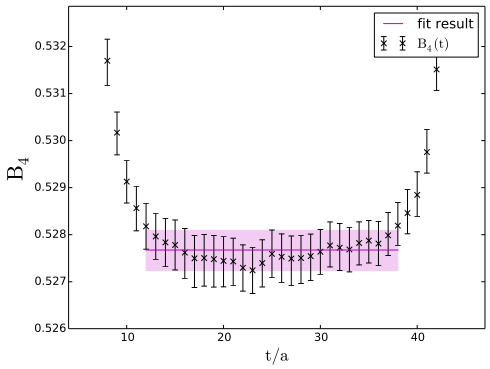

(d) *SS+PP*

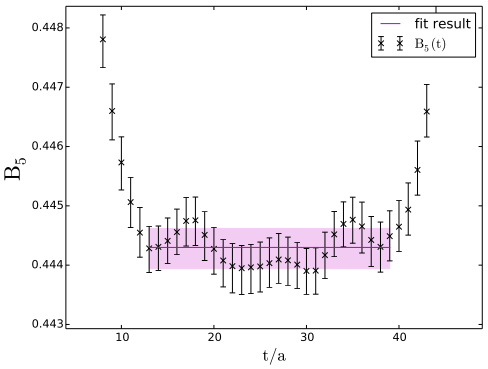

(e) *TT*

Figure 3.16 *Bag parameter fits for ensemble M0.*

Chapter 4

Non-Perturbative Renormalisation

4.1 The Rome-Southampton Method

In order to obtain physical results from measurements of lattice operators it is necessary to convert them to some perturbative renormalisation scheme, typically $\overline{\text{MS}}$. This can ideally be done with a non-perturbative intermediate scheme, such that all lattice calculations in the matching are performed to all orders and lattice perturbation theory is not used.

One such scheme, the Rome-Southampton momentum subtraction method (RI-MOM) [91] is a non-perturbative method in which the scale is defined by the momenta used. The scheme is constructed to be regularisation invariant. In order to match from a given bare theory to the RI scheme, all that is required is a self consistent determination of simple momentum space as an interface for converting between different regularisations, such as the lattice and $\overline{\text{MS}}$. The renormalisation conditions are fixed by requiring that a renormalised amputated vertex function, with a Landau fixed gauge, for a chosen set of external momenta calculated on the lattice is equal to the tree level operator. For example, for some two-quark operator, O_Γ, in a regularisation scheme S, the renormalisation condition imposed is,

$$\Lambda_{O_\Gamma}^{S,\text{ren}}(p_1,p_2) = \frac{Z_\Gamma^S}{Z_q}\Lambda_{O_\Gamma}(p_1,p_2) = O_\Gamma^{\text{tree}}. \tag{4.1}$$

Λ represents the projected amputated vertex function, Γ indicates the Dirac

structure of the operator ($\{S, P, V, A, T\}$), and the renormalisation scale μ, is determined by $\mu = p^2$ where $p^2 = p_1^2 = p_2^2$. The momenta are chosen from the Fourier modes of the simulated lattice,

$$ap_\mu = n_\mu \frac{2\pi}{L}, \tag{4.2}$$

where $n_\mu \in \{0, 1, \ldots, L_\mu\}$.

In order to ensure that the lattice calculation of the vertex function is precise, the momentum scale must be well below the lattice cut-off, $\frac{\pi}{a}$. The conversion to $\overline{\text{MS}}$ is perturbative and so accuracy depends upon the momentum scale being significantly larger than the QCD scale. These two conditions define the Rome-Southampton momentum window,

$$\Lambda_{\text{QCD}}^2 \ll p^2 \ll \left(\frac{\pi}{a}\right)^2 \tag{4.3}$$

in which the Rome-Southampton method can be reliably applied.

4.1.1 Choice of Kinematics

Originally the Rome-Southampton method chose exceptional kinematics defined by,

$$p = p_1 = p_2 \;\; ; \;\; q^2 = (p_1 - p_2)^2 = 0. \tag{4.4}$$

In this case it is possible for all the hard momenta to be carried through the vertex by a single gluon. This leads to chiral symmetry breaking and other infrared effects with a $1/p^2$ dependence. This is seen in the difference between the axial and vector vertex functions ($\Lambda_V - \Lambda_A$) and the pseudoscalar and scalar vertex functions ($\Lambda_S - \Lambda_P$). This effect can have a non-trivial dependence on the valence quark mass which makes mass extrapolations difficult. In some cases pion-pole subtraction is needed.

Since then, non-exceptional momentum (SMOM) kinematics, which are symmetric in all three channels, have been developed by RBC-UKQCD [99]. In this symmetric momentum subtraction scheme (RI-SMOM) the kinematics are defined as,

$$p_1 \neq p_2 \;\; ; \;\; q^2 = p_1^2 = p_2^2 \;\; ; \;\; q = (p_1 - p_2). \tag{4.5}$$

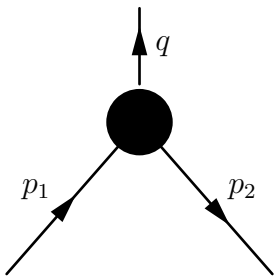

Figure 4.1 *Momentum flow diagram of some bilinear vertex function. The circle indicates some operator insertion and higher order effects.*

As there are no exceptional channels, chiral symmetry breaking and other infrared effects are reduced as discussed in [99][10]. It is no longer possible for one gluon to carry all the hard momentum through the vertex and we expect chiral symmetry breaking effects to fall as $1/p^6$ as suggested in [8]. However, non-perturbative condensate effects still exist within the non-exceptional scheme [90], which for Z_m are suppressed only by $1/p^2$ at leading order. One of the motivations for this chapter is to examine the infra-red region of the vertex functions, in particular the scalar operator. We aim to numerically check for these order $1/p^2$ effects.

4.1.2 Procedure for Bilinear Vertex Functions

In this subsection, the steps of the calculation to calculate the renormalisation constants for bilinear vertex functions are detailed.

We wish to calculate the momentum space Green's functions, $V_\Gamma(p_1, p_2)$, of the operator O_Γ where Γ indicates the dirac structure of the operator.

$$\begin{aligned} V(p_1,p_2) &= \int d^4x d^4y \, \langle \psi(x) O_\Gamma(y) \bar{\psi}(z) \rangle \, e^{-i(p_1\cdot(x-y)-p_2\cdot(y-z))} \\ &= \frac{1}{V} \sum_{x,y,z} S_1(x,y) e^{-i(p_1\cdot(x-y))} \Gamma e^{-i(p_2\cdot(z-y))} S_2(y,z), \end{aligned} \tag{4.6}$$

where S are the propagators. It should be noted that the term vertex function and Green's function are used interchangeably in this chapter.

The first step is defining the source to calculate the Green's function. Originally a single point source was used for this, but the volume source technique, developed by QCDSF [75], offers significant improvements in the statistical errors by averaging over all $L^3 \times T$ lattice sites.

The four-momentum source is defined as,

$$\eta_p(x) = e^{ip\cdot x}\delta_{ij}\delta_{\alpha\beta}, \tag{4.7}$$

where colour indices are shown by i, j and the spin by α, β. This is used on a Landau gauge-fixed configuration. The gauge is fixed using a Fourier accelerated conjugate gradient lattice gauge fixing algorithm [79].

The propagators S are then found by solving,

$$\sum_x D_{DWF}(y, x)S(x; p) = \eta_p(y), \tag{4.8}$$

on some gauge field $U_\mu(x)$, where D_{DWF} is the domain wall fermion Dirac matrix, and where we define $S(x; p) = \sum_y S(x, y)e^{ip\cdot y}$.

The bilinear vertex function is then formed by the contraction,

$$V_\Gamma^{\text{bilin}}(p_1, p_2) = \left[\sum_x \gamma_5 S'(x; p_1)^\dagger \gamma_5 \Gamma S'(x; p_2)\right]_{ij,\alpha\beta}, \tag{4.9}$$

where $\Gamma = \{\mathbf{I}, \gamma_5, \gamma_\mu\, \gamma_\mu\gamma_5, \sigma_{\mu\nu}\}$ indicates the Dirac structure of the vertex and $S'(x; p) = S(x; p)e^{-ip.x}$ are phased propagators. The external spin and colour indices are left free to allow for amputation and projection. By considering the form of the phased propagators and considering the definition of $S(x; p)$ it is clear that this is equal to the the form given in equation 4.6. The amputation is performed by contracting the gauge-averaged inverse momentum space propagators,

$$S(p; p) = \sum_x e^{-ip\cdot x} S(x; p), \tag{4.10}$$

with the vertex function,

$$\Pi_\Gamma^{\text{bilin}} = \langle S^{-1}(p_1, p_1)\rangle \langle V_\Gamma^{\text{bilin}}(p_1, p_2)\rangle \langle \gamma_5 [S^{-1}(p_2, p_2)]^\dagger \gamma_5\rangle\,, \tag{4.11}$$

giving the amputated Green's function $\Pi_\Gamma(p_1, p_2)$. It should be noted that, we amputate the gauge averaged vertex function with the gauge averaged

propagators, as we wish to recover the one particle irreducible Green's function.

Finally the bare vertex amplitudes are found by projecting the amputated Green's function onto their tree-level value,

$$\Lambda_\Gamma = \hat{P}^{\mathcal{S}}[\Pi], \tag{4.12}$$

where $\hat{P}$ denotes the projector. The definitions of the projectors will be given in the next subsection.

4.1.3 SMOM$^{\gamma_\mu}$ and SMOM$^{\not{q}}$ Schemes

In this section I define the two intermediate schemes. These are differentiated by their renormalisation conditions, and as such have different projectors. The SMOM$^{\gamma_\mu}$ scheme is defined by [99] the renormalisation conditions on the propagator,

$$\lim_{m_R\to 0}\frac{1}{12m_R}\left\{tr[S_R^{-1}(p)]_{p^2=-\mu^2}-\frac{1}{2}tr[q_\mu\Pi_\mu^{A,R}(p_1,p_2)\gamma_5]_{p_1^2=p_2^2=q^2}\right\}=1, \tag{4.13}$$

and,

$$\lim_{m_R\to 0}\frac{1}{48}\left\{tr[\gamma_\mu\frac{\partial S_R^{-1}(p)}{\partial p_\mu}]_{p^2=\mu^2}-\frac{1}{2}tr[q_\mu\gamma_\nu\frac{\partial}{\partial q_\nu}\Pi_\mu^{V,R}(p_1,p_2)\gamma_5]_{p_1^2=p_2^2=q^2}.\right\}=-1. \tag{4.14}$$

The projectors onto the tree-level for the bilinear vertices are then,

$$\hat{P}^{\gamma_\mu}[\Pi_S]=\frac{1}{12}tr(\Pi_S) \tag{4.15}$$

$$\hat{P}^{\gamma_\mu}[\Pi_P]=\frac{1}{12}tr(\gamma_5\Pi_P) \tag{4.16}$$

$$\hat{P}^{\gamma_\mu}[\Pi_T]=\frac{1}{12}tr(\sigma_{\mu\nu}\Pi_T) \tag{4.17}$$

$$\hat{P}^{\gamma_\mu}[\Pi_V]=\frac{1}{48}tr(\gamma_\mu\Pi_V) \tag{4.18}$$

$$\hat{P}^{\gamma_\mu}[\Pi_A]=\frac{1}{48}tr(\gamma_\mu\gamma_5\Pi_V) \tag{4.19}$$

The projectors define the renormalisation conditions of the vertex functions, and note that the trace is taken such that the conditions apply to the trace and not the full vertex function. The relations between the vertex functions and propagators in QCD are expressed in the Ward-Takahashi identities, and thus it is important that the renormalisation conditions on the vertex functions and propagators satisfy the identities.

The Ward-Takahashi identities for the vector and axial-vector currents are,

$$q \cdot \Pi_{V_C,B}(p_1,p_2) = S_B^{-1}(p_2) - S_B^{-1}(p_1) \tag{4.20}$$

$$-iq \cdot \Pi_{A_C,B}(p_1,p_2) = 2m_B \Pi_\mu^{P,B}(p_1,p_2) - i\gamma_5 S_B^{-1}(p_2) - S_B^{-1}(p_1) i\gamma_5. \tag{4.21}$$

Consider the object $\frac{1}{48} tr(q_\mu \gamma_\mu \Pi_\mu^{V,B})$ and apply the Ward identity 4.20.

$$\begin{aligned}
\frac{q_\mu}{48} tr(\gamma_\mu \Pi_\mu^{V,B}) &= \frac{1}{48}[tr(\gamma_\mu S_B^{-1}(p_2)) - tr(\gamma^\mu S_B^{-1}(p_1))] \\
\frac{1}{48} tr(\gamma_\mu \Pi_\mu^{V,B}) + \frac{1}{48} tr(q_\mu \gamma_\nu \frac{\partial}{\partial q_\nu} \Pi_\mu^{V,B}) &= \frac{1}{48} tr(\gamma_\mu \frac{\partial S_B^{-1}(q)}{\partial q_\mu}) \\
\frac{Z_q}{Z_V} + \lim_{m_R \to 0} \left[\frac{Z_q}{Z_V} \frac{1}{48} tr(q_\mu \gamma_\nu \frac{\partial}{\partial q_\nu} \Pi_\mu^{V,R}) \right] &= \lim_{m_R \to 0} \left[\frac{Z_q}{48} tr(\gamma_\mu \frac{\partial S_R^{-1}(q)}{\partial q_\mu}) \right].
\end{aligned} \tag{4.22}$$

Differentiating with respect to $\not{q}_\mu$, taking the limit of zero mass and rewriting in terms of the renormalised quantities leads to the above result. From this it is clear to see that the renormalisation condition 4.14 is met when $Z_V^C = 1$.

We now consider $\lim_{m_R \to 0} \frac{1}{24} tr(q_\mu \gamma_5 \Pi_\mu^{A,B})$, applying the Ward identity, writing in terms of the renormalised quantities and using the pseudo-scalar renormalisation condition.

$$\begin{aligned}
\lim_{m_R \to 0} \frac{1}{24} \frac{Z_q}{Z_A} tr(-q_\mu \gamma_5 \Pi_\mu^{A,R}) &= \lim_{m_R \to 0} \left[\frac{Z_q}{Z_m Z_P} \frac{m_R}{12i} tr(\gamma_5 \Pi_{P,R}) \right. \\
&\quad \left. - \frac{Z_q}{24} (tr(S_R^{-1}(p_2)) - tr(S_R^{-1}(p_1))) \right] \\
1 &= \lim_{m_R \to 0} \frac{1}{12 m_R} (Z_m Z_p) \left[tr(S^{-1}(p)) - Z_A^{-1} \frac{1}{2} tr(q_\mu \gamma_5 \Pi_\mu^{A,R}) \right]
\end{aligned} \tag{4.23}$$

This gives the renormalisation condition 4.13 provided $Z_A^C = 1$ and $Z_m Z_p = 1$. Note that Z_A^C and Z_V^C indicate the renormalisation of the conserved currents. The local current renormalisation factors (which from now on we will refer to exclusively with Z_A and Z_V) are not 1. $Z_V = Z_A$ holds for the local currents provided they are related by a chiral transformation [28] and chiral symmetry breaking effects can be neglected.

The SMOM$^{\not{q}}$ scheme is defined by the conditions,

$$\lim_{m_R \to 0} \frac{1}{12 m_R} \left\{ tr[S_R^{-1}(p)]_{p^2=-\mu^2} - \frac{1}{2} tr[q^\mu \Pi_\mu^{A,R}(p_1, p_2)\gamma_5]_{p_1^2=p_2^2=q^2} \right\} = 1, \tag{4.24}$$

and,

$$\lim_{m_R \to 0} \frac{1}{12 p^2} tr[S_R^{-1}(p) \not{p}]_{p^2=\mu^2} = 1. \tag{4.25}$$

The projectors of this scheme are identical for the scalar, pseudoscalar and tensor operators but the vector and axial projectors are given by,

$$\hat{P}^{\not{q}}[\Pi_V] = \frac{q_\mu}{12 q^2} tr(\Pi_V \not{q}) \tag{4.26}$$

$$\hat{P}^{\not{q}}[\Pi_A] = \frac{q_\mu}{12 q^2} tr(\Pi_A \gamma_5 \not{q}). \tag{4.27}$$

As for the RI-SMOM$^{\gamma_\mu}$ scheme the Ward identities are satisfied.

4.1.4 Procedure for Four-Quark Operators

For the non-perturbative renormalisation of the four-quark operators, required for BSM kaon mixing, the procedure greatly mirrors that of the bilinears. The vertex functions of interest are those for the transition,

$$q_1(p_1)\bar{q}_2(-p_2) \to \bar{q}_1(-p_1) q_2(p_2), \tag{4.28}$$

where q_1 and q_2 indicate the quark flavours and for kaon mixing are d and s respectively. This is shown in figure 4.2. The choice of momenta are such that the kinematics are non-exceptional, with $p_1^2 = p_2^2 = (p_1 - p_2)^2 \equiv p^2$.

The procedure is very similar as for the bilinear functions. The propagators are

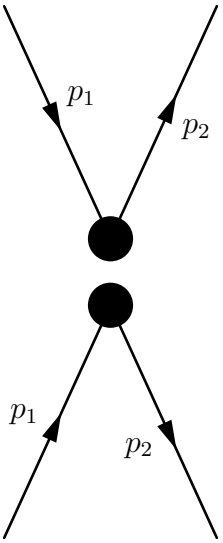

Figure 4.2 *Momentum flow diagram of some four-quark vertex function. The circle indicates some operator insertion and higher order effects.*

calculated from a momentum source in exactly the same way. The vertex function is then formed,

$$V_\Gamma^{\rm fq}(p_1,p_2) = \sum_x \Big[\gamma_5 S'(x;p_1)^\dagger \gamma_5 \Gamma S'(x;p_2)\Big]_{ij,\alpha\beta} \Big[\gamma_5 S'(x;p_1)^\dagger \gamma_5 \Gamma S'(x;p_2)\Big]_{kl,\gamma\delta}, \tag{4.29}$$

and then amputated by multiplying with the inverse propagators.

Recall that there exists a basis of 5 operators with structures (in the renormalisation basis) of VV+AA, VV-AA, SS-PP, SS+PP, TT. There can be mixing between these operators and so the renormalisation constants take the form of a matrix,

$$\Lambda_{ij} = \hat{P}_i[\Lambda_j] = [P_i]^{ba;dc}_{\beta\alpha;\delta\gamma}[\Lambda_j]^{ab;cd}_{\alpha\beta;\gamma\delta} \tag{4.30}$$

where $\hat{P}_i$ is the projection onto the tree-level operator O_i. The colour indices are a, b, c, d and the spin indices are $\alpha, \beta, \gamma, \delta$.

For the SMOM$^{\gamma}_{\mu}$ the projectors are defined as,

$$\begin{aligned}
[P^{\gamma_\mu}_{VV+AA}]^{ba;dc}_{\beta\alpha;\delta\gamma} &= [(\gamma^\mu)_{\beta\alpha}(\gamma^\mu)_{\delta\gamma} + (\gamma^\mu\gamma^5)_{\beta\alpha}(\gamma^\mu\gamma^5)_{\delta\gamma}]\delta^{ba}\delta^{dc} \\
[P^{\gamma_\mu}_{VV-AA}]^{ba;dc}_{\beta\alpha;\delta\gamma} &= [(\gamma^\mu)_{\beta\alpha}(\gamma^\mu)_{\delta\gamma} - (\gamma^\mu\gamma^5)_{\beta\alpha}(\gamma^\mu\gamma^5)_{\delta\gamma}]\delta^{ba}\delta^{dc} \\
[P^{\gamma_\mu}_{SS-PP}]^{ba;dc}_{\beta\alpha;\delta\gamma} &= [\delta_{\beta\alpha}\delta_{\delta\gamma} - (\gamma^5)_{\beta\alpha}(\gamma^5)_{\delta\gamma}]\delta^{ba}\delta^{dc} \\
[P^{\gamma_\mu}_{SS+PP}]^{ba;dc}_{\beta\alpha;\delta\gamma} &= [\delta_{\beta\alpha}\delta_{\delta\gamma} + (\gamma^5)_{\beta\alpha}(\gamma^5)_{\delta\gamma}]\delta^{ba}\delta^{dc} \\
[P^{\gamma_\mu}_{TT}]^{ba;dc}_{\beta\alpha;\delta\gamma} &= [\frac{1}{2}(\sigma^{\mu\nu})_{\beta\alpha}(\sigma^{\mu\nu})_{\delta\gamma}]\delta^{ba}\delta^{dc}.
\end{aligned} \tag{4.31}$$

For the $\not{q}$ scheme the projectors are,

$$\begin{aligned}
[P^{\not{q}}_{VV+AA}]^{ba;dc}_{\beta\alpha;\delta\gamma} &= \frac{1}{q^2}[(\not{q})_{\beta\alpha}(\not{q})_{\delta\gamma} + (\not{q}\gamma^5)_{\beta\alpha}(\not{q}\gamma^5)_{\delta\gamma}]\delta^{ba}\delta^{dc} \\
[P^{\not{q}}_{VV-AA}]^{ba;dc}_{\beta\alpha;\delta\gamma} &= \frac{1}{q^2}[(\not{q})_{\beta\alpha}(\not{q})_{\delta\gamma} - (\not{q}\gamma^5)_{\beta\alpha}(\not{q}\gamma^5)_{\delta\gamma}]\delta^{ba}\delta^{dc} \\
[P^{\not{q}}_{SS-PP}]^{ba;dc}_{\beta\alpha;\delta\gamma} &= \frac{1}{q^2}[(\not{q})_{\beta\alpha}(\not{q})_{\delta\gamma} - (\not{q}\gamma^5)_{\beta\alpha}(\not{q}\gamma^5)_{\delta\gamma}]\delta^{bc}\delta^{da} \\
[P^{\not{q}}_{SS+PP}]^{ba;dc}_{\beta\alpha;\delta\gamma} &= \frac{1}{p_1^2p_2^2 - (p_1\cdot_2)^2}[(p_1^\mu(\sigma^{\mu\nu}P_L)p_2^\nu)_{\beta\alpha}(p_1^\rho(\sigma^{\rho\sigma}P_L)p_2^\sigma)_{\delta\gamma}]_{\delta^{bc}\delta^{da}} \\
[P^{\not{q}}_{TT}]^{ba;dc}_{\beta\alpha;\delta\gamma} &= \frac{1}{p_1^2p_2^2 - (p_1\cdot_2)^2}[(p_1^\mu(\sigma^{\mu\nu}P_L)p_2^\nu)_{\beta\alpha}(p_1^\rho(\sigma^{\rho\sigma}P_L)p_2^\sigma)_{\delta\gamma}]_{\delta^{ba}\delta^{dc}}
\end{aligned} \tag{4.32}$$

where the Fierz relations have been used to "switch" the S and P Dirac Matrices for the V, A and T, resulting in the projectors $[P^{\not{q}}_{SS-PP}]$ and $[P^{\not{q}}_{SS+PP}]$ being colour mixed.

The projection of the tree level vertices is given by,

$$P_j[\Pi_i^{(0)}] = F_{ij}, \tag{4.33}$$

where the matrix F_{ij} is given for both schemes in [40]. In the chiral limit, there is only mixing between O_2 and O_3 and between O_4 and O_5, with all other off diagonal elements in the renormalisation matrix equal to zero. The domain wall action sufficiently approximates continuum chiral symmetry that we assume these elements to be negligible. We will numerically check that this is valid.

4.1.5 Twisted Boundary Conditions

When combining renormalised matrix elements in a global fit, it is important that the renormalisation occurs at the same energy scale. However different lattices have different values of momenta from the Fourier modes. It would be far more useful to arbitrarily select momentum. This way we could either directly calculate the renormalisation at a set scale on all lattices, or calculate the renormalisation at a large and well-sampled momentum range so that the dependence on scale can be well understood and extrapolation to an arbitrary scale can be done.

Twisted boundary conditions [23][61][67] are a solution to this. The twisted boundary conditions for the quark fields are,

$$q(x+L) = e^{-i\theta}q(x). \tag{4.34}$$

We define

$$\tilde{q}(x) = e^{-iBx}q(x), \tag{4.35}$$

where $aB_\mu = \theta/L_\mu$ such that $\tilde{q}(x)$ satisfies periodic boundary conditions. The Dirac operator is changed,

$$D = (\not{\partial} + m) \rightarrow \tilde{D} = (\not{\partial} + i\not{B} + m), \tag{4.36}$$

as is its inverse $\tilde{S}$,

$$\tilde{S}(x,y) = e^{-iB(x-y)}S(x,y). \tag{4.37}$$

Inverting the twisted Dirac operator with a momentum source gives the twisted propagator $\tilde{S}(z,p)$,

$$\sum_z \tilde{D}(y,z)\tilde{S}(z,p) = e^{ip\cdot y}. \tag{4.38}$$

We can see that twisting causes a shift in momentum $p \rightarrow p + B$ by considering the phased propagator,

$$\begin{aligned}
\tilde{S}'(z;p) &= \sum_x e^{-ip\cdot(z-x)}\tilde{S}(z;x) \\
&= \sum_x e^{-i(p+B)\cdot(z-x)}(z,x) \\
&= e^{-i(p+B)\cdot z}S(z,p+B) \\
&= S'(z;p+B).
\end{aligned} \tag{4.39}$$

In this way we can continuously shift the scale allowing us to perform the calculations at momenta between the fourier modes. This allows for effective extrapolation to an arbitrarily chosen scale, and can even allow for the calculations to be done directly at a chosen scale, provided the Fourier mode and twist are chosen well.

4.1.6 Step-scaling

Given it is possible to determine the relationship between the renormalisation and scale with a fit, it is also possible to scale the values of quantity renormalised at one scale to another scale, in a process called step-scaling [11]. This can be particularly useful given the limited range of the Rome-Southampton window. The non-perturbative renormalisation calculation is most precise at low scales where the momentum is well below the lattice cut-off, while the perturbative matching has smaller errors at large energy scales. Instead of having to find a compromise between the two requirements it is possible to perform the non-perturbative renormalisation at one scale, and then step-scale to a higher scale before conversion to $\overline{\text{MS}}$.

Recall that the scale of a continuum limit renormalised matrix element $\langle \mathcal{O}(\mu) \rangle$ is set completely by the renormalisation constant,

$$\langle \mathcal{O}(\mu) \rangle = \lim_{a^2 \to 0} Z_{\mathcal{O}}(a, \mu) \langle \mathcal{O}(a) \rangle . \tag{4.40}$$

For all lattices, the renormalisation constants must be at the same scale in order to perform the continuum extrapolation. Therefore we can define a scale evolution matrix $\sigma(\mu_1, \mu_2)$,

$$\sigma(\mu_1, \mu_2) = \lim_{a^2 \to 0} Z^{-1}(\mu_1, a) Z(\mu_2, a), \tag{4.41}$$

which defines the relationship between the continuum limit renormalised quantities at two different scales. This method can been done for operator mixing renormalisation matrices as well [12].

In this way we can express,

$$\begin{aligned} \langle \mathcal{O}(\mu_2) \rangle &= \lim_{a^2 \to 0} Z(\mu_2, a) \langle \mathcal{O}(a) \rangle \\ &= \lim_{a^2 \to 0} (Z(\mu_2, a) Z^{-1}(\mu_1, a))(Z(\mu_1, a) \langle \mathcal{O}(a) \rangle \\ &= \sigma(\mu_1, \mu_2) \langle \mathcal{O}(\mu_1) \rangle , \end{aligned} \tag{4.42}$$

which shows that the step-scaling factor allows for a renormalised quantity in the continuum limit at two different scales to be related.

This is useful given that different lattices included in the same continuum extrapolation have different Rome-Southampton windows. Choosing a momentum scale with small lattice artifacts in the region of accurate perturbative matching may not be possible. In this case step-scaling calculated excluding the coarsest lattice renormalisation will be immune to the lattice artifacts which contaminate the coarsest lattice. It can then be used to scale a continuum result (extrapolated from all lattices) at a lower scale to a higher scale for the matching to be done.

To calculate the scaling to 3GeV, the direct ratio of the renormalisation factors calculated directly at 3GeV and calculated directly at another lower scale μ_1 are taken for some ensemble with lattice spacing a,

$$\sigma^a(\mu_1, 3\text{GeV}) = Z(\mu_1, a)Z^{-1}(3\text{GeV}, a). \tag{4.43}$$

This is done for several values of μ_1, then an extrapolation in μ can be performed to obtain a continuous function $\sigma^a(\mu, 3\text{GeV})$. Provided this can be done for at least two ensembles with different lattice spacings there can then be an extrapolation in the lattice spacing to arrive at the continuum step-scaling function. This can then be applied to a lattice result that has been renormalised and extrapolated to the continuum to find the result at a different scale.

This manuscript relied upon step-scaling functions calculated using renormalisation calculated for the medium and fine ensembles only. In this way discretisation errors encountered on the coarsest lattice at 3GeV can be bypassed, while still performing the conversion to $\overline{\text{MS}}$ as 3GeV. The step-scaling factors were calculated by Nicolas Garron using the medium ensemble renormalisation factors presented in [40] and fine ensemble renormalisation factors calculated by Ava Khamseh. In figures 4.3 and 4.4 examples of the step-scaling extrapolation are shown for each scheme.

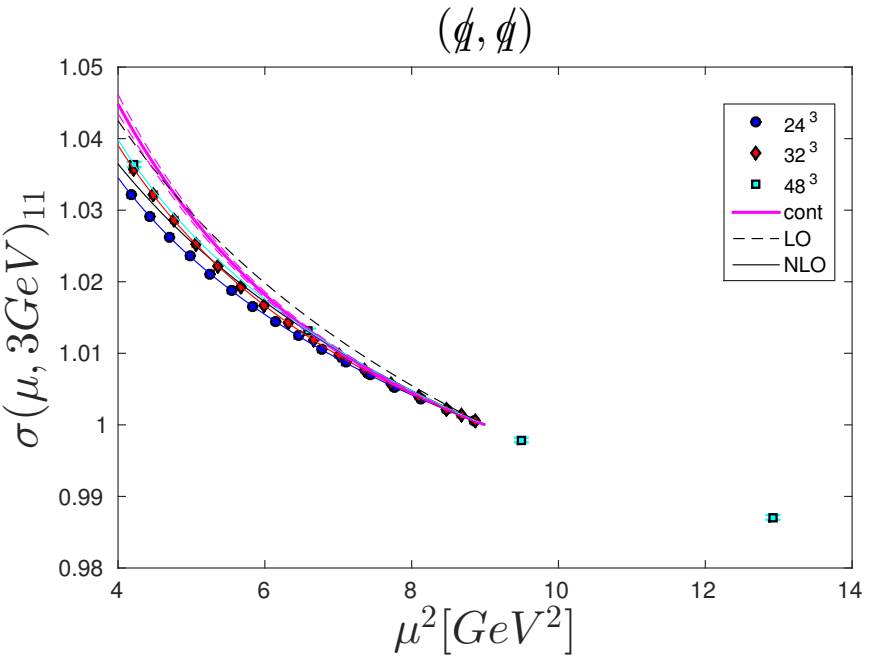

Figure 4.3 *The step-scaling function from μ to $3GeV$ is shown for the $(\not{q}, \not{q})$ scheme for Z_{11}. [70]*

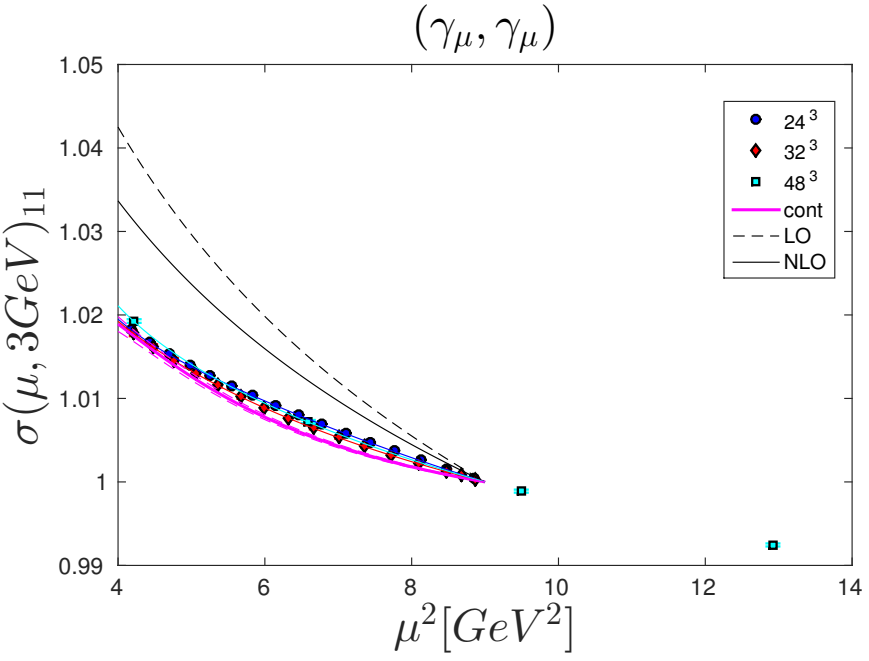

Figure 4.4 *The step-scaling function from μ to $3GeV$ is shown for the (γ, γ) scheme for Z_{11}. [70]*

4.1.7 Matching to $\overline{\text{MS}}$

It is typical to convert the renormalised results to $\overline{\text{MS}}$. This way they can be combined with Wilson coefficients so that phenomenological predictions and comparisons can be made. The symmetric momentum subtraction scheme, RI-SMOM, defined above, is regularisation invariant and can be implemented both with non-perturbative methods and in continuum perturbation theory. The conversion factors are then given by

$$C_{\mathcal{O}}^{\overline{\text{MS}}\leftarrow RI}(\mu) = \frac{Z_{\mathcal{O}}^{\overline{\text{MS}}}(\mu)}{Z_{\mathcal{O}}^{RI}(\mu)}. \tag{4.44}$$

As this is a perturbative calculation, the conversion is more accurate at higher energies where the QCD coupling, α is smaller. The calculation of the matching coefficients for the full BSM kaon mixing operators required are given in [40] at one loop. The calculation for the coefficients for O_1, O_2 and O_3 had been previously performed in [7] and [87].

4.2 Results on Coarse Lattices

I calculated the momentum source Green's functions on the $24^3 \times 48$ ensembles C1 and C2 and the larger $48^3 \times 96$ ensemble C0 with physical pions. C1(2) was calculated with the Shamir DWF action with $L_s = 16$, $M_5 = 1.8$ and $am_l = 0.005$, 0.01 respectively, while C0 was calculated with the Moebius DWF action with $L_s = 24$, $M_5 = 1.8$ and $am_l = 0.00078$. The calculation of the momentum source Green's functions, the projected amputated vertex function and the renormalisation constants $Z_{\mathcal{O}}$ follow the procedure described in the previous section. These calculations were performed using the Grid [38] lattice QCD library. I was responsible for developing the code to generate the Green's functions for both the bilinears and four-quarks. The calculations are performed on only a small subset of the configurations, as the errors are still well controlled even on this small subset. For C1 and C2 $n_{conf} = 10$ while for C0 I chose the smaller value $n_{conf} = 5$ as the cost of the calculations were significantly greater. The amputation and projection is performed on all configurations calculated with a bootstrap resampling. All subsequent calculations, fitting and extrapolation is then repeated for each bootstrap, allowing propagation of errors. It would be

	ap_1	ap_2	Minimum	Increment	Maximum
C0	$(0, x, x, 0)$	$(x, x, 0, 0)$	$x = \frac{2\pi}{L}(3)$	$\Delta x = \frac{2\pi}{L}$	$x = \frac{2\pi}{L}(10)$
C1/2	$(0, x, x, 0)$	$(x, x, 0, 0)$	$x = \frac{2\pi}{L}(2)$	$\Delta x = \frac{2\pi}{L}(0.25)$	$x = \frac{2\pi}{L}(5.75)$

Table 4.1 *The momenta at which the vertex functions were calculated. These momenta were chosen to cover a large range in order to probe the IR behaviour in the low momentum region.*

possible to instead perform jackknife resampling in the calculation of Λ_O but when deriving the renormalisation constants $Z_{\mathcal{O}}$ we require Z_A which is derived separately (as described in chapter 3) and hence is measured on a different number of configurations. By bootstrapping we are able to choose the number of resamples such that Z_A and the vertex functions can be combined. All these steps of the analysis, including the projection, extrapolation and resampling, were performed using C++ code I developed independently which uses Grid [38] and gsl as libaries.

The renormalisation conditions are defined in the chiral limit where the quark masses go to zero. The calculation of the vertex functions, however, were performed at finite mass. The ensembles C1 and C2 differ only in the quark mass, and hence it is possible to extrapolate them to the chiral limit. To do so we perform a linear fit in am_l to $-am_{res}$. The results of this extrapolation are given in table 4.2 and plots of the vertex functions, both at the finite masses and in the chiral limit, are shown in figures 4.9, 4.10 4.11, while an example of the chiral extrapolation is show in figure 4.7. It is clear to see that performing the calculation away from the chiral limit had a small effect even up to the heavier quark mass $am_l = 0.01$ ($m_\pi = 430$GeV) on C2. We are thus confident that for ensemble C0, with physical pions, we can ignore the effects of being away from the chiral limit.

In figure 4.5 the quantities $|\Lambda_A - \Lambda_V|$ and $|\Lambda_S - \Lambda_P|$ and their scale dependence are shown. Recall that when chiral symmetry is conserved we expect $Z_A = Z_V$ and $Z_S = Z_P = 1/Z_m$. The equalities are only broken as chiral symmetry is broken and so we can take the differences as a measure of the chiral symmetry breaking terms. The scale dependence of these terms is described well by a fit to $A + B/p^6$ indicating that the order $1/p^2$ chiral symmetry breaking terms observed in the exceptional kinematics scheme, are suppressed with non exceptional kinematics. Note differences in y-scale for each plot. $|\Lambda_S - \Lambda_P|$ exhibits the largest difference. At the lowest momentum scales explored this term reaches $\mathcal{O}(10\%)$, but for $\mu^2 \geq$ 4GeV, the difference is $\mathcal{O}(1\%)$ at most. The magnitude is far smaller for the

vector and axial-vector vertex functions.

We also consider the scale dependence of the vertex functions themselves, as shown in figure 4.8 and displayed in tables 4.2 and 4.3. In particular we consider the dependence of Λ_S and Λ_P. As can be seen in figure 4.8, Λ_S and Λ_P exhibit the largest dependence on the scale. The fit form $A + B/p^6$ is not sufficient to accurately describe the behaviour, and we need to include and a term proportional to $1/p^2$, as shown in figure 4.6.

The block diagonal elements of the vertex functions $\frac{\Lambda_{ij}}{\Lambda_A^2}$ are shown in figures 4.12 and 4.13. The off-diagonal elements are shown in figure 4.16. It is clear to see provided the momenta are sufficient these terms are negligible, as we expect in a chirally symmetric theory.

Given that we are able to accurately derive Z_A as described in section 3.2, it is practical to divide out Z_q and we can thus extract Z_m

$$Z_m = \frac{\Lambda_A}{Z_A \Lambda_S}. \tag{4.45}$$

Similarly we can extract the four-quark renormalisation constants,

$$\frac{Z_{ij}}{Z_V^2} = \frac{\Lambda_A^2}{\Lambda_{ij}} = \frac{\Lambda_V^2}{\Lambda_{ij}}, \tag{4.46}$$

where we rely on $Z_A \approx Z_V$ when chiral symmetry breaking is small. The renormalisation constants are given in 4.14 and 4.15. We also show the chirally forbidden elements in 4.16 at the chiral limit of C1 and C2 where we can see that at larger momenta the values are consistent with zero. As such we can justify, simply setting the values of these to zero.

In order to obtain the values of Z_m and $\frac{Z_{ij}}{Z_V^2}$ at 2GeV and 3GeV exactly, we perform an interpolation in momentum. We perform a fit over data within the range [1.9GeV,3.25GeV] to the fit form $A + Bp^2 + C^2$. This fit form does not necessarily describe the momentum dependence of the renormalisation constant over the complete range of momenta calculated. But over the small range chosen for the interpolation this fit form allows for an accurate interpolation. Final results for $\frac{Z_{ij}}{Z_V^2}$ appear in tables 4.7 to 4.10, while Z_m and Z_S are shown in tables 4.5 and 4.6.

The results in $\overline{\text{MS}}$ are also shown. The conversion factors for Z_{ij}/Z_V^2 to one loop

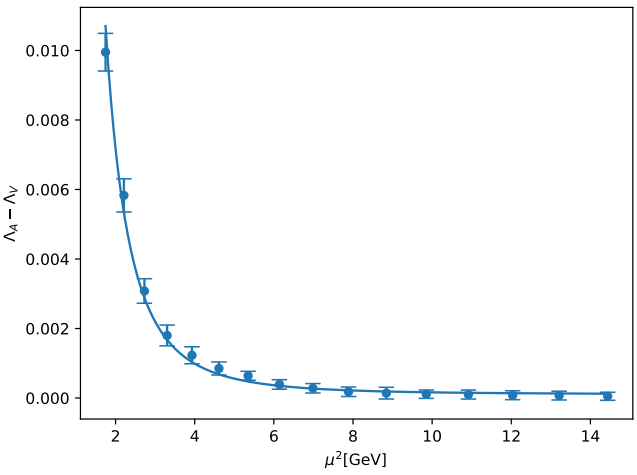

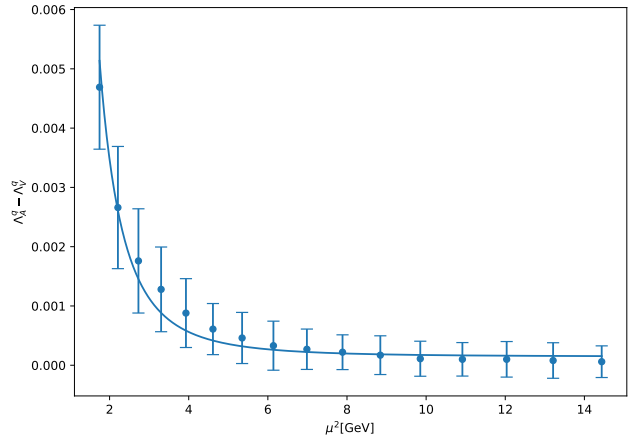

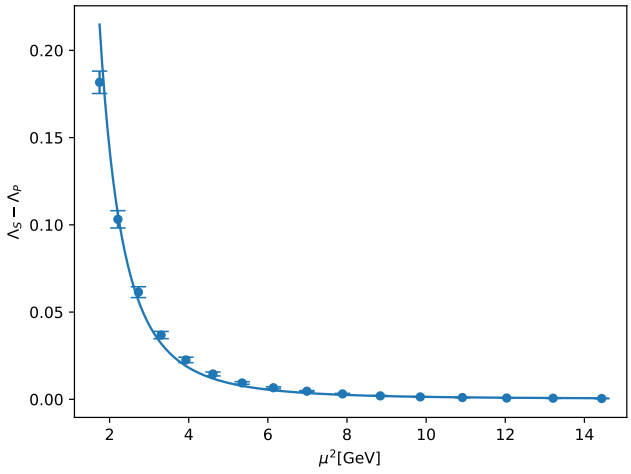

Figure 4.5 *The absolute difference between Λ_S and Λ_P, and between Λ_V and Λ_A are shown here for ensemble C1. The difference indicates the magnitude of the chiral symmetry breaking. Also shown is the fit to the form $A + B/p^6$. We can see that this describes the scale dependence well, reaffirming the suppression of order $1/p^2$ chiral symmetry breaking terms in the non-exceptional schemes.*

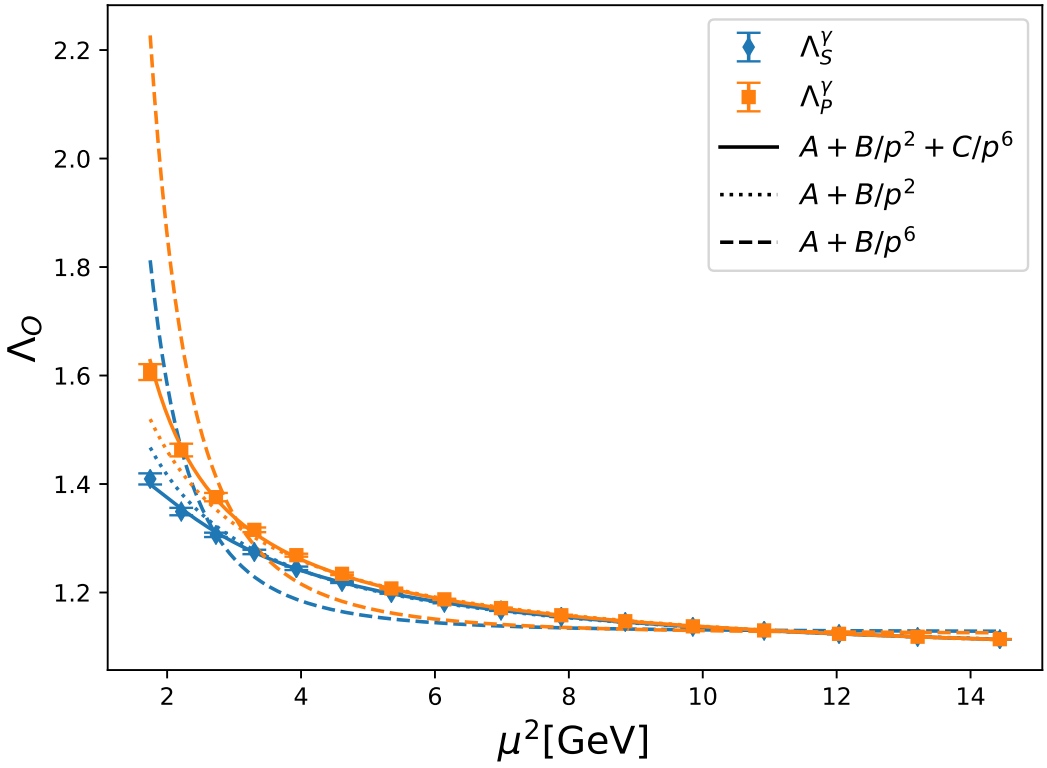

Figure 4.6 *The scalar and pseudoscalar vertex functions extrapolated to the chiral limit from C1 and C2 are shown alongside lines of best fit for different fit functions. It becomes clear that there is a leading $1/p^2$ term and that a fit including $1/p^6$ is not sufficient to describe the behaviour, but instead both terms are required.*

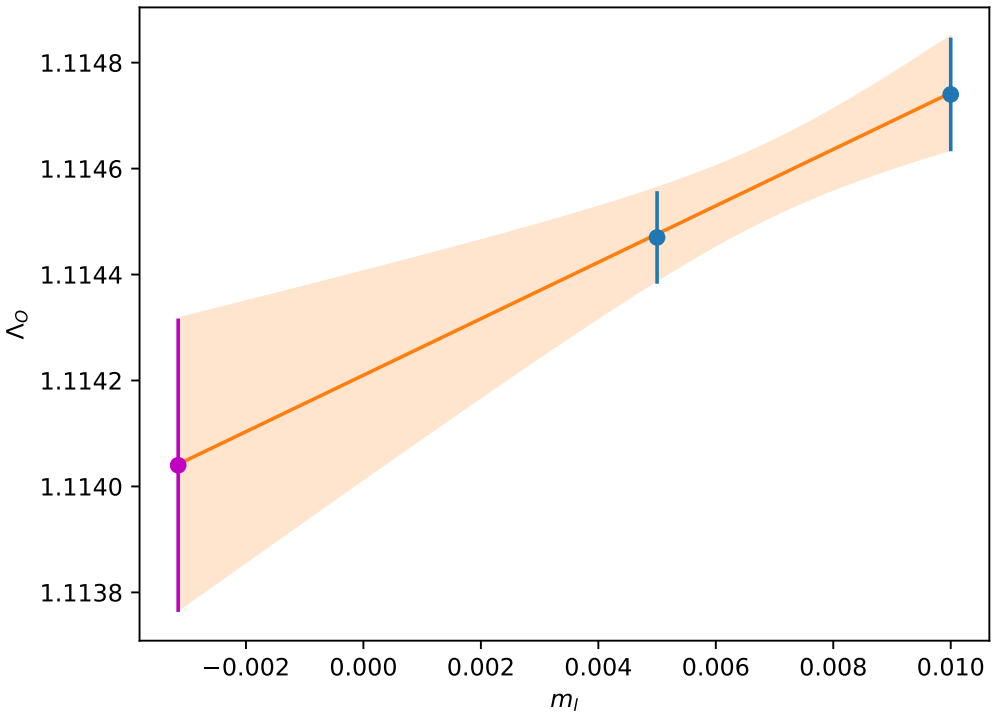

Figure 4.7 *The extrapolation of Λ_P^γ to the chiral limit for momenta $p = 2(2\pi/L)$, where the shaded region gives the uncertainty on the fit.*

Table 4.2 *The projected amputate bilinear vertex functions Λ_O for both intermediate schemes are presented for each momentum scale calculated on C1 and C2. The results of the chiral extrapolation are also shown.*

μ (GeV)	Λ_S^γ	Λ_P^γ	Λ_V^γ	Λ_A^γ	Λ_T^γ	$\Lambda_V^{\not q}$	$\Lambda_A^{\not q}$
			$m_l = 0.01$				
1.32	1.4148(18)	1.5875(43)	1.05800(60)	1.04325(50)	0.94494(60)	1.1685(16)	1.1605(16)
1.49	1.3628(12)	1.4598(17)	1.05281(37)	1.04457(41)	0.95840(43)	1.1547(10)	1.14974(98)
1.65	1.3179(12)	1.3744(14)	1.04971(32)	1.04504(30)	0.96968(29)	1.14396(66)	1.14078(65)
1.82	1.27994(86)	1.3144(10)	1.04829(26)	1.04542(25)	0.97929(24)	1.13560(67)	1.13352(64)
1.98	1.24849(72)	1.27010(58)	1.04780(21)	1.04598(20)	0.98768(19)	1.12917(55)	1.12780(53)
2.15	1.22214(46)	1.23647(40)	1.04796(20)	1.04678(19)	0.99525(17)	1.12440(45)	1.12347(44)
2.31	1.20056(36)	1.21064(39)	1.04859(18)	1.04777(17)	1.00207(14)	1.12093(35)	1.12024(35)
2.48	1.18294(33)	1.18993(35)	1.04954(13)	1.04895(13)	1.00828(10)	1.11842(28)	1.11791(28)
2.64	1.16829(24)	1.17304(30)	1.05073(13)	1.05031(12)	1.01400(11)	1.11687(28)	1.11649(28)
2.81	1.15597(19)	1.15932(23)	1.05215(12)	1.05184(11)	1.019369(99)	1.11621(23)	1.11591(23)
2.97	1.14565(16)	1.14810(22)	1.05375(11)	1.05352(11)	1.024452(98)	1.11633(23)	1.11610(22)
3.14	1.13706(15)	1.13887(17)	1.055553(99)	1.05531(10)	1.029340(94)	1.11716(19)	1.11698(19)
3.30	1.12982(14)	1.13116(12)	1.057518(99)	1.05737(10)	1.034092(99)	1.11865(18)	1.11850(18)
3.47	1.12370(12)	1.12473(11)	1.059616(89)	1.059502(91)	1.038719(94)	1.12075(16)	1.12063(16)
3.63	1.11854(32)	1.11934(11)	1.06186(19)	1.06177(26)	1.04328(36)	1.12355(27)	1.12346(34)
3.80	1.11412(10)	1.11474(11)	1.064238(96)	1.064160(96)	1.047832(97)	1.12712(15)	1.12704(15)
			$m_l = 0.005$				
1.32	1.4131(35)	1.5945(53)	1.05487(21)	1.04492(51)	0.94409(30)	1.16450(73)	1.15978(73)
1.49	1.3578(26)	1.4608(36)	1.05129(30)	1.04543(38)	0.95795(28)	1.15155(69)	1.14888(64)
1.65	1.3136(15)	1.3750(25)	1.04893(25)	1.04584(20)	0.96953(27)	1.14189(66)	1.14013(68)
1.82	1.2780(15)	1.3148(14)	1.04778(21)	1.04596(20)	0.97947(29)	1.13444(55)	1.13315(57)
1.98	1.2471(12)	1.26965(98)	1.04754(15)	1.04630(19)	0.98781(23)	1.12837(42)	1.12749(43)
2.15	1.22124(68)	1.23577(86)	1.04774(11)	1.04689(15)	0.99520(18)	1.12352(35)	1.12290(34)
2.31	1.20010(52)	1.20949(49)	1.048416(87)	1.04777(11)	1.00203(14)	1.12017(31)	1.11972(31)
2.48	1.18237(38)	1.18901(36)	1.049258(91)	1.04886(11)	1.00822(12)	1.11776(28)	1.11743(28)
2.64	1.16774(24)	1.17240(28)	1.050462(95)	1.05018(10)	1.01395(11)	1.11629(23)	1.11602(24)
2.81	1.15577(14)	1.15887(28)	1.05195(10)	1.05177(10)	1.01936(10)	1.11574(20)	1.11552(21)
2.97	1.14574(14)	1.14773(21)	1.05362(11)	1.05348(11)	1.02447(11)	1.11583(22)	1.11566(22)
3.14	1.13705(15)	1.13844(11)	1.055424(98)	1.05531(10)	1.02934(11)	1.11661(22)	1.11649(22)
3.30	1.12978(12)	1.13079(10)	1.057364(83)	1.057268(82)	1.034042(93)	1.11807(21)	1.11797(21)
3.47	1.12364(10)	1.12441(12)	1.059477(86)	1.059395(82)	1.038668(92)	1.12027(20)	1.12017(21)
3.63	1.118398(95)	1.11905(12)	1.061754(85)	1.0616880(80)	1.043258(89)	1.12319(20)	1.12311(20)
3.80	1.113986(88)	1.114474(87)	1.064136(82)	1.064089(81)	1.047799(88)	1.12676(19)	1.12670(19)
			$m_l = -m_{res}$				
1.32	1.4104(97)	1.606(16)	1.0498(12)	1.0476(16)	0.9427(12)	1.1580(35)	1.1586(34)
1.49	1.3498(73)	1.4626(98)	1.0488(10)	1.0468(13)	0.9572(11)	1.1465(25)	1.1475(24)
1.65	1.3065(44)	1.3760(68)	1.04766(85)	1.04714(66)	0.96927(87)	1.1385(20)	1.1391(20)
1.82	1.2750(39)	1.3156(40)	1.04695(68)	1.04684(63)	0.97975(84)	1.1325(17)	1.1326(17)
1.98	1.2448(33)	1.2689(28)	1.04711(52)	1.04681(58)	0.98801(67)	1.1271(15)	1.1270(15)
2.15	1.2198(19)	1.2346(23)	1.04737(46)	1.04705(49)	0.99513(55)	1.1221(12)	1.1220(12)
2.31	1.1994(15)	1.2076(14)	1.04813(39)	1.04777(41)	1.00195(43)	1.1189(10)	1.1189(10)
2.48	1.1814(12)	1.1875(11)	1.04881(33)	1.04872(37)	1.00813(37)	1.11669(89)	1.11666(90)
2.64	1.16685(79)	1.17135(81)	1.05003(30)	1.04997(31)	1.01388(32)	1.11535(75)	1.11527(77)
2.81	1.15545(45)	1.15816(81)	1.05164(34)	1.05167(33)	1.01934(32)	1.11497(68)	1.11487(69)
2.97	1.14588(46)	1.14714(65)	1.05341(34)	1.05342(33)	1.02451(33)	1.11500(65)	1.11494(65)
3.14	1.13704(47)	1.13774(42)	1.05521(33)	1.05522(33)	1.02934(34)	1.11570(67)	1.11569(67)
3.30	1.12972(42)	1.13019(36)	1.05711(27)	1.05710(27)	1.03396(28)	1.11713(64)	1.11710(65)
3.47	1.12354(35)	1.12389(37)	1.05925(26)	1.05922(25)	1.03858(27)	1.11949(60)	1.11941(60)
3.63	1.11816(60)	1.11858(36)	1.06158(40)	1.06156(50)	1.04321(65)	1.12260(72)	1.12254(81)
3.80	1.11376(26)	1.11404(28)	1.06397(27)	1.06397(26)	1.04774(29)	1.12619(56)	1.12616(56)

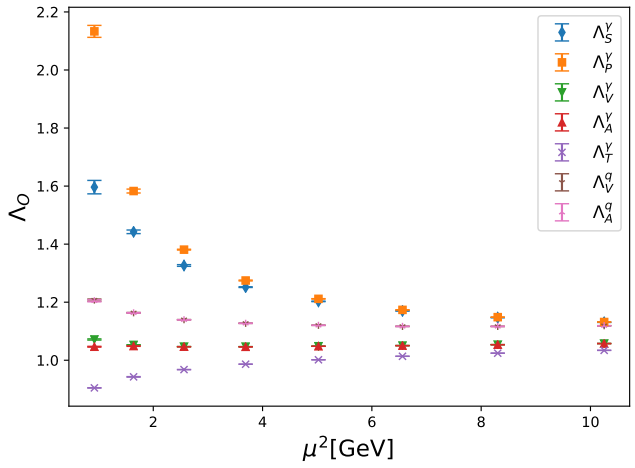

(a) *C0*

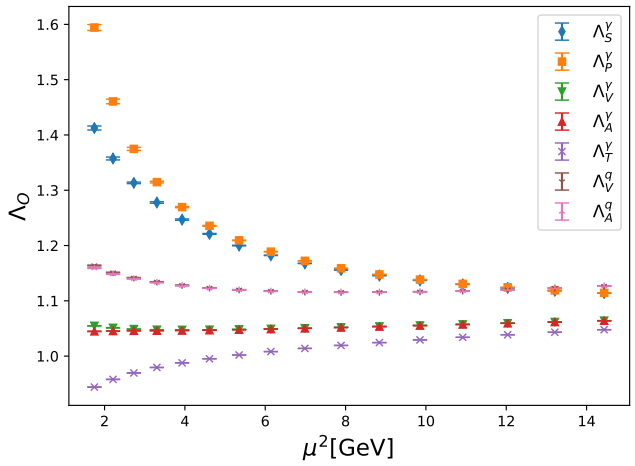

(b) *C1*

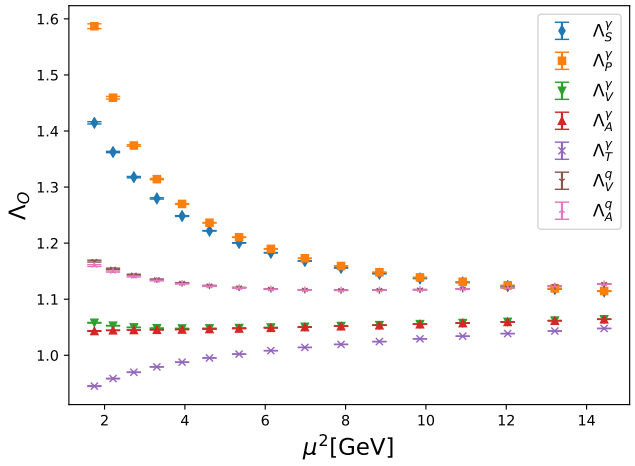

(c) *C2*

Figure 4.8 *The momentum dependence of all projected amputated bilinear vertex functions are shown here. One can see from these plots that at a scale of $\mu = 3GeV$ and above, the momentum dependence is becomes less pronounced, moving towards a plateau.*

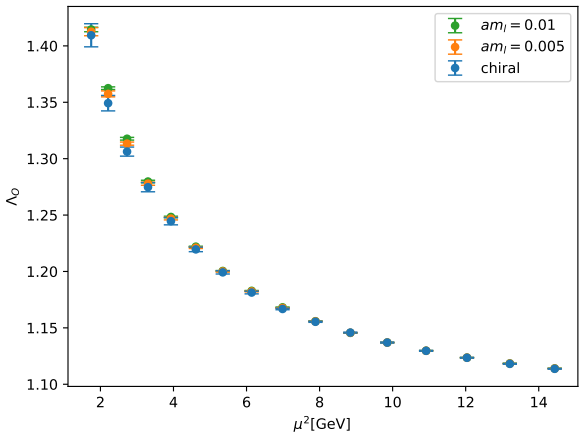

(a) Λ_S

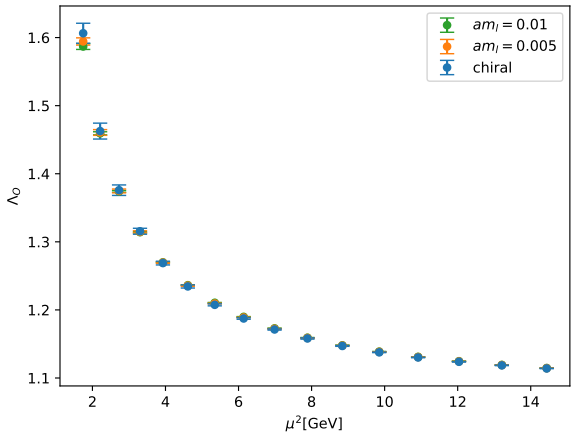

(b) Λ_P

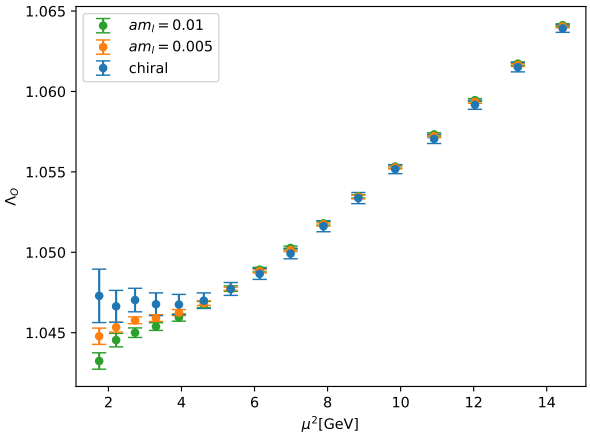

(c) Λ_T

Figure 4.9 *The chiral extrapolations of the projected amputated bilinear vertex functions calculated on C1 and C2 are shown. Even by eye, one can see evidence of* $1/p^2$ *dependence of* Λ_P *and* Λ_S*. While the* $RI - SMOM$ *scheme does reduce the infrared contamination for the scalar and pseudoscalar operators there are still effects that are only suppressed by* $1/p^2$*.*

Table 4.3 *The projected amputate bilinear vertex functions Λ_O for both intermediate schemes are presented for each momentum scale calculated on C0.*

μ (GeV)	Λ_S^γ	Λ_P^γ	Λ_V^γ	Λ_A^γ	Λ_T^γ	$\Lambda_V^{\not q}$	$\Lambda_A^{\not q}$
0.96	1.596(18)	2.132(16)	1.0713(16)	1.0465(11)	0.90467(43)	1.2073(37)	1.2048(38)
1.28	1.4422(59)	1.5830(65)	1.05287(52)	1.04884(88)	0.94272(85)	1.16358(92)	1.16330(90)
1.60	1.3265(29)	1.3811(15)	1.04695(33)	1.04670(19)	0.96777(19)	1.13980(43)	1.13936(37)
1.92	1.2519(12)	1.2747(14)	1.046882(82)	1.046220(93)	0.98640(24)	1.12722(44)	1.12722(43)
2.24	1.20274(76)	1.21153(66)	1.048218(77)	1.04809(10)	1.001592(58)	1.12028(19)	1.12023(17)
2.56	1.16994(18)	1.17351(18)	1.050498(53)	1.050360(91)	1.013633(74)	1.11660(20)	1.11657(19)
2.88	1.14685(19)	1.14842(21)	1.053725(59)	1.053698(41)	1.024322(55)	1.11652(16)	1.11653(15)
3.20	1.1304791(50)	1.13171(13)	1.0575533(50)	1.057525(34)	1.034055(57)	1.11899(12)	1.11898(11)

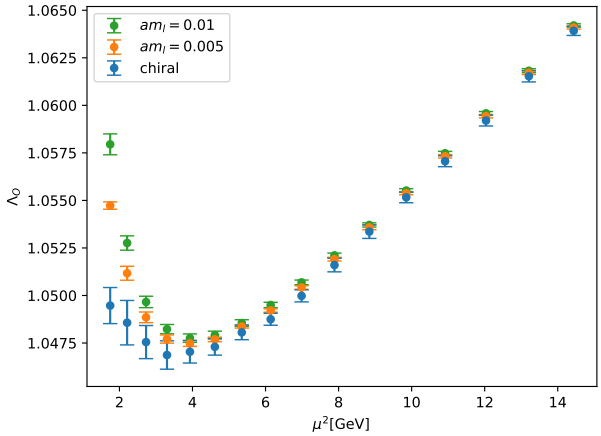

(a) Λ_V

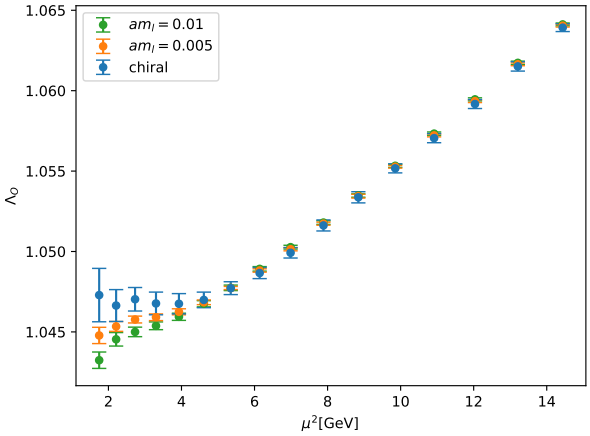

(b) Λ_A

Figure 4.10 *The chiral extrapolations of the projected amputated bilinear vertex functions calculated on C1 and C2 are shown.*

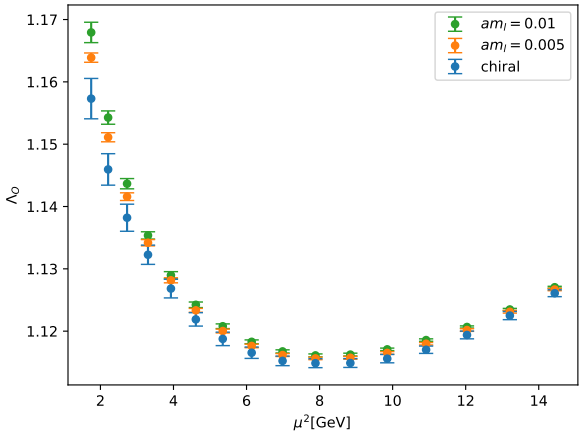

(a) $\Lambda_V^{\not q}$

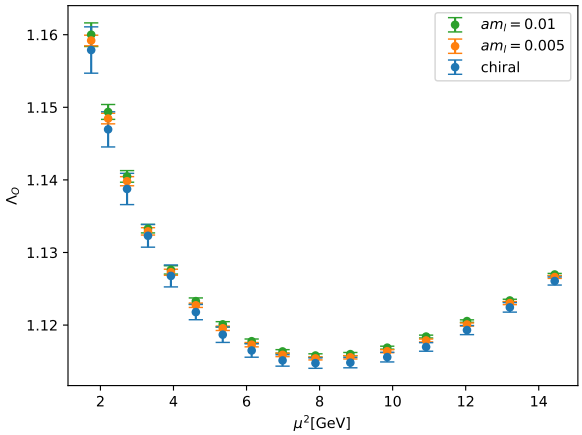

(b) $\Lambda_V^{\not q}$

Figure 4.11 *The chiral extrapolations of the projected amputated bilinear vertex functions calculated on C1 and C2 are shown. The difference between the values at the chiral limit and at even the heaviest mass are very small provided* $\mu \geq 2GeV$.

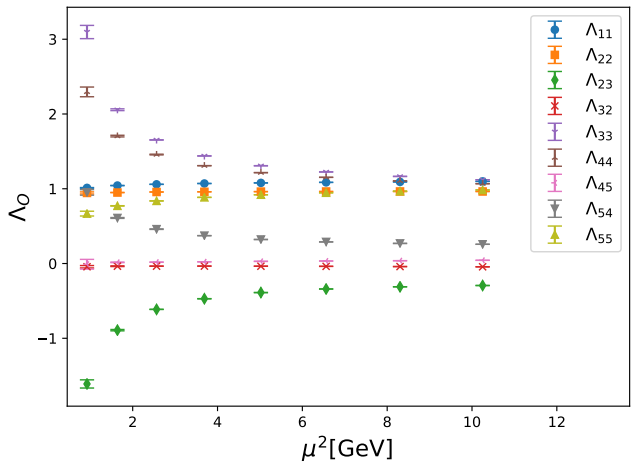

(a) *C0*

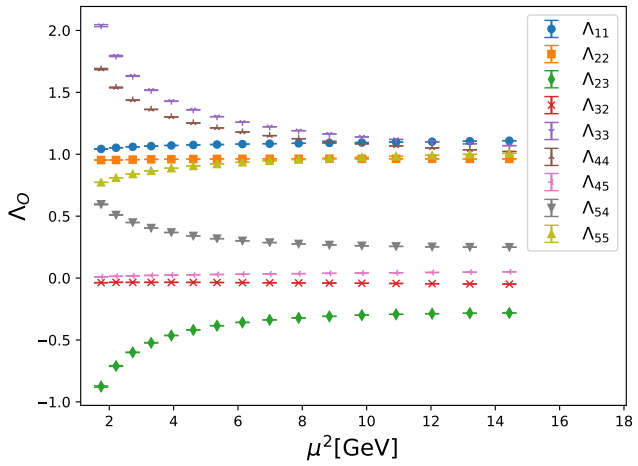

(b) *C1*

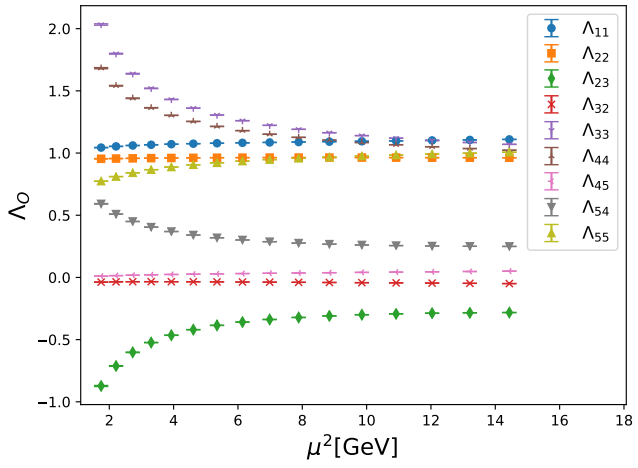

(c) *C2*

Figure 4.12 *The momentum dependence of the block diagonal projected amputated fourquark vertex functions in the scheme RI-SMOM$^{(\gamma,\gamma)}$ of the four quark operators are shown here.*

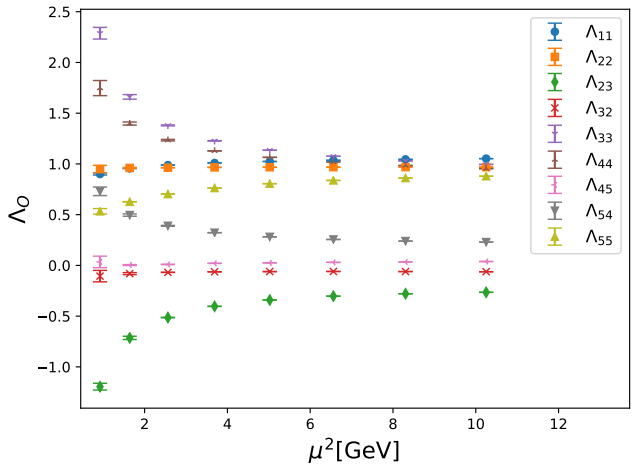

(a) *C0*

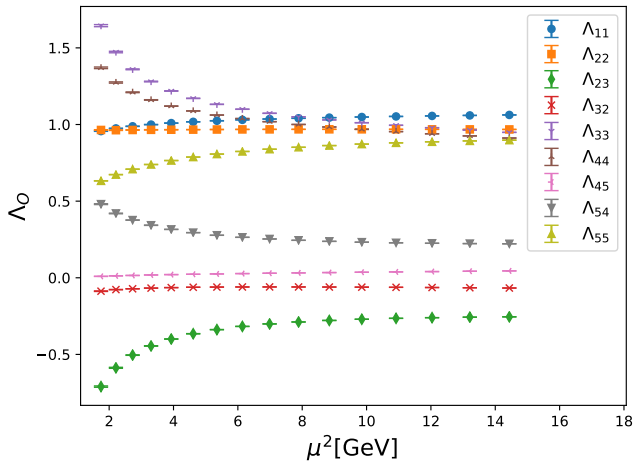

(b) *C1*

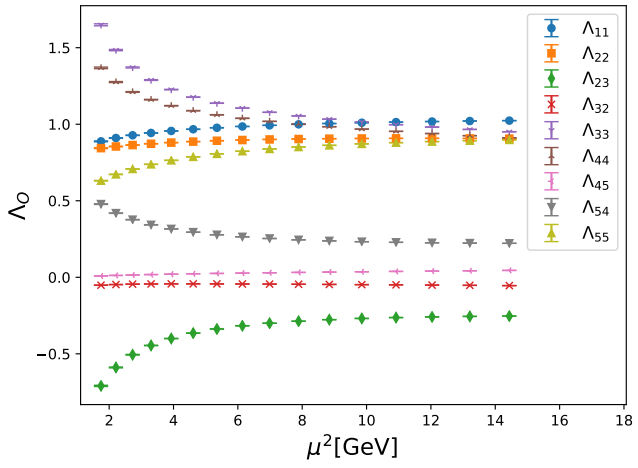

(c) *C2*

Figure 4.13 *The momentum dependence of all block diagonal projected amputated bilinear vertex functions in the scheme RI-SMOM$^{(q,q)}$ of the four quark operators are shown here.*

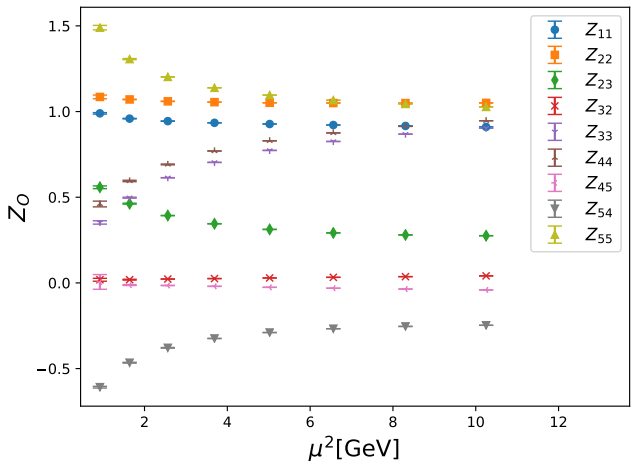

(a) *C0*

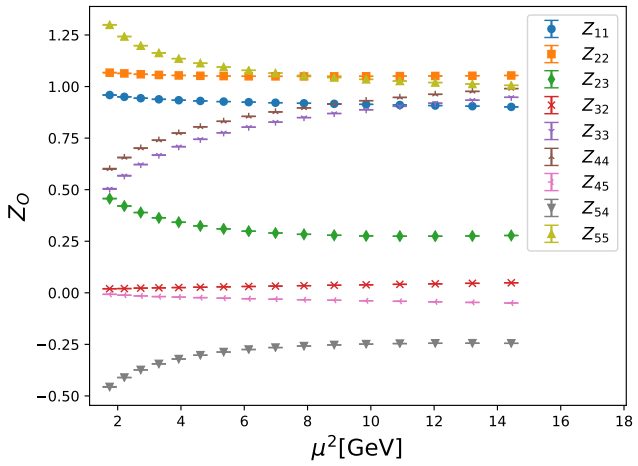

(b) *C1*

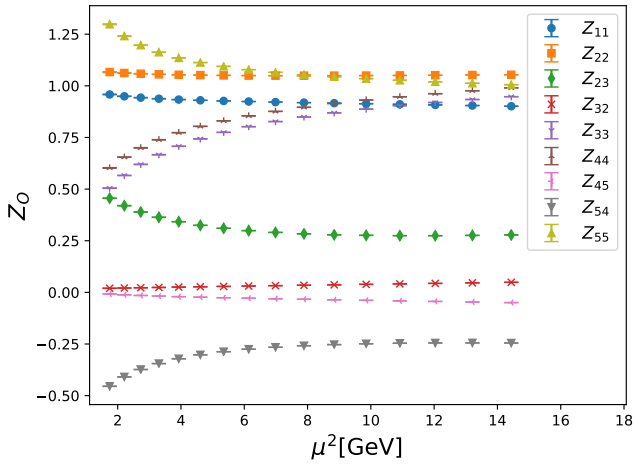

(c) *C2*

Figure 4.14 *The momentum dependence of block diagonal renormalisation constants Z_{ij}/Z_V^2 in the scheme RI-SMOM$^{(\gamma,\gamma)}$ of the four quark operators are shown here.*

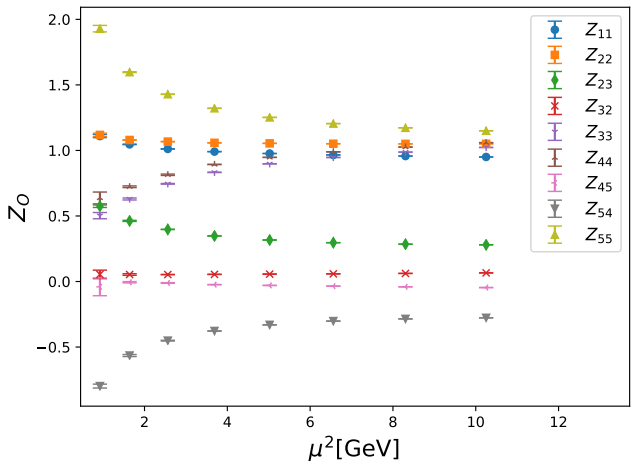

(a) *C0*

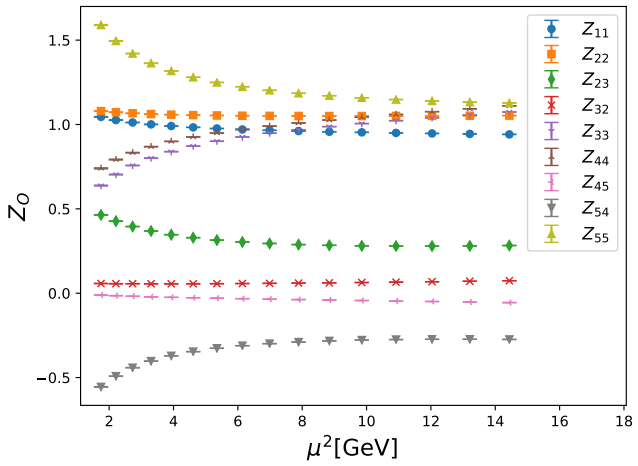

(b) *C1*

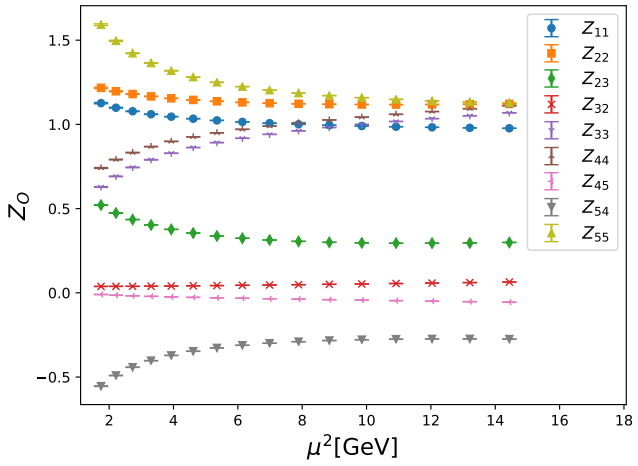

(c) *C2*

Figure 4.15 *The momentum dependence of all block diagonal renormalisation constants Z_{ij}/Z_V^2 in the scheme RI-SMOM$^{(q,q)}$ of the four quark operators are shown here.*

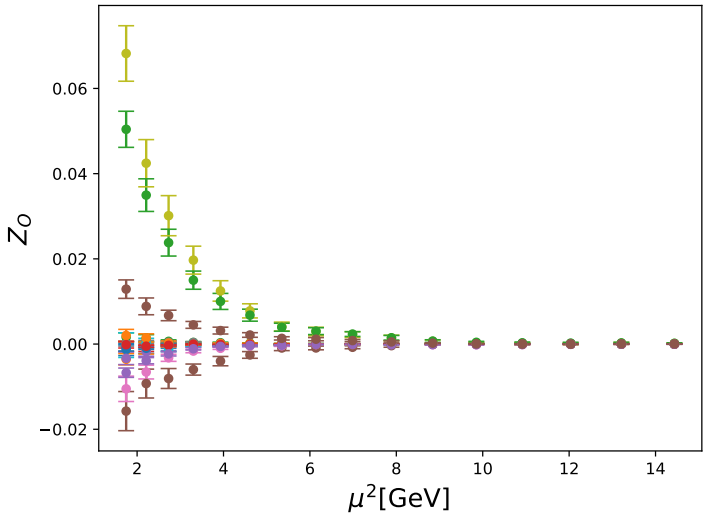

(a) $SMOM^{(\gamma_\mu,\gamma_\mu)}$

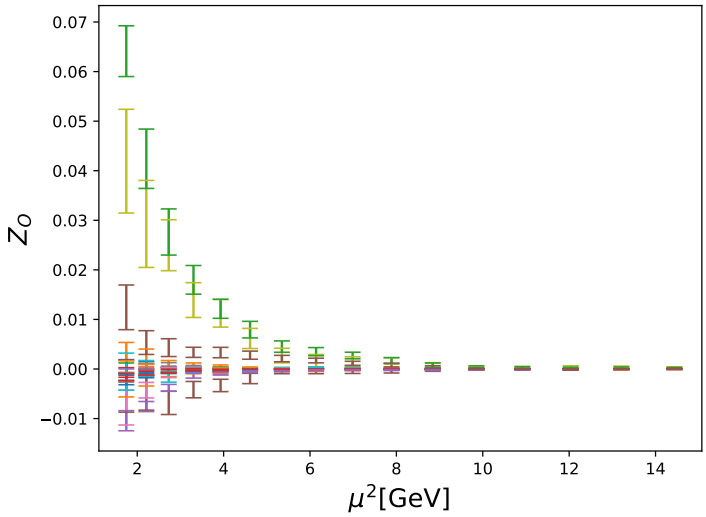

(b) $SMOM^{(\not{q},\not{q})}$

Figure 4.16 *Here are shown the elements of the four-quark renormalisation matrix that are chirally forbidden. It is clear that at large enough momenta they approach zero and can be neglected for both schemes.*

Table 4.4 *The values of α_S and the conversion factors for Z_m at both 2GeV and 3GeV.*

	μ=2GeV	μ=3GeV
$\alpha_s(\mu)$	0.2941	0.2442
$C_m^{\overline{\rm MS}\leftarrow {\rm SMOM}^{\gamma_\mu}}(\mu)$	0.95902	0.965297
$C_m^{\overline{\rm MS}\leftarrow {\rm SMOM}^{\not{q}}}(\mu)$	0.98625	0.988409

Table 4.5 *The values of Z_m at 2GeV and 3GeV presented in both $\overline{MS}$ and RI-SMOM via both intermediate RI-SMOM schemes. For C1/2 the results presented are in the chiral limit after extrapolation, while for C0 the results are calculated for physical light quark masses without extrapolation to the chiral limit.*

	μ (GeV)	$Z_m^{SMOM^{\gamma_\mu}}$	$Z_m^{\overline{\rm MS}\leftarrow SMOM^{\gamma_\mu}}$	$Z_m^{SMOM^{\not{q}}}$	$Z_m^{\overline{\rm MS}\leftarrow SMOM^{\not{q}}}$
C1/2	2	1.6548(43)	1.5870(41)	1.5382(49)	1.5170(48)
	3	1.51407(95)	1.46153(92)	1.4309(13)	1.4143(13)
C0	2	1.6603(34)	1.5923(33)	1.5437(37)	1.5225(36)
	3	1.51741(60)	1.46475(58)	1.43313(69)	1.41652(68)

are,

$$C_{ij}^{\overline{\rm MS}\leftarrow SMOM} = \mathbb{1} + \left(\frac{\alpha_s}{4\pi}\right)\Delta r_{ij} \tag{4.47}$$

where Δr_{ij} are given in [40].

For Z_m we follow [13], defining,

$$C_m^{\overline{\rm MS}\leftarrow SMOM} = \frac{c^{\overline{\rm MS}}(\mu)}{c^{SMOM}(\mu)}, \tag{4.48}$$

where

$$c^S(\alpha_s(\mu)) = c^S(\mu_0)\exp\left(\int_{a_S(\mu_0)}^{a_S(\mu)} dx \frac{\gamma_m^S}{\beta(x)}\right) \tag{4.49}$$

The values of $\alpha_s(\mu)$ were derived by running from $\alpha_s(\mu = M_Z) = 0.1181$ down to the charm threshold (reducing the number of flavours at each threshold) then to the chosen scale in the 3 flavour theory. We found $\alpha_s(2GeV) = 0.2941$ and $\alpha_s(3Gev) = 0.2442$. An expansion of $c^S(\alpha_s(\mu))$ in terms of α_s can be found in [56], while expressions for the anomalous dimension γ_m to two loops are given in [5].

These results for the renormalisation matrices are used to renormalise the four-quark bag and ratio parameters.

Table 4.6 *The values of Z_S at 2GeV and 3GeV presented in both $\overline{MS}$ and RI-SMOM via both intermediate RI-SMOM schemes. These values are obtained by inverting Z_m as presented in table 4.5 For C1/2 the results presented are in the chiral limit after extrapolation, while C0 the results are calculated for physical light quark masses without extrapolation to the chiral limit.*

	μ (GeV)	$Z_S^{SMOM^{\gamma_\mu}}$	$Z_S^{\overline{\text{MS}}\leftarrow SMOM^{\gamma_\mu}}$	$Z_S^{SMOM^{\not{q}}}$	$Z_S^{\overline{\text{MS}}\leftarrow SMOM^{\not{q}}}$
C1/2	2	0.6043(16)	0.63012(16)	0.6501(21)	0.6592(21)
	3	0.66054(40)	0.68422(43)	0.69889(63)	0.70706(65)
C0	2	0.6019(13)	0.6280(13)	0.6476(16)	0.6568(15)
	3	0.65906(25)	0.68271(27)	0.69779(33)	0.70596(34)

Table 4.7 *The renormalisation constants for the BSM kaon mixing operators for the coarse lattices C1 and C2 in the chiral limit extrapolated to 3GeV. The values for the non-exceptional intermediate schemes $SMOM^{(\gamma_\mu,\gamma_\mu)}$ and $SMOM^{(\not{q},\not{q})}$ are shown, as are the values after conversion to $\overline{MS}$.*

scheme	Z_{ij}/Z_V^2
$\text{SMOM}^{(\gamma_\mu,\gamma_\mu)}$	$\begin{pmatrix} 0.91613(94) & 0 & 0 & 0 & 0 \\ 0 & 1.04956(87) & 0.27804(59) & 0 & 0 \\ 0 & 0.03700(11) & 0.8729(11) & 0 & 0 \\ 0 & 0 & 0 & 0.9182(10) & -0.03675(13) \\ 0 & 0 & 0 & -0.25133(54) & 1.04187(93) \end{pmatrix}$
$\overline{\text{MS}} \leftarrow \text{SMOM}^{(\gamma_\mu,\gamma_\mu)}$	$\begin{pmatrix} 0.91990(95) & 0 & 0 & 0 & 0 \\ 0 & 1.05062(87) & 0.28266(58) & 0 & 0 \\ 0 & 0.05668(12) & 0.9535(11) & 0 & 0 \\ 0 & 0 & 0 & 0.9638(11) & -0.02863(14) \\ 0 & 0 & 0 & -0.33068(57) & 1.1601(10) \end{pmatrix}$
$\text{SMOM}^{(\not{q},\not{q})}$	$\begin{pmatrix} 0.9564(17) & 0 & 0 & 0 & 0 \\ 0 & 1.0503(19) & 0.28302(79) & 0 & 0 \\ 0 & 0.06178(24) & 0.9898(17) & 0 & 0 \\ 0 & 0 & 0 & 1.0248(18) & -0.03958(23) \\ 0 & 0 & 0 & -0.3405(20) & 1.1899(18) \end{pmatrix}$
$\overline{\text{MS}} \leftarrow \text{SMOM}^{(\not{q},\not{q})}$	$\begin{pmatrix} 0.9480(17) & 0 & 0 & 0 & 0 \\ 0 & 1.0515(19) & 0.28824(79) & 0 & 0 \\ 0 & 0.06985(25) & 1.0203(17) & 0 & 0 \\ 0 & 0 & 0 & 0.9838(18) & -0.02491(22) \\ 0 & 0 & 0 & -0.4435(21) & 1.2728(19) \end{pmatrix}$

Table 4.8 *The renormalisation constants for the BSM kaon mixing operators for the coarse lattices C1 and C2 in the chiral limit extrapolated to 2GeV. The values for the non-exceptional intermediate schemes SMOM$^{(\gamma_\mu,\gamma_\mu)}$ and SMOM$^{(\not{q},\not{q})}$ are shown, as are the values after conversion to $\overline{MS}$.*

scheme	Z_{ij}/Z_V^2
SMOM$^{(\gamma_\mu,\gamma_\mu)}$	$\begin{pmatrix} 0.9339(12) & 0 & 0 & 0 & 0 \\ 0 & 1.0546(14) & 0.3403(13) & 0 & 0 \\ 0 & 0.02580(18) & 0.7143(18) & 0 & 0 \\ 0 & 0 & 0 & 0.7798(16) & -0.02147(23) \\ 0 & 0 & 0 & -0.3192(11) & 1.1337(17) \end{pmatrix}$
$\overline{\text{MS}} \leftarrow$ SMOM$^{(\gamma_\mu,\gamma_\mu)}$	$\begin{pmatrix} 0.9387(12) & 0 & 0 & 0 & 0 \\ 0 & 1.0558(12) & 0.3447(12) & 0 & 0 \\ 0 & 0.048372(17) & 0.7959(21) & 0 & 0 \\ 0 & 0 & 0 & 0.8253(18) & -0.00960(24) \\ 0 & 0 & 0 & -0.4143(12) & 1.2875(17) \end{pmatrix}$
SMOM$^{(\not{q},\not{q})}$	$\begin{pmatrix} 0.9899(30) & 0 & 0 & 0 & 0 \\ 0 & 1.0583(34) & 0.3455(16) & 0 & 0 \\ 0 & 0.05565(53) & 0.8424(33) & 0 & 0 \\ 0 & 0 & 0 & 0.9040(29) & -0.02573(55) \\ 0 & 0 & 0 & -0.3705(47) & 1.3124(41) \end{pmatrix}$
$\overline{\text{MS}} \leftarrow$ SMOM$^{(\not{q},\not{q})}$	$\begin{pmatrix} 0.9795(26) & 0 & 0 & 0 & 0 \\ 0 & 1.0596(33) & 0.3505(19) & 0 & 0 \\ 0 & 0.06524(51) & 0.8748(31)) & 0 & 0 \\ 0 & 0 & 0 & 0.860093(26) & -0.00715(56) \\ 0 & 0 & 0 & -0.4836(48) & 1.4202(36) \end{pmatrix}$

Table 4.9 *The renormalisation constants for the BSM kaon mixing operators for the lattice C0 extrapolated to 3GeV. The values for the non-exceptional intermediate schemes SMOM$^{(\gamma_\mu,\gamma_\mu)}$ and SMOM$^{(\not{q},\not{q})}$ are shown, as are the values after conversion to $\overline{MS}$.*

scheme	Z_{ij}/Z_V^2
SMOM$^{(\gamma_\mu,\gamma_\mu)}$	$\begin{pmatrix} 0.91396(28) & 0 & 0 & 0 & 0 \\ 0 & 1.04962(29) & 0.27710(26) & 0 & 0 \\ 0 & 0.038224(80) & 0.88246(40) & 0 & 0 \\ 0 & 0 & 0 & 0.92659(42) & -0.037786(95) \\ 0 & 0 & 0 & -0.25069(25) & 1.03758(31) \end{pmatrix}$
$\overline{\text{MS}} \leftarrow$ SMOM$^{(\gamma_\mu,\gamma_\mu)}$	$\begin{pmatrix} 0.91772(28) & 0 & 0 & 0 & 0 \\ 0 & 1.05069(29) & 0.28178(25) & 0 & 0 \\ 0 & 0.058019(88) & 0.96389(43) & 0 & 0 \\ 0 & 0 & 0 & 0.97266(44) & -0.02977(10) \\ 0 & 0 & 0 & -0.33045(27) & 1.15536(35) \end{pmatrix}$
SMOM$^{(\not{q},\not{q})}$	$\begin{pmatrix} 0.95440(60) & 0 & 0 & 0 & 0 \\ 0 & 1.05012(74) & 0.28188(59) & 0 & 0 \\ 0 & 0.06317(12) & 1.00129(55) & 0 & 0 \\ 0 & 0 & 0 & 1.03319(94) & -0.04037(30) \\ 0 & 0 & 0 & -0.35145(73) & 1.1900(67) \end{pmatrix}$
$\overline{\text{MS}} \leftarrow$ SMOM$^{(\not{q},\not{q})}$	$\begin{pmatrix} 0.94597(60) & 0 & 0 & 0 & 0 \\ 0 & 1.05131(74) & 0.28716(59) & 0 & 0 \\ 0 & 0.071267(12) & 1.03207(56) & 0 & 0 \\ 0 & 0 & 0 & 0.99175(90) & -0.02567(30) \\ 0 & 0 & 0 & -0.45582(76) & 1.27298(71) \end{pmatrix}$

Table 4.10 *The renormalisation constants for the BSM kaon mixing operators for the lattice C0 extrapolated to 2GeV. The values for the non-exceptional intermediate schemes SMOM$^{(\gamma_\mu,\gamma_\mu)}$ and SMOM$^{(\not{q},\not{q})}$ are shown, as are the values after conversion to $\overline{MS}$.*

scheme	Z_{ij}/Z_V^2
SMOM$^{(\gamma_\mu,\gamma_\mu)}$	$\begin{pmatrix} 0.93206(77) & 0 & 0 & 0 & 0 \\ 0 & 1.05364(91) & 0.3361(12) & 0 & 0 \\ 0 & 0.02662(32) & 0.7227(18) & 0 & 0 \\ 0 & 0 & 0 & 0.7856(17) & -0.02180(41) \\ 0 & 0 & 0 & -0.31581(63) & 1.12695(92) \end{pmatrix}$
$\overline{\text{MS}} \leftarrow$ SMOM$^{(\gamma_\mu,\gamma_\mu)}$	$\begin{pmatrix} 0.93669(92) & 0 & 0 & 0 & 0 \\ 0 & 1.0549(12) & 0.3408(13) & 0 & 0 \\ 0 & 0.04031(34) & 0.8051(21) & 0 & 0 \\ 0 & 0 & 0 & 0.82314(19) & -0.01009(46) \\ 0 & 0 & 0 & -0.41110(69) & 1.2797(11) \end{pmatrix}$
SMOM$^{(\not{q},\not{q})}$	$\begin{pmatrix} 0.9876(14) & 0 & 0 & 0 & 0 \\ 0 & 1.0576(18) & 0.3407(19) & 0 & 0 \\ 0 & 0.05605(45) & 0.8525(24) & 0 & 0 \\ 0 & 0 & 0 & 0.9144(28) & -0.0287(19) \\ 0 & 0 & 0 & -0.3689(29) & 1.3048(19) \end{pmatrix}$
$\overline{\text{MS}} \leftarrow$ SMOM$^{(\not{q},\not{q})}$	$\begin{pmatrix} 0.9770(14) & 0 & 0 & 0 & 0 \\ 0 & 1.0590(18) & 0.3463(19) & 0 & 0 \\ 0 & 0.06561(46) & 0.8848(25) & 0 & 0 \\ 0 & 0 & 0 & 0.8694(27) & -0.0100(18) \\ 0 & 0 & 0 & -0.4848(31) & 1.4120(19) \end{pmatrix}$

4.3 Results on a Medium Physical Point Lattice

The renormalisation was also calculated for ensemble M0, summarised in table 3.1. The vertex functions for eight momenta (spanning from 1.96GeV to 3.27GeV) were calculated on 5 configurations. Given we have already explored the scale dependence in the infrared region with the coarse lattices, for this ensemble we will only present the final extrapolated results at 2GeV and 3GeV that will be used for the renormalisation of the quantities measured in the previous chapter.

Table 4.11 *The range of momenta chosen for M0.*

	ap_1	ap_2	Minimum	Increment	Maximum
M0	$(0, x, x, 0)$	$(x, x, 0, 0)$	$x = \frac{2\pi}{L}(6)$	$\Delta x = \frac{2\pi}{L}$	$x = \frac{2\pi}{L}(10)$

Table 4.12 *The values of Z_S at 2GeV and 3GeV presented in both $\overline{MS}$ and RI-SMOM via both intermediate RI-SMOM schemes for M0. These values are obtained by inverting Z_m.*

	μ (GeV)	$Z_S^{SMOM^{\gamma_\mu}}$	$Z_S^{\overline{\text{MS}}\leftarrow SMOM^{\gamma_\mu}}$	$Z_S^{SMOM^{\not{q}}}$	$Z_S^{\overline{\text{MS}}\leftarrow SMOM^{\not{q}}}$
M0	2	0.59162(45)	0.63119(49)	0.63528(39)	0.64867(40)
	3	0.659671(51)	0.694363(53)	0.695219(67)	0.706787(69)

Table 4.13 *The renormalisation constants for the BSM kaon mixing operators for the lattice M0 extrapolated to 3GeV. The values for the non-exceptional intermediate schemes $SMOM^{(\gamma_\mu,\gamma_\mu)}$ and $SMOM^{(\not{q},\not{q})}$ are shown, as are the values after conversion to $\overline{MS}$.*

scheme	Z_{ij}/Z_V^2
$\text{SMOM}^{(\gamma_\mu,\gamma_\mu)}$	$\begin{pmatrix} 0.94115(13) & 0 & 0 & 0 & 0 \\ 0 & 1.04602(11) & 0.27161(12) & 0 & 0 \\ 0 & 0.025356(76) & 0.80340(20) & 0 & 0 \\ 0 & 0 & 0 & 0.85468(15) & -0.022735(56) \\ 0 & 0 & 0 & -0.24819(14) & 1.08547(14) \end{pmatrix}$
$\overline{\text{MS}} \leftarrow \text{SMOM}^{(\gamma_\mu,\gamma_\mu)}$	$\begin{pmatrix} 0.94504(14) & 0 & 0 & 0 & 0 \\ 0 & 1.04703(11) & 0.27590(12) & 0 & 0 \\ 0 & 0.044067(84) & 0.87822(20) & 0 & 0 \\ 0 & 0 & 0 & 0.86941(15) & -0.012679(56) \\ 0 & 0 & 0 & -0.32404(15) & 1.20838(16) \end{pmatrix}$
$\text{SMOM}^{(\not{q},\not{q})}$	$\begin{pmatrix} 0.97817(33) & 0 & 0 & 0 & 0 \\ 0 & 1.04742(35) & 0.27551(18) & 0 & 0 \\ 0 & 0.04738(15) & 0.90464(35) & 0 & 0 \\ 0 & 0 & 0 & 0.95163(55) & -0.02632(20) \\ 0 & 0 & 0 & -0.27712(80) & 1.20625(41) \end{pmatrix}$
$\overline{\text{MS}} \leftarrow \text{SMOM}^{(\not{q},\not{q})}$	$\begin{pmatrix} 0.96948(32) & 0 & 0 & 0 & 0 \\ 0 & 1.04854(36) & 0.28032(19) & 0 & 0 \\ 0 & 0.05504(15) & 0.93272(39) & 0 & 0 \\ 0 & 0 & 0 & 0.91378(57) & -0.01188(20) \\ 0 & 0 & 0 & -0.37060(85) & 1.28967(42) \end{pmatrix}$

Table 4.14 *The renormalisation constants for the BSM kaon mixing operators for the lattice M0 extrapolated to 2GeV. The values for the non-exceptional intermediate schemes SMOM$^{(\gamma_\mu,\gamma_\mu)}$ and SMOM$^{(\not{q},\not{q})}$ are shown, as are the values after conversion to $\overline{MS}$.*

scheme	Z_{ij}/Z_V^2
SMOM$^{(\gamma_\mu,\gamma_\mu)}$	$\begin{pmatrix} 0.96038(44) & 0 & 0 & 0 & 0 \\ 0 & 1.06008(34) & 0.36189(15) & 0 & 0 \\ 0 & 0.01870(39) & 0.64064(70) & 0 & 0 \\ 0 & 0 & 0 & 0.72056(66) & -0.01255(12) \\ 0 & 0 & 0 & -0.34608(16) & 1.19925(56) \end{pmatrix}$
$\overline{\text{MS}} \leftarrow$ SMOM$^{(\gamma_\mu,\gamma_\mu)}$	$\begin{pmatrix} 0.96518(46) & 0 & 0 & 0 & 0 \\ 0 & 1.06128(34) & 0.36617(15) & 0 & 0 \\ 0 & 0.04084(42) & 0.71538(73) & 0 & 0 \\ 0 & 0 & 0 & 0.73393(65) & 0.00116(13) \\ 0 & 0 & 0 & -0.44172(19) & 1.36222(63) \end{pmatrix}$
SMOM$^{(\not{q},\not{q})}$	$\begin{pmatrix} 1.01486(62) & 0 & 0 & 0 & 0 \\ 0 & 1.06393(96) & 0.36570(47) & 0 & 0 \\ 0 & 0.04693(49) & 0.7538(11) & 0 & 0 \\ 0 & 0 & 0 & 0.8358(17) & -0.01719(98) \\ 0 & 0 & 0 & -0.38581(83) & 1.37528(86) \end{pmatrix}$
$\overline{\text{MS}} \leftarrow$ SMOM$^{(\not{q},\not{q})}$	$\begin{pmatrix} 1.00398(64) & 0 & 0 & 0 & 0 \\ 0 & 1.0653(10) & 0.37068(46) & 0 & 0 \\ 0 & 0.05628(50) & 0.7830(11) & 0 & 0 \\ 0 & 0 & 0 & 0.7937(16) & 0.00211(90) \\ 0 & 0 & 0 & -0.49644(92) & 1.48879(94) \end{pmatrix}$

4.4 Renormalisation of the Bag and Ratio Parameters

The BSM ratio and bag parameters, as measured in chapter 3, must be renormalised as,

$$R_i(\mu)^{\text{ren}} = \frac{Z_{ij}}{Z_{11}} R_j(\mu, a), \tag{4.50}$$

and,

$$B_i(\mu)^{\text{ren}} = \frac{Z_{ij}}{Z_P^2} B_i(\mu, a), \tag{4.51}$$

while the SM bag parameter is renormalised as,

$$B_i(\mu)^{\text{ren}} = \frac{Z_{ij}}{Z_V^2} B_i(\mu, a). \tag{4.52}$$

For the ensembles, C1, C2 and M1, M2, M3, the renormalisation constants have been calculated, as presented in [40]. While in [31] it was proposed that the renormalisation constants of C0(M0) and C1(M1) would differ by such a small amount that the renormalisation factors could be reused, given the precision of the data in this latest calculation, it was prudent to calculate the renormalisation for C0 and M0, as has been done in this section. It should be noted, that the values of the conversion factor for Z_S differ slightly between this work and [40], likely due to the value of α_s. Therefore for the renormalisation of the bag parameters, we chose to use the values of conversion factor presented in [40], and not those presented in table 4.4. This choice was made as the renormalisation was not calculated for M1, M2 and M3, and F1, in this work, and hence the conversions for those were not available except in [40].

Chapter 5

Continuum Results of Beyond the Standard Model Kaon Mixing

The kaon bag parameter has been the subject of many lattice calculations [7, 15, 16, 26, 31, 55, 57]. It is now known to a very high precision, and is reviewed by the FLAG [6] collaboration with consistent results from multiple collaborations. It is a significant lattice input into searches for new physics, which dictates the width of the ϵ_K band in the unitary triangle. Provided the value from FLAG is used, it is now precise enough that is is not the dominant error on ϵ_K. Instead the uncertainty on the measurement of V_{cb} dominates. For the standard model operator the field is now at the point where isospin and electromagnetic effects are as large as the total error quoted in the isospin symmetric pure QCD theory. For greater precision to be meaningful, we would also need to move beyond the OPE to include the long-distance, bi-local V-A currents where there are two weak Hamilton insertions connected by quark loops. Initial progress in this direction has been made in [18, 58, 59].

BSM kaon mixing amplitudes are not yet known to the same precision. Early studies of BSM kaon mixing [3, 14, 63] were performed in the quenched approximation. This was followed by dynamical simulations wih N_f number of quark flavours by: RBC-UKQCD in $(N_f = 2 + 1)$ [33, 71], SWME $(N_f = 2 + 1)$ [15, 57, 86] and ETM $(N_f = 2)$ [26] and $N_f = 2 + 1 + 1$ [55] flavour QCD. In contrast to the standard model operator, there exist some tensions between different collaborations' results of some of the BSM operators, as

shown in table 5.14 and summarised in the FLAG report [6] [1]. In references [40, 71], it was proposed that the source of these tensions was the choice of the intermediate renormalisation scheme. Specifically, it was proposed that the symmetric momentum subtraction scheme RI-SMOM (which has non-exceptional kinematics) advocated by RBC-UKQCD has several beneficial features compared to the previously used RI-MOM (which has exceptional kinematics). This is likely due to the exceptional, infrared non-perturbative "pion pole" behaviour in the RI-MOM vertex functions which must be correctly modelled and subtracted if exceptional RI-MOM kinematics are used. This behaviour is absent in the RI-SMOM scheme giving greater theoretical control. When RI-SMOM was chosen the results of [71] agreed with the SWME [15, 57, 86] perturbatively renormalised results, while the calculation with RI-MOM agreed with previous RBC-UKQCD [33] and ETM [26, 55] results which also used RI-MOM.

This manuscript improves upon our most recent RBC-UKQCD BSM kaon mixing calculation [40, 71] by including data points at the physical light quark mass and with physical valence strange quark masses. We present results in the isospin symmetric limit of pure $N_f = 2 + 1$ QCD with improved precision upon previous results.

5.1 Extrapolation to the Physical Point

Chapter 3 presented lattice results for bag parameters and ratios of kaon mixing four-quark operators for several ensembles, and these were renormalised as described in chapter 4. At this stage it is necessary to perform an extrapolation to the physical point. I perform a simultaneous chiral-continuum global fitting procedure to recover the physical point continuum results. Given the use of domain-wall fermions the dominant lattice artifacts are expected to be linear in a^2 with a and a^3 corrections disallowed by chiral symmetry. It should be noted that while the continuum extrapolation is necessary for all ensembles' results, that ensembles C0 and M0 have physical values for the light quark mass and therefore do not require chiral extrapolation. However the other results (which help guide the continuum extrapolation) do require chiral extrapolation, thus a combined chiral continuum fit strategy is chosen. RBC-UKQCD's most recent calculation of the standard model bag parameter [31] included several of the same

[1] The most recent version published online at http://flag.unibe.ch (accessed 06/19) contains a more complete review of BSM kaon mixing.

gauge ensembles as this analysis, including the two physical point ensembles. In that work an over-weighting strategy was employed to force the fit through the physical point data, while the role of the non-physical point data was merely to guide the continuum extrapolation. In this work I did not find it necessary to employ an over-weighting strategy. The physical point data points were typically more precise than the other points, and therefore the fit tended to favour the physical point results anyway. While this work's emphasis is on the beyond the standard model kaon mixing results, in section 5.3.2 the results for the standard model bag parameter are presented and discussed. Given the different strategies employed, it is useful to compare the results here to those in [31] as a cross check.

One other effect we also consider in one of our fit forms is the partial quenching in the strange mass. In the original generation of the ensembles C1/2 and M1/2/3 unphysical values of the strange quark mass were used, while there was a slight mistuning of the strange quark mass for C0, M0 and F1 leading to slightly unphysical values of the strange quark mass. For all ensembles the calculations were rerun with only one physical value of the strange quark mass, however this means the strange quark is partially quenched while the sea quark strange mass is unphysical. This deviation from the physical mass in the sea strange mass ranges from 0.5% (consistent within error) for F1 to 25% for C1/2.

5.1.1 Fit Forms

A number of different fit forms are considered:

1. An analytic fit form derived from a Taylor expansion. This fit function is linear in the lattice spacing squared and the square of the simulated pion mass over decay constant:

$$Y\left(a^2, \frac{m_{ll}^2}{f_{ll}^2}\right) = Y\left(0, \frac{m_\pi^2}{f_\pi^2}\right)\left[1 + \alpha_i a^2 + \beta_i \frac{m_{ll}^2}{f_{ll}^2}\right]. \tag{5.1}$$

2. A fit according to SU(2) chiral perturbation theory:

$$Y\left(a^2, \frac{m_{ll}^2}{f_{ll}^2}\right) = Y\left(0, \frac{m_\pi^2}{f_\pi^2}\right)\left[1 + \alpha_i a^2 + \frac{m_{ll}^2}{f_{ll}^2}\left(\beta_i + \frac{C_i}{(4\pi)^2}\log\left(\frac{m_{ll}^2}{\Lambda^2}\right)\right)\right]. \tag{5.2}$$

   This has the same form as the fit above except for the chiral logarithm term.

3. A linear fit which includes a term to account for the unphysical values of the sea-quark strange mass.

$$Y\left(a^2, \frac{m_{ll}^2}{f_{ll}^2}, \delta_{m_s^{sea}}\right) = Y\left(0, \frac{m_\pi^2}{f_\pi^2}, 0\right)\left[1 + \alpha_i a^2 + \beta_i \frac{m_{ll}^2}{f_{ll}^2} + \gamma_i \delta m_s^{sea}\right], \quad (5.3)$$

where $\delta m_s^{sea} = \frac{m_s^{sea} - m_s^{phys}}{m_s^{phys}}$. The strange mass in all ensembles is partially quenched with the values of the valence strange quark masses at the physical values. Hence the term $\delta_{m_s^{sea}}$ can also be considered a term measuring the partial quenching of the strange quarks.

For the BSM matrix elements the analytic fit form is chosen for the central values, as will be justified in later discussion. For the standard model matrix elements, it was found necessary to use analytic fit form including the sea strange mass deviation term, as will be explained in greater detail in the section 5.3.2. For the other matrix fits it was excluded to avoid overfitting.

5.1.2 Correlations in the Data

As stated in chapter 3 the lattice spacings were determined in [31] from some of the same ensembles included in this work, hence a correlation between the data exists, although all data points are from different ensembles and so it is only through the lattice spacing that correlations are introduced. We perform an uncorrelated fit to decouple this work from the previous work. We propagate the error on the lattice spacing by generating bootstraps following a Gaussian distribution with width equal to the error on the lattice spacing. Given that the error on the lattice spacings are of order 0.5% and the size of the correction contributed by the taking the lattice spacing to the continuum is at most of order 15%, we believe that neglecting these correlations has only a small effect. When fitting the data we calculate χ^2 from the deviation of the data from the model in the y-axis only. The value of χ^2 when including the deviation in all axes is close to the value from our approach provided the gradient multiplied by the error in the x-axis of the datapoint is small compared to the error in the y-axis. The gradients of the slopes we determine in our fit are small, and so the change in χ^2 we would observe if we were to include all axes is negligible. We consider both linear and chiral fits, and in fact directly compare them, and so given there is no straightforward way to include x-axis errors for non-linear fits, we also choose to

exclude them from the linear fit too to ensure consistency. Further discussion on this is given in appendix C.

5.2 Fit Results

5.2.1 Beyond the Standard Model Operators

I first discuss the results for the beyond the standard model ratio and bag parameters. The standard model bag parameter is treated separately in subsection 5.3.2.

The results of the global fit for the analytic and resulting chiral-continuum extrapolation are presented here for the ratio and bag BSM parameters renormalised via the SMOM$^{(\gamma_\mu\gamma_\mu)}$ intermediate scheme at both 2GeV and 3GeV.

For our central value we choose the the fit form given in equation 5.1 renormalised at 2GeV via the SMOM$^{(\gamma_\mu\gamma_\mu)}$ intermediate scheme, excluding the datapoint on F1. The plots for this fit are presented in figures 5.1 and 5.2. When presenting these we show the dependence on a^2 or the mass separately. To do so we use the fit results to extrapolate to the physical point in the variable not being shown so that only the dependence on one is shown. We do not take the errors on the fit results into account when extrapolating here, but only use the central value as I believe that this more clearly represents the quality of fit. The fit results are presented in table 5.1 alongside the results for the data renormalised at 3GeV.

		Y_{phys}	χ^2/d.o.f.	p_0	p_1	p_2
SMOM$^{(\gamma_\mu\gamma_\mu)}$(2GeV)	R_2	-15.39(22)	0.44	-15.74(22)	48.6(25)	0.22(69)
	R_3	4.728(75)	0.42	4.846(77)	-16.17(96)	0.92(25)
	R_4	29.74(41)	0.03	30.70(41)	-131.3(43)	-7.9(13)
	R_5	8.09(11)	0.16	8.31(13)	-30.1(12)	-3.72(36)
	B_2	0.5564(39)	1.42	0.5491(37)	0.995(97)	0.221(18)
	B_3	0.8460(82)	0.71	0.8349(80)	1.52(20)	0.555(37)
	B_4	0.9092(63)	0.79	0.9104(60)	-0.17(15)	0.041(29)
	B_5	0.7491(52)	1.35	0.7470(49)	0.28(12)	-0.147(25)
SMOM$^{(\not{q},\not{q})}$(2GeV)	R_2	-16.80(24)	0.42	-17.20(25)	54.7(27)	-0.04(79)
	R_3	4.944(94)	0.21	5.081(94)	-18.8(13)	1.85(34)
	R_4	32.36(47)	0.02	33.41(47)	-143.47(50)	-8.4(15)
	R_5	7.64(11)	0.20	7.85(11)	-28.7(13)	-3.60(36)
	B_2	0.5546(53)	1.93	0.5478(49)	0.932(98)	0.232(24)
	B_3	0.804(13)	0.7	0.794(12)	1.30(26)	0.724(58)
	B_4	0.9056(69)	0.7	0.9068(64)	-0.17(15)	0.051(32)
	B_5	0.6469(60)	1.6	0.6454(57)	0.20(12)	-0.131(29)
SMOM$^{(\gamma_\mu\gamma_\mu)}$(3GeV)	R_2	-18.69(25)	0.48	-19.12(26)	58.6(28)	1.18(79)
	R_3	5.591(85)	0.50	5.735(88)	-19.80(98)	2.07(27)
	R_4	39.04(51)	0.13	40.25(52)	-165.7(51)	-16.3(16)
	R_5	10.93(13)	0.72	11.20(14)	-37.6(14)	-8.49(41)
	B_2	0.5128(16)	1.0	0.5054(16)	1.019(55)	0.2906(62)
	B_3	0.7479(42)	1.1	0.7358(43)	1.65(11)	0.898(16)
	B_4	0.9137(20)	0.24	0.9145(21)	-0.110(79)	0.0565(81)
	B_5	0.7846(21)	1.1	0.7827(20)	0.266(55)	-0.3343(83)
SMOM$^{(\not{q},\not{q})}$(3GeV)	R_2	-20.03(27)	0.49	-20.49(27)	62.9(29)	1.41(84)
	R_3	5.459(95)	0.61	5.622(97)	-22.4(11)	5.34(30)
	R_4	41.58(54)	0.12	42.87(55)	-177.6(54)	-16.7(17)
	R_5	10.50(13)	0.79	10.76(13)	-35.9(13)	-8.48(41)
	B_2	0.5177(19)	1.2	0.5103(18)	1.015(50)	0.2688(76)
	B_3	0.6637(61)	1.2	0.6515(61)	1.68(13)	1.387(23)
	B_4	0.9146(23)	0.26	0.9155(23)	-0.117(74)	0.0499(94)
	B_5	0.7102(23)	1.3	0.7085(22)	0.230(54)	-0.349(10)

Table 5.1 *The fit results including the extrapolated value, $\chi^2/d.o.f$ and the parameters are presented for the central value fit (SMOM$^{(\gamma_\mu\gamma_\mu)}$(2GeV)) and for the fit with same fit form and data points but with the renormalisation $\overline{MS} \leftarrow$ SMOM$^{(\gamma_\mu\gamma_\mu)}$(3GeV), $\overline{MS} \leftarrow$ SMOM$^{(\not{q}\not{q})}$(2GeV) and $\overline{MS} \leftarrow$ SMOM$^{(\not{q}\not{q})}$(3GeV). Note the the values of p_0, p_1 and p_2 do not directly translate to the parameters given in equation 5.1 but are a linear combination of them. The actual fit form used was $p_0 + p_1 \frac{m_{ll}^2}{16\pi^2 f_{ll}^2} + p_2 a^2$. The values of $\chi^2/d.o.f.$ are typically good, being of order or less than 1. The very small values for $\chi^2/d.o.f.$ for R_4 and R_5 in the central value fit may give some cause for concern. Typically very low values of χ^2 can possibly indicate either over-fitting or overly conservative errors. However given the low number of parameters over-fitting is not a concern in this case. The errors on the data points are derived from the bootstrap fits described previously and there is no reason to think that they are overly conservative.*

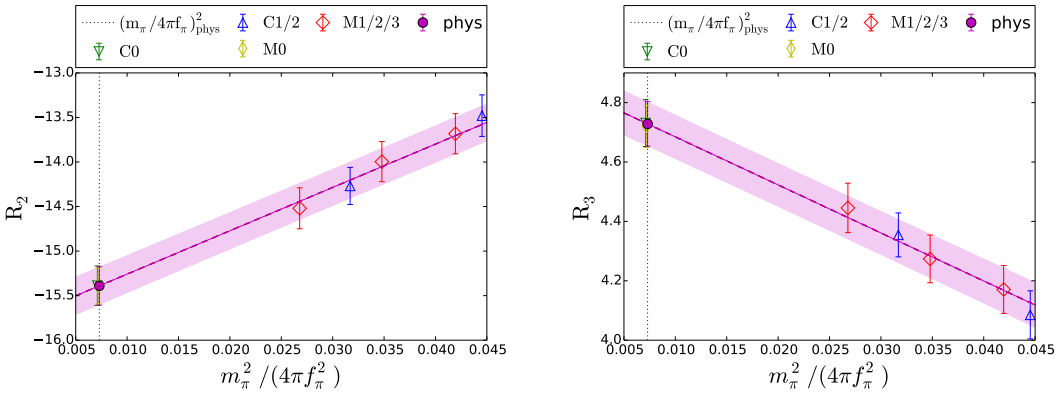

(a) R_2 **(b)** R_3

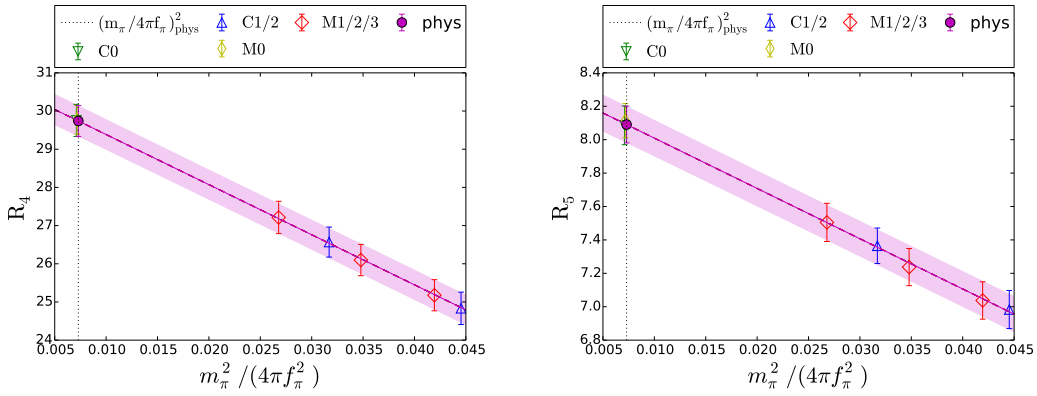

(c) R_4 **(d)** R_5

Figure 5.1 *Central value chiral extrapolation of the ratio parameters renormalised at 2GeV in the SMOM$^{(\gamma_\mu,\gamma_\mu)}$ scheme according to the linear fit form described in equation 5.1. All medium and coarse data points are included here, but have been corrected to the continuum for plotting.*

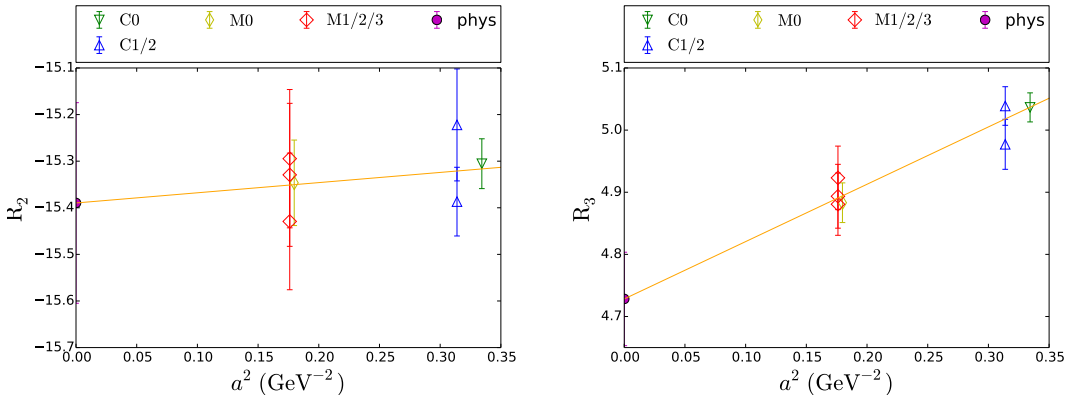

(a) R_2

(b) R_3

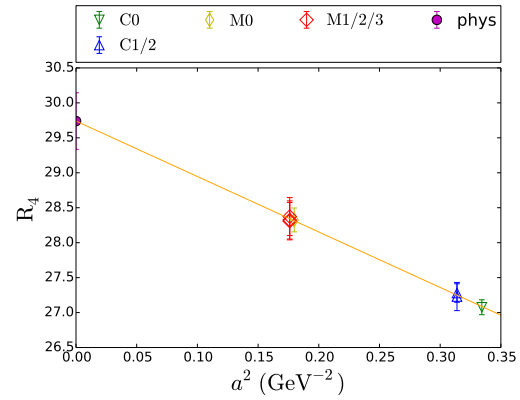

(c) R_4

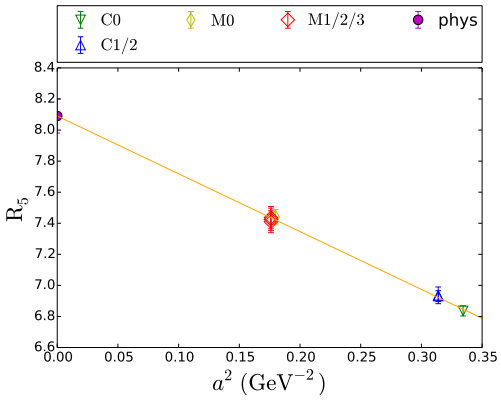

(d) R_5

Figure 5.2 *Central value continuum extrapolation of the ratio parameters renormalised at 2GeV in the SMOM$^{(\gamma_\mu,\gamma_\mu)}$ scheme according to the linear fit form described in equation 5.1. All medium and coarse data points are included here, but have been corrected to the physical pion mass for plotting.*

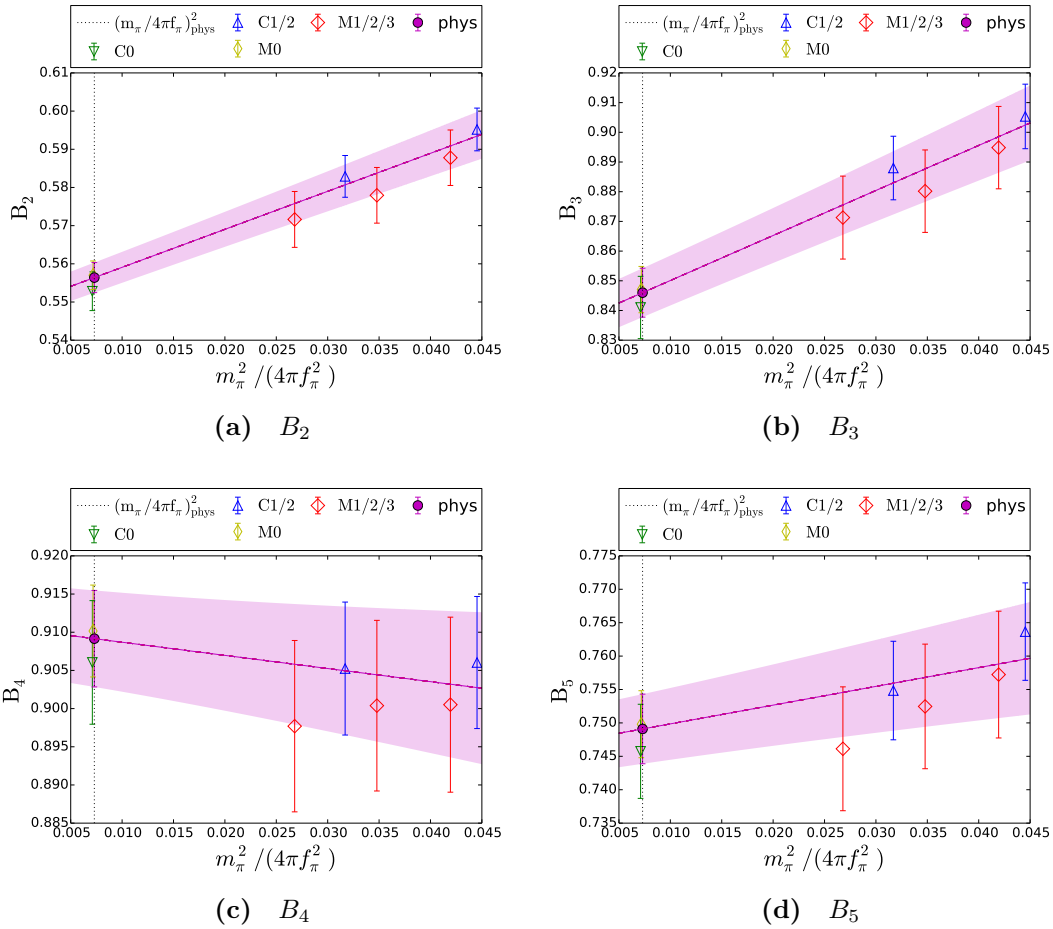

(a) B_2 **(b)** B_3

(c) B_4 **(d)** B_5

Figure 5.3 *Central value chiral extrapolation of the BSM bag parameters renormalised at 2GeV in the SMOM$^{(\gamma_\mu,\gamma_\mu)}$ scheme according to the linear fit form described in equation 5.1. All medium and coarse data points are included here, but have been corrected to the continuum for plotting.*

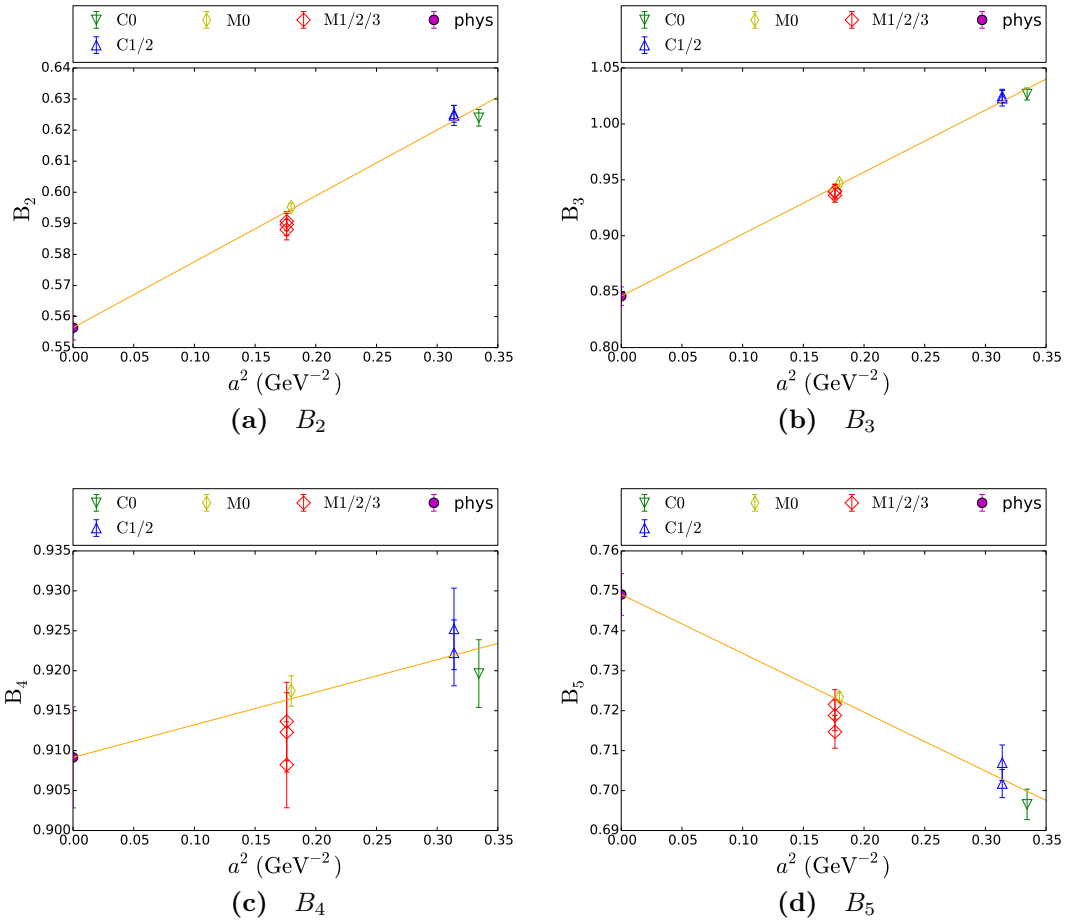

(a) B_2 **(b)** B_3

(c) B_4 **(d)** B_5

Figure 5.4 *Central value continuum extrapolation of the BSM bag parameters renormalised at 2GeV in the SMOM$^{(\gamma_\mu,\gamma_\mu)}$ scheme according to the linear fit form described in equation 5.1. All medium and coarse data points are included here, but have been corrected to the physical pion mass for plotting.*

5.3 Discussion of Systematic Errors

In this section we discuss all potential sources of systematic errors and assumptions made in the fitting strategy. For all our lattices with non-physical pions, $m_P L > 4$. This is the empirically derived limit at which it has been established that finite volume effects can be ignored. Even for our physical point lattices $m_P L \approx 3.8$. Previous studies [31] of lattice quantities which included the same physical point ensembles found the finite volume effects to be sub-statistical. Thus finite volume effects are assumed to be negligible here. We also neglect isospin corrections, believing them to be sub-dominant compared to our final systematic error on the isospin symmetric result. The effects that will be considered in more detail are: the systematics introduced by including far from the chiral limit; the discretisation effects arising both from the bare lattice calculations and the renormalisation procedure; the effect of partially quenching the strange quark mass; and the errors arising from the truncation of the perturbative matching.

Before discussing the calculation of the systematic error, let us first consider the effect of partially quenching the strange quark mass. While the values of the valence strange quark masses in all our simulations are physical, the same does not hold for the sea-quark mass, as there is partial quenching. The fit form 5.2 is based on SU(2) chiral perturbation with unitary masses. It is important to consider whether there is a dependence on the sea strange quark mass, so we also consider fit form 5.3. A similar strategy was considered in [31], in which the global fit form for B_k included a term, linear in δ_{m_s}, the difference between the simulated and physical sea strange quark mass. It is important to note that the fit strategy here differed from the one in this thesis in other ways as will be elaborated on in subsection 5.3.2. Presented in table 5.2 are the values of the parameters γ_i controlling the dependence on the strange quark mass. Given their consistency with zero (which is not unexpected given it is an $\mathcal{O}(\alpha_s^2 \delta_{m_s}) \approx 0.008\alpha_s^2$ effect) and the limited degrees of freedom in the fit we choose to not include the sea-strange mass in the fit for our central values. We are satisfied by this check that the effect of the strange quark partial quenching can be neglected and so we do not take it into account when calculating the systematic error.

scheme	parameter	γ_2	γ_3	γ_4	γ_5
SMOM$^{(\gamma_\mu\gamma_\mu)}(2GeV)$	R	-1.3(11)	0.38(42)	0.63(21)	0.18(47)
	B	0.025(19)	0.054(41)	-0.011(32)	-0.031(23)
SMOM$^{(\gamma_\mu\gamma_\mu)}(3GeV)$	R	-1.6(13)	0.45(47)	1.2(25)	0.43(55)
	B	0.023(15)	0.059(31)	-0.021(25)	-0.035(15)

Table 5.2 *The values of the the parameter γ_i which controls the dependence of the extrapolation on the sea strange quark mass are shown. All values are within 2σ of zero, and so there is no evidence that the extrapolation to the physical mass has any non-negligible dependence on the sea strange quark mass.*

Light Mass Interpolation Effects

As stated we consider both an analytic fit form based on the first order Taylor expansion in the pion mass and a fit according to SU(2) chiral perturbation theory. These fits are identical save for a chiral logarithm term. While we expect chiral perturbation theory to better describe the behaviour of systems moving away from the chiral limit, there is a limited range of applicability. Therefore it is important to also consider an analytic fit. In practice, it was found that the analytic fits better described the data. In the analysis there are two data points at the physical pion mass, which require no chiral extrapolation. In order to guide the continuum extrapolation there is further data included with larger pion masses, ranging from 300 to 430 MeV, therefore necessitating the chiral extrapolation. But given that we expect the more precise physical point data to dominate the fit, we expect that the difference between the two choices in the pion mass extrapolation to be small. In practice we find that the analytic fit better describes the data for the ratio parameters, with values of χ^2/d.o.f consistently below 1 for the analytic fit form but rising as high as order 3 when we include a chiral logarithm term. For the bag parameter we see that both the analytic and chiral fits describe the data well with the values of χ^2/d.o.f typically of order 1.

Therefore when taking the central value we choose the analytic fit form, believing it to be more reliable. We can estimate the error arising from the chiral extrapolation from the difference between the results for each fit form, and we define it as,

$$\delta_i^{\text{Chiral.}}(\mu) = \frac{|R_i^{\text{linear}} - R_i^{\chi\text{PT}}|}{\frac{1}{2}(R_i^{\text{linear}} + R_i^{\chi\text{PT}})}. \tag{5.4}$$

For the ratio and bag parameters the chiral systematic is very small, of order 0.5% for the ratio parameters and of order 0.1% for the bag parameters. This

		Y_{phys}	χ^2/d.o.f.	p_0	p_1	p_2
SMOM$^{(\gamma_\mu\gamma_\mu)}$(2GeV)	R_2	-15.42(21)	2.0	-16.13(22)	-21.2(23)	0.29(69)
	R_3	4.739(75)	1.6	4.969(79)	5.21(92)	0.89(25)
	R_4	29.84(40)	2.8	31.99(43)	98.9(44)	-8.2(13)
	R_5	8.12(11)	2.8	8.66(12)	32.1(12)	-3.76(35)
	B_2	0.5563(39)	1.7	0.5449(37)	0.219(96)	0.213(18)
	B_3	0.8456(82)	0.8	0.8283(79)	0.33(20)	0.556(37)
	B_4	0.9095(63)	0.5	0.9177(60)	1.14(15)	0.040(29)
	B_5	0.7493(52)	0.9	0.7529(49)	1.35(12)	-0.148(25)

Table 5.3 *The fit results including the extrapolated value, $\chi^2/d.o.f$ and the parameters are presented for the fit of data renormalised with scheme (SMOM$^{(\gamma_\mu\gamma_\mu)}$(2GeV)) for the chiral fit form. Note that the $\chi^2/d.o.f$ are larger for the ratio parameters, while they are approximately the same for the bag parameters as in the analytic fit. This motivates the choice of the the analytic fit for the central values.*

shows that, as we expected, the chiral extrapolation of a dataset including data at the physical point is benign.

Figures 5.5 shows the chiral extrapolation for the chiral fit form.

Discretisation Errors

The good chiral symmetry of domain wall fermions constrains $\mathcal{O}(a)$ and $\mathcal{O}(a^3)$ terms to be small. We include the $\mathcal{O}(a^2)$ effects in our global fit. Power counting suggests that $\mathcal{O}(a^4)$ effects for hadronic physics scales with a 1.73 GeV coarsest inverse lattice spacing will remain small on all data points. By excluding the third lattice spacing from our global fit the ability to remove the discretisation effects in the data is reduced. Given the partial quenching on the fine lattice it is prudent to exclude this data point when taking the central value. We cannot completely guarantee that fit forms derived by considering chiral perturbation theory apply to a simulation with different residual masses and different chiral symmetry breaking effects, in the sea and valence sector. We can however still gain some information about the discretisation effects by examining a chiral continuum fit including this third lattice spacing. The sea sector pion mass is approximately 266MeV (assuming leading order χ^{PT}) compared to 234MeV in the valence sector, a difference of order O(10%). The lattice spacing was originally derived assuming a unitary m_{res} and so the true value will differ somewhat. But given that we see a change of lattice spacing of 1%(3%) between C1/2(M1/2/3) and C0(M0) we expect this effect to be fairly benign. The effect of the action

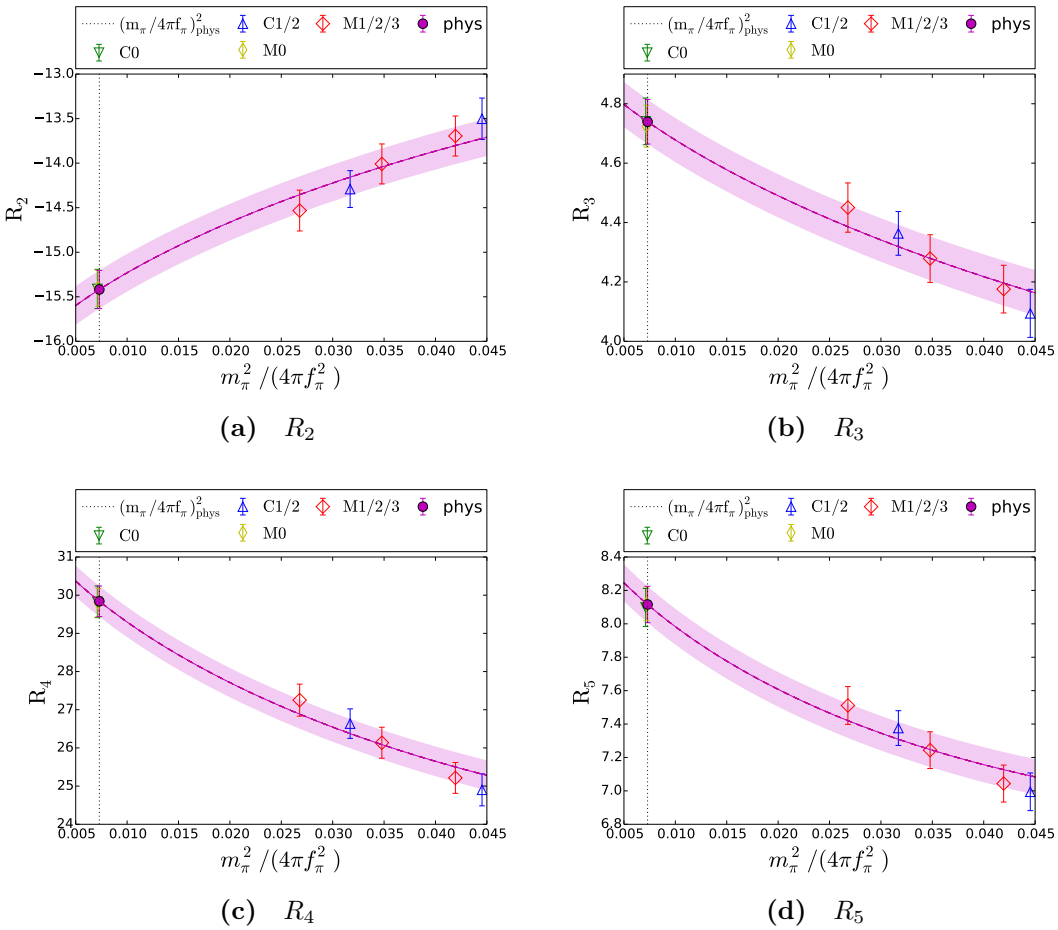

(a) R_2 **(b)** R_3

(c) R_4 **(d)** R_5

Figure 5.5 *Chiral extrapolation of the ratio parameters renormalised at 2GeV in the SMOM$^{(\gamma_\mu,\gamma_\mu)}$ scheme according to the chiral fit form described in equation 5.2. All medium and coarse data points are included here, but have been corrected to the continuum for plotting.*

and L_s on the lattice spacing is explored in more detail in [31].

The fits including the fine ensemble are shown in figures 5.6 and 5.7, while the equivalent BSM bag parameter fits are shown in figures 5.8 and 5.9. The fit results are given in table 5.4.

One can see that the quality of fit is reduced upon including the fine data point. It is not known whether this effect would still exist if there were no partial quenching, it is possible that they are independent, but we cannot be sure. Nonetheless, these fits do not enter the central value. We do however, still feel confident in using these results to estimate a discretisation error on the results that would otherwise be hard to quantify with results only two lattice spacings.

		Y_{phys}	χ^2/d.o.f.	p_0	p_1	p_2
SMOM$^{(\gamma_\mu\gamma_\mu)}$(2GeV)	R_2	-15.17(13)	1.3	-15.51(14)	47.4(25)	-0.46(45)
	R_3	4.668(51)	0.9	4.784(53)	-15.85(97)	1.11(18)
	R_4	29.09(24)	2.30	30.02(24)	-127.5(44)	-5.97(83)
	R_5	7.940(65)	1.8	8.154(67)	-29.2(12)	-3.27(23)
	B_2	0.5480(26)	3.8	0.5413(26)	0.916(88)	0.247(13)
	B_3	0.8378(63)	1.4	0.8271(64)	1.46(19)	0.587(30)
	B_4	0.8877(42)	7.6	0.8903(42)	-0.36(14)	0.129(21)
	B_5	0.7336(36)	7.6	0.7329(35)	0.10(11)	-0.079(18)

Table 5.4 *The fit results including the extrapolated value, χ^2/d.o.f and the parameters are presented for the fit of data renormalised with scheme (SMOM$^{(\gamma_\mu\gamma_\mu)}$(2GeV)) for the fit including F1. The χ^2/d.o.f are acceptable for the ratio parameters, but for the bag parameters are typically large.*

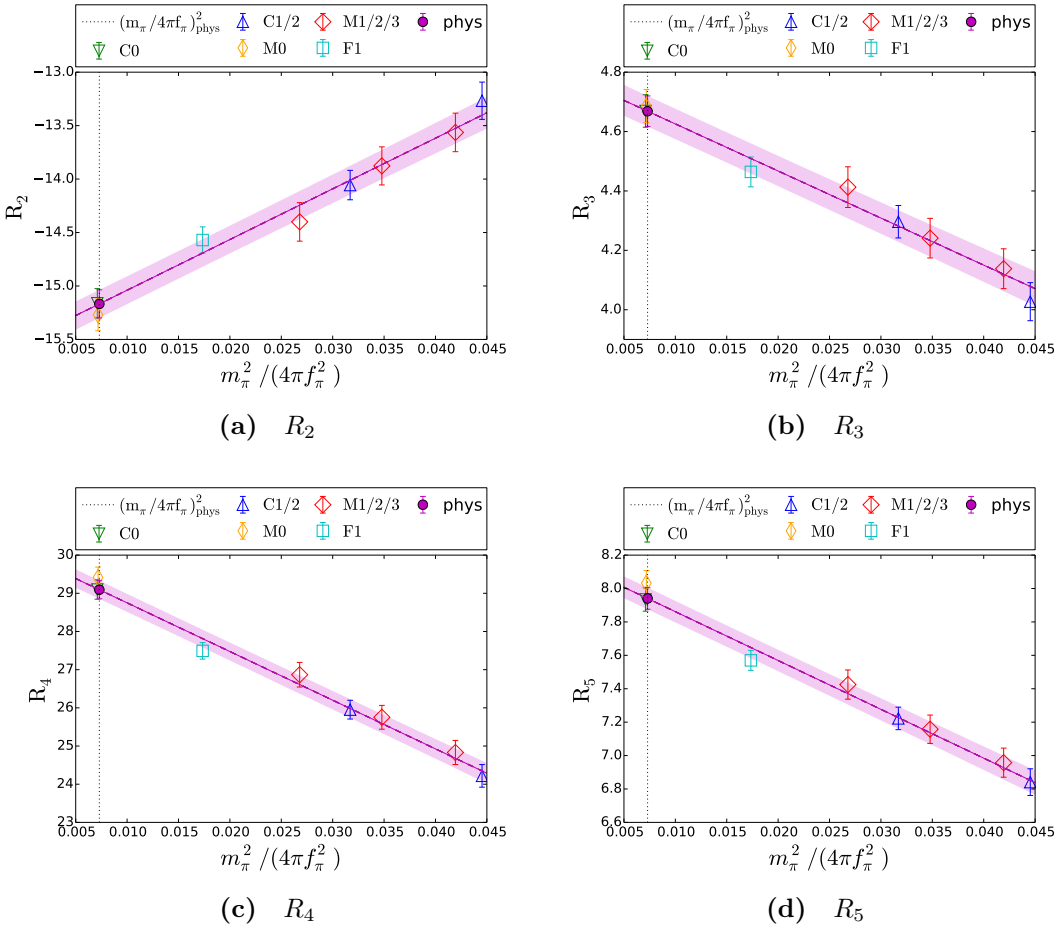

(a) R_2 **(b)** R_3

(c) R_4 **(d)** R_5

Figure 5.6 *Chiral extrapolation of the ratio parameters renormalised at 2GeV in the SMOM$^{(\gamma_\mu,\gamma_\mu)}$ scheme according to the linear fit form described in equation 5.1. All medium, coarse and fine data points are included here, but have been corrected to the continuum for plotting.*

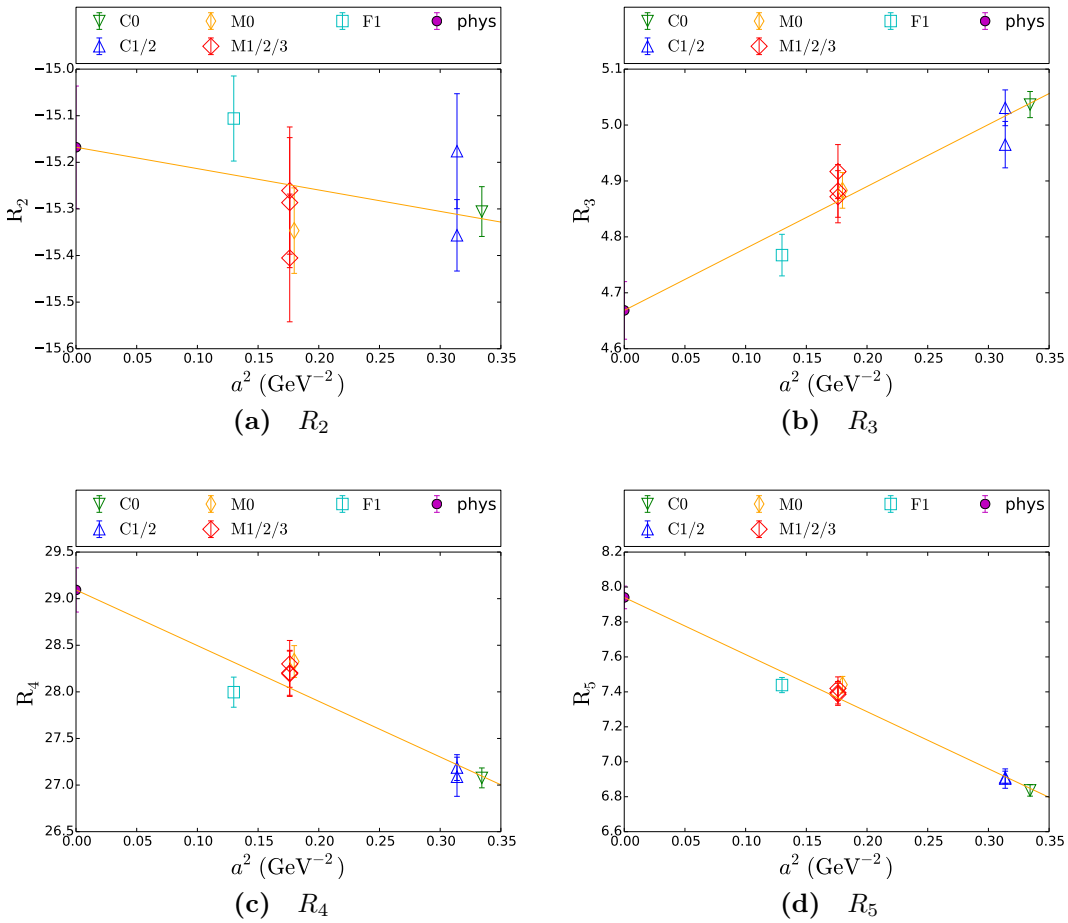

(a) R_2 **(b)** R_3 **(c)** R_4 **(d)** R_5

Figure 5.7 *Continuum extrapolation of the ratio parameters renormalised at 2GeV in the SMOM$^{(\gamma_\mu,\gamma_\mu)}$ scheme according to the linear fit form described in equation 5.1. All medium, coarse and fine data points are included here, but have been corrected to the physical pion mass for plotting.*

We define a discretisation systematic as,

$$\delta_i^{Discr} = \frac{|R_i^{\text{incl.}F1} - R_i^{\text{excl. F1}}|}{\frac{1}{2}(R_i^{\text{incl. F1}} - R_i^{\text{excl.}F1})}. \tag{5.5}$$

For all parameters this difference between a fit including and excluding F1 is typically of order 1% to 2%.

If we wish to reassure ourselves of the validity of these errors, we can also consider the procedure of scaling for fits with poor χ^2 often used by PDG. The data is fit

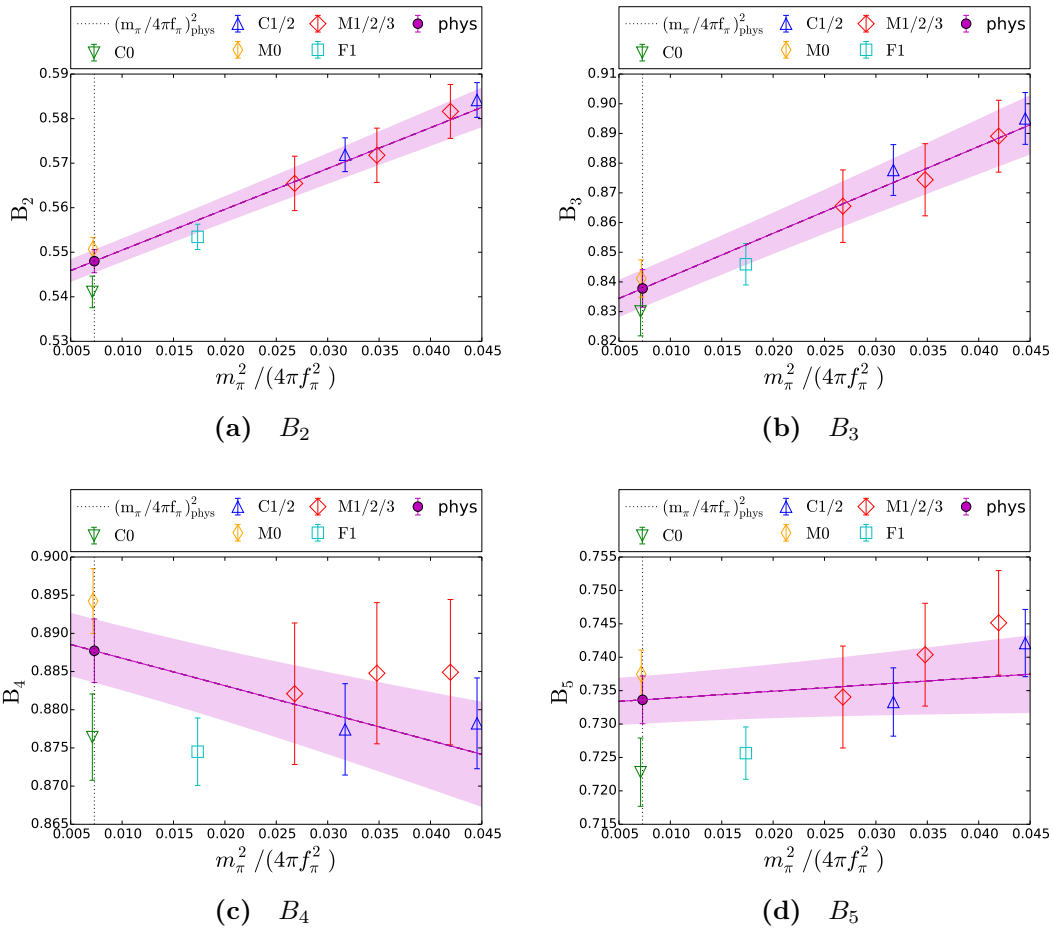

(a) B_2 **(b)** B_3

(c) B_4 **(d)** B_5

Figure 5.8 *Chiral extrapolation of the BSM bag parameters renormalised at 2GeV in the SMOM$^{(\gamma_\mu,\gamma_\mu)}$ scheme according to the linear fit form described in equation 5.1. All medium, coarse and fine data points are included here, but have been corrected to the continuum for plotting.*

as usual but then the error is scaled by a factor, S, defined by,

$$S = \sqrt{\chi^2/\text{d.o.f.}}, \tag{5.6}$$

so that the value of χ^2/d.o.f. reduces to 1. The justification for this is if the errors on some data points have been underestimated. Given that we lack certainty in the effects of the partial quenching of the action of the F1 data point, and that we have not attached a systematic to this, it would be reasonable to adopt this procedure. This would lead to a scaling of the statistical error for the B_4 and B_5 in the scheme SMOM$^{(\gamma,\gamma)}$ of 2.77, and of 1.94 for B_2. This would inflate the statistical errors on the fit including F1 to 0.92%, 1.31% and 1.36% for B_2, B_4 and B_5 respectively. If instead we take the central value from the fit excluding

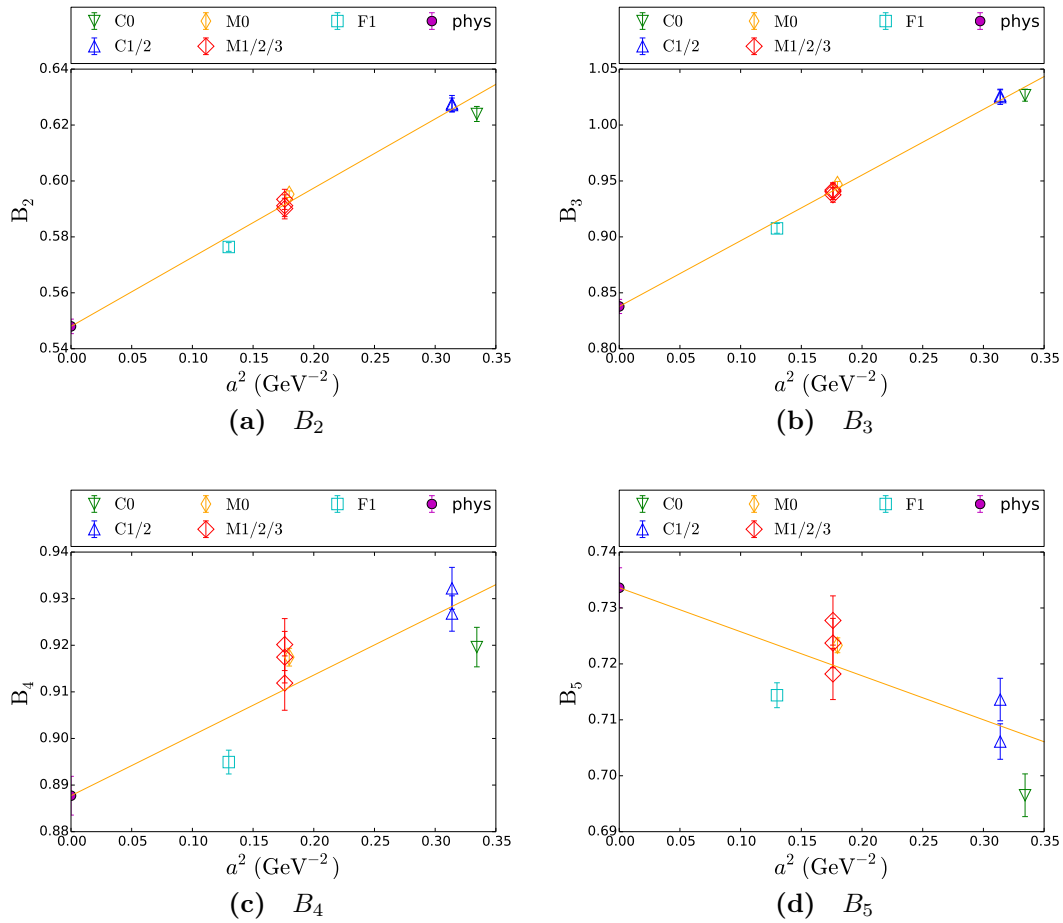

(a) B_2 **(b)** B_3 **(c)** B_4 **(d)** B_5

Figure 5.9 *Continuum extrapolation of the BSM bag parameters renormalised at 2GeV in the SMOM$^{(\gamma_\mu,\gamma_\mu)}$ scheme according to the linear fit form described in equation 5.1. All medium, coarse and fine data points are included here, but have been corrected to the physical pion mass for plotting.*

F1 and take the discretisation errors as given by equation 5.5, the corresponding errors are 1.51%, 2.39% and 2.16% in that order. Therefore we feel confident that even with the poor χ^2/d.o.f in the fine fits that we are not underestimating the discretisation errors. RBC-UKQCD is in the process of rerunning the calculations for the fine lattice spacing without the partial quenching. In due course this calculation could be repeated including that data allowing for the discretisation errors to be better controlled. It is plausible, but by no means guaranteed, that the new fine data is found to be more compatible with the current coarse and medium data and a fit form with and a^2 dependence, effectively controlling for the discretisation effects. Until then is it prudent to estimate these errors as described.

Discretisation effects in the renormalisation

For hard, off-shell vertex functions where the momenta are chosen as the best compromise for a Rome-Southampton window, the higher order discretisation effects are likely not benign. Further discretisation effects are thus likely to come from the non-perturbative renormalisation, and may be probed by comparing different ways to treat the momentum probe on the coarsest lattice spacing. We compare two different approaches as follows. We take the 3GeV renormalisation point on each ensemble, and match this to $\overline{\text{MS}}$ bar perturbatively in each of the two schemes. We also take a different approach with a 2GeV renormalisation point to the momentum scheme. This will have reduced lattice artifacts in the vertex functions associated with the momentum scale which is further from the high end of the Rome-Southampton window. This result is run non-perturbatively using a continuum, non-perturbative step scaling function [11, 35] obtained using only the two finest $a^{-1} = 2.38$ GeV and $a^{-1} = 2.77$ GeV ensembles. Results for this method are in tables 5.6 and 5.7. Since the most susceptible 3 GeV vertex function on the coarsest ensemble is removed entirely from the procedure in the approach, it is a viable and data driven way to estimate the systematic impact of non-removed a^4 lattice artifacts.

We will present the full error budget for the results from both the two different approached described above in tables 5.6 and 5.7.

We define the magnitude of this discretisation systematic as,

$$\delta_i^{Discr,NPR} = \frac{|R_i^{3\text{GeV}} - R_i^{3\text{GeV}\leftarrow 2\text{GeV}}|}{\frac{1}{2}(R_i^{3\text{GeV}} + R_i^{3\text{GeV}\leftarrow 2\text{GeV}})}, \tag{5.7}$$

and we list the values in tables 5.6 and 5.7 labelled as "Discr,NPR". While these values are fairly small for the ratio parameters in both schemes, they become more significant for the bag parameters for the SMOM$^{(\not{q},\not{q})}$ scheme. This suggests that the SMOM$^{(\not{q},\not{q})}$ scheme is more vulnerable to these discretisation effects. This vulnerability motivates us to choose the SMOM$^{(\gamma_\mu,\gamma_\mu)}$ scheme for our central values. Then the SMOM$^{(\not{q},\not{q})}$ scheme is used only in assessing the size of the perturbative matching errors, as described below, thus protecting the central value from these effects.

5.3.1 Perturbative Matching Error

A significant source of error arises in the conversion of our results to $\overline{\text{MS}}$ where the matching is done in perturbation theory to one-loop. The truncation of the perturbative series leads to an uncertainty. Given that we have defined two intermediate RI-SMOM schemes, differentiated by their projectors we are able to estimate the size of this error. We should expect results in $\overline{\text{MS}}$ to be independent of the intermediate renormalisation scheme. Thus we can estimate the magnitude of this error, $\delta_i^{\text{PT}}(\mu)$, by considering the difference between the results from each intermediate scheme, SMOM$^{(\gamma_\mu,\gamma_\mu)}$ and SMOM$^{(\not{q},\not{q})}$,

$$\delta_i^{\text{PT}}(\mu) = \frac{|R_i^{\overline{\text{MS}}\leftarrow(\gamma_\mu,\gamma_\mu)}(\mu) - R_i^{\overline{\text{MS}}\leftarrow(\not{q},\not{q})}(\mu)|}{\frac{1}{2}(R_i^{\overline{\text{MS}}\leftarrow(\gamma_\mu,\gamma_\mu)}(\mu) + R_i^{\overline{\text{MS}}\leftarrow(\not{q},\not{q})}(\mu))}. \tag{5.8}$$

Motivation for 2GeV Renormalisation Scale

Recalling that the SMOM$^{(\not{q},\not{q})}$ scheme is more vulnerable to discretisation effects at a momentum scale of 3GeV, the difference between the schemes renormalised at this scale reflects these discretisation effects instead of being purely a measure of the perturbative matching error. Instead we take the central value as the results renormalised via SMOM$^{(\gamma_\mu,\gamma_\mu)}$ at 2GeV, then step-scaled to 3GeV. The difference between schemes renormalised at this lower scale will be less vulnerable to the discretisation effects, and thus reflect a more accurate estimate of the perturbative matching error. To support this let us consider B_3 as presented in table 5.5. It becomes clear that the result renormalised via SMOM$^{(\not{q},\not{q})}$ at 3GeV is the outlier, and has been compromised by the discretisation effects. We choose to take the results renormlised via SMOM$^{(\gamma,\gamma)}$ as our central value, so the central value is not compromised at either renormalisation scale. However, the estimation of the perturbative matching error would be affected were we to choose to renormalise directly at 3GeV. For this reason we choose our central value as those renormalised at 2GeV via the SMOM$^{(\gamma,\gamma)}$ scheme, and then step-scaled to 3GeV as our central value. This approach is tried and tested, having been used several times in work before [11–13, 29]. We obtain results after non-perturbative running to 3GeV without having to insert 3GeV offshell momenta on the coarsest lattice spacing. We should also warn that while we present the error budget for results renormalised directly at 3GeV, one should bear in mind that the quoted

perturbative matching error is not reliable for the reasons given above.

Intermediate Renormalisation Scale	(γ_μ, γ_μ)	$(\not{q}, \not{q})$
2GeV	0.739(7)(21)(33)	0.723(12)(68)(16)
3GeV	0.714(4)(36)(55)	0.660(6)(52)(60)

Table 5.5 *The values and error budget of $B_3^{\overline{MS}}$ for intermediate renormalisation scales of 2GeV and 3GeV. In both cases the conversion to $\overline{MS}$ is done at 3GeV. For the results calculated at 2GeV step-scaling to 3GeV (calculated excluding the coarse data) is performed before matching.*
.

scheme		R_2	R_3	R_4	R_5	B_1	B_2	B_3	B_4	B_5
$SMOM^{(\gamma_\mu,\gamma_\mu)}$	Value	-18.69	5.591	39.04	10.93	0.5175	0.5128	0.7479	0.9137	0.7846
	Stat.	1.34%	1.52%	1.31%	1.19%	0.25%	0.31%	0.56%	0.22%	0.27%
	Chiral	0.16%	0.20%	0.31%	0.18%	0.66%	0.00%	0.04%	0.01%	0.01%
	Disc,NPR	0.53%	0.50%	1.40%	2.26%	1.99%	1.68%	3.39%	1.65%	1.03%
	Disc.	1.73%	1.59%	2.31%	1.78%	0.77%	0.08%	0.19%	0.21%	0.26%
	Total	2.25%	2.26%	3.01%	3.12%	2.25%	1.71%	3.44%	1.68%	1.09%
$SMOM^{(\not{q},\not{q})}$	Value	-20.03	5.459	41.58	10.50	0.5349	0.5177	0.6637	0.9146	0.7102
	Stat.	1.35%	1.74%	1.30%	1.24%	0.24%	0.37%	0.92%	0.25%	0.32%
	Chiral	0.15%	0.18%	0.24%	0.19%	0.68%	0.02%	0.05%	0.01%	0.00%
	Disc,NPR	0.40%	2.01%	1.48%	2.54%	4.32%%	8.83%	3.27%	2.41%	
	Disc.	1.51%	0.68%	2.26%	1.73%	0.67%	0.23%	1.11%	0.58%	0.75%
	Total	2.07%	2.75%	3.01%	3.32%	4.43%	2.59%	8.95%	3.33%	2.54%
$\overline{\text{MS}}^{(\gamma_\mu,\gamma_\mu)}$	Value	-19.06	5.895	41.95	10.79	0.5196	0.4739	0.7137	0.8897	0.7025
	Stat.	1.38%	1.76%	1.28%	1.24%	0.25%	0.32%	0.57%	0.21%	0.26%
	Chiral	0.20%	0.18%	0.26%	0.19%	0.66%	0.00%	0.03%	0.01%	0.00%
	Disc,NPR	0.20%	1.75%	1.25%	2.17%	2.08%	1.67%	3.48%	1.65%	1.02%
	Disc.	1.49%	0.81%	2.28%	1.78%	0.77%	2.21%	3.71%	0.30%	0.20%
	PT.	2.64%	3.71%	2.59%	2.72%	2.00%	2.36%	7.77%	2.04%	3.14%
	Total	3.34%	4.54%	3.89%	4.10%	3.06%	3.65%	9.31%	2.65%	3.31%

Table 5.6 *Here central values and a full error budget for the ratio and bag parameter results renormalised directly at 3GeV and converted to $\overline{MS}$ prior to fitting are presented. For all ratio operators the final results ($\overline{MS} \leftarrow SMOM^{(\gamma_\mu,\gamma_\mu)}$) the total error is of order 4% or less. As discussed, the perturbative errors for B_3 has been contaminated by discretisation effects in the $SMOM^{(\not{q},\not{q})}$ scheme, and should not be take as a true value.*

scheme		R_2	R_3	R_4	R_5	B_1	B_2	B_3	B_4	B_5
$SMOM^{(\gamma_\mu,\gamma_\mu)}$	Value	-18.79	5.619	39.59	11.18	0.5279	0.5215	0.7737	0.9289	0.7927
	Stat.	1.38%	1.57%	1.39%	1.34%	0.25%	0.77%	0.97%	0.78%	0.76%
	Chiral	0.21%	0.18%	0.35%	0.36%	0.08%	0.04%	0.03%	0.03%	0.03%
	Disc,NPR	0.53%	0.50%	1.40%	2.26%	1.99%	1.68%	3.39%	1.65%	1.03%
	Disc.	1.45%	1.60%	2.20%	1.92%	0.76%	1.53%	1.79%	2.39%	2.17%
	Total	2.08%	2.30%	2.97%	3.28%	2.15%	1.68%	3.95%	3.00%	2.52%
$SMOM^{(\not{q},\not{q})}$	Value	-20.07	5.56	42.1	10.73	0.5347	0.5313	0.726	0.9449	0.7272
	Stat.	1.54%	1.98%	1.52%	1.40%	0.47%	1.05%	1.65%	0.88%	0.92%
	Chiral	0.20%	0.18%	0.24%	0.37%	0.07%	0.04%	0.14%	0.01%	0.04%
	Disc,NPR	0.20%	1.83%	1.24%	2.17%	0.77%	2.59%	8.97%	3.26%	2.37%
	Disc.	1.20%	1.21%	2.19%	1.86%	0.04%	2.15%	2.54%	3.36%	3.13%
	Total	1.98%	2.96%	2.95%	3.20%	0.90%	3.53%	9.46%	4.76%	4.03%
$\overline{\text{MS}} \leftarrow \text{SMOM}^{(\gamma_\mu,\gamma_\mu)}$	Value	-19.17	5.924	42.54	11.05	0.5186	0.4819	0.739	0.9045	0.7097
	Stat.	1.41%	1.57%	1.39%	1.40%	0.25%	0.77%	0.99%	0.78%	0.75%
	Chiral	0.16%	0.19%	0.33%	0.28%	0.08%	0.02%	0.01%	0.03%	0.03%
	Disc,NPR	0.37%	0.25%	1.09%	1.98%	0.46%	1.67%	3.51%	1.64%	1.02%
	Disc.	1.47%	1.60%	2.21%	1.88%	0.76%	1.51%	1.79%	2.39%	2.16%
	PT.	2.27%	2.46%	2.44%	2.94%	2.16%	3.27%	2.19%	3.65%	1.76%
	Total	3.08%	3.34%	3.75%	4.34%	2.35%	4.04%	4.61%	4.73%	3.06%

Table 5.7 *Here central values and a full error budget for the ratio and bag parameter results renormalised at 2GeV, then step-scaled to 3GeV and converted to $\overline{MS}$ after fitting are presented. For all operators the final results ($\overline{MS} \leftarrow SMOM^{(\gamma_\mu,\gamma_\mu)}$) the total error is less than 5%.*

5.3.2 Standard Model Bag Parameter

For the standard model bag parameter fit, a different approach is taken. As summarised in table 5.2, for the BSM bag parameters and ratios it was found that there was no non-negligible dependance on the unphysical sea masses of the partially quenched strange quark. However this was not the case for the standard model bag parameter B_1, where the parameters were found to be,

$$\begin{aligned} \gamma_1^{SMOM^{\gamma\gamma}(2\text{GeV})} &= -0.036(11) \\ \gamma_1^{SMOM^{\gamma\gamma}(3\text{GeV})} &= -0.033(10). \end{aligned} \tag{5.9}$$

These parameters are not consistent with zero, even beyond 2σ. As such I could not justify excluding the effect of the unphysical sea strange mass. Therefore fit 5.3 was chosen to derive the central value of the standard model bag parameter. The fits are shown in figure 5.10. The error budgets are presented in tables 5.6 and 5.7 alongside the other results. The approach to calculating the systematic errors was identical.

It is worth noting that calculating the standard model bag parameter was not the aim of this work, especially given there is a calculation of B_k by RBC-UKQCD [31] including data with physical light quarks. This work does make it possible to

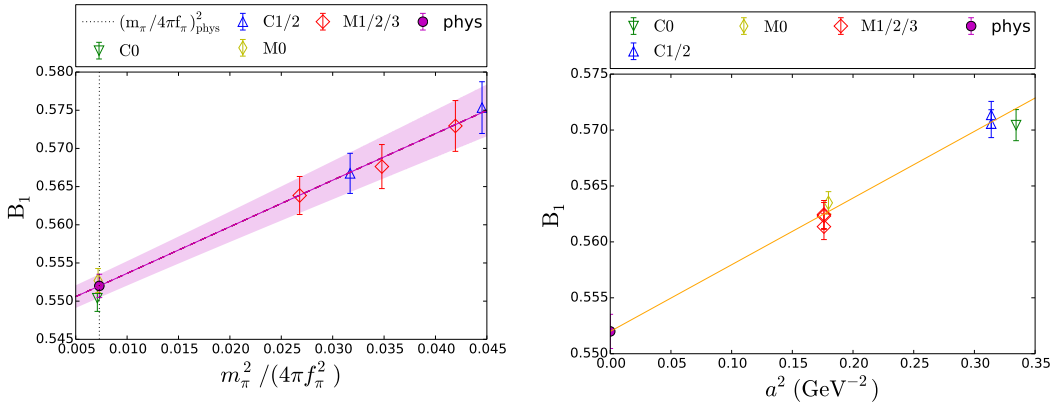

(a) *Chiral Extrapolation* **(b)** *Continuum Extrapolation*

Figure 5.10 *Chiral extrapolation and continuum extrapolation of the standard model bag parameters renormalised at 2GeV in the SMOM$^{(\not{q},\not{q})}$ scheme and converted to $\overline{MS}$ according to the linear fit form described in equation 5.1. All medium and coarse data points are included here, but have been corrected to the physical pion mass (continuum) for plotting the continuum (chiral) extrapolation.*

	This Work	Previous Work
$B_K^{\overline{\text{MS}}\leftarrow\text{SMOM}^{(\not{q},\not{q})}}(3\text{GeV})$	0.5299(58)(48)	0.5293(17)(106).

Table 5.8 *Comparison of the standard model bag parameter as calculated in this work and in [31]. The latter error represents the perturbative matching error, while the former represent the remaining errors.*

cross-check the result for B_k. Before we do so, it is important to note some key difference in approach taken. While the datasets for both works include many of the same gauge ensembles, the calculation of propagators and lattice operators was redone with partially quenched strange quarks and a multi-hit strategy, resulting in very precise data. On top of this, [31] employed overweighting of the physical point data in the fits to force the fit through the physical point data. This means the quality of fits of both works cannot be directly compared. This bag parameter in $\overline{\text{MS}}$ at 3GeV renormalised via SMOM$^{(\not{q},\not{q})}$ for both works, including systematic errors, are shown in table 5.8.

The values are completely consistent. The fact that we can replicate this result using a different fitting method acts as a useful validation of our approach.

Table 5.9 *The correlation matrix for the ratio parameters in the SMOM$^{(\gamma,\gamma)}$ scheme at 2GeV.*

	R_3	R_4	R_5
R_2	-0.9488	-0.8894	-0.8529
R_3		0.8071	0.7863
R_4			0.8618

Table 5.10 *The correlation matrix for the BSM bag parameters in the SMOM$^{(\gamma,\gamma)}$ scheme at 2GeV.*

	B_3	B_4	B_5
B_2	0.8768	0.6631	0.6218
B_3		0.5066	0.4969
B_4			0.6317

5.3.3 Correlations

We can consider the correlations between the operators by calculating the correlation matrices of our bootstrap data. We should recall that as well as the bare lattice calculations, our final results have the renormalisation factors as input. The renormalisation factors are calculated on only a small subset of configurations, therefore the bootstraps of these do not represent the same resampling as for the lattice quantities derived in chapter 3. We can still find the correlations by taking the correlation matrix of the bootstraps for operators with the same renormalisation factors. This does mean we cannot meaningfully find the correlations between B_1 and the other bag parameters.

For the bag and ratio parameters the correlations are highest between B_2 and B_3 as we might expect. We see higher correlations between the ratios, which is to be expected given the shared SM matrix element as denominator.

5.3.4 Matrix Elements

Finally, we present the the BSM matrix elements derived from both the bag parameter and from the ratio parameter at 3GeV both in SMOM$^{(\gamma,\gamma)}$ and in $\overline{\text{MS}}$. Recall that the BSM matrix elements derived from the bag parameter have a dependence on the strange and light quark masses, whereas to derive them from the ratio parameters we require only the standard model bag parameter, and the experimentally known kaon mass and decay constant. For the kaon mass we take

Table 5.11 *The matrix elements for the BSM four-quark operators derived from the ratio parameters renormalised at $\mu = 3GeV$ in both the RI-SMOM$_{(\gamma_\mu,\gamma_\mu)}$ scheme, and converted to $\overline{MS}$.*

	RI-SMOM$_{(\gamma_\mu,\gamma_\mu)}$	$\overline{\text{MS}} \leftarrow$ RI-SMOM$_{(\gamma_\mu,\gamma_\mu)}$
$\langle \bar{K}^0 \vert O_2 \vert K^0 \rangle$	-0.1544(22)(27) 2.3%	-0.1574(22)(28)(50) 3.9%
$\langle \bar{K}^0 \vert O_3 \vert K^0 \rangle$	0.04616(73)(86) 2.4%	0.04867(77)(91)(159) 4.1%
$\langle \bar{K}^0 \vert O_4 \vert K^0 \rangle$	0.3253(45)(89) 3.1%	0.3495(48)(93)(114) 4.4%
$\langle \bar{K}^0 \vert O_5 \vert K^0 \rangle$	0.0919(12)(29) 3.4%	0.0908(12)(27)(33) 4.9%

Table 5.12 *The matrix elements for the BSM four-quark operators derived from the bag parameters renormalised at $\mu = 3GeV$ in both the RI-SMOM$_{(\gamma_\mu,\gamma_\mu)}$ scheme, and converted to $\overline{MS}$*

	RI-SMOM$_{(\gamma_\mu,\gamma_\mu)}$	$\overline{\text{MS}} \leftarrow$ RI-SMOM$_{(\gamma_\mu,\gamma_\mu)}$
$\langle \bar{K}^0 \vert O_2 \vert K^0 \rangle$	-0.1548(12)(35) 2.4%	-0.1636(13)(37)(53) 4.0%
$\langle \bar{K}^0 \vert O_3 \vert K^0 \rangle$	0.04594(45)(178) 4.0%	0.05018(49)(197)(110) 4.6%
$\langle \bar{K}^0 \vert O_4 \vert K^0 \rangle$	0.3309(26)(96) 3.0%	0.3685(29)(107)(135) 4.7%
$\langle \bar{K}^0 \vert O_5 \vert K^0 \rangle$	0.0941(7)(23) 2.6%	0.0964(7)(23)(17) 3.1%

the average of the neutral and charged masses (given by the PDG [24] as 497.6 and 493.7 MeV respectively), while for the decay constant we take the value of 155.5 MeV as given in [31]. We take the PDG values for the quark masses.

For all matrix elements the total errors are at a value of 5% or less.

5.4 Final Results

Here I present the final results obtained from the analysis and compare them to the literature.

In table 5.13 the ratio parameters obtained in this work are compared to the previous results by RBC-UKQCD [71]. In all cases there is complete consistency. The results are consistent well within 1σ. In addition the precision of the results have mostly been improved. For all parameters significant reduction in the statistical errors can be seen. The reduction in statistical error is largely due to a reduction in the variance of the lattice quantities resulting from the multi-hit strategy. There has been a reduction in the systematic error for all quantities other than B_4. This is largely due to the different approach taken to estimating the discretisation errors in [71]. Once the fine lattice spacing data is recalculated without partial quenching and can be included in a future analysis the errors

Table 5.13 *The final results for the ratio parameters given in $\overline{MS}(\mu = 3GeV)$ are presented and compared to RBC-UKQCD's previous calculation. The statistical, systematic and perturbative matching errors are presented in that order.*

	This Work	RBC-UKQCD16 [71]
R_2	-19.17(27)(52)(44)	-19.48(44)(32)(42)
R_3	5.92(9)(17)(15)	6.08(15)(18)(14)
R_4	42.54(59)(141)(104)	43.11(89)(201)(112)
R_5	11.05(15)(39)(33)	10.99(20)(82)(32)
B_1	0.5186(13)(46)(112)	0.525(9)(7)(11)
B_2	0.4819(4)(17)(16)	0.488(7)(17)(4)
B_3	0.739(7)(21)(16)	0.743(14)(64)(8)
B_4	0.905(7)(40)(33)	0.920(12)(10)(13)
B_5	0.710(5)(20)(13)	0.707(8)(35)(27)

Table 5.14 *The BSM bag parameters at 3GeV calculated in this work are compared with the literature.*

Scheme	study	B_2	B_3	B_4	B_5
RI-MOM	ETM15 [55]	0.46(1)(3)	0.79(2)(5)	0.78(2)(4)	0.49(3)(3)
	ETM12 [26]	0.47(2)(1)	0.78(4)(2)	0.76(2)(2)	0.58(2)(2)
	RBC-UKQCD16 [71]	0.417(6)(2)	0.655(12)(44)	0.745(9)(28)	0.555(6)(53)
Perturbative	SWME14 [86]	0.525(1)(23)	0.774(6)(64)	0.981(3)(61)	0.748(9)(79)
	SWME 15 [57]	0.525(1)(23)	0.773(6)(35)	0.981(3)(62)	0.751(7)(68)
RI-SMOM	RBC-UKQCD16	0.488(7)(17)	0.743(14)(65)	0.920(12)(16)	0.707(8)(44)
	This work	0.4819(4)(23)	0.739(7)(26)	0.905(7)(52)	0.710(5)(24)

should be constrained further.

I also compare the central values of the BSM bag parameters from this work with a range of results from the literature in table 5.14 and figure 5.11. One can see that there is some tension in B_4 and B_5 between the different collaborations. The data from [71] strongly suggests that this is a consequence of the choice of renormalisation scheme. It is clear that there is no tension between any of the results renormalised perturbatively or with non-exceptional RI-SMOM. This work adds evidence to the claims that the tensions previously seen are due to the exceptional RI-MOM scheme, which is vulnerable to pion-pole effects in the infrared region.

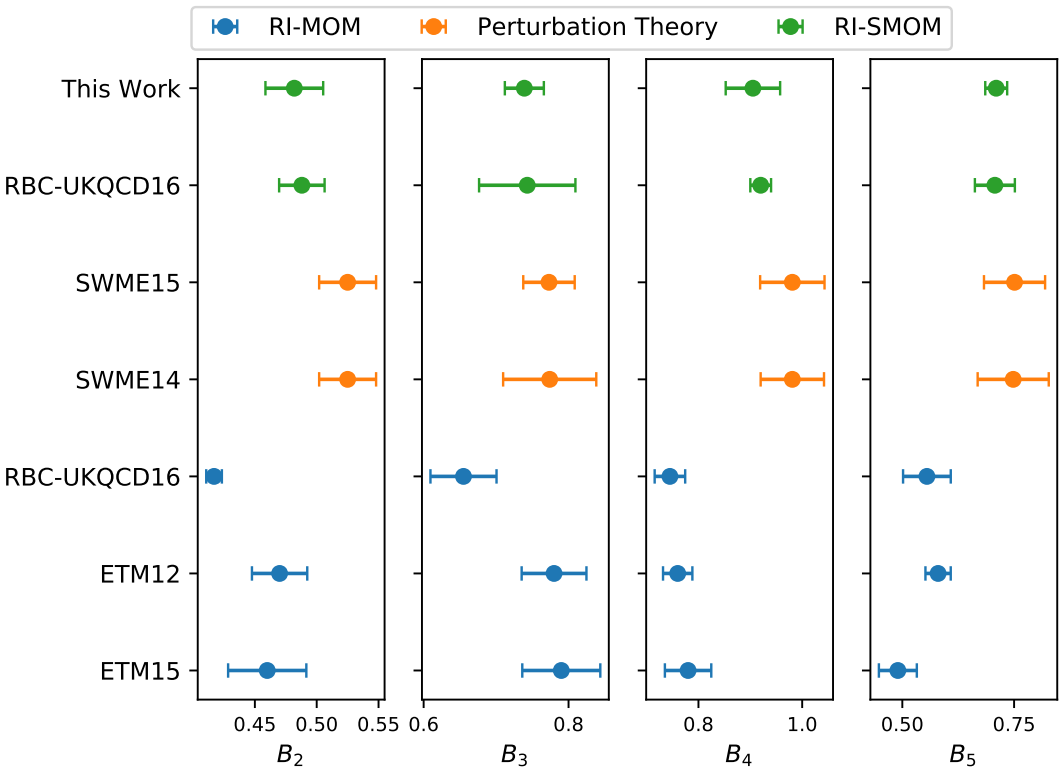

Figure 5.11 *BSM bag parameter results from the literature and this work at 3GeV.*

Chapter 6

Conclusions and Outlook

In this body of work I have calculated renormalisation constants in the non-exceptional renormalisation scheme for the physical point ensembles. The exploration of the low momentum infra-red region of quark bilinears, has confirmed order $1/p^2$ effects in the pseudoscalar and scalar bilinear vertex functions.

We present the first calculation of beyond the standard model kaon mixing with data at the physical point. The use of the multi-hit strategy used in the calculation of propagators has led to significantly increased statistical precision. As a part of this work I implemented the calculation of the gauge fixed non-exceptional momentum source vertex functions into RBC-UKQCDs high performace lattice QCD C++ library, Grid and a separate analysis code which calculated the amputation, projection and statistical analysis allowing which allowed for the calculation of the renormalisation factors for the two ensembles at physical point. The result for the standard model bag parameter using physical data given in [31] has been replicated despite different approaches to fitting. This calculation including physical pions, helps address the tensions seen in B_4 and B_5. The results obtained improve upon those in [71] by improving the statistical precision as well as a better controlled continuum extrapolation, but are in complete agreement with them. This helps add weight to the argument that the tensions observed are in fact a result of the renormalisation scheme, resolving a significant puzzle in the field. Future work must better address the continuum extrapolation by including a third lattice spacing. Any significant body of further work must start to include isospin breaking effects and consider

the longer distance effects, non-perturbative running to a higher scale and the charm threshold. We are close to the limits of the isospin symmetric and local four-quark operator approximation limits. RBC-UKQCD is regenerating F1 with a Moebius domain wall action in both the gauge configuration generation and in the calculation of the propagators, so that there is no partial quenching, so that this calculation will soon be possible. While this result has used F1 at a fine lattice spacing to help address the discretisation systematic, a third lattice spacing included in the central value would allow for greater control over the continuum extrapolation and could allow for the elimination of the not insignificant discretisation uncertainty.

Appendix A

Plots of bare lattice fit results

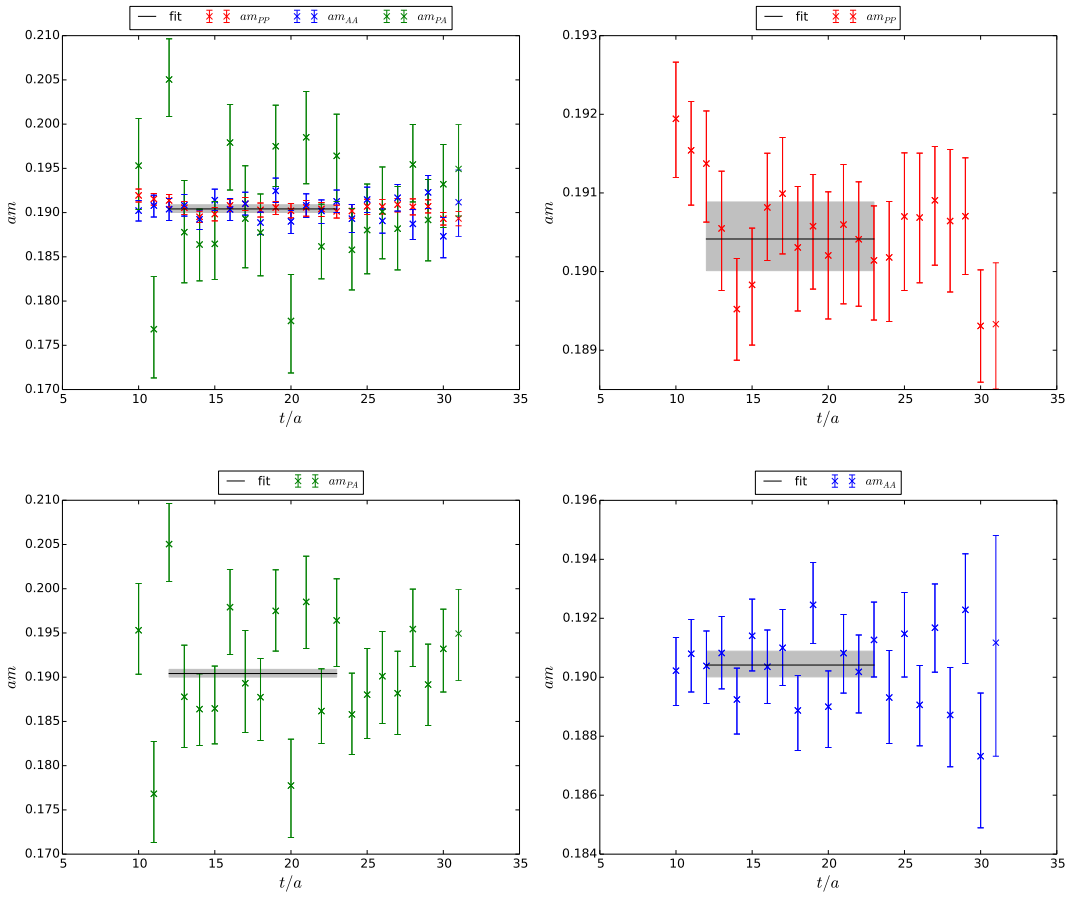

Figure A.1 *Effective mass for the pion on ensemble C1.*

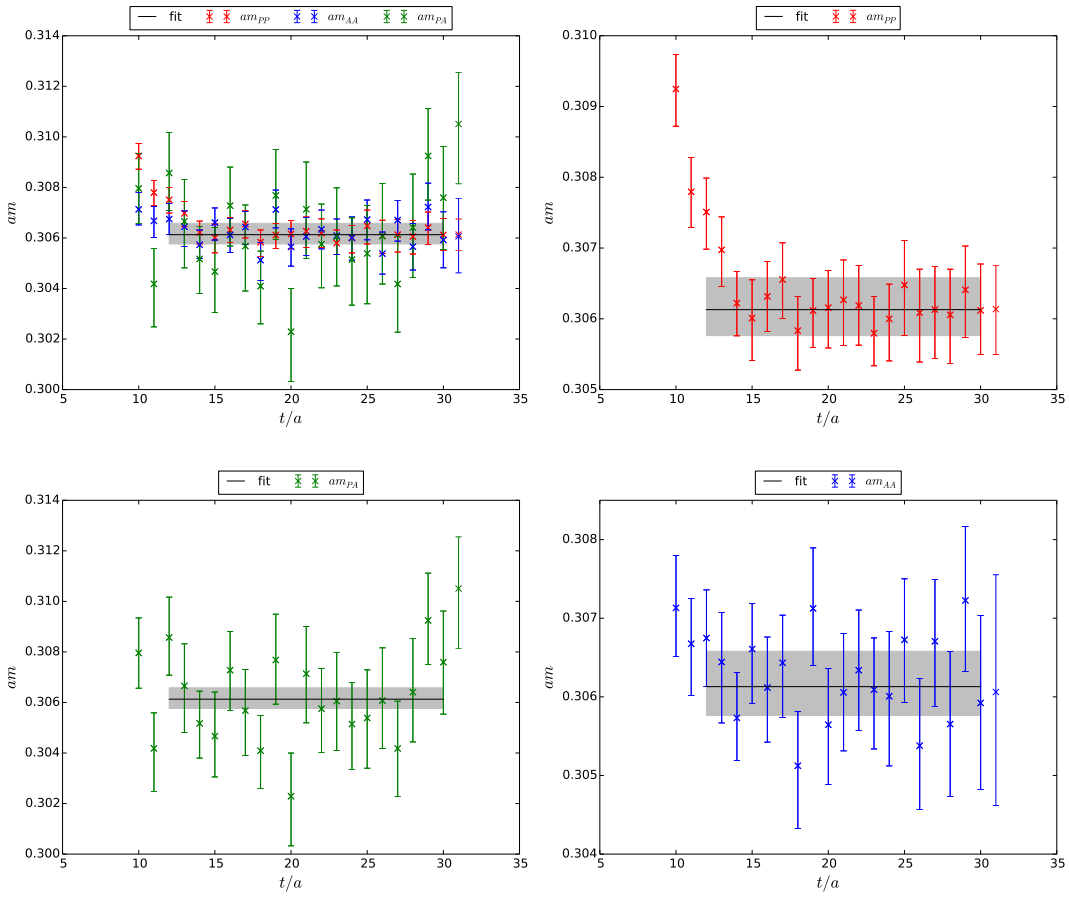

Figure A.2 *Effective mass for the kaon on ensemble C1.*

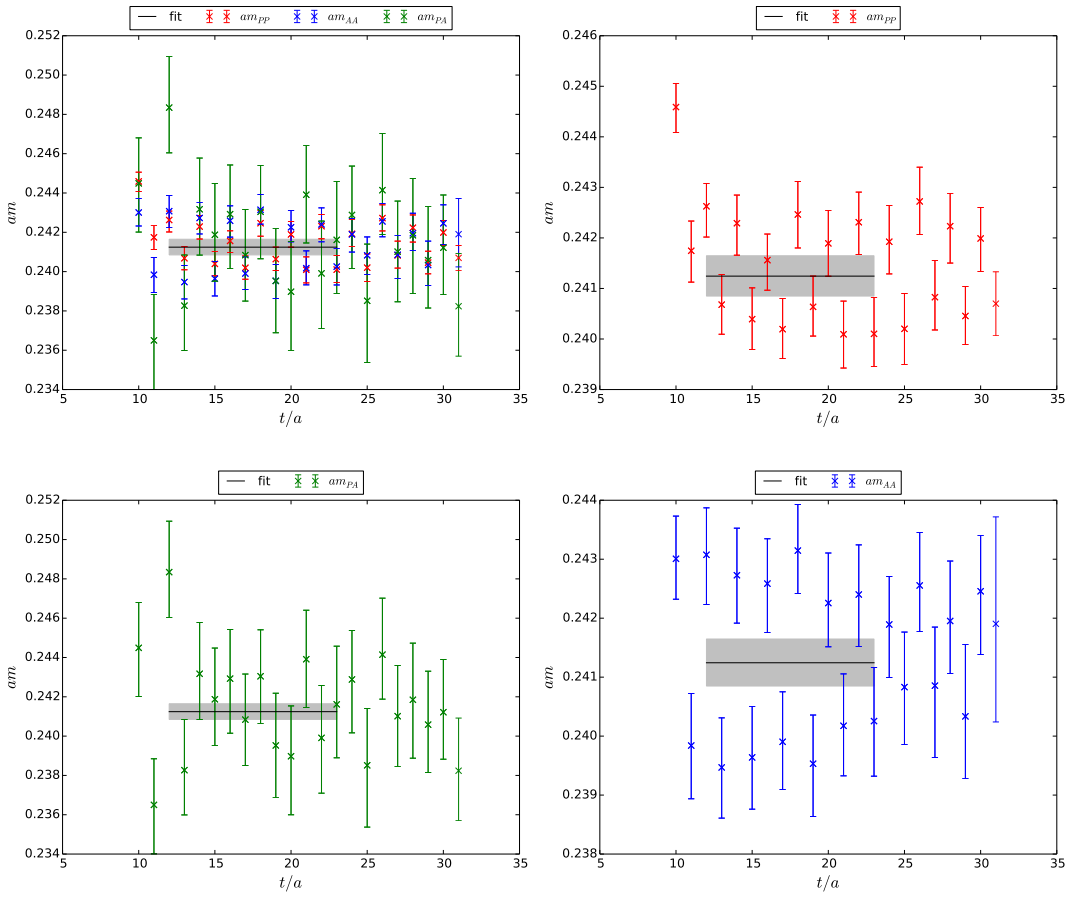

Figure A.3 *Effective mass for the pion on ensemble C2.*

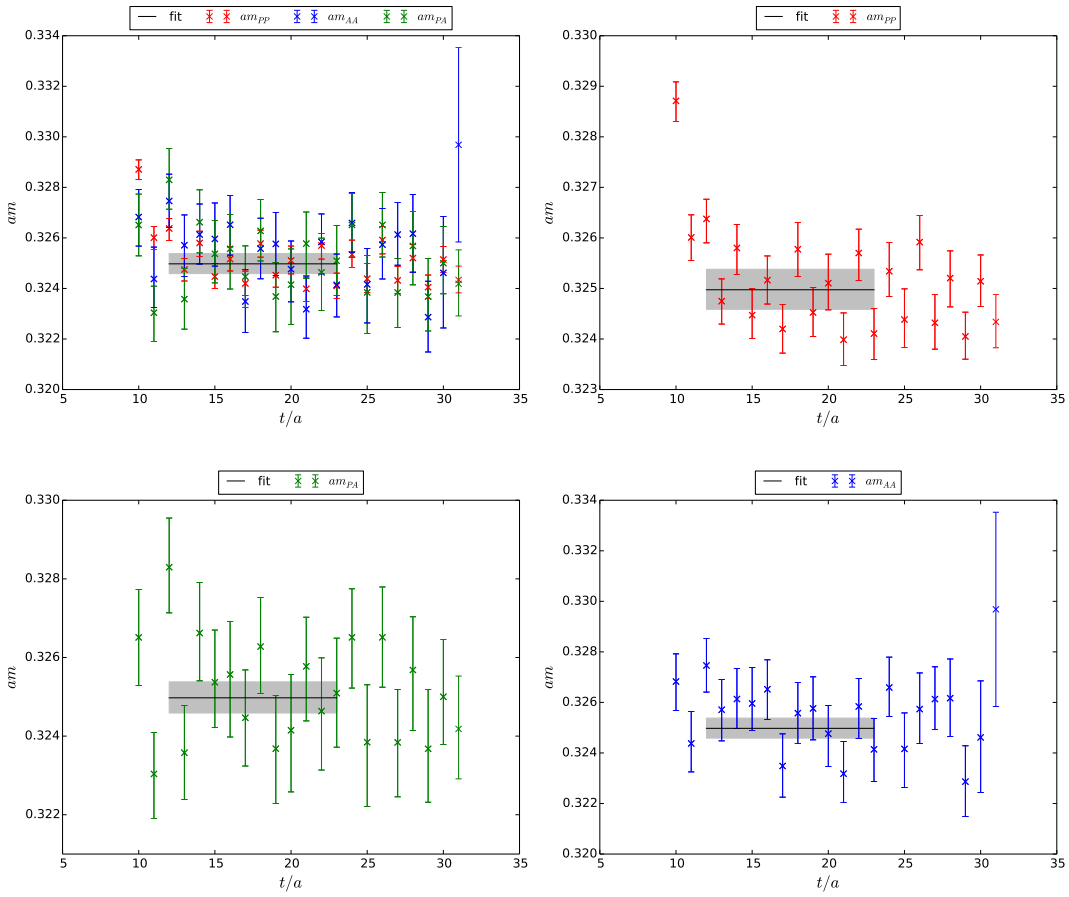

Figure A.4 *Effective mass for the kaon on ensemble C2.*

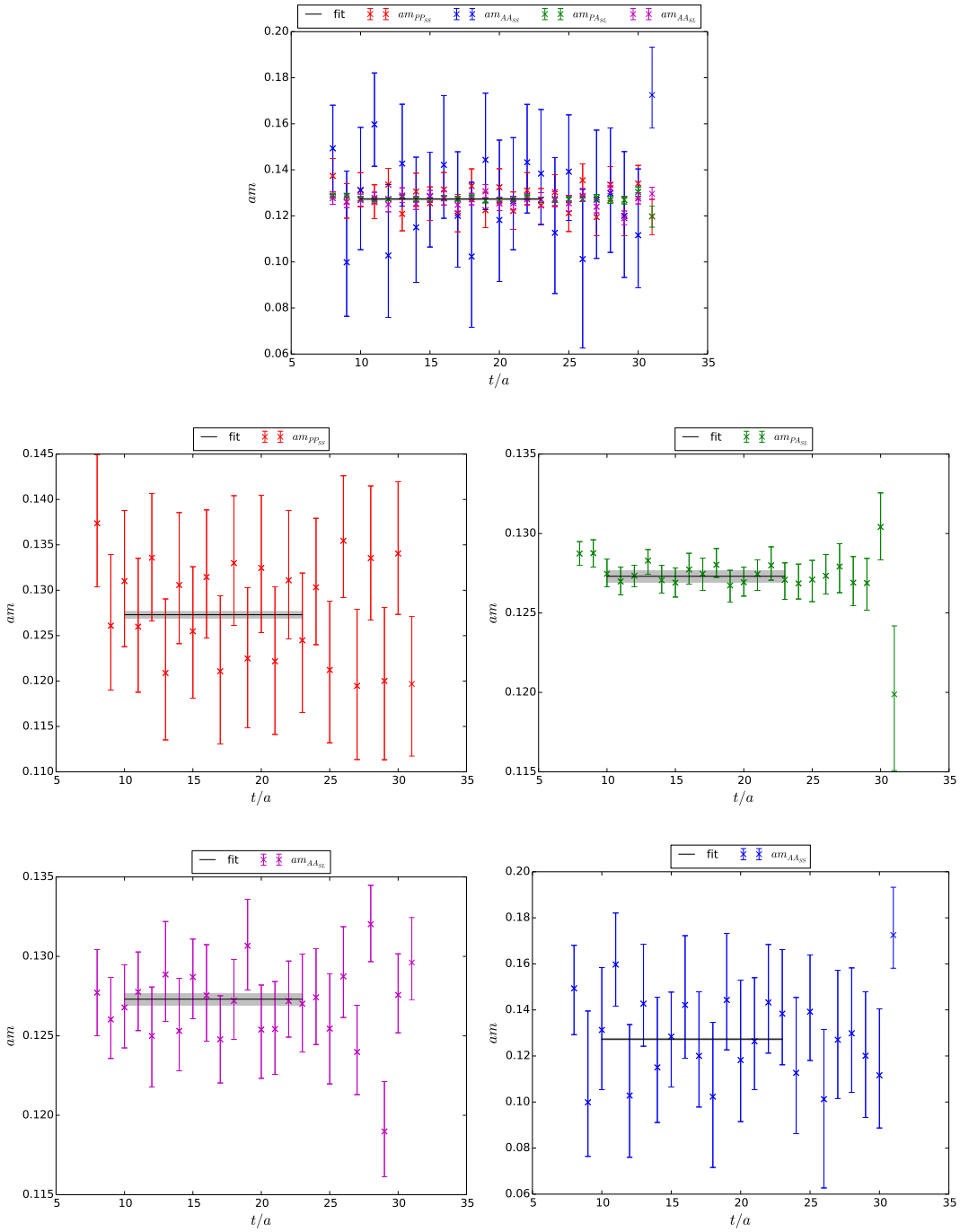

Figure A.5 *Effective mass for the pion on ensemble M1.*

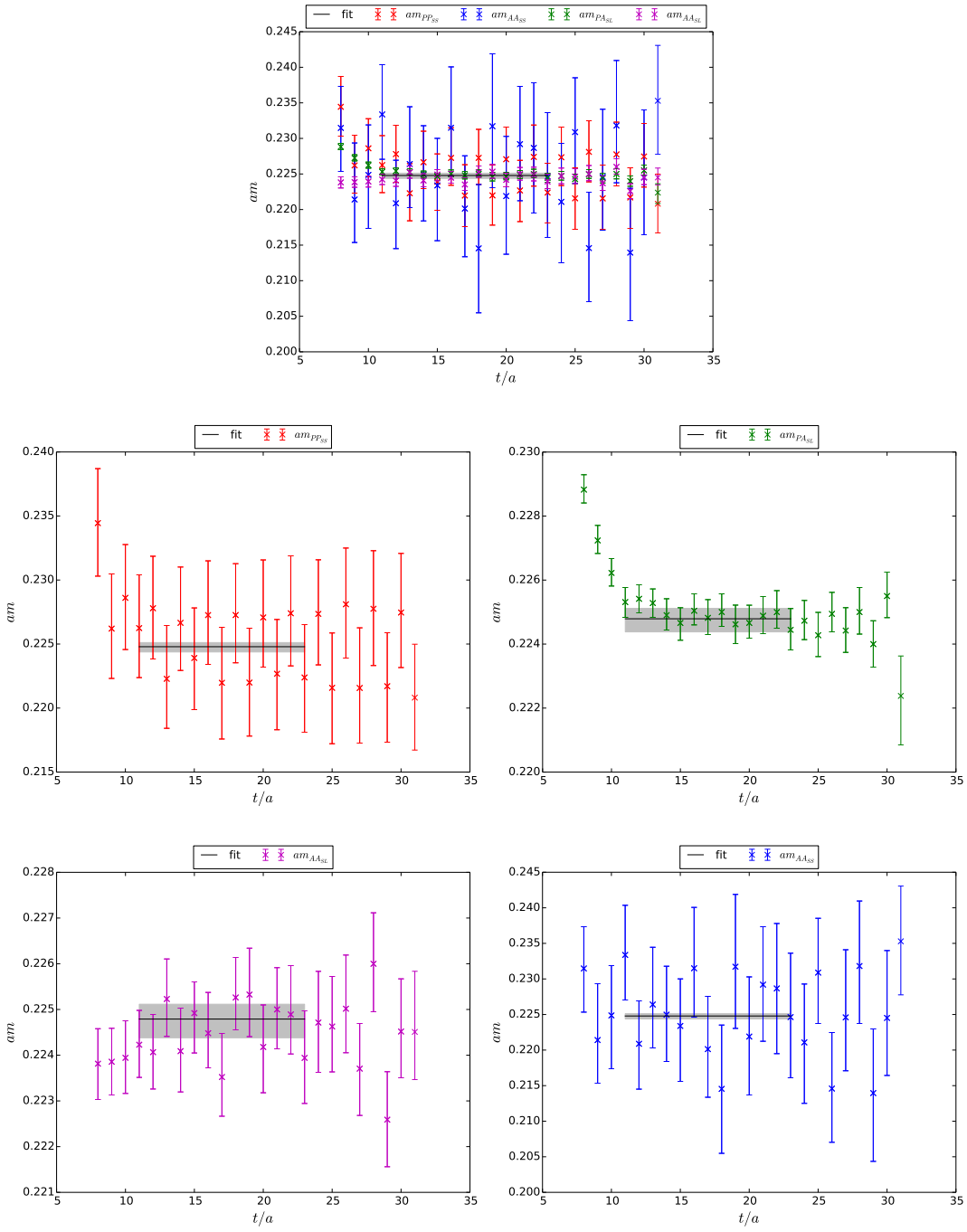

Figure A.6 *Effective mass for the kaon on ensemble M1.*

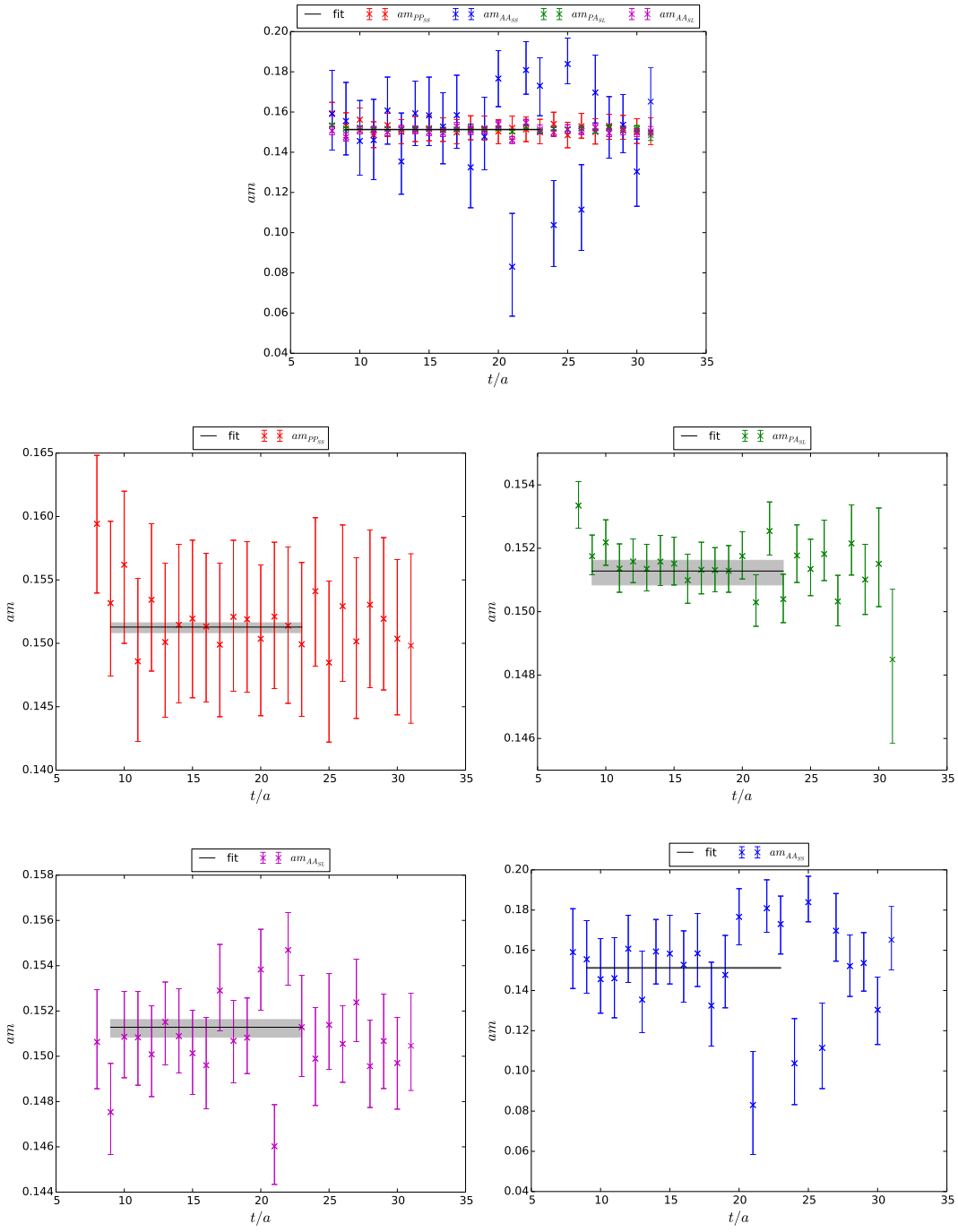

Figure A.7 *Effective mass for the pion on ensemble M2.*

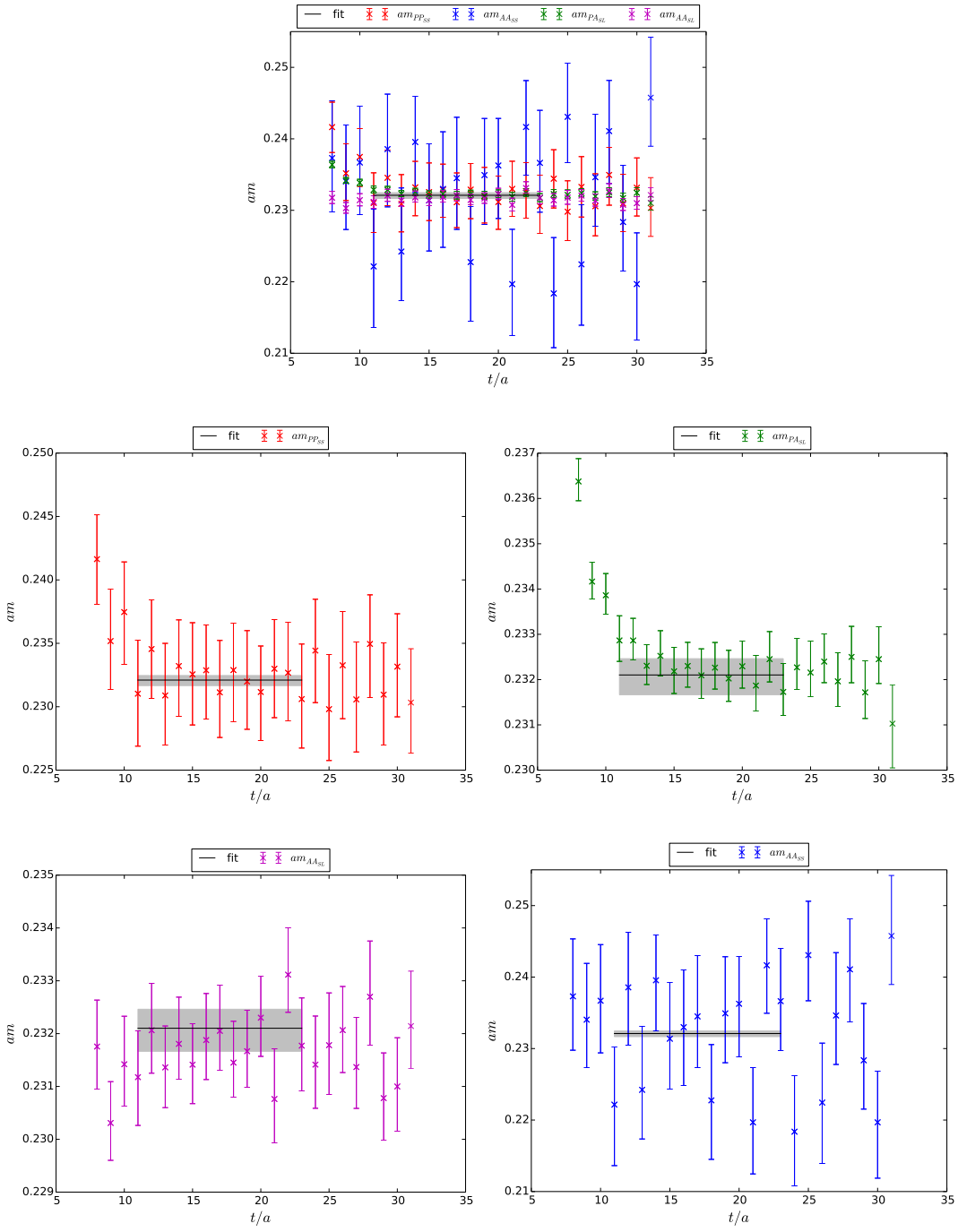

Figure A.8 *Effective mass for the kaon on ensemble M2.*

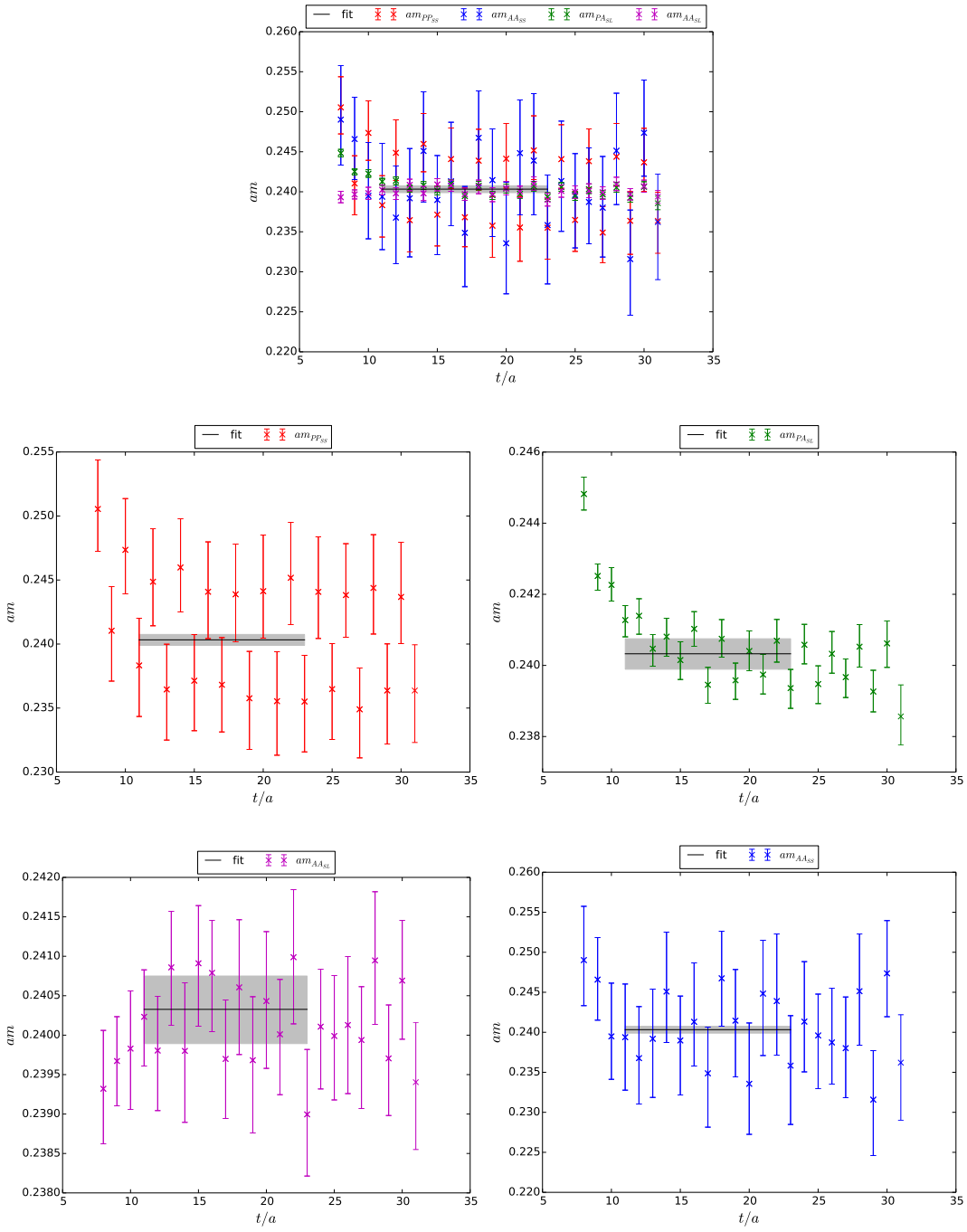

Figure A.9 *Effective mass for the pion on ensemble M3.*

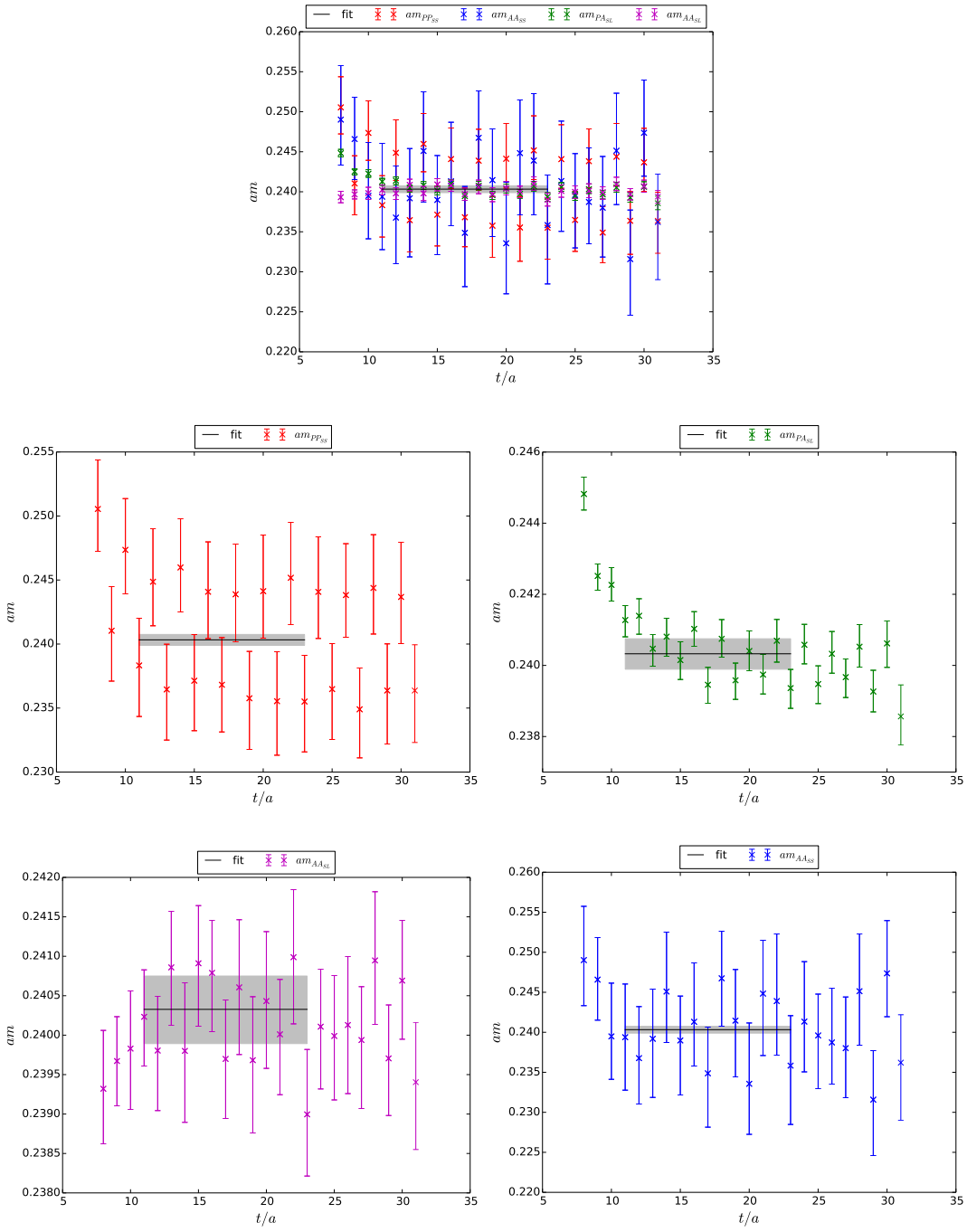

Figure A.10 *Effective mass for the kaon on ensemble M3.*

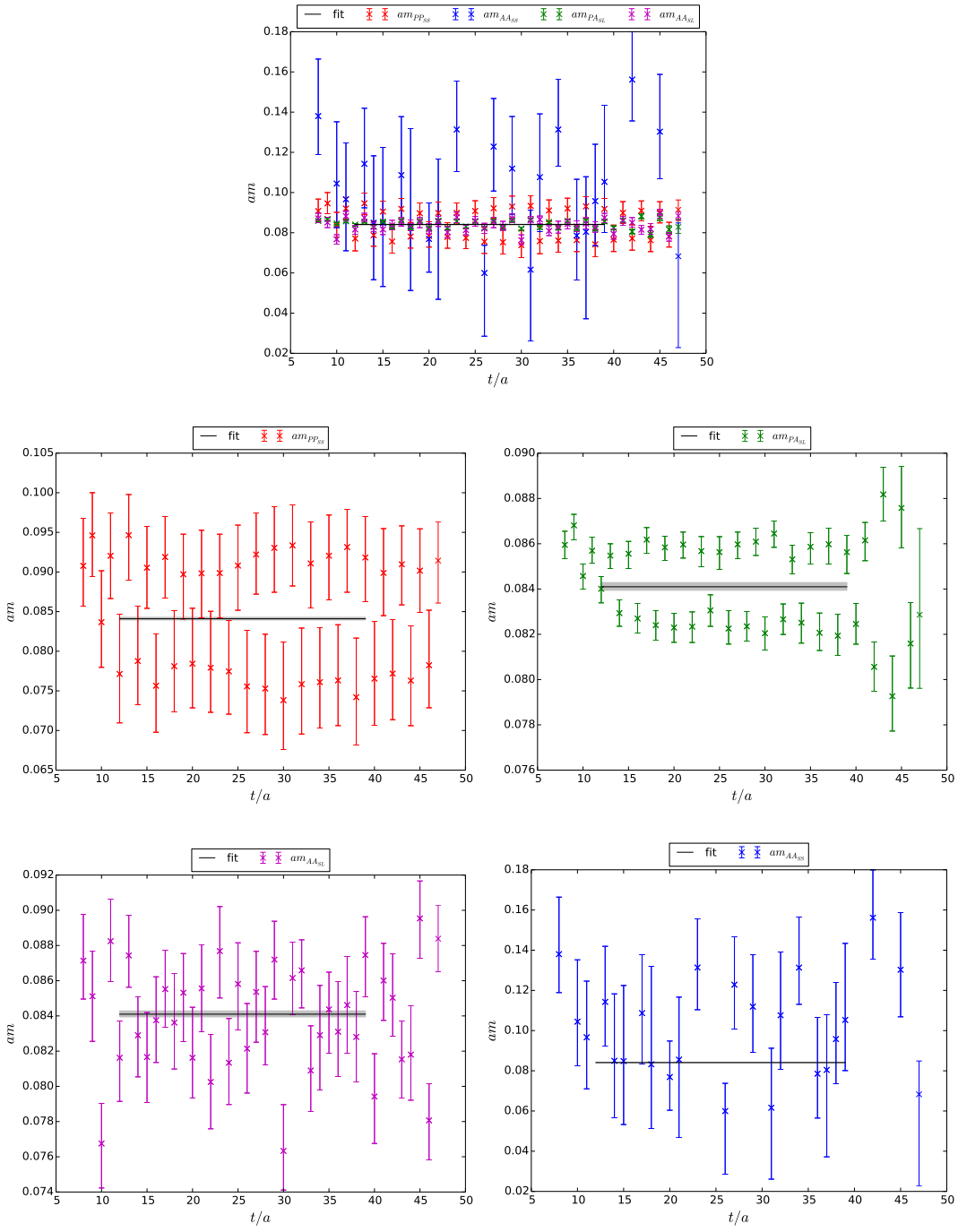

Figure A.11 *Effective mass for the pion on ensemble F1.*

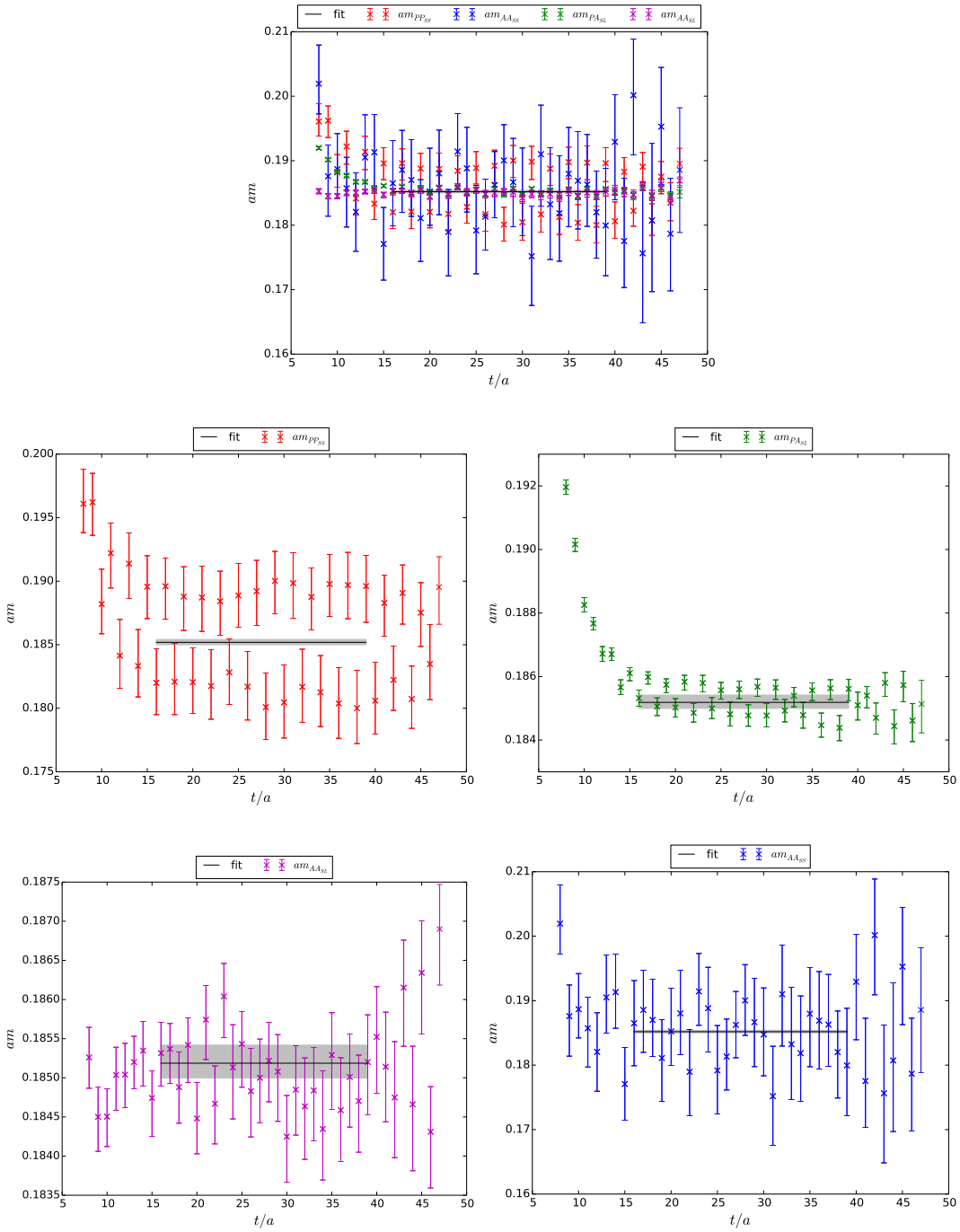

Figure A.12 *Effective mass for the kaon on ensemble F1.*

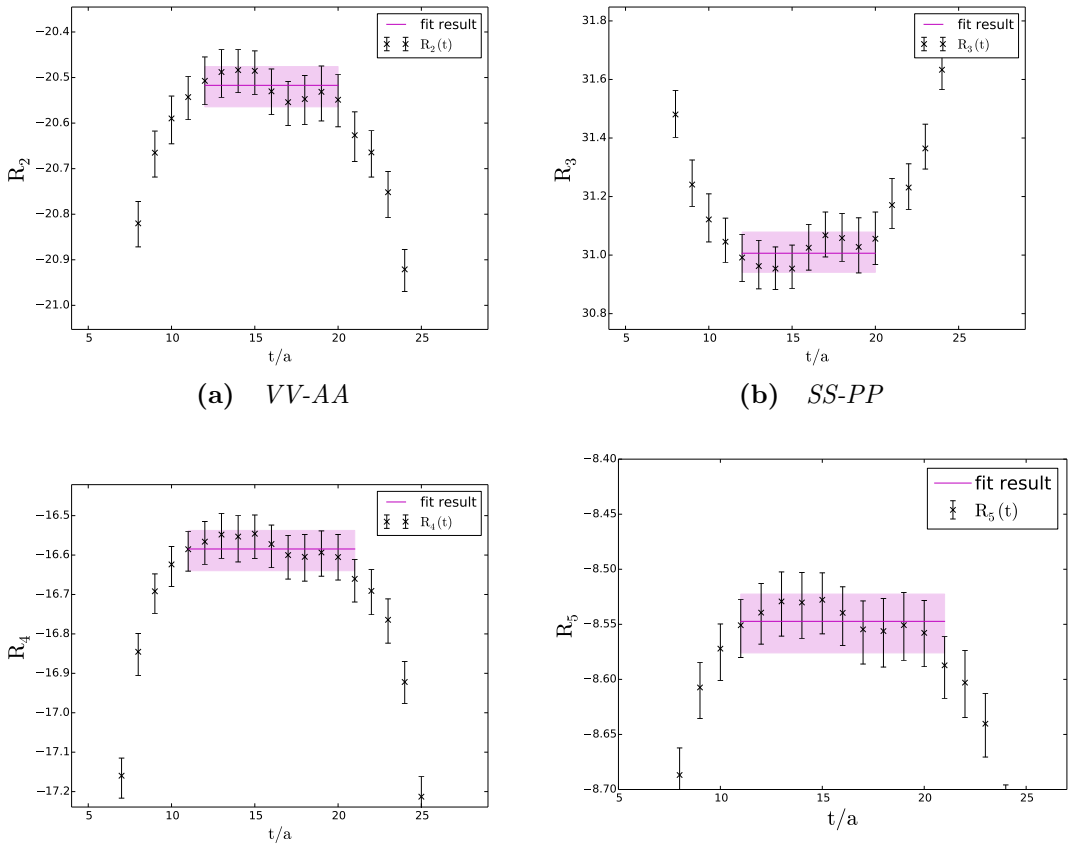

(a) *VV-AA* **(b)** *SS-PP*

(c) *SS+PP* **(d)** *TT*

Figure A.13 *Ratio parameter fits for ensemble C1.*

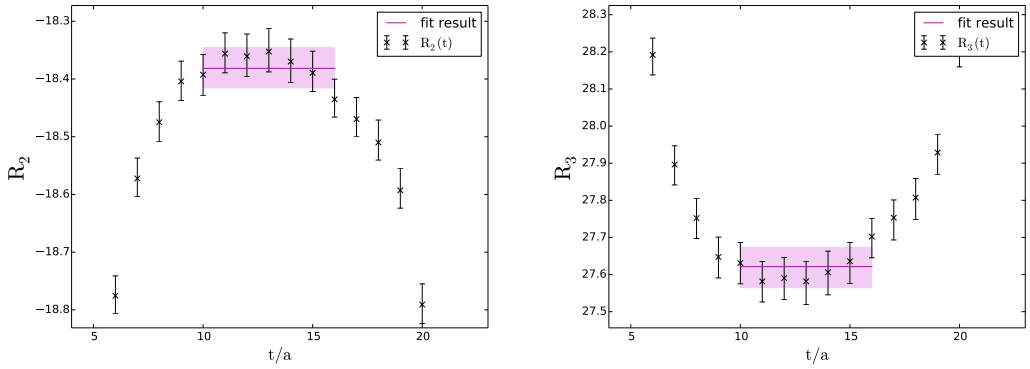

(a) *VV-AA* **(b)** *SS-PP*

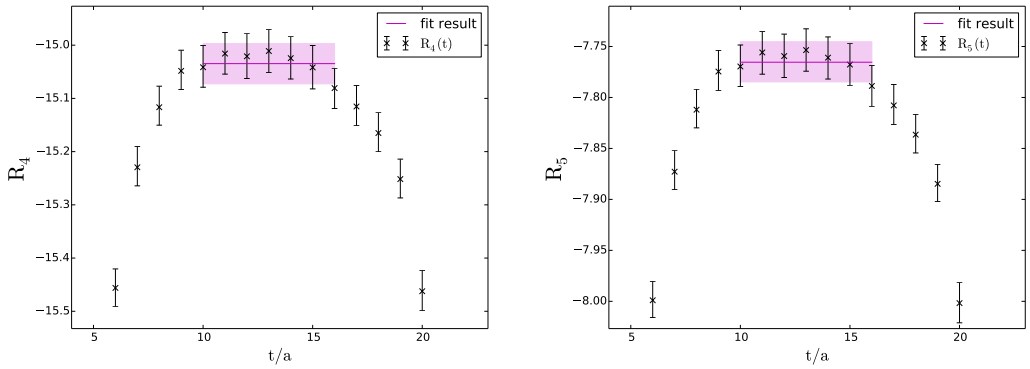

(c) *SS+PP* **(d)** *TT*

Figure A.14 *Ratio parameter fits for ensemble C2.*

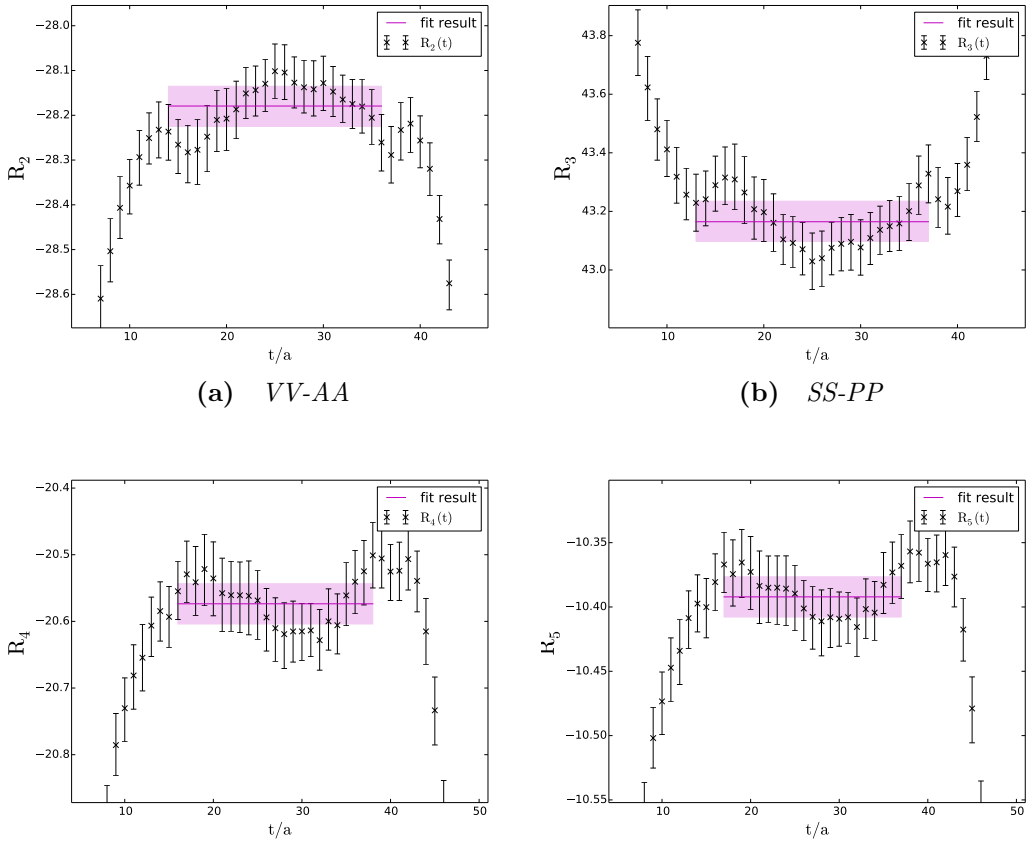

(a) *VV-AA* **(b)** *SS-PP*

(c) *SS+PP* **(d)** *TT*

Figure A.15 *Ratio parameter fits for ensemble M0.*

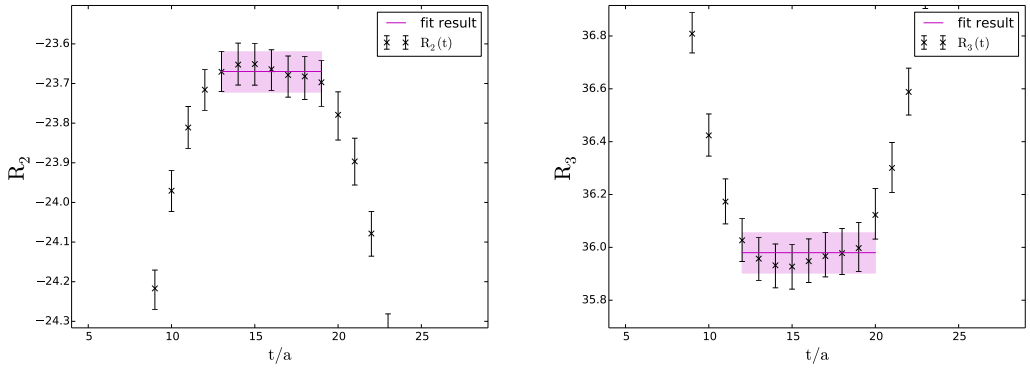

(a) *VV-AA* **(b)** *SS-PP*

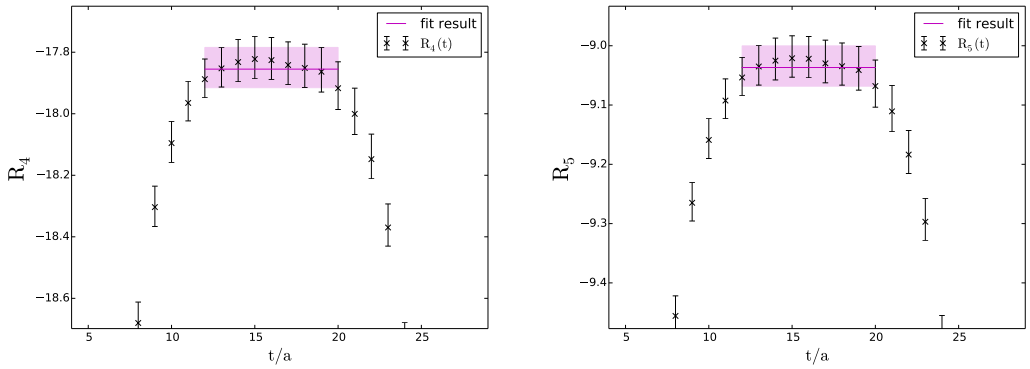

(c) *SS+PP* **(d)** *TT*

Figure A.16 *Ratio parameter fits for ensemble M2.*

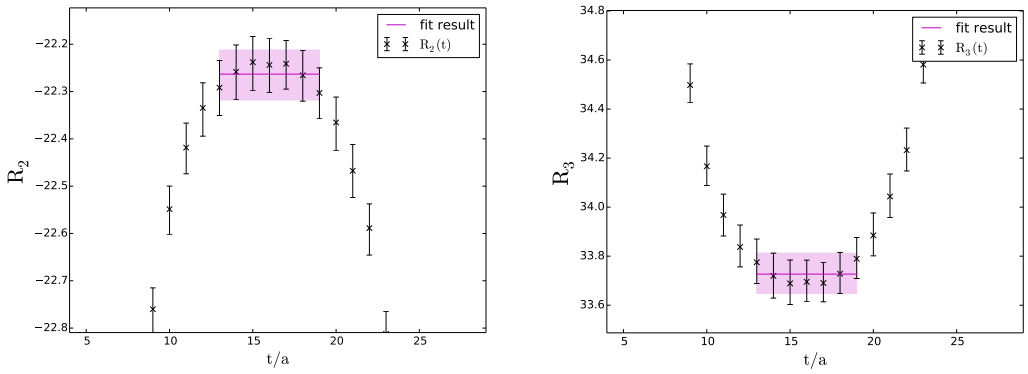

(a) *VV-AA* **(b)** *SS-PP*

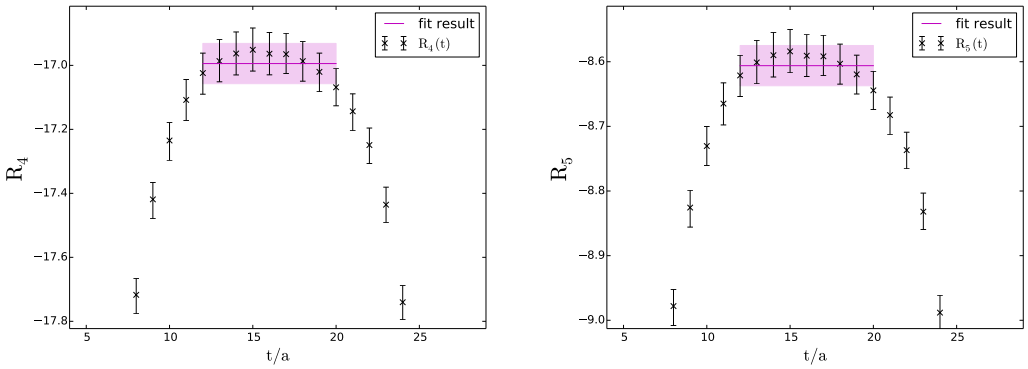

(c) *SS+PP* **(d)** *TT*

Figure A.17 *Ratio parameter fits for ensemble M3.*

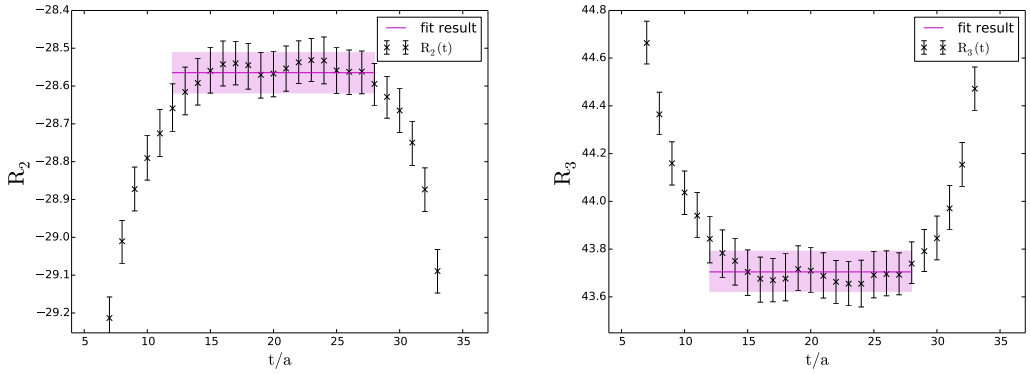

(a) *VV-AA*

(b) *SS-PP*

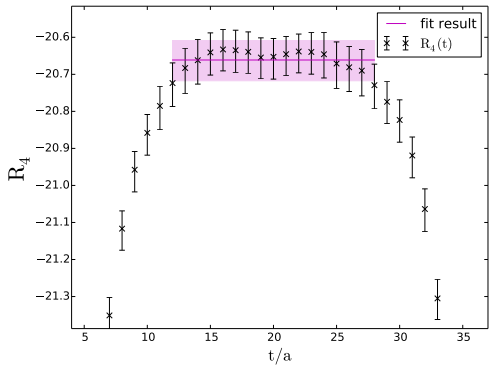

(c) *SS+PP*

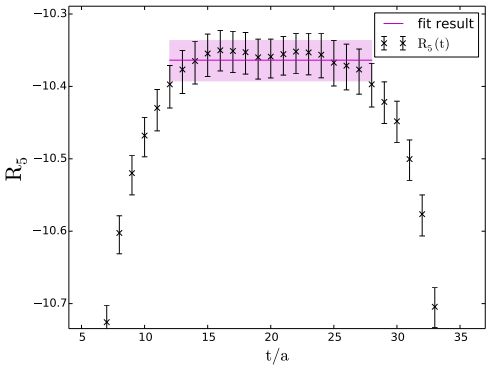

(d) *TT*

Figure A.18 *Ratio parameter fits for ensemble F1.*

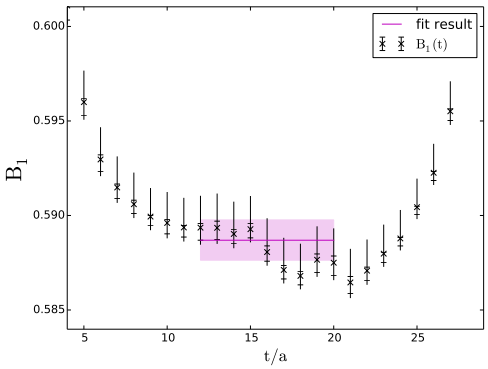

(a) *VV+AA*

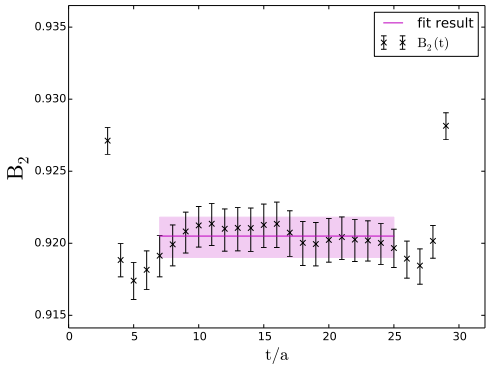

(b) *VV-AA*

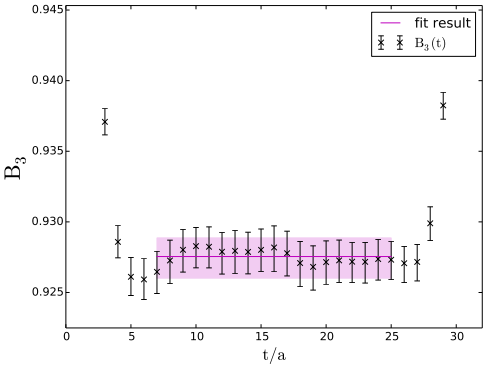

(c) *SS-PP*

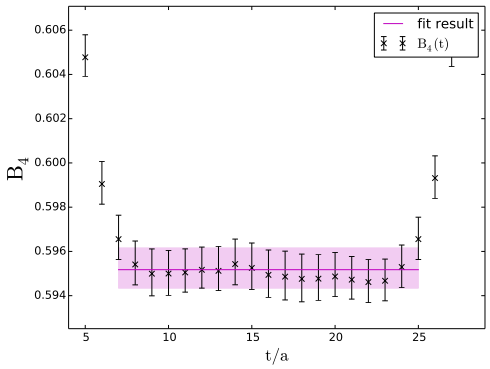

(d) *SS+PP*

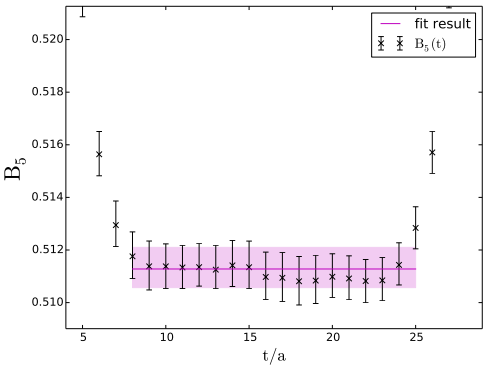

(e) *TT*

Figure A.19 *Bag parameter fits for ensemble C1.*

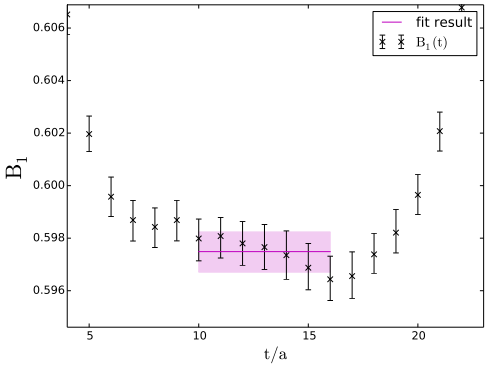

(a) *VV+AA*

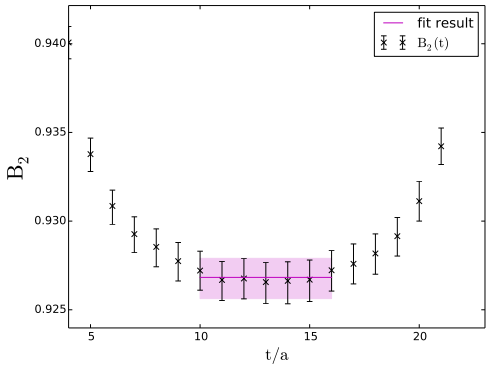

(b) *VV-AA*

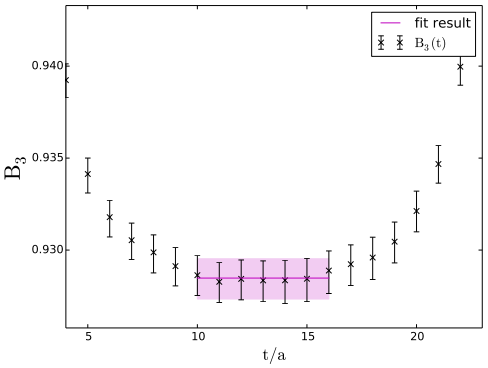

(c) *SS-PP*

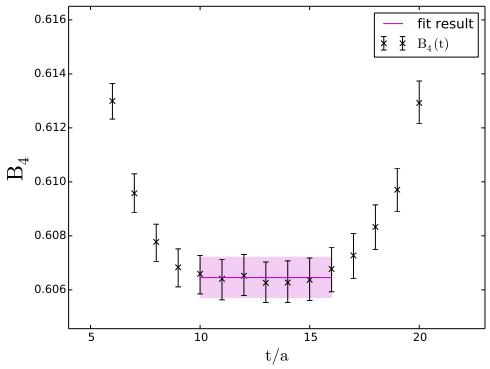

(d) *SS+PP*

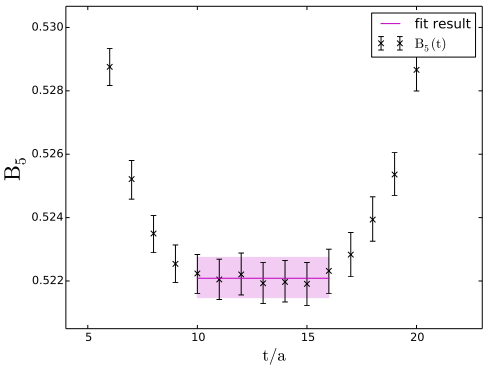

(e) *TT*

Figure A.20 *Bag parameter fits for ensemble C2.*

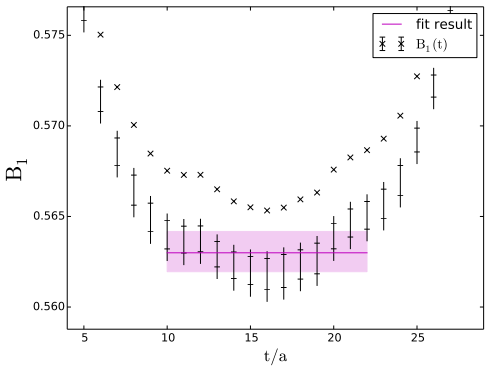

(a) *VV+AA*

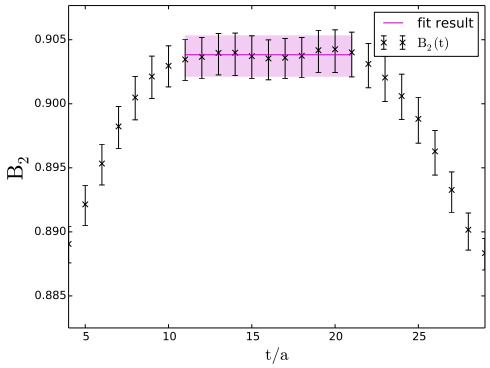

(b) *VV-AA*

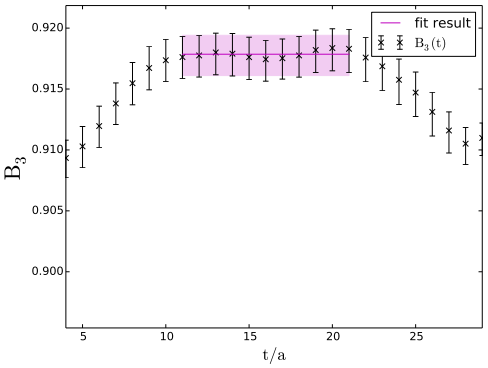

(c) *SS-PP*

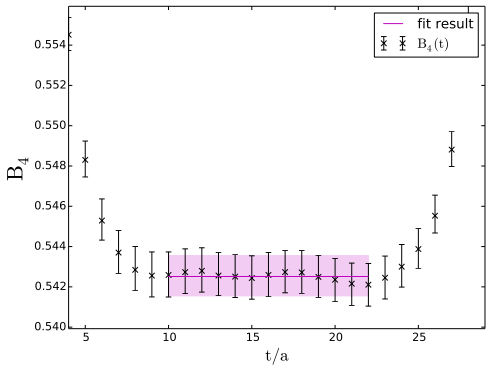

(d) *SS+PP*

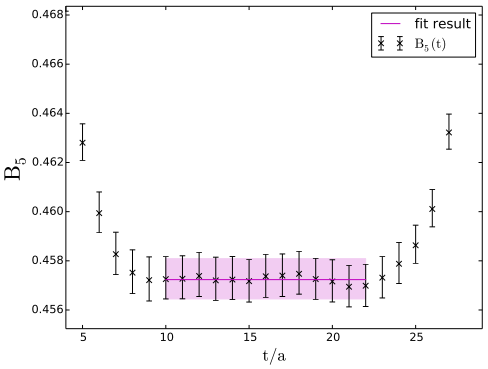

(e) *TT*

Figure A.21 *Bag parameter fits for ensemble M1.*

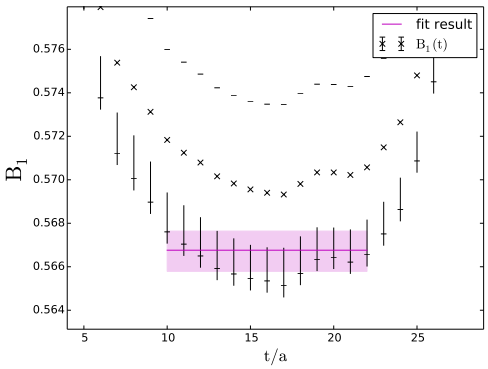

(a) *VV+AA*

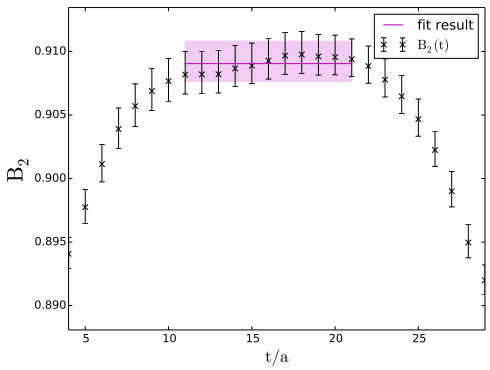

(b) *VV-AA*

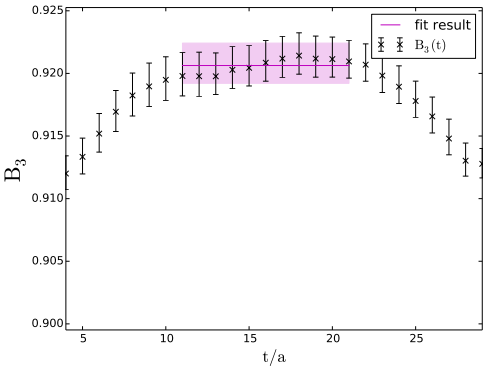

(c) *SS-PP*

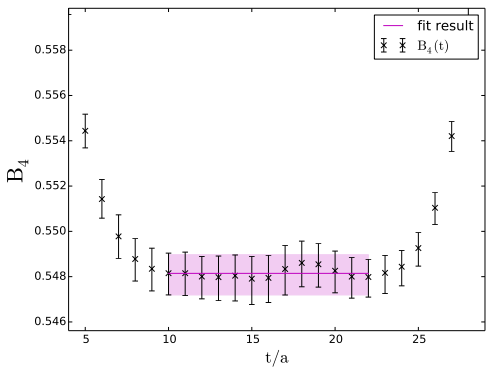

(d) *SS+PP*

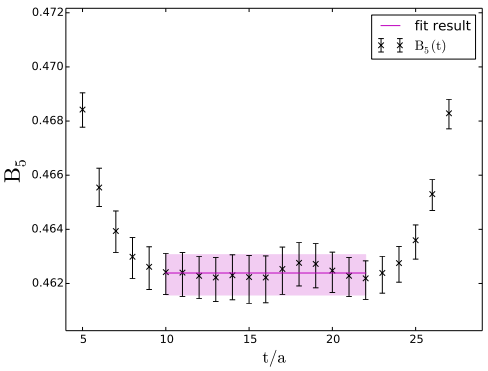

(e) *TT*

Figure A.22 *Bag parameter fits for ensemble M2.*

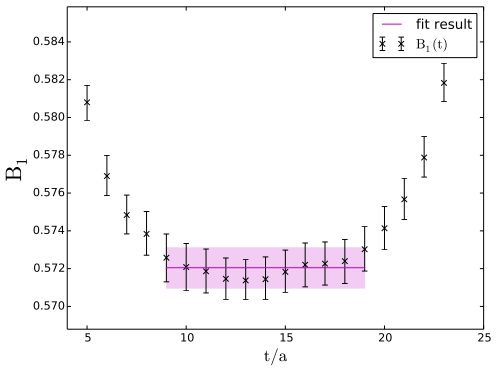

(a) *VV+AA*

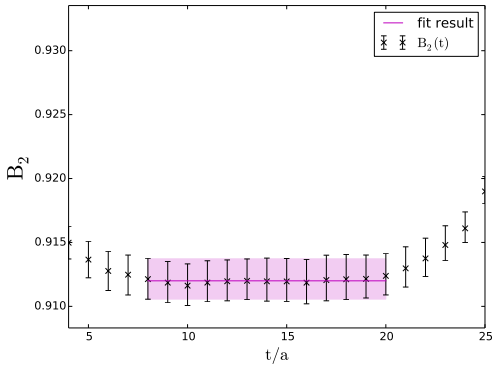

(b) *VV-AA*

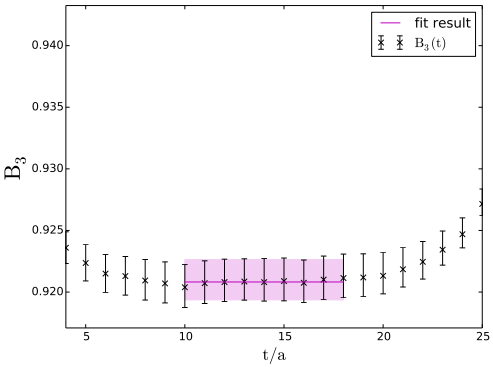

(c) *SS-PP*

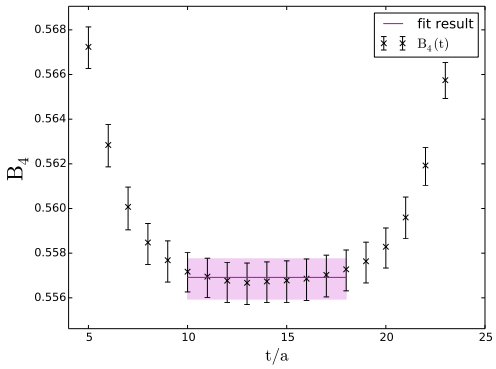

(d) *SS+PP*

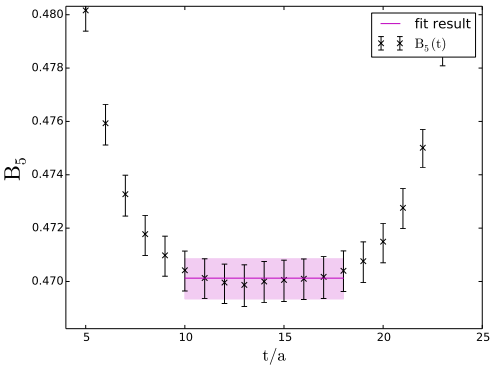

(e) *TT*

Figure A.23 *Bag parameter fits for ensemble M3.*

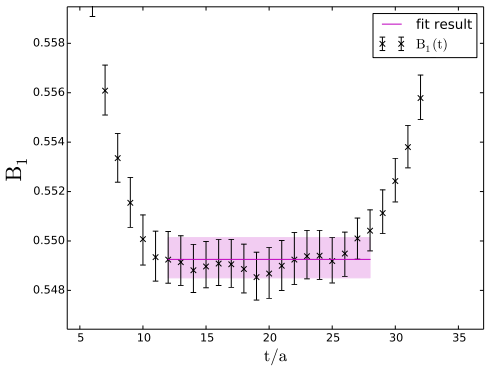

(a) *VV+AA*

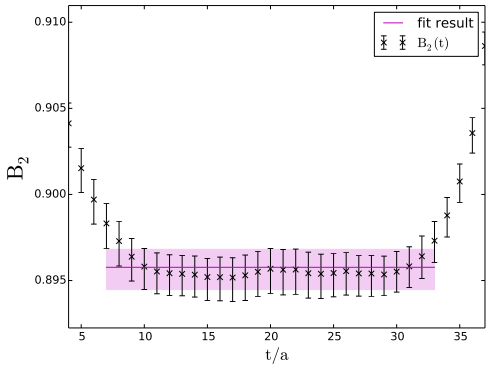

(b) *VV-AA*

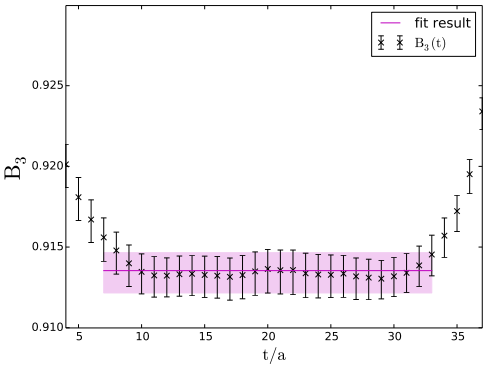

(c) *SS-PP*

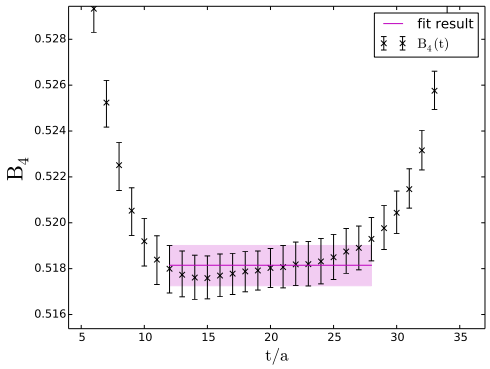

(d) *SS+PP*

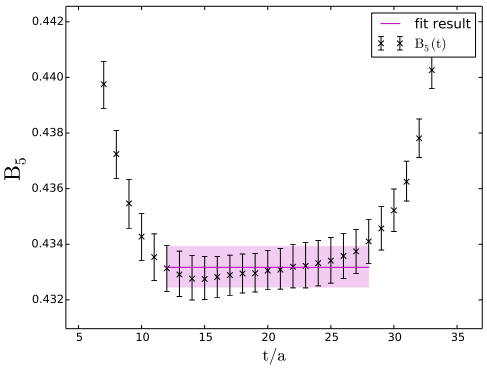

(e) *TT*

Figure A.24 *Bag parameter fits for ensemble F1.*

Appendix B

Uncorrected plots of fit results

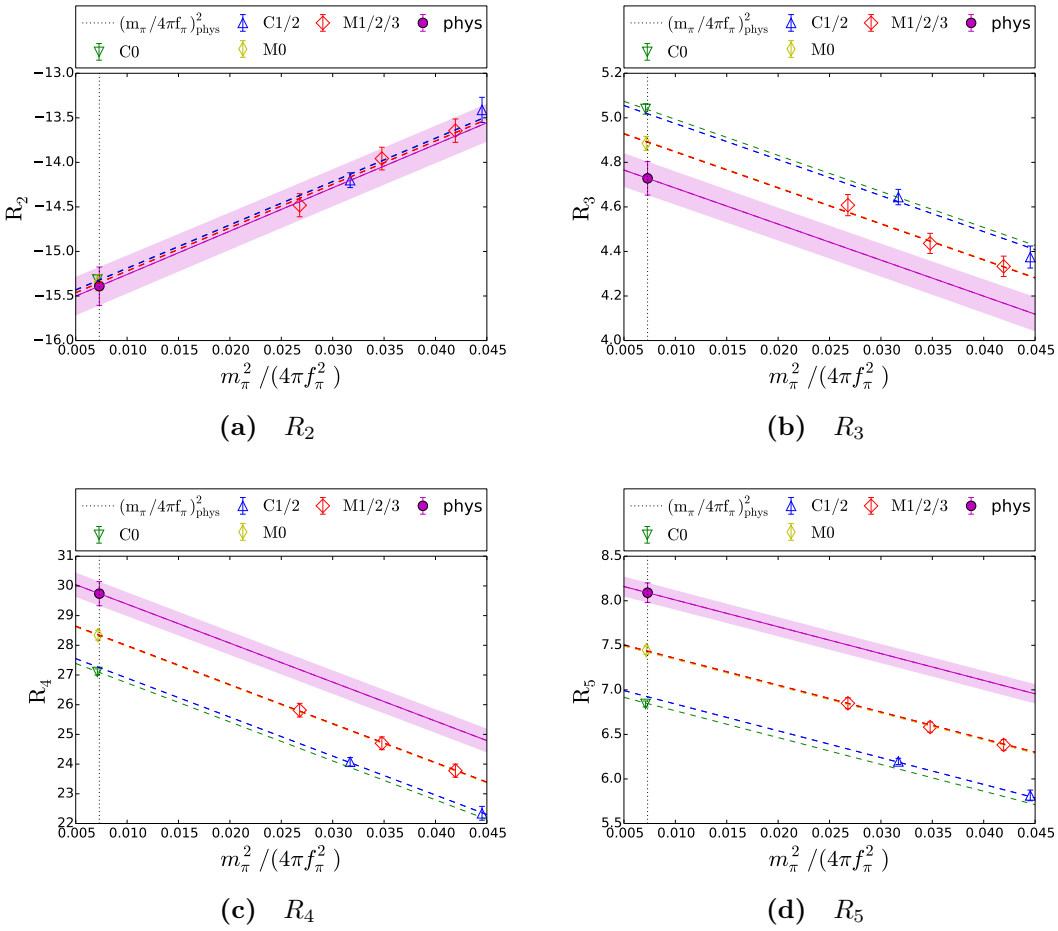

(a) R_2 **(b)** R_3

(c) R_4 **(d)** R_5

Figure B.1 *Central Value combined chiral continuum extrapolation of the ratio parameters renormalised at 2GeV in the SMOM$^{(\gamma_\mu,\gamma_\mu)}$ scheme according to the linear fit form described in equation 5.1.*

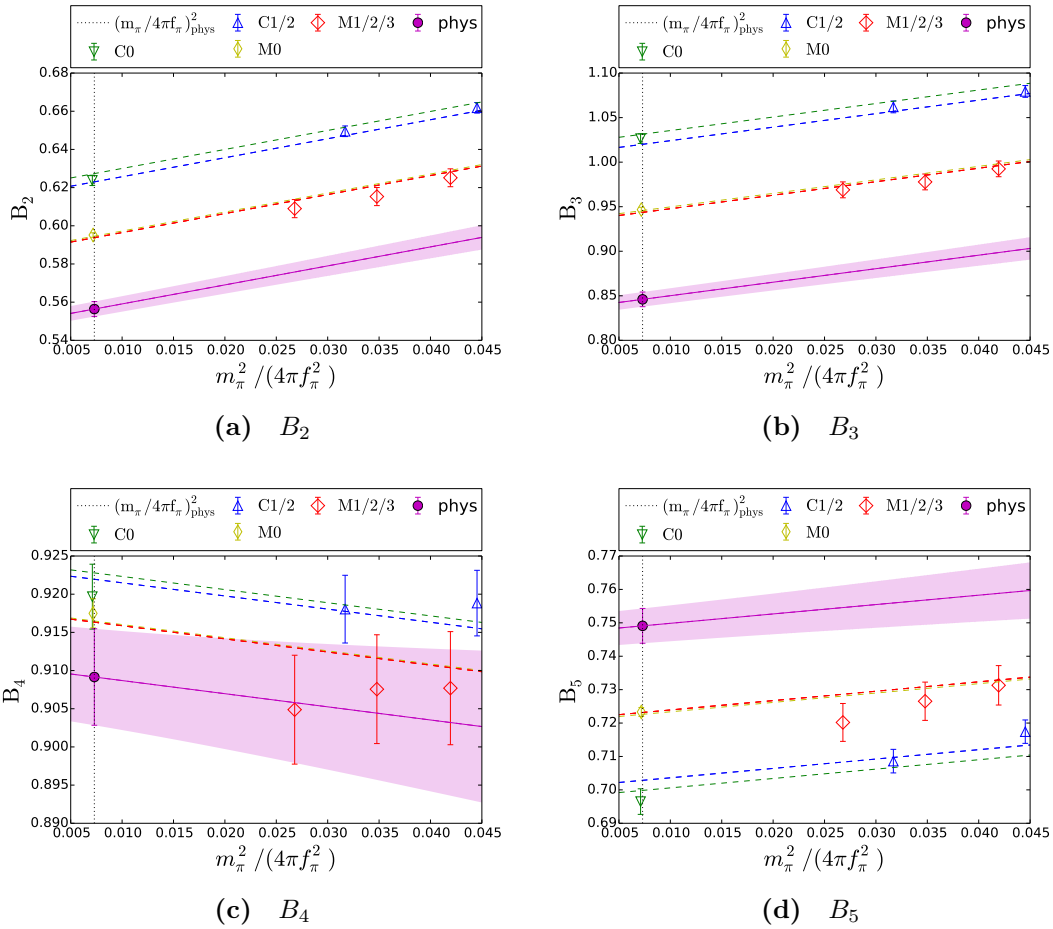

(a) B_2 **(b)** B_3

(c) B_4 **(d)** B_5

Figure B.2 *Central Value combined chiral continuum extrapolation of the BSM bag parameters renormalised at 2GeV in the SMOM$^{(\gamma_\mu,\gamma_\mu)}$ scheme according to the linear fit form described in equation 5.1.*

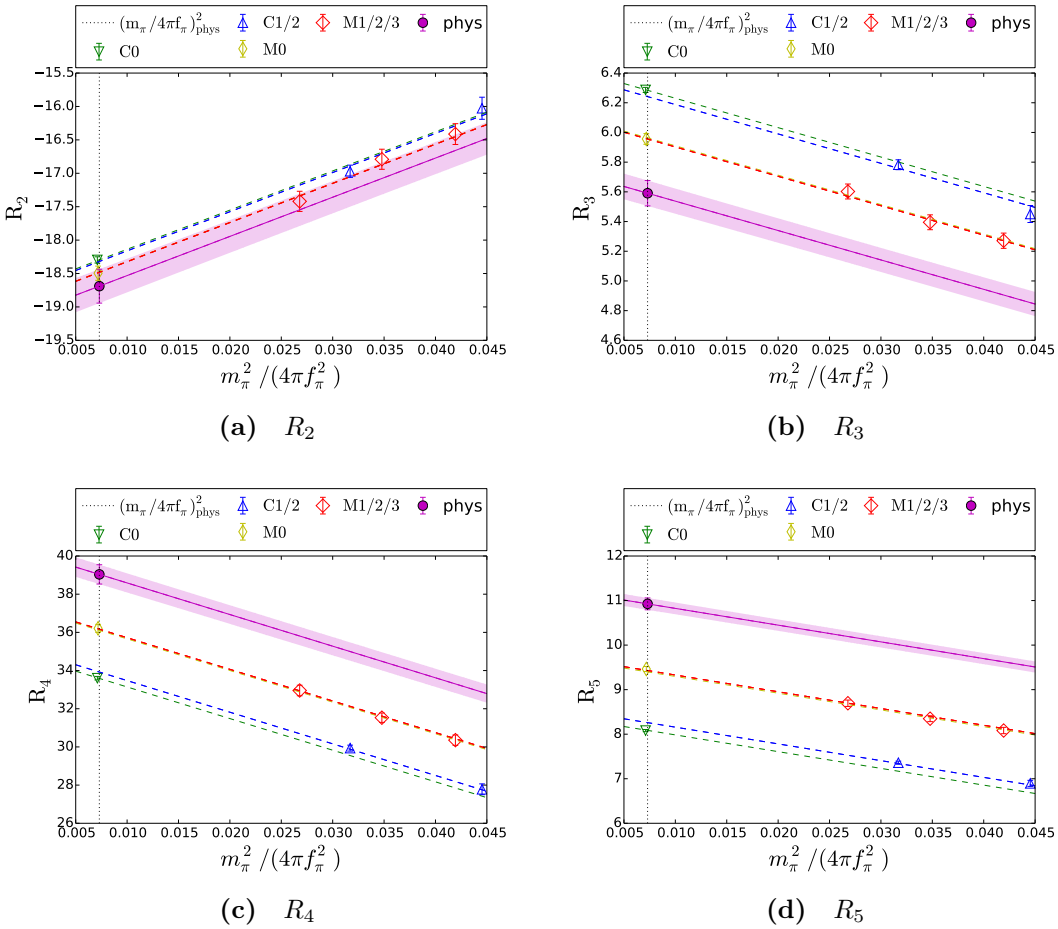

(a) R_2 **(b)** R_3

(c) R_4 **(d)** R_5

Figure B.3 *Central Value combined chiral continuum extrapolation of the ratio parameters renormalised at 3GeV in the SMOM$^{(\gamma_\mu,\gamma_\mu)}$ scheme according to the linear fit form described in equation 5.1.*

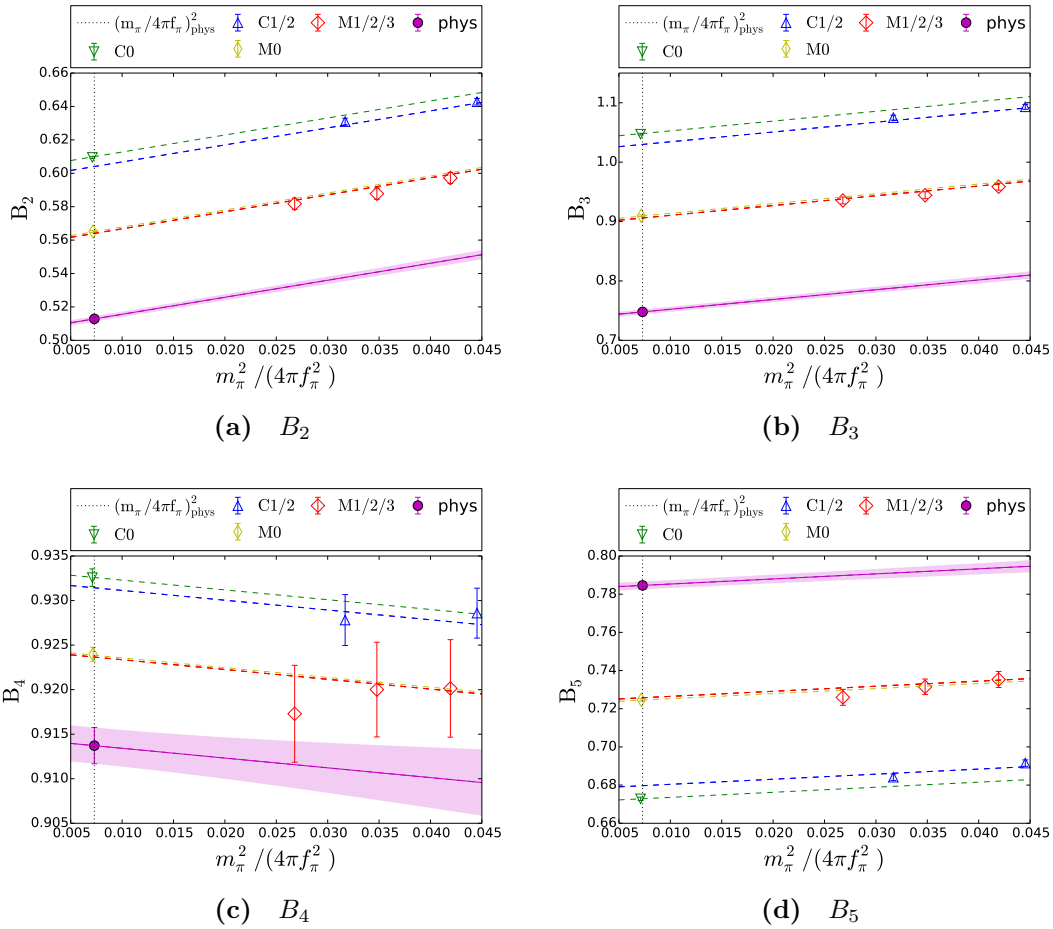

(a) B_2 **(b)** B_3

(c) B_4 **(d)** B_5

Figure B.4 *Central Value combined chiral continuum extrapolation of the BSM bag parameters renormalised at 3GeV in the SMOM$^{(\gamma_\mu,\gamma_\mu)}$ scheme according to the linear fit form described in equation 5.1.*

Appendix C

Minimisation of χ^2

In order to obtain the optimal values of the parameters we perform a minimisation in the value of χ^2 defined by,

$$\chi^2 = \sum_{j=0}^{N} \frac{(y_j - f(\mathbf{x}_j|\mathbf{p}))^2}{\sigma_j^2}, \tag{C.1}$$

where y_j and σ_j are the values and errors of y (R_i, B_i) for the data points, $\mathbf{x}_j$ indicate the vector of independent variables ($\frac{m_{ll}^2}{f_{ll}^2}, a^2, \delta_{m_s^{sea}}$) for each data point, f is the fit function, and $\mathbf{p}$ the vector of parameters. The minimisation is performed using the Marquardt-Levenburg algorithm.

Justification of defining χ^2 in y direction only

Notice that the only error that is taken into account is that for R_i and B_i, while the error on the lattice spacing, pion mass and decay constant and unphysicality of the strange sea mass are neglected. Here I justify this decision by considering the linear fit form given in 5.1. In practice the form used is,

$$Y_i(\frac{m_{ll}^2}{f_{ll}^2}, a^2) = p_0 + p_1\frac{m_{ll}^2}{f_{ll}^2} + p_2 a^2. \tag{C.2}$$

The linear fit form is a plane defined by the equation,

$$Ax + By + Cz = D, \tag{C.3}$$

where the variables are

$$x = a^2 \ ; \ y = Y\left(\frac{m_{ll}^2}{f_{ll}^2}, a^2\right) \ ; \ z = \frac{m_{ll}^2}{f_{ll}^2} \tag{C.4}$$

and the parameters

$$A = p_1 \ ; \ B = -1 \ ; \ C = p_2 \ ; \ D = -p_0. \tag{C.5}$$

Now let us rescale our coordinates by the error in order to simplify,

$$x' = \frac{x}{\sigma_x} \ , \ y' = \frac{y}{\sigma_y} \ , \ z' = \frac{z}{\sigma_z}, \tag{C.6}$$

such that the error on a data point (x'_0, y'_0, z'_0) is defined by a sphere of radius 1 centred at the data point.

The plane can now be written as

$$A'x' + B'y' + C'z' = D' \tag{C.7}$$

where the parameters have also been rescaled,

$$A' = \sigma_x A \ , \ B' = \sigma_y B \ , \ C' = \sigma_z C \ , \ D' = D. \tag{C.8}$$

The difference between taking into account all errors or only the y error is the difference between defining the residual as the length of the shortest approach to the fit function plane, and the distance to the plane in the y direction.

We can express the residual in the y direction only R_y as,

$$\begin{aligned} R_y &= y'_0 - \frac{(D' - A'x'_0 - C'z'_0)}{B} \\ &= \frac{1}{B'}(A'x'_0 + B'y'_0 + C'z'_0 - D') \end{aligned} \tag{C.9}$$

The shortest approach from a point $\vec{p} = (x_p, y_p, z_p)$ to a plane is given by the projection of the vector $\vec{v} = (x_p - x, y_p - y, z_p - z)$ where x, y, z define any coordinate the plane, onto the normal of the plane $\hat{n}$.

Table C.1 *The values of* $\left(\frac{\sigma_{m_\pi^2/(4\pi f_\pi)^2}}{\sigma_{Y_i}} p_{m_\pi^2/(4\pi f_\pi)^2, Y_i}\right)^2$ *to 5 decimal places, where* $Y_i = \{B_2, R_2, \cdots, B_5, R_5\}$*, and p is the parameter giving the gradient of* Y_i *w.r.t* $m_\pi^2/(4\pi f_\pi)^2$*. All values are* $O(5e^{-4})$ *or less, indicating this is an effect of less than 0.01%. Thus we can safely neglect the errors in* $m_\pi/(4\pi f_\pi)^2$ *in the global fit.*

	B_2	B_3	B_4	B_5	R_2	R_3	R_4	R_5
C0	0.00000	0.00001	0.00000	0.00000	0.00000	0.00000	0.00001	0.00001
C1	0.00019	0.00022	0.00000	0.00012	0.00000	0.00002	0.00011	0.00052
C2	0.00017	0.00020	0.00000	0.00010	0.00000	0.00001	0.00004	0.00016
M0	0.00006	0.00008	0.00000	0.00005	0.00000	0.00000	0.00001	0.00002
M1	0.00013	0.00025	0.00000	0.00009	0.00000	0.00002	0.00009	0.00035
M2	0.00017	0.00033	0.00000	0.00012	0.00000	0.00002	0.00013	0.00052
M3	0.00025	0.00048	0.00000	0.00016	0.00000	0.00003	0.00018	0.00068

Therefore the true residual R_t is

$$\begin{aligned} R_t &= \frac{\vec{v}.\hat{n}}{\hat{n}} \\ &= \frac{A'(x'_0 - x) + B'(y'_0 - y) + C'(z'_0 - z)}{A'^2 + B'^2 + C'^2} \\ &= \frac{A'x'_0 + B'y'_0 + C'z'_0 - D'}{A'^2 + B'^2 + C'^2} \end{aligned} \tag{C.10}$$

It is then trivial to show that:

$$R_t^2 = R_y^2 \frac{1}{1 + \frac{\sigma_x^2 A^2}{\sigma_y^2 B^2} + \frac{\sigma_z^2 C^2}{\sigma_y^2 B^2}}. \tag{C.11}$$

Recall that

$$\frac{\sigma_x^2 A^2}{\sigma_y^2 B^2} = \frac{\sigma_x^2}{\sigma_y^2} p_1 \text{ and } \frac{\sigma_z^2 C^2}{\sigma_y^2 B^2} = \frac{\sigma_z^2}{\sigma_y^2} p_2. \tag{C.12}$$

Provided these values are much less than 1 then our decision to consider the errors only in y was justified. While this expression does not hold for the chiral fits, given the chiral curvature observed is typically small, this result can still justify neglecting the spacing and mass errors, especially as deriving an expression for the true residuals for a non-linear fit function is non-trivial. We present these results in tables C.1 and C.2.

Table C.2 *The values of* $\left(\frac{\sigma_{a^2}^2}{\sigma_{Y_i}} p_{a^2,Y_i}\right)^2$ *to 5 decimal places, where* $Y_i = \{B_2, R_2, \cdots, B_5, R_5\}$*, and* p *is the parameter giving the gradient of* Y_i *w.r.t* a^2*. For most of the parameters this and effect of O(1%) or less. It is worth noting that for* B_2*,* B_3 *and* R_5 *where there is steeper gradient, that the effect rises closer to and order 5% effect some of the data points. However this is still small enough that we feel comfortable neglecting the error in* a^2*.*

	B_2	B_3	B_4	B_5	R_2	R_3	R_4	R_5
C0	0.01112	0.01733	0.00026	0.00191	0.00056	0.00096	0.01263	0.02521
C1	0.01807	0.01985	0.00042	0.00389	0.00039	0.00075	0.01211	0.03837
C2	0.01844	0.02001	0.00044	0.00394	0.00014	0.00037	0.00452	0.01306
M0	0.03892	0.04781	0.00087	0.01050	0.00013	0.00035	0.00344	0.00862
M1	0.00309	0.00543	0.00008	0.00075	0.00008	0.00020	0.00229	0.00625
M2	0.00311	0.00547	0.00008	0.00073	0.00008	0.00022	0.00264	0.00714
M3	0.00318	0.00556	0.00007	0.00069	0.00008	0.00021	0.00245	0.00653

Appendix D

Fierz Transformations

D.1 General Fierz identity

Fierz identities [66] relate to the reordering of spinor fields in a four particle interaction. $(\psi_1 M\bar{\psi}_2)(\psi_3 N\bar{\psi}_4)$ can be reordered as $(\psi_1 A\bar{\psi}_4)(\psi_3 B\bar{\psi}_2)$?

We have a vector space of spinors $\mathcal{R}$. Assume we know a basis in the matrix space $\mathcal{R}\otimes\mathcal{R}$ called Γ_a. The trace of basis matrices gives rise to a metric:

$$\mathrm{Tr}(\Gamma_a\Gamma_b) = g_{ab} \tag{D.1}$$

with which we can raise and lower indices as usual $\Gamma^a = \sum_b g^{ab}\Gamma_b$. Every matrix in this basis may be expanded in the basis:

$$M = \sum_a M^a\Gamma_a, \tag{D.2}$$

where $M^a = \mathrm{Tr}(M\Gamma^a)$. As discussed in [94], it can be shown that there exists a

completeness relation.

$$\begin{aligned}\Gamma^b_{ij} &= \left(\sum_a \mathrm{Tr}(\Gamma^b\Gamma_a)\Gamma^a\right)_{ij} \\ &= \sum_a \Gamma^b_{lk}\Gamma_{akl}\Gamma^a_{ij} \\ &= \Gamma^b_{lk}\sum_a \Gamma^a_{ij}\Gamma_{akl} \\ &= \Gamma^b_{lk}\delta_{il}\delta_{jk}.\end{aligned} \tag{D.3}$$

Therefore,

$$\sum_a \Gamma^a_{ij}\Gamma_{akl} = \delta_{il}\delta_{jk}. \tag{D.4}$$

Two matrices M and N can be written as

$$M_{ij}N_{kl} = \sum_{a,b} M^a N^a (\Gamma_a)_{ij}(\Gamma_b)_{kl}. \tag{D.5}$$

To find the relation between the reorderings of a four particle interaction consider two gamma matrices, twice multiplied by the expressions in the completeness relation.

$$\begin{aligned}(\Gamma_a)_{ij}(\Gamma_b)_{kl}\delta_{mn}\delta_{op}\delta_{qr}\delta_{st} &= (\Gamma_a)_{ij}(\Gamma_b)_{kl}\sum_c(\Gamma_c)_{mo}(\Gamma^c)_{pn}\sum_d(\Gamma_d)_{qs}(\Gamma^d)_{tr} \\ &= \sum_{c,d}(\Gamma_a)_{ij}(\Gamma^c)_{pn}(\Gamma_b)_{kl}(\Gamma^d)_{tr}(\Gamma_c)_{mo}(\Gamma_d)_{qs} \\ (\Gamma_a)_{ij}(\Gamma_b)_{kl}\delta_{mn}\delta_{op}\delta_{qr}\delta_{st}\delta_{jp}\delta_{nk}\delta_{lt} &= \sum_{c,d}(\Gamma_a\Gamma^c\Gamma_b\Gamma^d)_{ir}(\Gamma_c)_{mo}(\Gamma_d)_{qs} \\ (\Gamma_a)_{ij}(\Gamma_b)_{kl}\delta_{mk}\delta_{oj}\delta_{qr}\delta_{sl} &= \sum_{c,d}(\Gamma_a\Gamma^c\Gamma_b\Gamma^d)_{ir}(\Gamma_c)_{mo}(\Gamma_d)_{qs} \\ (\Gamma_a)_{io}(\Gamma_b)_{ms}\delta_{qr}\delta_{ir} &= \sum_{c,d}(\Gamma_a\Gamma^c\Gamma_b\Gamma^d)_{rr}(\Gamma_c)_{mo}(\Gamma_d)_{qs} \\ (\Gamma_a)_{qo}(\Gamma_b)_{ms} &= \sum_{c,d}\mathrm{Tr}(\Gamma_a\Gamma^c\Gamma_b\Gamma^d)(\Gamma_c)_{mo}(\Gamma_d)_{qs}\end{aligned} \tag{D.6}$$

We define:

$$C_{abcd} = \sum_{c,d}\mathrm{Tr}(\Gamma_a\Gamma_d\Gamma_b\Gamma_c) \tag{D.7}$$

such that the previous equation can be expressed as

$$(\Gamma_a)_{ij}(\Gamma_b)_{kl} = \sum_{c,d} C_{ab}^{cd}(\Gamma_c)_{il}(\Gamma_d)_{kj}. \tag{D.8}$$

This represents the most general Fierz rearrangement formula.

D.2 The Fierz transformation between the colour mixed and unmixed bases

For this work we are interested in the transformation from $(\bar{s}_\alpha \Gamma d_\alpha)(\bar{s}_\beta \Gamma d_\beta)$ to $(\bar{s}_\alpha \Gamma d_\beta)(\bar{s}_\beta \Gamma d_\alpha)$, where we have used Greek letters to denote the colour indices to avoid confusion.

It is worth noting that C_{aa}^{cd} is non-zero only when $c = d$, such that,

$$\begin{aligned}
(SS)^{mix} &= \sum_i tr(\Gamma_i\Gamma_i)(\Gamma_i\Gamma_i)^{unm} \\
(PP)^{mix} &= \sum_i tr(\gamma_5\Gamma_i\gamma_5\Gamma_i)(\Gamma_i\Gamma_i)^{unm} \\
(VV)^{mix} &= \sum_i tr(\gamma_\mu\Gamma_i\gamma_\mu\Gamma_i)(\Gamma_i\Gamma_i)^{unm} \\
(AA)^{mix} &= \sum_i tr(\gamma_\mu\gamma_5\Gamma_i\gamma_\mu\gamma_5\Gamma_i)(\Gamma_i\Gamma_i)^{unm} \\
(TT)^{mix} &= \sum_i^{16} tr(\frac{1}{2}\sigma_{\mu\nu}\Gamma_i\frac{1}{2}\sigma_{\mu\nu}\Gamma_i)(\Gamma_i\Gamma_i)^{unm},
\end{aligned} \tag{D.9}$$

Therefore the task is to calculate all traces in the above equation. It is fairly straightforward to arrive at,

$$\begin{pmatrix} SS \\ PP \\ VV \\ AA \\ TT \end{pmatrix}^{mix} = \frac{1}{4}\begin{pmatrix} 1 & 1 & 1 & -1 & -1 \\ 1 & 1 & -1 & 1 & -1 \\ 4 & -4 & -2 & -2 & 0 \\ -4 & 4 & -2 & -2 & 0 \\ -6 & -6 & 0 & 0 & -2 \end{pmatrix}\begin{pmatrix} SS \\ PP \\ VV \\ AA \\ TT \end{pmatrix}^{unm}, \tag{D.10}$$

where there has been a division by $n_\Gamma = 16$ to normalise. Which leads to,

$$\begin{pmatrix} VV+AA \\ VV-AA \\ SS-PP \\ SS+PP \\ TT \end{pmatrix}^{mix} \begin{pmatrix} -1 & 0 & 0 & 0 & 0 \\ 0 & 0 & 2 & 0 & 0 \\ 0 & 1/2 & 0 & 0 & 0 \\ 0 & 0 & 0 & 1/2 & -1/2 \\ 0 & 0 & 0 & -3/2 & 1/2 \end{pmatrix} \begin{pmatrix} VV+AA \\ VV-AA \\ SS-PP \\ SS+PP \\ TT \end{pmatrix}^{unm} , \tag{D.11}$$

D.3 The Fierz transformation between the SUSY and NPR basis

The even parity part of the SUSY basis can be written as,

$$\begin{pmatrix} VV+AA^{unm} \\ SS+PP^{unm} \\ SS+PP^{mix} \\ SS-PP^{unm} \\ SS-PP^{mix} \end{pmatrix} \tag{D.12}$$

It is simple to show that,

$$\begin{pmatrix} VV+AA^{unm} \\ SS+PP^{unm} \\ SS+PP^{mix} \\ SS-PP^{unm} \\ SS-PP^{mix} \end{pmatrix} \begin{pmatrix} 1 & 0 & 0 & 0 & 0 \\ 0 & 0 & 0 & 1 & 0 \\ 0 & 0 & 0 & 1/2 & -1/2 \\ 0 & 0 & 1 & 0 & 0 \\ 0 & 1/2 & 0 & 0 & 0 \end{pmatrix} \begin{pmatrix} VV+AA \\ VV-AA \\ SS-PP \\ SS+PP \\ TT \end{pmatrix}^{unm} , \tag{D.13}$$

Bibliography

[1] A. Alavi-Harati et al. Observation of direct CP violation in $K_{S,L} \to \pi\pi$ decays. *Phys. Rev. Lett.*, 83:22–27, 1999.

[2] C. Allton et al. Physical Results from 2+1 Flavor Domain Wall QCD and SU(2) Chiral Perturbation Theory. *Phys. Rev.*, D78:114509, 2008.

[3] C. R. Allton, L. Conti, A. Donini, V. Gimenez, Leonardo Giusti, G. Martinelli, M. Talevi, and A. Vladikas. B parameters for Delta S = 2 supersymmetric operators. *Phys. Lett.*, B453:30–39, 1999.

[4] C. R. Allton et al. Gauge invariant smearing and matrix correlators using Wilson fermions at Beta = 6.2. *Phys. Rev.*, D47:5128–5137, 1993.

[5] Leandro G. Almeida and Christian Sturm. Two-loop matching factors for light quark masses and three-loop mass anomalous dimensions in the RI/SMOM schemes. *Phys. Rev.*, D82:054017, 2010.

[6] S. Aoki et al. Review of lattice results concerning low-energy particle physics. *The European Physical Journal C*, 77(2):112, Feb 2017.

[7] Y. Aoki, R. Arthur, T. Blum, P.A. Boyle, D. Brommel, et al. Continuum Limit of B_K from 2+1 Flavor Domain Wall QCD. *Phys.Rev.*, D84:014503, 2011.

[8] Y. Aoki, P.A. Boyle, N.H. Christ, C. Dawson, M.A. Donnellan, et al. Non-perturbative renormalization of quark bilinear operators and B(K) using domain wall fermions. *Phys.Rev.*, D78:054510, 2008.

[9] Y. Aoki et al. Continuum Limit Physics from 2+1 Flavor Domain Wall QCD. *Phys. Rev.*, D83:074508, 2011.

[10] Yasumichi Aoki. Quark mass renormalization with non-exceptional momenta. *PoS*, LATTICE2008:222, 2008.

[11] R. Arthur and P.A. Boyle. Step Scaling with off-shell renormalisation. *Phys.Rev.*, D83:114511, 2011.

[12] R. Arthur, P.A. Boyle, N. Garron, C. Kelly, and A.T. Lytle. Opening the Rome-Southampton window for operator mixing matrices. *Phys.Rev.*, D85:014501, 2012.

[13] R. Arthur et al. Domain Wall QCD with Near-Physical Pions. *Phys.Rev.*, D87:094514, 2013.

[14] Ronald Babich, Nicolas Garron, Christian Hoelbling, Joseph Howard, Laurent Lellouch, and Claudio Rebbi. K0 - anti K0 mixing beyond the standard model and CP-violating electroweak penguins in quenched QCD with exact chiral symmetry. *Phys. Rev.*, D74:073009, 2006.

[15] Taegil Bae et al. Neutral kaon mixing from new physics: matrix elements in $N_f = 2 + 1$ lattice QCD. *Phys. Rev.*, D88(7):071503, 2013.

[16] Taegil Bae et al. Improved determination of BK with staggered quarks. *Phys. Rev.*, D89(7):074504, 2014.

[17] Z. Bai et al. Standard Model Prediction for Direct CP Violation in K Decay. *Phys. Rev. Lett.*, 115(21):212001, 2015.

[18] Ziyuan Bai. Long distance part of ϵ_K from lattice QCD. *PoS*, LATTICE2016:309, 2017.

[19] Jon A. Bailey, Yong-Chull Jang, Weonjong Lee, and Sungwoo Park. Standard Model evaluation of ε_K using lattice QCD inputs for $\hat{B}_K$ and V_{cb}. *Phys. Rev.*, D92(3):034510, 2015.

[20] Jon A. Bailey, Sunkyu Lee, Weonjong Lee, Jaehoon Leem, and Sungwoo Park. Updated evaluation of ϵ_K in the standard model with lattice QCD inputs. *Phys. Rev.*, D98(9):094505, 2018.

[21] E. Barberio. Inclusive and exclusive determination of —vcb— and form factors. *Nuclear Physics B - Proceedings Supplements*, 170:102 – 106, 2007. Proceedings of the 11th International Conference on B-Physics at Hadron Machines.

[22] Damir Becirevic and Giovanni Villadoro. Remarks on the hadronic matrix elements relevant to the SUSY K0 - anti-K0 mixing amplitude. *Phys. Rev.*, D70:094036, 2004.

[23] Paulo F. Bedaque. Aharonov-Bohm effect and nucleon nucleon phase shifts on the lattice. *Phys. Lett.*, B593:82–88, 2004.

[24] J. Beringer et al. Review of Particle Physics (RPP). *Phys.Rev.*, D86:010001 (and 2013 partial update for the 2014 edition.), 2012.

[25] Florian U. Bernlochner, Zoltan Ligeti, Michele Papucci, and Dean J. Robinson. Tensions and correlations in $|V_{cb}|$ determinations. *Phys. Rev.*, D96(9):091503, 2017.

[26] V. Bertone et al. Kaon Mixing Beyond the SM from N_f=2 tmQCD and model independent constraints from the UTA. *JHEP*, 03:089, 2013. [Erratum: JHEP07,143(2013)].

[27] Dante Bigi, Paolo Gambino, and Stefan Schacht. A fresh look at the determination of $|V_{cb}|$ from $B \to D^* \ell \nu$. *Phys. Lett.*, B769:441–445, 2017.

[28] T. Blum et al. Nonperturbative renormalization of domain wall fermions: Quark bilinears. *Phys. Rev.*, D66:014504, 2002.

[29] T. Blum et al. Lattice determination of the $K \to (\pi\pi)_{I=2}$ Decay Amplitude A_2. *Phys. Rev.*, D86:074513, 2012.

[30] T. Blum et al. $K \to \pi\pi$ $\Delta I = 3/2$ decay amplitude in the continuum limit. *Phys. Rev.*, D91(7):074502, 2015.

[31] T. Blum et al. Domain wall QCD with physical quark masses. *Phys. Rev.*, D93(7):074505, 2016.

[32] Artan Borici. Truncated overlap fermions: The Link between overlap and domain wall fermions. pages 41–52, 1999.

[33] P. A. Boyle, N. Garron, and R. J. Hudspith. Neutral kaon mixing beyond the standard model with $N_f = 2 + 1$ chiral fermions. *Phys. Rev.*, D86:054028, 2012.

[34] P. A. Boyle, A. Juttner, C. Kelly, and R. D. Kenway. Use of stochastic sources for the lattice determination of light quark physics. *JHEP*, 08:086, 2008.

[35] P.A. Boyle, N. Garron, and A.T. Lytle. Non-perturbative running and renormalization of kaon four-quark operators with nf=2+1 domain-wall fermions. *PoS*, LATTICE2011:227, 2011.

[36] Peter Boyle, Nicolas Garron, Renwick James Hudspith, Andreas Juttner, Julia Kettle, Ava Khamseh, and Justus Tobias Tsang. Beyond the Standard Model Kaon Mixing with Physical Masses. *PoS*, LATTICE2018:285, 2019.

[37] Peter Boyle, Nicolas Garron, Julia Kettle, Ava Khamseh, and Justus Tobias Tsang. BSM Kaon Mixing at the Physical Point. *EPJ Web Conf.*, 175:13010, 2018.

[38] Peter Boyle, Azusa Yamaguchi, Guido Cossu, and Antonin Portelli. Grid: A next generation data parallel C++ QCD library. 2015.

[39] Peter A. Boyle, Luigi Del Debbio, Andreas Jttner, Ava Khamseh, Francesco Sanfilippo, and Justus Tobias Tsang. The decay constants $\mathbf{f_D}$ and $\mathbf{f_{D_s}}$ in the continuum limit of $\mathbf{N_f = 2 + 1}$ domain wall lattice QCD. *JHEP*, 12:008, 2017.

[40] Peter A. Boyle, Nicolas Garron, Renwick J. Hudspith, Christoph Lehner, and Andrew T. Lytle. Neutral kaon mixing beyond the Standard Model with $\mathrm{n}_f = 2 + 1$ chiral fermions. Part 2: non perturbative renormalisation of the $\Delta F = 2$ four-quark operators. *JHEP*, 10:054, 2017.

[41] Joachim Brod and Martin Gorbahn. Epsilon$_K$ at Next-to-Next-to-Leading Order: The Charm-Top-Quark Contribution. *Phys. Rev.*, D82:094026, 2010.

[42] Joachim Brod and Martin Gorbahn. Next-to-Next-to-Leading-Order Charm-Quark Contribution to the CP Violation Parameter ϵ_K and ΔM_K. *Phys. Rev. Lett.*, 108:121801, 2012.

[43] R.C. Brower, H. Neff, and K. Orginos. Möbius fermions. *Nucl.Phys.Proc.Suppl.*, 153:191–198, 2006.

[44] Richard Brower, Ron Babich, Kostas Orginos, Claudio Rebbi, David Schaich, and Pavlos Vranas. Moebius Algorithm for Domain Wall and GapDW Fermions. *PoS*, LATTICE2008:034, 2008.

[45] Richard C. Brower, Harmut Neff, and Kostas Orginos. The Möbius Domain Wall Fermion Algorithm. 2012.

[46] Richard C. Brower, Hartmut Neff, and Kostas Orginos. Möbius fermions: Improved domain wall chiral fermions. *Nucl.Phys.Proc.Suppl.*, 140:686–688, 2005.

[47] Andrzej J. Buras. Weak Hamiltonian, CP violation and rare decays. In *Probing the standard model of particle interactions. Proceedings, Summer School in Theoretical Physics, NATO Advanced Study Institute, 68th session, Les Houches, France, July 28-September 5, 1997. Pt. 1, 2*, pages 281–539, 1998.

[48] Andrzej J. Buras and Diego Guadagnoli. Correlations among new CP violating effects in Δ F = 2 observables. *Phys. Rev.*, D78:033005, 2008.

[49] Andrzej J. Buras, Diego Guadagnoli, and Gino Isidori. On ϵ_K Beyond Lowest Order in the Operator Product Expansion. *Phys. Lett.*, B688:309–313, 2010.

[50] Andrzej J. Buras, Matthias Jamin, and Peter H. Weisz. Leading and next-to-leading qcd corrections to ϵ-parameter and b0b0 mixing in the presence of a heavy top quark. *Nuclear Physics B*, 347(3):491 – 536, 1990.

[51] Andrzej J. Buras, Mikolaj Misiak, and Jorg Urban. Two loop QCD anomalous dimensions of flavor changing four quark operators within and beyond the standard model. *Nucl. Phys.*, B586:397–426, 2000.

[52] H. Burkhardt et al. First Evidence for Direct CP Violation. *Phys. Lett.*, B206:169–176, 1988.

[53] Nicola Cabibbo. Unitary symmetry and leptonic decays. *Phys. Rev. Lett.*, 10:531–533, Jun 1963.

[54] Curtis G. Callan, Jr. and Jeffrey A. Harvey. Anomalies and Fermion Zero Modes on Strings and Domain Walls. *Nucl. Phys.*, B250:427–436, 1985.

[55] N. Carrasco, P. Dimopoulos, R. Frezzotti, V. Lubicz, G. C Rossi, S. Simula, and C. Tarantino. DeltaS=2 and DeltaC=2 bag parameters in the standard model and beyond from N_f=2+1+1 twisted-mass lattice QCD. *Phys. Rev.*, D92(3):034516, 2015.

[56] K. G. Chetyrkin and A. Retey. Renormalization and running of quark mass and field in the regularization invariant and MS-bar schemes at three loops and four loops. *Nucl. Phys.*, B583:3–34, 2000.

[57] Benjamin J. Choi et al. Kaon BSM B-parameters using improved staggered fermions from $N_f = 2 + 1$ unquenched QCD. *Phys. Rev.*, D93(1):014511, 2016.

[58] Norman H. Christ. Computing the long-distance contribution to the kaon mixing parameter ϵ_K. *PoS*, LATTICE2011:277, 2011.

[59] Norman H. Christ and Ziyuan Bai. Computing the long-distance contributions to ε_K. *PoS*, LATTICE2015:342, 2016.

[60] J. H. Christenson, J. W. Cronin, V. L. Fitch, and R. Turlay. Evidence for the 2π decay of the k_2^0 meson. *Phys. Rev. Lett.*, 13:138–140, Jul 1964.

[61] G.M. deDivitiis, R. Petronzio, and N. Tantalo. On the discretization of physical momenta in lattice qcd. *Physics Letters B*, 595(1):408 – 413, 2004.

[62] Shao-Jing Dong and Keh-Fei Liu. Stochastic estimation with z2 noise. *Physics Letters B*, 328(1):130 – 136, 1994.

[63] A. Donini, V. Gimenez, Leonardo Giusti, and G. Martinelli. Renormalization group invariant matrix elements of Delta S = 2 and Delta I = 3/2 four fermion operators without quark masses. *Phys. Lett.*, B470:233–242, 1999.

[64] B. Efron. Bootstrap methods: Another look at the jackknife. *Ann. Statist.*, 7(1):1–26, 01 1979.

[65] V. Fanti et al. A New measurement of direct CP violation in two pion decays of the neutral kaon. *Phys. Lett.*, B465:335–348, 1999.

[66] Markus Fierz. Zur fermischen theorie des β-zerfalls. *Zeitschrift für Physik*, 104(7):553–565, Jul 1937.

[67] J. M. Flynn, A. Juttner, and C. T. Sachrajda. A Numerical study of partially twisted boundary conditions. *Phys. Lett.*, B632:313–318, 2006.

[68] Vadim Furman and Yigal Shamir. Axial symmetries in lattice QCD with Kaplan fermions. *Nucl. Phys.*, B439:54–78, 1995.

[69] F. Gabbiani, E. Gabrielli, A. Masiero, and L. Silvestrini. A Complete analysis of FCNC and CP constraints in general SUSY extensions of the standard model. *Nucl. Phys.*, B477:321–352, 1996.

[70] N. Garron. personal communication.

[71] Nicolas Garron, Renwick J. Hudspith, and Andrew T. Lytle. Neutral Kaon Mixing Beyond the Standard Model with $N_f = 2 + 1$ Chiral Fermions Part 1: Bare Matrix Elements and Physical Results. *JHEP*, 11:001, 2016.

[72] Christof Gattringer and Christian B. Lang. Quantum chromodynamics on the lattice. *Lect. Notes Phys.*, 788:1–343, 2010.

[73] Paul H. Ginsparg and Kenneth G. Wilson. A Remnant of Chiral Symmetry on the Lattice. *Phys. Rev.*, D25:2649, 1982.

[74] S. L. Glashow, J. Iliopoulos, and L. Maiani. Weak interactions with lepton-hadron symmetry. *Phys. Rev. D*, 2:1285–1292, Oct 1970.

[75] M. Gockeler, R. Horsley, H. Oelrich, H. Perlt, D. Petters, et al. Nonperturbative renormalization of composite operators in lattice QCD. *Nucl.Phys.*, B544:699–733, 1999.

[76] Benjamin Grinstein and Andrew Kobach. Model-Independent Extraction of $|V_{cb}|$ from $\bar{B} \to D^* \ell \overline{\nu}$. *Phys. Lett.*, B771:359–364, 2017.

[77] S. Gusken. A Study of smearing techniques for hadron correlation functions. *Nucl. Phys. Proc. Suppl.*, 17:361–364, 1990.

[78] Stefan Herrlich and Ulrich Nierste. Enhancement of the K(L) - K(S) mass difference by short distance QCD corrections beyond leading logarithms. *Nucl. Phys.*, B419:292–322, 1994.

[79] R. J. Hudspith. Fourier Accelerated Conjugate Gradient Lattice Gauge Fixing. *Comput. Phys. Commun.*, 187:115–119, 2015.

[80] Takeo Inami and C. S. Lim. Effects of Superheavy Quarks and Leptons in Low-Energy Weak Processes KL, K++ and K0K0. *Progress of Theoretical Physics*, 65(1):297–314, 01 1981.

[81] Y. Iwasaki. Renormalization Group Analysis of Lattice Theories and Improved Lattice Action: Two-Dimensional Nonlinear O(N) Sigma Model. *Nucl. Phys.*, B258:141–156, 1985.

[82] Y. Iwasaki and T. Yoshie. Renormalization Group Improved Action for SU(3) Lattice Gauge Theory and the String Tension. *Phys. Lett.*, 143B:449–452, 1984.

[83] David B. Kaplan.

[84] David B. Kaplan. A Method for simulating chiral fermions on the lattice. *Phys. Lett.*, B288:342–347, 1992.

[85] Makoto Kobayashi and Toshihide Maskawa. CP-Violation in the Renormalizable Theory of Weak Interaction. *Progress of Theoretical Physics*, 49(2):652–657, 02 1973.

[86] Jaehoon Leem et al. Calculation of BSM Kaon B-parameters using Staggered Quarks. *PoS*, LATTICE2014:370, 2014.

[87] Christoph Lehner and Christian Sturm. Matching factors for Delta S=1 four-quark operators in RI-SMOM schemes. *Phys. Rev.*, D84:014001, 2011.

[88] Laurent Lellouch. Flavor physics and lattice quantum chromodynamics. In *Modern perspectives in lattice QCD: Quantum field theory and high performance computing. Proceedings, International School, 93rd Session, Les Houches, France, August 3-28, 2009*, pages 629–698, 2011.

[89] Martin Luscher. Exact chiral symmetry on the lattice and the Ginsparg-Wilson relation. *Phys. Lett.*, B428:342–345, 1998.

[90] A. T. Lytle, C. T. H. Davies, D. Hatton, G. P. Lepage, and C. Sturm. Determination of quark masses from $\mathbf{n_f = 4}$ lattice QCD and the RI-SMOM intermediate scheme. *Phys. Rev.*, D98(1):014513, 2018.

[91] G. Martinelli, C. Pittori, Christopher T. Sachrajda, M. Testa, and A. Vladikas. A General method for nonperturbative renormalization of lattice operators. *Nucl.Phys.*, B445:81–108, 1995.

[92] Rajamani Narayanan and Herbert Neuberger. A construction of lattice chiral gauge theories. *Nuclear Physics B*, 443(1):305 – 385, 1995.

[93] Holger Bech Nielsen and M. Ninomiya. No Go Theorem for Regularizing Chiral Fermions. *Phys. Lett.*, 105B:219–223, 1981.

[94] Jose F. Nieves and Palash B. Pal. Generalized Fierz identities. *Am. J. Phys.*, 72:1100–1108, 2004.

[95] C. Patrignani et al. Review of Particle Physics. *Chin. Phys.*, C40(10), 2016.

[96] M. H. Quenouille. Problems in plane sampling. *Ann. Math. Statist.*, 20(3):355–375, 09 1949.

[97] M. H. QUENOUILLE. NOTES ON BIAS IN ESTIMATION. *Biometrika*, 43(3-4):353–360, 12 1956.

[98] Yigal Shamir. Chiral fermions from lattice boundaries. *Nucl.Phys.*, B406:90–106, 1993.

[99] C. Sturm, Y. Aoki, N.H. Christ, T. Izubuchi, C.T.C. Sachrajda, et al. Renormalization of quark bilinear operators in a momentum-subtraction scheme with a nonexceptional subtraction point. *Phys.Rev.*, D80:014501, 2009.

[100] Kenneth G. Wilson. Confinement of quarks. *Phys. Rev. D*, 10:2445–2459, Oct 1974.

[101] Wolfenstein, Lincoln. Parametrization of the Kobayashi-Maskawa Matrix. *Phys. Rev. Lett.*, 51:1945–1947, Nov 1983.

[102] C.S. Wu, E. Ambler, R.W. Hayward, D.D. Hoppes, and R.P. Hudson. Experimental test of parity conservation in beta decay. *Physical Review (U.S.) Superseded in part by Phys. Rev. A, Phys. Rev. B: Solid State, Phys. Rev. C, and Phys. Rev. D*, 2 1957.